ANNUAL REPORT

OF THE

INSTITUTE OF PHYSICS

ACADEMIA SINICA
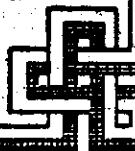
1970

IN COMMEMORATION OF

THE SIXTIETH ANNIVERSARY YEAR

OF

THE REPUBLIC OF CHINA

中央研究院物理研究所集刊

第 一 卷

中華民國建國六十年紀念特刊

中央研究院物理研究所印行

CONTENTS 目 錄

On the Nature of Theories of Irreversible Processes

Ta-You Wu (吳大猷)

Abstract

The purpose of the present article is to give an elementary discussion of the nature of the theories used to describe the observed irreversible processes in gases to the equilibrium state, with special regard to the explicit mathematical time–reversal invariance or non–invariance of the theories.

1. Introduction

1.1. Macroscopic Irreversibility and Empirical Laws

We are concerned with the non–equilibrium behavior of a gas. In order to be definite, let us state the nature of our observations. Consider a gas in an enclosure, which at a certain instant is in a non–equilibrium state. Observation shows that within a short time the gas approaches a steady state in which the molecular velocities are distributed according to Maxwell's law and the spatial distribution is uniform (in the case of no external field). Experience also shows that the approach to equilibrium, except for small fluctuations, is monotonic, the fluctuations being the smaller the greater is the average density of the gas. Other familiar irreversible processes are the mixing of gases by diffusion, the production of heat in viscous flows and the conduction of heat.

The above description of these processes as irreversible is a macroscopic view and is expressed in terms of concepts, or macroscopic variables, such as the density, temperature, pressure, etc. The mathematical expressions of the irreversibility are the familiar Fourier equations of heat conduction, the equation of diffusion, and the Navier–Stokes equation for viscous flow. All these equations are not invariant upon time reversal, i.e., are irreversible in time. This irreversibility is not the consequence of the basic dynamical laws governing the motion of the molecules; it is introduced into the equations on an empirical basis. We shall call these theories "phenomenological" theories, to distinguish them from others which we attempt to construct on the basis of more fundamental theories.

1.2. Thermodynamics

At the macroscopic level, classical thermodynamics deals with the properties of matter in the equilibrium state. The laws of thermodynamics are based on empirical experience in dealing with macroscopic phenomena. Even the axiomatic form of Carathecdory for the Second Law still depends on the validity of an empirical fact. The methods of thermodynamics are general in the sense that they do not depend on any specific or detailed knowledge of the system at the atomic level. For this reason, the thermodynamic method is powerful and its range of application wide. But it is for the same reason that it has its limitations. Thus thermodynamics can give no information on such a simple question as the equation of state of a given gas.

In thermodynamics, the concept of macroscopically irreversible processes plays a very basic role. The Second Law definitely determines the direction of the natural processes in a system not in thermodynamic equilibrium, namely, the direction of increasing entropy. This

irreversibility is not explained by the Second Law; rather, it is a part of the empirical experience that has gone into the formulation of the Second Law itself (in the induction and generalization process).

Modern non-equilibrium (or irreversible) thermodynamics has been developed to treat certain problems, in particular, processes in systems having small deviations from the equilibrium state. The conditions for the stablilty of an equilibrium state according to the Second Law determine the irreversible returns to the equilibrium state. A most important development is Onsager's (1931) theory of irreversible thermodynamics, which is beyond the scope of the present article. It is, however, so important in the subject of irreversible processes that a brief reference will be made below.

Consider a system in which there are temperature and density gradients. The heat flux J and the mass flux N can be expressed by equations of the form

$$J = a_{11} \nabla T + a_{12} \nabla n$$
$$N = a_{21} \nabla T + a_{22} \nabla n$$

where a_{11}, a_{22} are, up to proportional factors, the coefficients of heat conduction and diffusion, $a_{21} \triangle T$ gives the thermal diffusion and $a_{12} \triangle n$ the heat flow due to diffusion. These equations are the generalizations of the heat conduction and diffusion equations and are themselves parts of an irreversible theory. They can be regarded as phenomenological equations, or they can be derived from such a theory as Boltzmann's transport equation (Section 3.1), which itself is an irreversible theory.

In this particular case, Onsager's theory gives the following reciprocity relation (when all quantities are expressed in units of appropriate dimensions)

$$a_{12} = a_{21}$$

Such reciprocity relations, however, are not empirical in origin but can be proved from general principles such as the fundamental reversibility of microscopic processes.

Thus, important as the reciprocity relations are, they do not bear on the question of the basis of irreversible theories or on the origin of the observed macroscopic irreversibility, which is the subject of the present article.

1.3. Statistical-Kinetic Theories

In the kinetic theory of gases, one starts with a system of molecules. One is, however, not interested in a detailed knowledge of the individual molecules, but only in some macroscopic properties of the gas. These macroscopic properties must then be related to some average properties of the molecules. It is in dealing with extremely large numbers (Avogadro's number $= 6 \times 10^{23}$) that the probability concepts and statistical methods enter into the theory.

For systems in equilibrium, theories have been developed in which some basic postulates form the foundation. These theories have been called statistical mechanics. For systems not in equilibrium, equilibrium thermodynamics and equilibrium statistical mechanics are not sufficient. The aim is to formulate theories for describing the observed irreversible processes in the macroscopic view.

There have been many different theories of irreversible processes. They can be grouped into two categories. In one, the theories are based on some assumptions of a probability nature. To this category belong the Boltzmann transport theory, the Fokker-Planck theory and the so-called Master Equation (theory). In these theories, the basic equation is time-reversal non-invariant, or as one may say, has a time arrow. In the other category are the theory of Boltzmann and Gibbs, and the many recent theories of Bogoliubov, Born, Green, Kirkwood and others. All these theories start from the Liouville equation, which is the consequence of classical dynamical laws and is time-reversal invariant.

In the following sections we shall discusss the nature of these theories.

1.4. Quantum Theory

In quantum mechanics there is an analogue to each of the basic classical features. The classical equations of motion and the Schrödinger equation are both time–reversal invariant. To the Liouville equation (Section 2.2) for the density in phase space, there is an exact quantum analogue for the density matrix, and both are time–reversal invariant. To the classical Master Equation (Section 3.3) for the probability, there is an exact quantum analogue, called the Pauli equation, for the diagonal elements of the density matrix. Both equations are irreversible in time, the classical one on account of the Smoluchowski hypothesis for Markovian processes, the quantum one because of the random phase hypothesis.

It is generally believed that the observed macroscopic irreversibility is of classical statistical origin and is not a quantum effect. For this reason, we shall confine our discussions in the present article to the classical theories.

2. Statistical–Kinetic Theory of Boltzmann and Gibbs*

2.1. Poincaré Theorem (1890)

In the statistical–kinetic theory, a gas is a system of molecules whose motions are governed by the dynamical laws. Let $H(q,p)$ be the Hamiltonian of the system, where q,p stands for $q_1, \cdots q_N, p_1, \cdots, p_N$. The equations of motion are

$$\dot{q}_k = \frac{\partial H}{\partial p_k}, \quad -\dot{p}_k = \frac{\partial H}{\partial q_k}, \quad k = 1, 2, \cdots, N \tag{2.1.1}$$

In the $6N$–dimensional Γ phase space of q,p, the dynamical state of the system is represented by a point $P(q,p)$. If the state at a certain instant t_0 is given, say $P_0 (q^0, p^0)$, then the whole history of the system is represented by the trajectory through P_0. As equations (2.1.1) are first–order differential equations in time, there is one, and only one, trajectory through any point which is uniquely determined by the equations (2.1.1). Therefore, a trajectory never crosses itself, nor another, at any time. Hence, in the course of time, the phase point P goes all over the accessible portion of the Γ–space, for example, the hypersurface corresponding to the relation: total energy = constant (or, an energy shell of thickness ΔE).

From Poincaré's theorem, the trajectory of the phase point of a gas contained in a finite volume will pass, in the course of time, arbitrarily close to the point P_0 itself, without going through it. The time of this quasi–cycle depends on how close one wants it to approach P_0, and is extremely long for large N. The length of this quasi–cycle has been estimated by Boltzmann*. Thus for a gas containing 10^{18} molecules in 1 cc with mean velocity 5×10^4 cm/sec, the time required for all the molecules to come within a range of 10^{-7} cm and 10^2 cm/sec in each of the coordinate and velocity components respective to the initial P_0 is greater than $10^{10^{19}}$ years (Chandrasekhar, 1943). This theorem is of basic importance in our understanding of the "irreversibility" of the approach of a gas toward equilibrium.

2.2. Liouville Equation

Let $\rho(q,p,t) \, dq dp$, where $dp dq$ stands for $dq_1, \cdots dq_N, dp_1, \cdots, dp_N$, be the probability of the phase point $P(q,p)$ being the volume element $dq \, dp$, so that

$$\int \cdots \int \rho dq dp = 1 \text{ for all } t \tag{2.2.1}$$

---

* L. Boltzmann's work appeared in the Journal *Sitzungsberichte der Akademie der Wissenschaften in Wien*, during the years 1860 to 1890. A good deal of the discussions can be found in his *Vorlesungen über Gastheorie*, Leipzig (1896–98) ;and its English translation in *Lectures on Gas Theory*, University of California Press, Berkeley (1964). See also, Gibbs, J.W. (1902), *Elementary Principles in Statistical Mechanics*. This work is included in his *Collected Works*, Vol. II. Yale University Press (1948).

the integral being taken over the accessible volume. This convention will always be used in the following discussion. It follows from the equations (2.1.1) that any volume in the Γ space remains unchanged in time if we follow the points in that volume along their trajectories, although the shape of the volume will change. From this and the conservation of probability in that volume, the Liouville epuation follows (Liouville, 1838):

$$\frac{\partial \rho}{\partial t} = -\sum_i \left(\frac{\partial \rho}{\partial q_i} \frac{\partial H}{\partial p_i} - \frac{\partial \rho}{\partial p_i} \frac{\partial H}{\partial q_i} \right) \tag{2.2.2}$$

An important property of the Liouville equation is that it is time-reversal invariant, i.e., upon time reversal

$$t \to -t = \tau, \quad q \to q, \quad p \to -p, \quad \rho(q,p,t) \to \bar{\rho}(q,-p,\tau) \tag{2.2.3}$$

equation (2.2.2) becomes

$$\frac{\partial \bar{\rho}}{\partial \tau} = -\sum_i \left(\frac{\partial \bar{\rho}}{\partial q_i} \frac{\partial H}{\partial p_i} - \frac{\partial \bar{\rho}}{\partial p_i} \frac{\partial H}{\partial q_i} \right)$$

which has the same form as (2.2.2).

From (2.2.2), it follows that for any function $F(\rho)$ of ρ,

$$\frac{d}{dt} \int \cdots \int F(\rho) dq\, dp = 0 \tag{2.2.4}$$

If we define the function $H(t)$

$$H(t) \equiv \int \cdots \int \rho \ln \rho\, dq\, dp \tag{2.2.5}$$

then from (2.2.4), it follows that

$$\frac{dH(t)}{dt} = 0 \tag{2.2.6}$$

If we look at H in (2.2.5) as a functional of $\rho(q,p)$, the requirement that H be stationary subject to (2.2.1) as an auxiliary condition leads to

$$\rho = \text{constant} \tag{2.2.7}$$

From the second variation and $\rho > 0$, we find:

$$H(t/\rho) \text{ is minimum if } \rho \text{ is a constant, independent of } q,p \tag{2.2.8}$$

In this connection, let us prove the following theorem. Let a function $P = P(q,p,t), P \geq 0$, satisfy the condition

$$\int \cdots \int P(q,p,t) dq\, dp = 1 \tag{2.2.9}$$

Also let $\rho(q,p,t)$ be any function satisfying

$$\rho \geq 0, \quad \int \cdots \int \rho\, dq\, dp = 1$$

Define the functional $\bar{\bar{H}}$ of $P(q,p,t)$

$$\bar{\bar{H}}(t/P) = \int \cdots \int \rho(q,p,t) \ln P\, dq\, dp \tag{2.2.10}$$

It can readily be shown, for example by the variational method, that

'$\bar{\bar{H}}$ (t/P) has a maximum value when P equals ρ' $\tag{2.2.11}$

Hence we obtain

$$\int \cdots \int \rho \ln \rho\, dq\, dp \geq \int \cdots \int \rho \ln P\, dq\, dq \tag{2.2.12}$$

the equality sign holding when $P = \rho$. Note that this theorem (2.2.11), or (2.2.12), is purely a mathematical result.

2.3. Theory of Boltzmann*

To obtain the essential statistical features of the problem, we shall consider a system of

---

* *See footnote p.3*

non-interacting and therefore independent particles. In this case it is sufficient to consider the 6-dimensional μ phase space of one particle. Imagine the μ space as being divided into a large number of cells each of volume ω. ω must be small on the macroscopic scale but must not be too small, so that each cell still contains a number of particles. Let $n_1, n_2, \cdots$ be the number of molecules in cells 1,2,...The number of permutations of N molecules in the above distribution is

$$G_{n_1, n_2 \ldots} = \frac{N!}{n_1! n_2! \ldots}, \qquad \sum n_i = N$$

The weight of each distribution is $(\omega/V)^N$, where V is the volume of the accessible μ space. The distribution that can be realized in the largest number of ways is found by maximizing G subject to the conditions $\sum n_i = N$ and $\sum n_i \epsilon_i = E$, where ϵ_i is the energy of a molecule when its phase lies in the cell ω_i, and E is the total (constant) energy of the gas. The calculations are familiar, and we shall only state the qualitative result here. It is found that G has a very strong and sharp maximum, it being the sharper the larger N is. This result means that of all the possible permutations and distributions of the N molecules, an overwhelmingly large number corresponds to the few distributions near the maximum of G. The distribution giving the maximum G is the most probable state. Boltzmann identified this most probable state with the equilibrium state.

The probability of the distribution $n_1, n_2, n_3, \ldots$ is now

$$W_{n_1, n_2, \ldots} = G_{n_1, n_2, \ldots} (\omega/V)^N$$

and

$$\sum W_{n_1, n_2, \ldots} = 1$$

the summation being taken over all partitions $n_1, n_2 \ldots$ of N.

Let us translate the above result to the Γ space. In the Γ Space, ω^N is the volume Ω of a cell and V^N is the volume of the Γ space. The sharp maximum for $G_{n_1, n_2, \ldots}$ now means that an overwhelmingly large portion of the Γ space corresponds to the most probable state which is identified with the equilibrium state.

Consider now a gas which at an instant t_0 is in a non-equilibrium state represented by a point P_0. According to the discussions in Section 2.1, the phase point will move endlessly in the Γ space. Since an overwhelmingly large proportion of the Γ space corresponds to the equilibrium state, the phase point will pass from P_0 in a time of the order of the relaxation time into this large portion of the Γ space, and the system will approach rapidly, and will mostly be found in the equilibrium state.

The question as to the non-observation of the recurrence of the initial state P_0 is answered by noting the extremely long quasi-period of the Poincaré quasi-cycle. In the Γ space, there are of course many points Q which correspond to highly non-equilibrium states. However, starting from any point P_0, it also takes a very long time in general to come very close to one of them. Compared to the points corresponding to the equilibrium state, these non-equilibrium points have measure zero. Rigorously speaking, there is no irreversibility. But the reverse of the approach to equilibrium is so improbable that for practical purposes it can be excluded.

As the phase point P moves endlessly all over the Γ-space, it is plausible to assume that on average it spends an equal amount of time in volume elements of equal size at different points in the Γ-space, i.e., the probability of the phase point P being found anywhere will be the same. This means that μ approaches a constant value over the Γ-space. As an overwhelmingly large proportion of the Γ-space corresponds to the equilibrium state, this suggests that the equilibrium state corresponds to a uniform ρ.

In Section 2.2, the $H(t)$ function defined in equation (2.2.5) is minimum for a constant

value of ρ. Thus one would have a theory for an irreversible approach to equilibrium in a gas if one could show that $H(t)$ keeps on decreasing until it reaches its minimum at which ρ is uniform, i.e., if

$$\frac{dH}{dt} < 0 \tag{2.3.1}$$

This hypothesis is known as the H theorem of Boltzmann (1872, 1875).

We have seen in equation (2.2.6), however, that as a consequence of the Liouville equation, $dH/dt=0$. Thus the H theorem cannot be established on the basis of the laws of dynamics alone. There had been the criticism of Loschmidt (1877) that if $H(t)$ decreases with time for one state of motion, then it will have to increase with time for another state in which all the molecular velocities are just opposite to those of the first state. There had also been the criticism of Zermelo (1896) that since the state in the course of time returns arbitrarily close to any initial state according to Poincaré's theorem, H could not be monotonically decreasing at times.

To sum up, we may state the following. In the probability sense, it is possible to understand the macroscopically irreversible approach of a gas, from any initial state, to the equilibrium state. The H theorem, however, cannot be established on dynamical laws alone and attempts to maintain it must be made on probability grounds, with additional assumptions outside of dynamical laws.

2.4. Theory of Gibbs–Microcanonical Ensemble (Tolman, 1935)*

Gibbs introduced the concept of ensembles. An ensemble is a very large number of systems which all have the same macroscopic variables as, but different dynamical states (q,p) to the system under consideration. The ensemble is represented by a distribution function $\rho(q,p,t)$ in the Γ-space which is now normalized to N instead of unity in equation (2.2.1). All the results of Section 2.2 hold.

Consider those points that lie within a volume element $\Delta=dqdp$, namely, $\rho\Delta$. Each point will move in accordance with the equations of motion (2.1.1) as described is Section 2.1, and the points $\rho\Delta$ will move as an incompressible fluid, keeping volume Δ but changing shape. In the course of time these points will deform into a thin filament over the accessible part of ithe Γ-space. Similarly, for other systems lying outside Δ. The result is that, from any nitial distribution $\rho(q,p)$, the ensemble will in the course of time spread out "uniformly" over the Γ-space.

In Boltzmann's theory, it is assumed that the equilibrium properties of a gas are given by a long time average (i.e., long compared with all the relaxation times of the system). In Gibbs's theory, the fundamental hypothesis is made that the time average over one system is equal to the average taken over the ensemble. As the phase points of an ensemble extend, in time, over the Γ-space "uniformly", the ensemble average (average over the Γ-space) gives the equilibrium value.

These qualitative discussions make plausible, in the probability sense, the "irreversible" approach of a system from any non-equilibrium state (for example, all systems initially lying within a volume Δ) to the equilibrium state represented by a "uniform" distribution in the Γ-space. The words "uniform" and "uniformly" are to be taken in the coarse-grained sense defined below.

The concept of coarse-graining is introduced on the following considerations. In the macroscopic obesrvations made on a gas, one does not know the positions and the momenta of the molecules except to within ranges Δq and Δp. The coarse-grained density is defined as the average value of the "fine-grained" $\tilde{\rho}$ over a volume $\Delta=\Delta q\Delta p$ of size corresponding to the limits of accuracy of experimental observation, i.e.,

*See also, footnote on 15

$$\bar{\rho}(q,p) = \frac{1}{\varDelta}\int \cdots \int dq\,dp\,\rho \tag{2.4.1}$$

$\bar{\rho}$ is a function of phase (q,p), but is constant over the volume $\varDelta$. With this definition, we obtained for the coarse-grained ensemble average of a function $F(\rho)$

$$\bar{F} = \int \cdots \int \bar{\rho} F(\bar{\rho})dq\,dp = \int \cdots \int \frac{1}{\varDelta_{pq}}\int \cdots \int \rho(q',p')\,dq'\,dp'\,F\,(\bar{\rho}(q,p))dq\,dp$$

$$= \int \cdots \int \rho F(\bar{\rho})dq\,dp \tag{2.4.2}$$

Let us now come back to the ideas of Gibbs on the spreading of the phase points in $\varDelta$ over the $\varGamma$-space. The foregoing qualitative discussions make it plausible that $\rho(q,p)$ will approach a uniform coarse-grained $\bar{\rho}$. Now, we may define a coarse-grained H function $\bar{\bar{H}}$ (t) by (2.4.2)

$$\bar{\bar{H}}(t) = \int \cdots \int \bar{\rho}\ln\bar{\rho}\ dq\,dp$$

$$= \int \cdots \int \rho\ln\bar{\rho}\ dq\,dp \tag{2.4.2a}$$

Using the theorem in equation (2.2.12), we immediately obtain

$$\int \cdots \int \rho\ln\rho\,dq\,dp \geq \int \cdots \int \rho\ln\bar{\rho}\,dq\,dp \tag{2.4.3}$$

or

$$H(t) \geq \bar{\bar{H}}(t) \tag{2.4.3a}$$

i.e., the fine-grained H is always greater than the coarse-grained $\bar{\bar{H}}$. It is to be noted that the relation (2.4.3) or (2.4.3a) is a consequence of the definition (2.4.1) and the mathematical inequality (2.2.12), and has nothing to do with the time variation of the ensemble or the system in question.

We have seen in equation (2.2.6) that the fine-grained H remains constant in time. The coarse-grained $\bar{\bar{H}}$ as defined by (2.4.1) is not governed by the Liouville equation, and one may ask whether $\bar{\bar{H}}$ decreases monotonically in time, i.e., whether

$$\frac{d\bar{\bar{H}}}{dt} < 0 \tag{2.4.4}$$

If the coarse-grained $\bar{\bar{H}}$ satisfies the H theorem (2.4.4), then (2.4.4) is the mathematical expression of the qualitative ideas of Gibbs on the approach of a gas from any arbitrary state to equilibrium.

To express Gibbs's ideas in terms of the coarse-grained density, let us prepare an ensemble such that at an instant t_1 (Tolman, 1935; ter Haar, 1954, 1955),

$$\rho_1 = \text{constant} = \bar{\rho}_1 \text{ inside a volume } \varDelta$$
$$= 0 \text{ elsewhere} \tag{2.4.5}$$

At a later time t_2, the phase points will have spread so that in general

$$\rho_2 \neq \bar{\rho}_2 \tag{2.4.6}$$

Then

$$\bar{\bar{H}}(t_2) - \bar{\bar{H}}(t_1) = \int \cdots \int \bar{\rho}_2\ln\bar{\rho}_2 dq\,dp - \int \cdots \int \bar{\rho}_1\ln\bar{\rho}_1 dq\,dp$$

by (2.4.2) and (2.4.5),

$$= \int \cdots \int \rho_2\ln\bar{\rho}_2 dq\,dp - \int \cdots \int \rho_1\ln\rho_1 dq\,dp$$

by (2.2.6),

$$= \int \cdots \int \rho_2\ln\bar{\rho}_2 dq\,dp - \int \cdots \int \rho_2\ln\rho_2 dq\,dp.$$

and by (2.4.3)

$$< 0 \tag{2.4.7}$$

— 7 —

Thus $\overline{H}$ does decrease from the initial condition (2.4.5) at $t=t_1$ to a smaller value at any later time $t_2 > t_1$.

The above proof depends entirely on the special initial condition $\rho_1 = \bar{\rho}_1$ in (2.4.5). Without it, it would not have been possible to proceed beyond the first line in (2.4.7). What has been, and can be, proved is that the initial non-equilibrium state (2.4.5) with $\rho_1 = \bar{\rho}_1$ in Δ does evolve with a decrease in $\overline{H}$, and this is the qualitative discussions of Gibbs's ideas given before. There is, however, no proof that $\overline{H}(t_3) - \overline{H}(t_2) < 0$ for a later time $t_3 > t_2$, i.e., there is no proof that $\overline{H}$ decreases monotonically, in contrast to the arguments of Tolman that $\overline{H}$ continues to decrease (Tolman, 1935.). It is true that $\overline{H}$, unlike H, is not bound by any law to remain constant, but the H theorem for the coarse-grained $\overline{H}$ cannot be proved without some additional assumption concerning the time behavior of the coarse-grained density $\overline{H}$. Through the years, the H theorem has been the subject of discussions, by Boltzmann, Loschmidt, Zermelo and the Ehrenfests, and it became clear that the theorem must be interpreted on a probability basis. It will be shown in Section 3.3 that an assumption on the time relation of the state probabilities does introduce a time arrow and lead to an H theorem.

To summarize, we may conclude as follows. On the basis of the Liouville equation, although no mathematically irreversible law (such as the H-theorem) can be derived, it is still possible to "understand" the irreversible approach of a gas to equilibrium in the probability sense. The basic reason is because of the large number of permution of molecules that all correspond to the equilibrium (the most probable) state and the long quasi-cycle, by virtue of the large number of molecules in a macroscopic amount of gas.

3. Theories with Explicit Time-Reversal Non-Invariance

We shall next consider a few theories of the other category mentioned in Section 1.3, namely, those that are by construction, by making assumptions of some sort, explicitly time-reversal non-invariant. Such theories do not claim to be the consequences of the fundamental dynamical laws and are therefore not to be criticized on that basis. The criteria will be their plausibility, simplicity and ultimately their success in applications to actual problems.

3.1. Boltzmann's Theory

The earliest theory of transport processes is that of Boltzmann. Instead of dealing with the N molecules of a gas in the Γ-space, it is assumed that a theory for describing the gas can be formulated in terms of the one-particle distribution function $f(r,v,t)$ in the μ phase space of one particle. The justification for this has become clear only comparatively recently through the work of Bogoliubov, from the observation that in a gas there exist two rather widely different physical time scales corresponding to the short range of intermolecular interactions and the long mean-free path at ordinary gas densities. It is not the purpose of the present article to analyze this aspect of Boltzmann's theory or Bogoliubov's theory. Our interest is in the time-reversal property.

The Boltzmann equation is so familiar that we shall simply write it down (Boltzmann, 1876). The distribution function f is normalized according to

$$\int f(r,v,t)dv = n(r,t) = \text{number of molecules per unit volume}$$

The equation for $f(r,v,t)$ is

$$\frac{\partial f}{\partial t} + v \cdot \frac{\partial f}{\partial r} + \frac{K}{m} \cdot \frac{\partial f}{\partial v} = \left(\frac{\partial f}{\partial t}\right)_{collision} = \int dv_1 \int d\omega \, \sigma |v - v_1| (f'f_1' - ff_1) \quad (3.1.1)$$

where K is the external force, the subscript 1 denotes another molecule with which the one under consideration in $f(r,v,t)$ collides, $d\omega = \sin\theta d\theta d\phi$, θ the scattering angle, σ the collision cross section, and

$$f' = f(r, v', t), \quad f_1' = f_1'(r, v_1', t), \text{ etc.}$$

the prime denoting quantities after a two-body collision. The first term in the integral gives the rate of increase of $f(r, v, t)$ due to the restitution collisions, and the second term gives the rate of decrease due to direct collisions. The specific form of the right-hand side constitutes the basic assumption (*Ansatz*, in German, is the more appropriate expression) of Boltzmann's theory. This Ansatz is not a consequence of the dynamical laws but is based on plausibility considerations. As a consequence of this Ansatz, the Boltzmann equation has the following properties:

(*i*) Equation (3.1.1) is not invariant upon the reversal of the direction of time. On reversing t as in equations (2.2.3), and writing

$$\bar{f} = f(r, -v, -t) = f(r, -v, \tau)$$

etc., one obtains the equation for $\bar{f}$ in τ which differs from that for f in t by the presence of a minus sign between the two sides of the equation. In fact this equation for f in τ does not have plausible physical meaning. Equation (3.1.1), so to speak, has a definite time arrow built in.

(*ii*) This definite direction of time built in in (3.1.1) is the one along which the H function

$$H(t) = \int \int f \ln f \, dr \, dv \tag{3.1.2}$$

decreases monotonically with time, for with (3.1.1), one readily finds

$$\frac{dH}{dt} = \int \int (1 + \ln f) \frac{\partial f}{\partial t} dr \, dv \le 0 \tag{3.1.3}$$

Thus the Boltzmann equation (3.1.1) satisfies the H theorem.

Now on a comparison and identification between the results from classical thermodynamics and those from the Boltzman statistics of Section 2.3, Boltzmann obtained the following relation between the probability W of Section 2.3 and entropy

$$S = k \ln W$$

k being the Boltzmann constant.

It is also easy to obtain the following relation between the H function defined in (3.1.2) and the probability W,

$$NH = -\ln W$$

(*H* here being for one molecule).

Thus, up to an additive constant,

$$S = -NkH$$

The H theorem (3.1.3) thus is equivalent to the Second Law of Thermodynamics, i.e., the law of increasing entropy for the irreversible approach of a gas to equilibrium.

We must repeat that the H theorem (3.1.3) has been established by the explicit use of the Boltzman equation (3.1.1) which is not a dynamical law but which has been constructed to be irreversible by the Ansatz for $(\partial f / \partial t)_{collision}$ in (3.1.1). In this case, the criticisms of Loschmidt and of Zermelo do not apply.

3.2. Fokker–Planck Equation (Fokker, 1914; Planck, 1917; Chandrasekhar, 1943)

Another theory with time irreversibility is that of Fokker (1914) and Planck (1917). It is based on a less specific assumption than the collision number *Ansatz* of Boltzmann in (3.1.1). A molecule is considered to have random collisions with other molecules. Let $Q(v - \Delta v, \Delta v)$ be the transition probability that in a time interval $\Delta t (> 0)$, a molecule changes its velocity from $v - \Delta v$ to v, and

$$\int Q(v - \Delta v, \Delta v) d\Delta v = 1 \tag{3.2.1}$$

$Q(v, \Delta v)$ depends on the present state, i.e., the velocity v of the particle, and not on the past history. It is not an explicit function of time, but depends on the length of the interval Δt, and Δt must not be too short in order that the molecule may have suffered a sufficiently large number of random collisions with other molecules. The postulate is now made that the distribution function at time $t + \Delta t$ is related to that at time t through the Smoluchowski law

$$f(v, t + \Delta t) = \int d\Delta v f(v - \Delta v, t) Q(v - \Delta v, \Delta v) \tag{3.2.2}$$

It is important to note that this is not a consequence of dynamical laws, but is an assumption connecting the probabilities at two different times irrespective of the past history before the time t.

On calculating the rate of change of $f(v)$ and introducing the averages

$$<\Delta v> = \int \Delta v Q(v, \Delta v) d\Delta v$$

$$<\Delta v_x \Delta v_y> = \int \Delta v_x \Delta v_y Q(v, \Delta v) d\Delta v, \quad etc.$$

one obtains, on writing $\partial/\partial v = \nabla_v$,

$$\left(\frac{\partial f}{\partial t}\right)_{collision} = -\nabla_v \cdot \left(\frac{<\Delta v>}{\Delta t} f\right) + \tfrac{1}{2} \Delta_v \Delta_v : \left(\frac{<\Delta v \Delta v>}{\Delta t} f\right) + \cdots \tag{3.2.3}$$

On equating this to the left-hand side of (3.1.1), one obains the Fokker-Planck equation. One immediate application of this equation is to the Brownian motion, leading to the result obtained earlier by Einstein by other methods. We shall not go into further discussions of this equation, except to emphasize that it is not invariant upon time reversal, and that this non-invariance comes from from the assumed relation (3.2.2). That this relation inntroduces a time arrow will be more clearly brought out in the following section.

3.3. The Master Equation (Wu, 1966)

Here we shall formulate a time-reversal non-invariant theory in a formal manner, leaving out detailed physical interpretation, in order to bring out the far-reaching consequences of a relation of the type (3.2.2).

Let $w_i, i = 1, 2, \cdots$, be the probability that a system be in state i at time t. Let the probabilities at a later time $t + \Delta t$ be w_k', $k = 1, 2, \cdots$ We have

$$\sum_i w_i = 1, \qquad \sum_i w_i' = 1 \tag{3.3.1}$$

Assume that the system in state k at time t has the transition probability A_{ik}, in the interval Δt, of going into state i at time $t + \Delta t$. The transition probabilities depend on the length of the interval Δt, but are independent of the past history of the system. They are to satisfy the requirements, by virtue of their being probabilities,

$$0 \leq A_{ik} \leq 1 \tag{3.3.2}$$

and

$$\sum_i A_{ik} = 1 \tag{3.3.3}$$

Let us make the hypothesis that relates the probabilities w_i' $(t + \Delta t)$ and $w_k(t)$:

$$w_i'(t + \Delta t) = \sum_k A_{ik} w_k(t) \tag{3.3.4}$$

It is to be noted that, except for the use of discrete states here, this relation is of the same nature as (3.2.2).

From (3.3.4), together with (3.3.3), one obtains

$$w_i'(t+\Delta t)-w_i(t)=\sum_k A_{ik}\,w_k-\left(\sum_k A_{ki}\right)w_i$$

or

$$\frac{\Delta w_i(t)}{\Delta t}=\sum_k\left(\frac{A_{ik}}{\Delta t}w_k-\frac{A_{ki}}{\Delta t}w_i\right) \tag{3.3.5}$$

which is the so-called Master Equation. If we introduce the transition probabilities per unit time

$$a_{ik}=A_{ik}/\Delta t$$

we may write (3.3.5) in the differential form

$$\frac{dw_i}{dt}=\sum_k(a_{ik}w_k-a_{ki}w_i) \tag{3.3.6}$$

The theory above has the following properties:

(*i*) Once the assumption (3.3.4) is made expressing w_i' at $t+\Delta t$ in terms of the w_k at time t, it is not possible to go backward in time to find the $w_k(t)$ in terms of the $w_i'(t+\Delta t)$ and still to have the same probability meaning given in (3.3.4). Let us assume that the inverse matrix A^{-1} exists so that equation (3.3.4) can be solved

$$w_k(t)=\sum_i A^{-1}_{ki}w_i'(t+\Delta t) \tag{3.3.7}$$

From $A^{-1}A=$ unit matrix, we have

$$\sum_i A^{-1}_{ki}A_{ii}=\delta_{ki} \tag{3.3.8}$$

Take $k\neq j$. Since all A_{ij} are ≥ 0, it follows from (3.3.8) that not all A^{-1}_{ki} are greater than zero. Again, take $k=j$. Since all $A_{ik}\leq 1$, it follows from (3.3.8) and (3.3.3) that the A^{-1}_{ki} cannot all be <1.

From this it also follows that the Master Equation (3.3.6) has no probability meaning if one simply reverses the sign of t.

(*ii*) Let us define, similarly to (2.4.2a), an H function by

$$H(t)\equiv\sum_i w_i(t)\,\ln w_i(t) \tag{3.3.9}$$

Using (3.3.5), we have

$$\frac{dH}{dt}=-\frac{1}{\Delta t}\sum_{i,k}(A_{ik}w_k-A_{ki}w_i)\,(1+\ln w_i)$$

$$=-\frac{1}{\Delta t}\sum_{i,k}(A_{ik}w_k-A_{ki}w_i)\ln w_i \qquad\text{on using (3.3.3)}$$

$$=-\frac{1}{\Delta t}\sum_i(w_i'-w_i)\ln w_i \qquad\text{on using (3.3.3) and (3.3.4)}$$

By use of the same method as that used in proving the mathematical inequality (2.2.12) (which differs from the present problem in involving integration instead of summation), it can be seen that the right-hand side of the last line in the equations above is negative. Hence

$$\frac{dH}{dt}\leq 0 \tag{3.3.10}$$

This shows that the theory has a definite direction of time.* (next page)

(iii) The Master Equation, subject to the basic assumption (3.3.4), is quite general. By replacing the discrete states by continuous states, the H function defined in (3.3.9) can be compared with the H function in (2.2.5). It may be recalled that on the basis of the dynamical laws, the H function in (2.2.5) remains unchanged in time, whereas on the basis of the probability assumption (3.3.4) the H function in (3.3.9) decreases monotonically with time.

(iv) The linearity of the Master Equation is only apparent, because the transition probabilities a_{ik} can depend on the probabilities w_k. In fact the Boltzmann equation (3.1.1) can be thrown into the form (3.3.6) in which the transition probabilities a_{ik} are proportional to the $w_i = f(r, vi, t)$ in (3.1.1). One may regard the Boltzmann equation as a special case of the Master Equation. They are both time–reversal non–invariant.

3.4 Theories Based on the Liouville Equation

As seen in Section 2, the Liouville equation is time–reversal invariant and it is not possible to obtain an irreversible equation from it without additional assumptions. But it is also seen that the theories of Boltzmann and Gibbs make the approach of a gas to equilibrium extremely probably irreversible. In recent years many attempts have been made to formulate a theory of gases (and plasmas) by starting from the Liouville equation. The common initial step in many of these theories is to transform the Liouville equation into a system of coupled

---

*The proof of the relation (3.3.10) can be carried out without appealing to (2.2.12) but by using an extra normalization for the A_{ik}, namely,

$$\sum_k A_{ik} = 1 \qquad (3.3.3a)$$

The meaning of this condition is not as obvious as (3.3.3). But both (3.3.3) and (3.3.3a) are suggested in a quantum mechanical version of the theory where the relations (3.3.3) and (3.3.3a) are properties of the unitary transformation in time (Wu, 1966).

We calculate, from (3.3.4) and (3.3.9),

$$H(t+\Delta t) - H(t) = \sum_{i,k} A_{ik} w_k \ln w_i' - \sum_i w_i \ln w_i$$

Now we have the following inequality due to Gibbs. For any positive x, we have

$$\int_1^x \ln y \, dy = x \ln x - x + 1 \geq 0$$

Set $x = w_k / w_i'$, multiply the above inequality relation by w_i' and we get

$$w_k \ln w_k - w_k + w_i' \geq w_k \ln w_i'$$

Since all $A_{ik} \geq 0$, we obtain

$$H(t+\Delta t) - H(t) \leq \sum_{i,k} A_{ik} (w_k \ln w_k - w_k + w_i') - \sum_i w_i \ln w_i$$

On using (3.3.3) and (3.3.3a), it is seen that the right–hand side is zero, and we obtain

$$H(t+\Delta t) - H(t) \leq 0$$

It might have appeared at first thought that had one used the inverse relation (3.3.7), all the above steps could have been repeated, with A_{ik}^{-1} replacing A_{ik}, and one would have arrived at

$$H(t) - H(t+\Delta t) \leq 0$$

and this would have meant

$$H(t+\Delta t) - H(t) = 0$$

This result, however, it not true, because the A_{ik}^{-1} are not all >0 as we have shown before, and one cannot arrive at the inequality $H(t) - H(t+\Delta t) \leq 0$.

equations by defining s-particle distribution functions

$$F_s(x_1,x_2,...,x_s,t)$$

(in which x_t stands for $q_t, p_t, s=1,2,...N$) by

$$F_s = V^s \int \cdots \int F_N dx_{s+1},...,dx_N, \qquad F_N \text{ proportional to } \rho \text{ in (2.2.1)}$$

V is the volume of the gas. Let ϕ_{ij} denote the intermolecular interaction between particles i and j. The Hamiltonian of an s-particle subsystem of the gas is

$$H_s = \sum_i \left(\frac{1}{2m} p_i^2 + U(q_i) \right) + \sum_{1 \leq i < j} \phi^{ij}$$

Let us introduce the Poison bracket expression

$$\{A,B\} = \sum_i \left(\frac{\partial A}{\partial q_i} \frac{\partial B}{\partial p_i} - \frac{\partial A}{\partial p_i} \frac{\partial B}{\partial q_i} \right)$$

Then simply by integration of the Liouville equation (2.2.2), one obtains the system of coupled differential-integral equations

$$\frac{\partial F_s}{\partial t} - \{H_s, F_s\} = \frac{N-s}{V} \int dx_{s+1} \left\{ \sum_{i=1}^{s} \phi_{i, s+1}, F_{s+1} \right\}, \quad s=1,2,...(3.4.1) \qquad (3.4.1)$$

which is known as the B-B-G-K-Y hierarchy (Bogoliubov, 1946; Bron & Green, 1946, 1947; Kirkwood, 1946,1947; Yvon, 1935). This system of equations is completely equivalent to the Liouville equation and is time-reversal invariant.

Different theories differ at this point in their different expansions of the F_s and the different methods of introducing a time-irreversibility into the theory. It is beyond the scope of the present article to describe the various theories. We wish only to emphasize the time-irreversibility aspect of these theories.

In the theory of Bogoliubov, a time direction is introduced by the "initial condition" which defines that direction as the past in which the s-particle distribution function F_s is uncorrelated, i.e.,

$$\lim_{t \to -\infty} F_s = F_1(1)F_1(2), \cdots, F_1(s), \qquad s=2,3,\cdots,N \qquad (3.4.2)$$

The positive direction of time, or the future, is the one along which the particles become correlated on account of their interactions. When the conditions (3.4.2) is used in integrating (3.4.1), the result is no longer time-reversal invariant. It might be mentioned in passing that by expanding the F_s in powers of the gas density and terminating the equation for F_1 from (3.4.1) at the first order in density, Bogoliubov obtained an equation which, in some approximations, reduces to Boltzmann's equation (3.1.1). This is a most satisfactory feature of Bogoliubov's theory, since it furnishes a foundation for the Boltzman equation. A similar theory of obtaining Boltzmann's equation from the Liouville equation has been independently given by Kirkwood.

In the theories of other authors, either an initial condition on the many particle function F_s is used, or a Laplace transform in time is made

$$f(k,v,\omega) = \int_0^\infty f(k,v,t)\exp(-\omega t)dt \qquad (3.4.3)$$

where the real part of ω is positive. Such a transform automatically excludes negative values of t from the theory, and only positive values of t are permissible.

4. Concluding Remarks

From the preceding sections, we can summarize the discussions as follows.

(1) There are the observed irreversible processes in gases. If we are interested only in formulating laws to describe them in the macroscopic view, then we have already satisfactory laws.

(2) But if we are interested in formulating theories from the atomic level, i.e., in understanding the macroscopic irreversibility on the basis of dynamical laws governing the motions of the molecules, then there are two major problems. One is the impracticability, and irrelevance, of dealing with the large number of molecules in any macroscopic amount of gas. Probability concepts and statistical mehods are introduced to deal with this aspect. The other problem is to get out, from the fundamentally reversible dynamical laws, theories that will describe the observed irreversible processes.

(3) The marriage between probability concepts and dynamics leads to the Liouville equation which however is dominated by dynamics and is time-reversible invariant. Without the addition of other assumptions outside of dynamical laws, one cannot obtain from the Liouville equation a theory which is time-irreversible explicitly. In particular, one cannot establish such an irreversibility as the H theorem on purely dynamical ground.

(4) On the other hand, on the basis of the Liouville equation, it is possible to understand the extremely high probability of "irreversible" approach of a gas toward equilibrium. This is achieved in the theory of Boltzmann for one single system and that of Gibbs for an ensemble. Thus the Liouville equation, although mathematically reversible in the time, does contain the essence of "physical" or "macroscopic" irreversibility in the probability sense. This property of the Liouville equation has its origin in the largeness of the number of particles in the system under consideration.

(5) Because of this last-named property of the Liouville equation, it follows that any theory based on it and rendered time-reversal noninvariant by any plausible assumption or artifice will also describe the irreversible approach to equilibrium. This is illustrated by the theories of Bogoliubov and others who introduce certain initial conditions that in essence define a time arrow. In such theories, the objections of Loschmidt and of Zermelo will not arise.

(6) Now we may ask ourselves the question as to what we really want regarding a theory for irreversible processes. If we allow ourselves to be less puritanical as far as strict adherence to dynamical laws is concerned, then our object is to formulate a theory with the purpose of describing the irreversible processes. We may retain dynamics as far as possible but are ready to introduce additional ideas which are not deducible from dynamics.

It is on this philosophy that many theories have been proposed. Boltzmann's equation, the Fokker-Planck equation and the Master Equation are briefly referred to in Sections 2 and 3.

(7) There are authors who are not happy with this attitude. Some try to trace this irreversibility (in the macroscopic scale) to something more basic. It seems that at the moment not much can be reported about such ideas.

Acknowledgements

References

Bogoliubov, N.N. (1946). *Fiziologicheskii Zhurnal SSSR im. I.M. Sechenova*, 10, 265. Monograph translated in *Studies in Statistical Mechanics*. Edited by de Boer and Uhlenbeck (1962), Interscience.

Boltzmann, L.(1872). *Sitzungsberichte der Akademie der Wissenschhaften in Wien*, 66, 275.

Boltzmann, L.(1875). *Sitzungsberichte der Akademie der Wissenschaften in Wien*, 72, 427.

Boltzmann, L.(1876). *Sitzungsberichte der Akademie der Wissenschaften in Wien*, 74, 503.

Born, M. and Green, H.S. (1946). *Proceedings of the Royal Society* (London), A188, 10

Bron, M. and Green, H.S. (1947). *Proceedings of the Royal Society* (London), A189, 103; A190, 455; A191, 168.

Chandrasekhar, S. (1943). *Reviews of Modern Physics*, 15,1.

Fokker, A.D. (1914). *Annalen der Physik*, 43,812.

ter Haar, D.(1954). *Elements of Statistical Mechanics*. Rhinehart & Co.

ter Haar, D.(1955). *Reviews of Modern Physics*, 27,289.

Kirkwood, J.G. (1946). *Journal of Chemical Physics*, 14,180.

Kirkwood, J.G. (1947). *Journal of Chemical Physics*, 15,72.

Liouville, J. (1838). *Journal de mathématique pures et appliquee*, 3, 343. See also. Whittaker, E.T. (1927). *Analytical Dyamics*. Cambridge University Press.

Loschmidt, J. (1876). *Sitzungsberichte der Akademie der Wissenschaften in Wien*, 73, 139.

Loschmidt, J. (1877). *Sitzungsberichte der Akademie der Wissenschaften in Wien*, 75, 67.

Onsager, L. (1931). *Physical Review*, 37, 405.

Onsager, L. (931). *Physical Review*, 38, 2865. See also Casimir, H.B.G. (1945). *Reviews of Modern Physics*, 17, 343, for a proof of the reciprocity relations on the principle of microscopic reversibility.

Planck, M.(1917). *Sitzungsberichte der Preussischen Akademie der Wissenschaften zu Berlin*, 5, 324.

Poincaré, H.(1890). *Acta mathematica*, Stockholm, 13, 67.

Tolman, R.C. (1935). *Principles of Statistical Mechanics*. Oxford University Press.

Wu, T.Y. (1966). *Kinetic Equations of Gases and Plasmas*. Addison-Wesley.

Yvon, J. (1935). *La Theore Statistique des Fluids et d'Equation d'Etat*. Paris.

Zermelo, E.(1896). *Annalen der Physik*, 57, 485.

For general references, in addition to the works of Tolman, R.C. (1935) and ter Haar, D. (1954), see Uhlenbeck, G.E. and Ford, G.W. (1963). *Lectures in Statistical Mechanics*. American Mathematical Society, Providence, Rhode Island; and the classic work of Ehrenfest, P. and Ehrenfest, T. (1911). *Enzyklopädie der mathematischen Wissenshaften*, Vol. IV, Part 32 (English translation published by Cornell University Press, 1959).

不可逆程序理論之性質

本文之目的係討論各種描述氣體中不可逆程序理論之基本性質。對由半經驗半理論性之輸送方程式，波爾茲曼之H定理，Gibbs 氏理論，以至基於機遇論性質之所謂 Master 方程式等各理論之對時間不變性式非不變性，作分析討論。結論是：以力學理論，如 Liouville 方程式爲出發點之理論對不可逆程序，祇能獲一機遇性，而非絕對性之不可逆性。如欲得一數學上之不可逆方程式，則必須另加力學外之基本假設，如機遇性觀念等。

The Reaction ^{27}Al(d,p)^{28}Al in the Energy Range of the Deuteron from 2.0 MeV to 3.0 MeV$^{(*)}$

C. S. LIN and E. K. LIN (林爾康)

Institute of Physics, Tsing Hua University and Academia Sinica

Abstract.—The ^{27}Al$(d,p)^{28}$Al reaction was studied at bombarding energes between 2.0 and 3.0 MeV. Excitation functions in steps of 15 keV at two angles of 90° and 150° and angular distridntions from 15° to 150° were measured for four proton groups leading to the low–lying levels of ^{28}Al. Two mechanisms of compound nucleus and direct interaction were found to be contemporaneously present in the reaction. The direct effect contribution for the group p_0 corresponding to the ground–state transition was calculated by the DWBA stripping theory. The experimental total cross–sections at 2.5 MeV compared to the Hauser–Feshbach calculations are given and discussed.

1. Introduction.

It has been shown[1-8] that the (d,p) reactions on medium light nuclei $(A \approx 25)$ at rather low deuteron energy can go through the stripping process and both compound nucleus and direct interaction were responsible for the reaction mechanism in the reactions. This can be seen from the shape of the excitations and of the angular distributions. In the last several years the ^{27}Al$(d,p)^{28}$Al reaction has been extensively studied at a few MeV deuterons. Gadioli et al.[7] have made detailed measurements for the ^{27}Al$(d,p)^{28}$Al reation in the deteron energy range (1.4÷2.3) MeV. Corti et al.[8] have investigated the same reaction at one angle in the forward direction for deuteron energies ranging from 1.5 to 2.9 MeV and from 1.5 to 2.3 MeV at one other angle in the backward direction. Their quantitative results have been obtained showing both compound nucleus and direct effect contributing to the the ^{27}Al$(d,p)^{28}$Al reaction. In the present work we extended measurements on this reaction at deuteron energies (2.0÷3.0) MeV with an aim to investigate the behaviour of the ^{27}Al$(d,p)^{28}$Al reaction leading to the low–lying levels of residual nucleus ^{28}Al over a range of low energies.

(1) H.M. Omar, I. I. Zaloubovsky, M. H. S. Bark, R. Zaghloul and V. J. Gontchar: *Nucl. Phys.*, **56**, 97(1964)

(2) V. Bobyr, M. Corti. G. M. Marcazzan, L, Milazzo Colli and M. Milazzo: *Eneryia Nucleare,* **13**, 420(1966).

(3) S. M. Lee, Y. Hiratate, K. Miura, S. Kato and S. Morita: *Nucl. Phys.*, A **122**, 97 (1968)

(4) G. Calvi, S. Cavallaro, A. S. Figura and M. Sandoli: *Nuovo Cimento*, **58**, 363 (1968).

(5) E. Gadioli, G. M. Marcazzan and G. Pappalardo: *Phys. Lett.*, **11**, 130(1964).

(6) G. Corleo and S. Sambatro: *Nuovo Cimento*, **56**, 83(1968).

(7) E. Gadioli, I. Iori, M. Mangialaio and G. Pappalardo: *Nuovo Cimento*, **38**, 1105 (1965).

(8) M. CORTI, G. M. Marcazzan, L. Milazzo Colli and M. Milazzo: *Nucl. Phys.*, **77**, 625 (1966).

2. Experimental method.

The experiment was performed with a 14" scattering chamber on the 3.0 Mev Van de Graaff accelrator. A detailed description of the experimental method has been described in a preceding paper[9]. The alumnium target was a thin self-supporting natural Al foil of thickness $\approx 150 \mu g/cm^2$. Only one target foil was used throughout the experiment. The protons emitted from the reaction were detected by a Li-drifted junction detector in conjunction with a 1024-channel analyser and standard electronics. The deuteron beam is monitored by means of a Faraday cup and a current integrator. The elastically scattered deuterons and reaction alpha-particles are removed by an absorber of alumnium foils of thickness $15 mg/cm^2$ being stacked in front of the detector.

Measurements were made for the excitation functions ranging from 1.5 t0 3.0 MeV in steps of 15 keV at two angles of 90° and 150°, and data were taken at eighteen angles between 15° and 150° to obtain the angular distributions at $E_d = 2.5$ MeV. The differential cross-sections were computed for the four proton groups leading to the low-lying levels of ^{28}Al. The uncertainty on the calculated absolute cross-sections was estimated to be less than 20%.

3. Results and discussion.

The typical proton energy spectrum of the $^{27}Al(d,p)^{28}Al$ reaction is shown in Fig. 1. The energy resolution is about 80 keV. In the spectrum groups p_2 and p_3 corresponding to the states of ^{28}Al with excitation 1.37 and 1.63 MeV were well separated, while the group p_0 consists of the unresolved ground and 0.03 MeV states, and the group p_1 consists of the unresolved 0.97 and 1.01 MeV states of ^{28}Al.
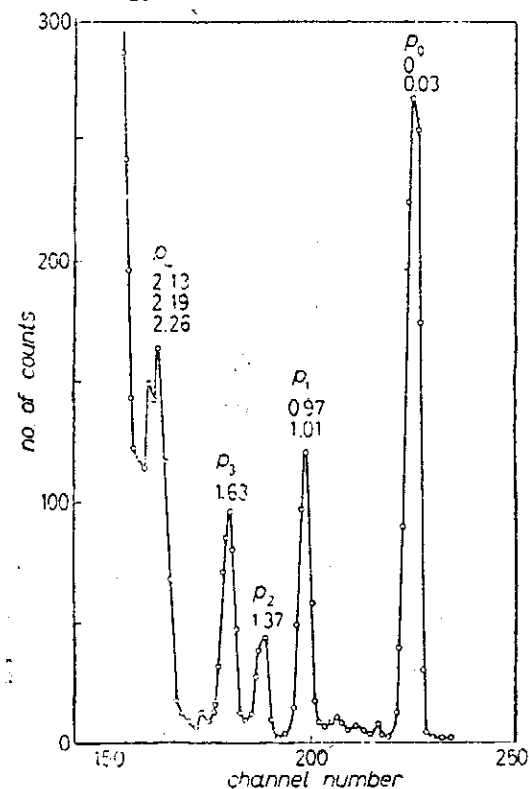
The results of the measurements of eight excitation functions for different proton groups are shown in Fig 2 to 5. The angular distribution measured at $E_d = 2.5$ MeV are shown in Fig. 6 and 7. The existence of fluctuations in the excitation functions clearly indicates the presence of the compound nucleus mechanism in the transitions. The observed angular distribution for the group p_0, as shown in Fig. 6, presents a maximum at forward angles near 0°, which is typical of a stripping reaction with transferred angular momentum $l=0$. As is seen from Fig. 7, the groups p_2 and p_3 have an angular distibution without any typical behaviour; however, the angular distribution of group p_1 shows somewhat noneglible contribution from stripping effects. It is evident that the reaction for the p_1, p_2 and p_3 transitions proceeds mainly through compound nucleus formation and the direct effect would be very small for p_2 and p_3 trantitions, while for p_1 transitions the interference effect apparently exists. It has been suggested by Holt et al. [10] that both $l=0$ and $l=2$ contributions may be present in the p_1 transition.

Fig. 1. -Typical proton enegy spectrum for the $^{27}Al(d,p)^{28}Al$ reaction. Numbers over peaks refer to excitation energy in MeV of levels in ^{28}Al. $E_d = 2.615$ MeV, $\theta_{lab} = 90°$

(9) C. C. Hsu, E. K. Lin and W. N. Wang: Nuovo Cimento, 59, 39(1969).

(10) J. R. Holt and T. N. Marsham: Proc. Phys. Soc.,A 66, 249(1953).

The direct effect contribution for the group p_0 was calculated by the DWBA stripping theory. The calculation was made for a transferred angular momentum $l=0$, using the programme JULIE developed by Bassel et al.[11]. The optical potentials used in the calculation are of the Saxon-Woods type with the deuteron and proton parameters listed in Table I.
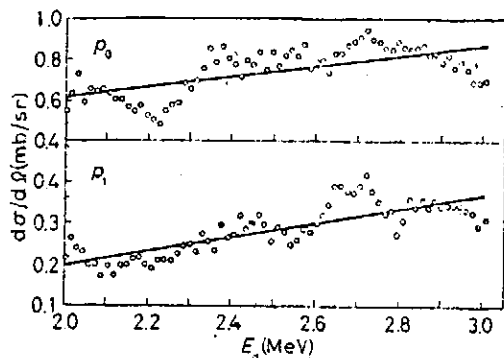

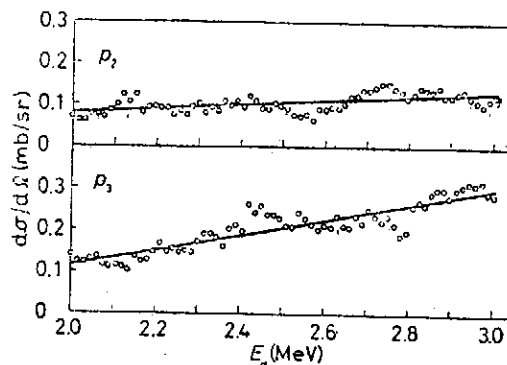Fig. 2.-Excitation functiuns of groups p_0 and p_1 from the $^{27}Al(d,p)^{28}Al$ reaction at angle $\theta=90°$.

Fig. 3.-Excitation functions of groups p_2 and p_3 form the $^{27}Al(d,p)^{28}Al$ reaction at at angle $\theta=90°$

Fig. 4.-Excitation functions of groups p_0 and p_1 from the $^{27}Al(d,p)^{28}Al$ reaction at angle $\theta=150$.
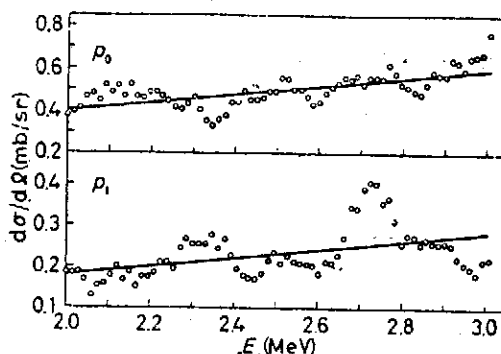
Fig. 5 -Excitation functions of groups p_2 and p_3 from the $^{27}Al(d,p)^{28}Al$ reaction at angle $\theta=150°$

Table I. - Optical model parameters for the DWBA stripping calculations.

	Deuteron	Proton
V (MeV)	60	52
r_0 (fm)	1.40	1.25
a_0 (fm)	0.70	0.50
W (MeV)	40	24
r'_0 (fm)	1.40	1.25
a'_0 (fm)	2.70	0.50

For both deuterons and protons, the real optical potential used is of the Saxon form and the imaginary optical is in the form of surface absorption.

(11) R.H. Bassel, R.M. Drisko and G.R. Satcher: *Oak Ridge National Laboratory Report ORNL-3240 (1962).*
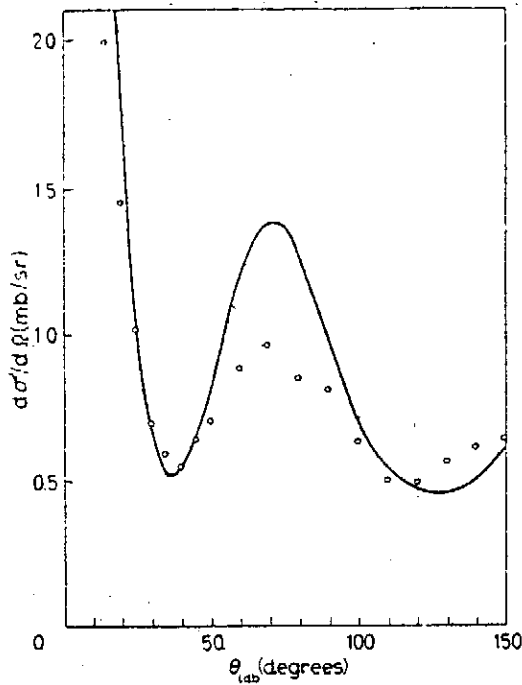
Fig. 6. - *Angular distibution of the p_0 group from the $^{27}Al(d,p)^{28}Al$ reaction at $E_d=2.5MeV$. The full line represents the DWBA caclulations.*

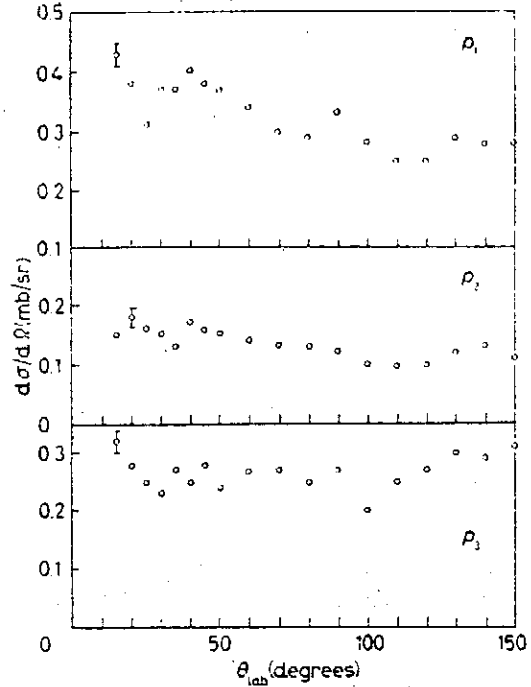Fig. 7. - *Angular distribution of groups p_1, p_2 and p_3 from the $^{27}Al(d,p)^{28}Al$ reaction at $E_d=2.5MeV$.*

Table II. - Results of the analysis for the $^{27}Al(d,p)^{28}Al$ reaction.

Group	Level	Level energy (MeV)	I	$<d\sigma/d\Omega>_{90°}$ (mb/sr)[a]	$<d\sigma/d\Omega>_{150°}$ (mb/sr) [a]	σ_{exp}(mb)[b]	σ_{th}(mb)[c]
p_0	g.s	0	3^+	0.74	0.50	8.7	5.8
	1	0.03	2^+				
p_1	2	0.97	0^+	0.28	0.23	4.28	2.9
	3	1.01	(3^+)				
p_2	4	1.37	1^+	0.12	0.10	1.47	1.5
p_3	5	1.63	(3^+)	0.25	0.20	3.14	2.5

(a) *The average diffential cross-sections $<d\sigma/d\Omega>_{90}$ and $<d\sigma/d\Omega>_{159}$ were obtained by averaging over deuteron energies (2.0÷3.0)MeV at angles 90° and 150° respectively.*

(b) *The experimental total cross-sections σ_{exp} were obtained by integrating over the angles (15÷150)° at $E_d=2.5MeV$.*

(c) *The theoretical cross-section σ_{th} was tha Hauser-Feshbach calculation at $E_d=2.5 MeV$.*

The result of DWBA calculation for the group p_0, as shown in Fig 6, gives a reasonable fit to the experimental data. This indicates that the p_0 transition in the reaction $^{27}Al(d,p)^{28}Al$ the energies investigated goes principally through the stripping reaction. In the case of the

groups p_1, p_2 and p_3 the direct effect is not large, the evaporation contribution to the differential cross-section was calculated with the Hauser-Feshbach formula [12] using the set of parameters given in ref. [7]. In the present energy range, the compound nucleus ^{29}Si is excited at about 20 MeV in the continuum region, and the use of the statistical analysis is justified. The result of this analysis at an incident deuteron energy of 2.5 MeV is presented in Table II. Also listed in Table II are the measured values of the differential cross-sections at $\theta_L = 90°$ and 150° averaged on the whole energy interval. Figure 8 shows the experimental values of the total cross-sections for the different p transitions of the ^{27}Al$(d,p)^{28}$Al reaction, compared with the theoretical calculation at 2.5 MeV. The agreement is quite reasonable for groups p_2 and p_3, while a discrepancy appears for the first two p groups, in particular for the p_0 group the experimental value lies far above the straight line. This is not surprising, since the direct is present significantly in the p_0 transition.

In conclusion, the structures of energy excitation functions and angular distributions found in the present experiment are about the same as those observed in the earlier measurements [6,7] in the deuteron energy range (1.5÷2.3) MeV. The present data give further indication that two mechanisms of compound nucleus and direct interaction are contemporaneously present in the ^{27}Al$(d,p)^{28}$Al reaction at deuteron energies (2.0÷3.0) MeV, and the direct stripping and possible interference effects gives considerable contribution to the p_0 transition

Fig. 8. – *Experimental values of the total cross-sections for the different proton groups form the* ^{27}Al$(d,p)^{28}$Al *reaction compared with the Hauser-Feshbach calculation at 2.5 MeV.*

and for the higher transitions the compound nucleus plays a significant role in the reaction.

氘子在能量2.0—3.0MeV時產生^{27}Al$(d,p)^{28}$Al核反應

本文研究氘子在能量 2.0—3.0MeV 對鋁二十七原子核產生之 ^{27}Al$(d,p)^{28}$Al 核反應。在實驗過程中測得四羣質子在 90°及 15°之激發函數，及其能譜在 15° 至 150° 間角分佈情形。此四羣質子相當於鋁二十八原子核之四個低能階。結果發現在此核反應中有複核反應及直接反應同時出現。直接反應對於鋁二十八核基態躍遷之效果以 DWBA 剝奪反應理論分析之，實驗測得核反應截面積再與 Hauser-Feshbach 理論比較並詳加討論之。
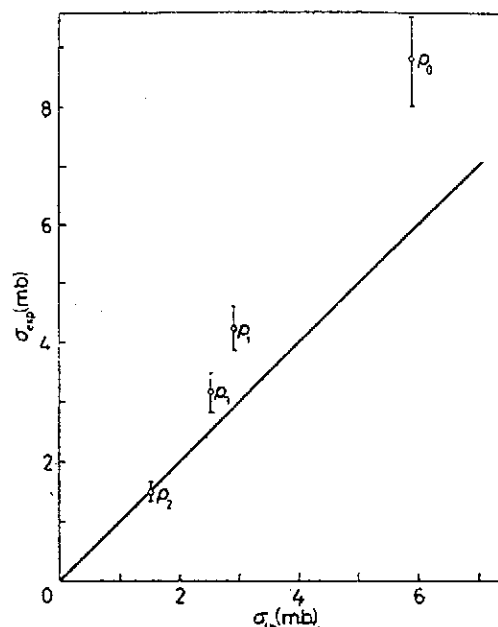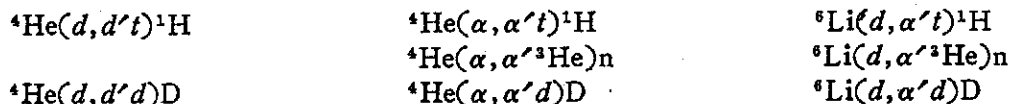
(12) W. Hauser and H. Feshbach: *Phys. Rev.*, 87, 366(1952)

Investigation of T=0 Excited States of 4He Using

Three-Particle Reactions

E.L. Haase, R. Hagelberg, W.N. Wang (王唯農) *,E.K. Lin (林爾康)*,
D.P. Saylor and M.A. Fawzi

Kernforschungszentrum Karlsruhe, West Germany

Abstract

Using 52 MeV deuterons and 104 MeV α-particles coincidence measurements in three entrance channels were carried out for the following reactions:

$^4He(d,d't)^1H$	$^4He(\alpha,\alpha't)^1H$	$^6Li(d,\alpha't)^1H$
	$^4He(\alpha,\alpha'{}^3He)n$	$^6Li(d,\alpha'{}^3He)n$
$^4He(d,d'd)D$	$^4He(\alpha,\alpha'd)D$	$^6Li(d,\alpha'd)D$

In measuring the correlations, the detector of the inelastic particle was kept at a fixed position and the second detector scanned over a range of coplanar angles favouring ^4He final state interactions.

The data can be fitted consistently with six $T=0$ excited states of ^4He, at 20.2 MeV, 21.1 MeV, 21.9 MeV, 25.5 MeV, 28.5 MeV and 31.8 MeV with widths (Γ) of 0.2 MeV, 0.8 MeV, 1.8 MeV, 2.9 MeV, 5.3 MeV and 5.6 MeV respectively. The validity of the sequential reaction mechanism is examined. The internal consistency of the level parameters for the three entrance and three decay channels as well as the symmetry of the extracted angular correlations about 0 and 90° in the recoil system centre of mass agree very well with the model of sequential decay. The angular correlations agree well with the predictions of a simple theory using the impulse approximation.
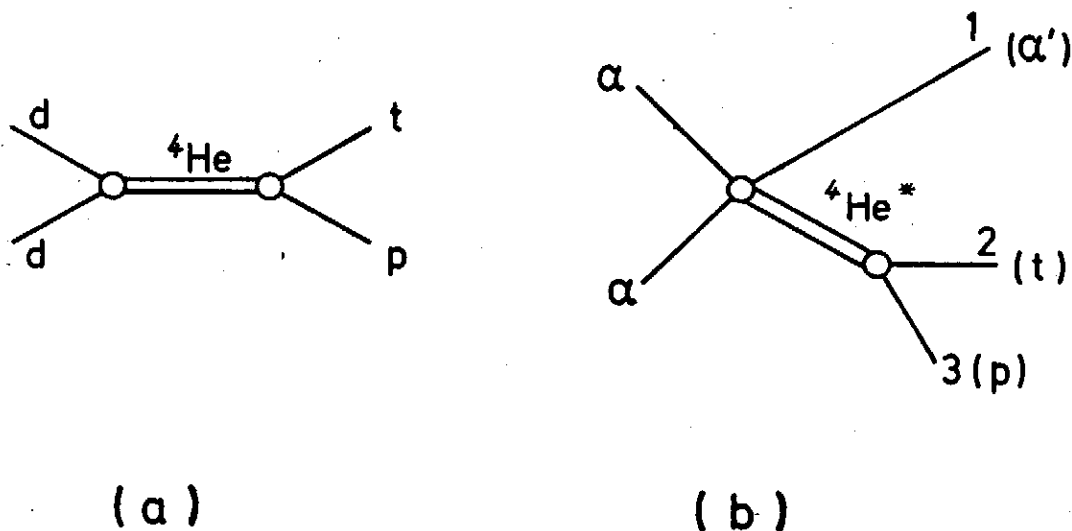
Fig. 1. *Diagrams (a) for a reaction and (b) for a reaction with three particles in the exit channel, both forming* ^4He *as intermediate system.*

1. Introduction

The ^{4}He nucleus is the lightest nucleus with an extensive system of excited states. It is a doubly magic nucleus with a high degree of symmetry. These facts have stimulated a number of theoretical calculations in recent years[1,7]. The splittings of the 7 members of the $l=1$ supermultiplet yield information on the strength of tensor forces[3]. Also model independent calculations starting from nucleon-nucleon forces are now coming within the realm of possibilities[7].
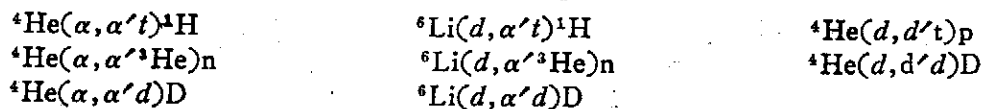
The fact that all the excited states in ^{4}He are particle unstable and that their widths are appreciable in comparison with their energies above threshold make both measurements and interpretation of ^{4}He resonances difficult. So far practically all of the information on resonances in the mass 4 system has been obtained from phase-shift analyses of elastic scattering and of reactions, proceeding through a mass 4 compound nucleus[8] (Fig. 1a).

An alternate approach is to study reactions with three particles in the exit channel in which ^{4}He resonances appear through final state interactions (FSI) between a pair of the outgoing particles.

Here ^{4}He is formed in a direct reaction and decays into one of the three possible decay channels $T+p$ ($Q=19.81$ MeV), ^{3}He$+n$ ($Q=20.58$ MeV) and $d+d$ ($Q=23.84$ MeV above the ^{4}He ground state). The assumption of sequential decay appears reasonable at our incident energies.

During the mean life of the lowest excited state the inelastic particle and the intermediate system separate by about 100 times the range of their nuclear interaction. Conservation of isospin and parity, and possibly the reaction mechanism, lead to considerable selectivity in the levels that can be excited. This is a great help in untangling the overlapping resonances. The problem of overlap between the 21.1 MeV, 0^- and the 21.9 MeV, 2^- states is particularly severe. As the 0^- state is forbidden on account of parity conservation in the inelastic scattering of α-particles off ^{4}He, this reaction offers a unique possibility to determine level parameters for the 2^-, $T=0$ state. Previous[14,15] kinematically complete experiments have only been able to positively identify the 20.2 MeV, 0^+ state. Reactions with three particles in the exit channel lend themselves to a reasonably simple interpretation if the reaction proceeds via sequential decay.

To test the validity of this hypothesis of sequentiatl decay and to extend the available information on excited states of the α-particle is the aim of the present work. It attempts also to extract the energy and width of higher excited states of ^{4}He. To this end we investigated the following reactions using 104 MeV α-particles and 52 MeV deuterons:

^{4}He($\alpha,\alpha't$)^{1}H	^{6}Li($d,\alpha't$)^{1}H	^{4}He($d,d't$)p
^{4}He(α,α'^3He)n	^{6}Li(d,α'^3He)n	^{4}He($d,d'd$)D
^{4}He($\alpha,\alpha'd$)D	^{6}Li($d,\alpha'd$)D	

Within the validity of isospin conservation all three entrance channels excite only $T=0$ levels.

Preliminary data contained in the present work have previously been published[9].

2. Kinematics and Experimental Procedure

In discussing the kinematics we follow the notation of Ohlson[10]. Let us consider coplanar events, as all present measurements were done in the reaction plane. A projectile p is inelastically scattered off the target t and emerges as particle 1 at the laboratory angle θ^4_1 (Fig. 2). If for convenience we treat the reaction as sequential, the intermediate system 2-3 recoils in the direction θ^4_{23} and carries a definite energy E_{23} above the two particle threshold. This corresponds to a definite excitation energy $E_s=E_{23}+Q$ referred to its ground state. The
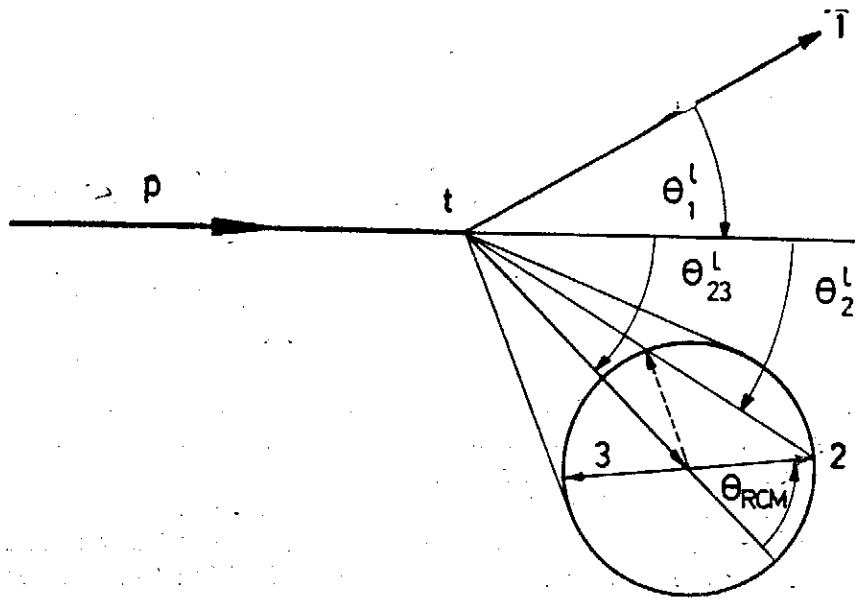
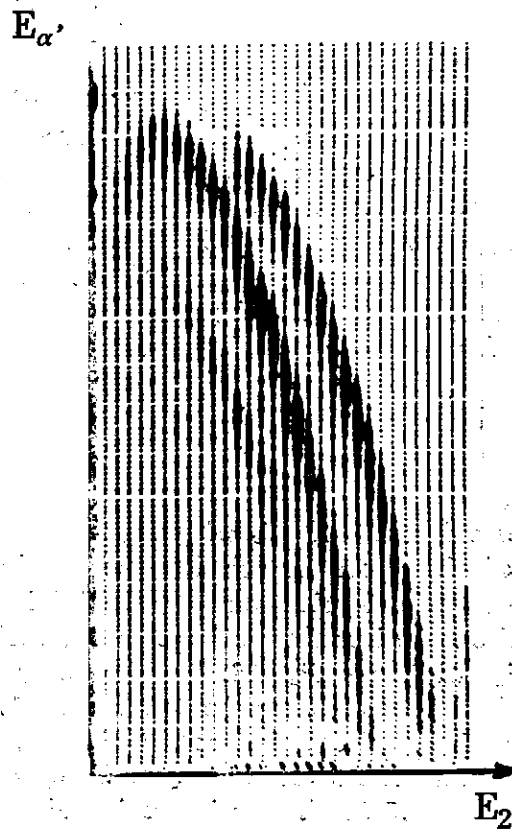Fig. 2. *Kinematics of sequential decay.* t=*target*, p=*projectile*.

Fig. 3. *Map display of raw data. From left to right, events lie along the kinematic curves for the* $^4He(\alpha,\alpha'd)D$, $^4He(\alpha,\alpha't)^1H$ *and* ^4He $(\alpha,\alpha'^3He)n$ *reactions.*

intermediate system then decays into two particles forming an angle $\theta_{RCM}(=\theta^{c'(1)})$ with the recoil axis in its centre of mass system, and the energy E_{23} is shared by the particles 2 and 3. The recoil momentum combines with the momentum set free in the decay, so particle 2 emerges at θ^t_2. In the case $E_{23} < E_{Recoil}$, for a given E_{23} particle 2 (having mass 2 or mass 3) can only emerge within a definite decay cone. To a given θ^t_2 generally two values of θ_{RCM} are associated, one for θ_{RCM} less than about 90° and another (shown dashed in Fig. 2) for θ_{RCM} larger than about 90°.

To gain "kinematically complete" information we have carried out coincidence measurements between the inelastic particle 1 and the decay particle 2, simultaneously measuring T, ^{3}He and d for the three possible 2-particles decay channels. θ^t_1 was kept fixed and θ^t_2 was varied in up to 20 steps over a range of angles favouring ^{4}He final state interactions. After transformation into the recoil system center of mass (RCM), one obtains the angular correlation in the RCM system. The beam of 104 MeV α-particles and 52 MeV deuterons was provided by the Karlsruhe Isochronous cyclotron.

Fig. 3 shows a typical map display of a two-parameter coincidence measurement for the inelastic α-scattering off ^{4}He. One can see events along the kinematically allowed curves for the three decay modes. For the triton curve one can see in addition to the upper branch (large E^t_2, $\theta_{RCM} < = 90°$) also the lower branch (small E^t_2, $\theta_{RCM} > = 90°$). Using ^{4}He gas and ^{6}Li self-supporting targets, data were recorded for the eight reactions investigated.

To facilitate particle identification, solid state detectors were used for both telescopes. Timing signals from the two telescopes were sent to a start-stop time to amplitude converter. A discriminator window corresponding to 30 nsec was set on the output. This corresponds to about twice the value needed to compensate for time of flight differences. E^t_1 singles spectra, gated with the ORTEC particle identifier discriminator output, were recorded throughout the measurements simultaneously. E^t_2 singles gated with discriminator outs for d, t, and ^{3}He windows on the E_2 particle identifier signal, measured for each θ^t_2, permitted the small remaining correction for random coincidences to be carried out. The shift of the ^{3}He curve was carried out by adding a standard pulse to the E^t_2 signal when ever the ^{3}He discriminator triggered. For the ^{6}Li+d reactions all ADC outputs were also recorded event by event on magnetic tape for later analysis. The events are summed up across each ridge and are projected onto the $E\alpha'$-axis; there is a definite, slightly non-linear relationship between $E\alpha'$ and E_2 for the resonances in ^{4}He.

3. Results and analysis of the energy distributions

3.1 The ^{4}He$(\alpha,\alpha't)^1$H reaction

Fig. 4 shows for fixed θ^t_1 as a function of E_x with θ^t_2 as parameter a representative set of spectra from projections of the upper branch for the ^{4}He$(\alpha,\alpha't)^1$H reaction. The transformation from $E^t\alpha'$ to E_x has been carried out by multiplying with $\Delta E^t_1/\Delta E_x$. Just above the threshold at 19.81 MeV one notices the well known 0^+, 20.2 MeV state. It appears only within the limits between $\theta^t_2 = 44.5°$ and $\theta^t_2 = 56.3°$ of its decay cone. Outside the cone a broad peak at $E_x = 21.9$ MeV can be seen. As the 0^- state at 21.4 MeV[5] is forbidden on account of parity conservation (identical spin 0 bosons incident), this reaction is particularly suited to determine resonance parameters for third (2^-, $T=0$) state of ^{4}He. Beyond that there is a broad structure peaking at 28.5 MeV. For increasing θ^t_2 this gets obscured by a peak moving in from the left and arising from the p-^{4}He FSI in the ground state. It occurs at the kinematically predicted positions. For changing θ^t_2 this peak must shift.
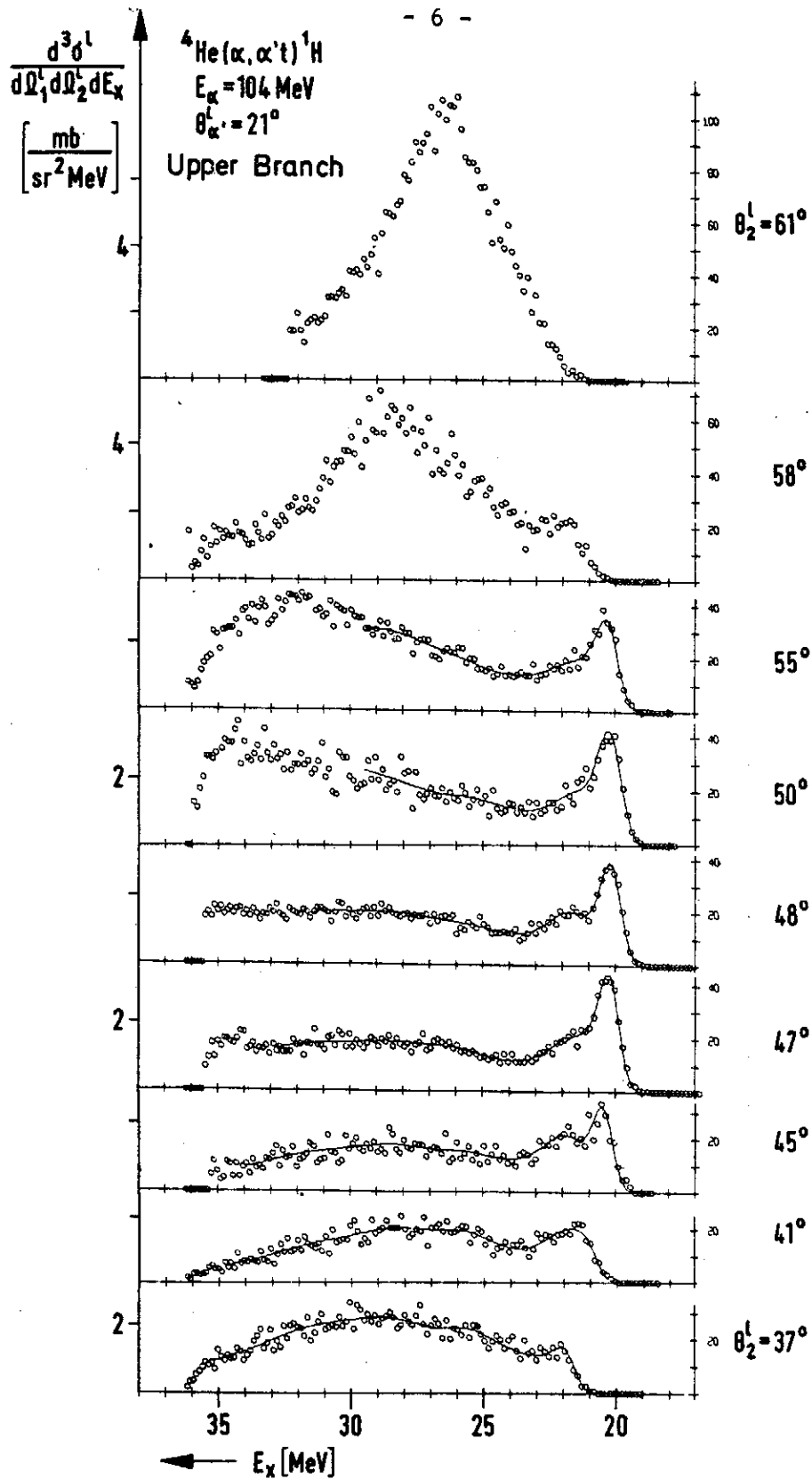
- 6 -
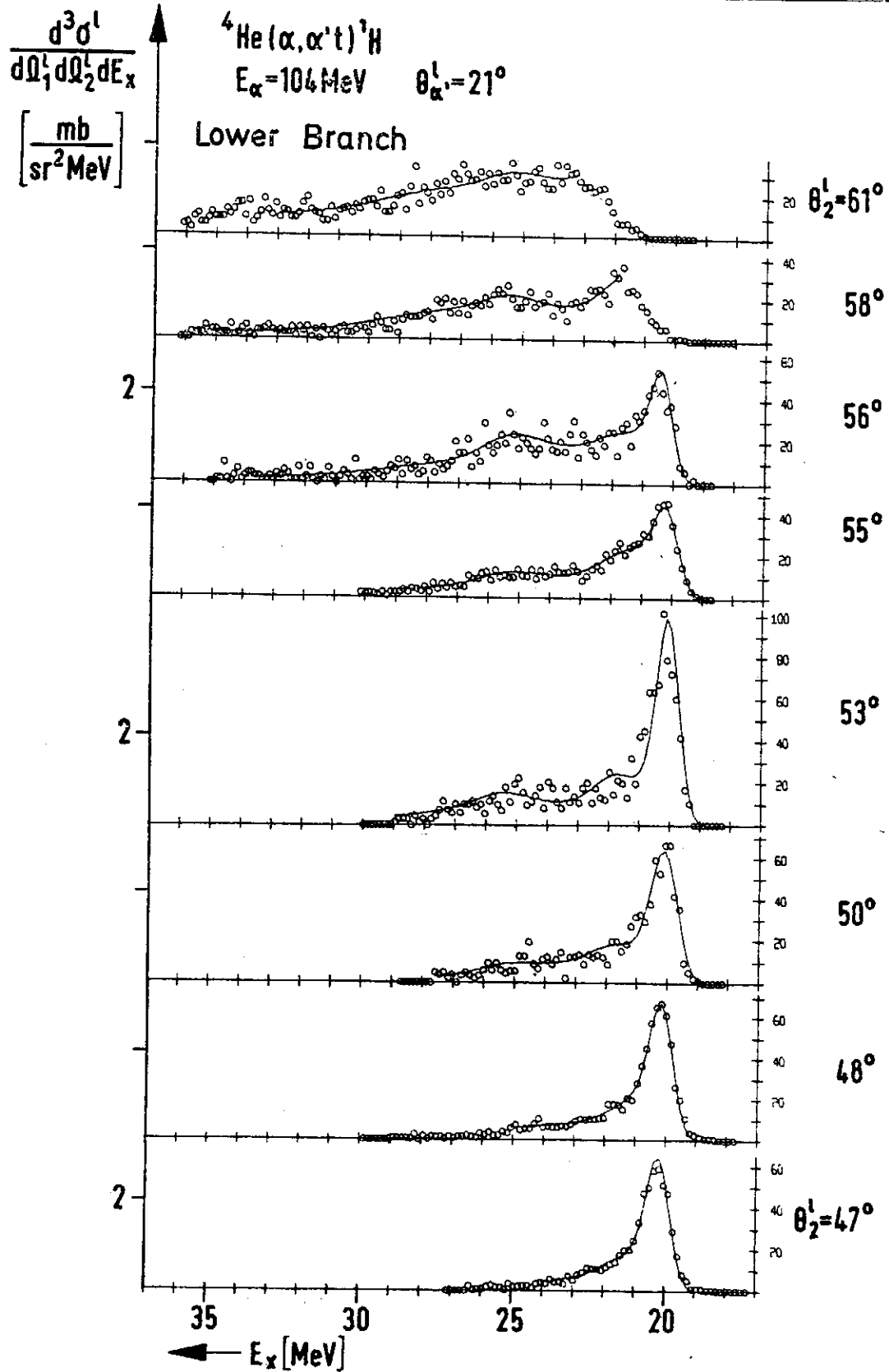

Fig. 4. *Representative family of spectra for the $^4He(\alpha, \alpha' t)^1H$ reaction as a function of excitation energy in ^4He.*

Fig. 5. *Representative family of spectra for the* $^4He(\alpha,\alpha't)^1H$ *reaction as a function of excitation energy in* ^4He.
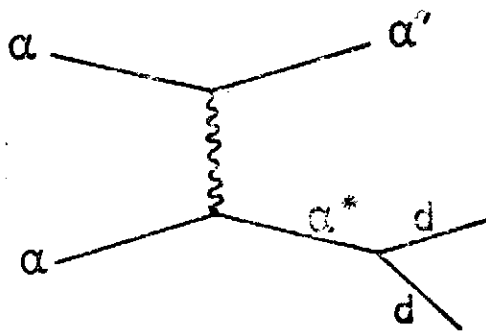
Fig. 5 shows 8 spectra for the lower branch of the same reaction. The rapid fall of the phase-space distribution leads to a small laboratory cross section for higher excitation energies. Together with the increased random rate this makes evaluation for higher excitation energies more uncertain. Beyond the resonances at 20.2 and 21.9 MeV already noted for the upper triton branch, with increasing θ^l_2 another bump at 25.5 MeV starts coming up. The low energy regions of the two spectra for the largest values of θ^l_2 are partly disturbed by tails from ^{4}Li resonances.

3.2 Method of analysis and theoretical interpretation

Generally for each decay channel c we have

$$\frac{d^3\sigma^l_c}{d\Omega^l_1 d\Omega^l_2 dE^l_1} = |M_c|^2 \cdot \rho_c \simeq |U_c|^2 \cdot |M^{seq}_c|^2 \cdot \rho_c \qquad (1)$$

where ρ_c is the phase-space factor the decay channel under consideration. The matrix element M_c combines both vertices in Fig. 1b. Following Goldberger and Watson[11] we factorise M_c into a term U_c independent of internal coordinates of the 2-3 system arising from the first vertex and an enhancement factor M^{seq}_c which describes the final state interaction between particles 2 and 3 and which reflects resonances in the 2-3 system. For the case of the PWBA this formula lends itself to a simple interetation and permits explicit calculation of both energy and angular dependence: Levinson[12] and others have shown that the zero range PWBA treatment is formally identical with that of the exchange of a fictious spinless particle. This has momentum along the recoil axis, and angular momentum l relative to the target.

Then we have the problem of the scattering of this fictious $S=0$ particle off an $S=0$ α-particle forming an intermediate state possessing a series of resonances with J^π decay into the three possible decay channels.

PWBA model of sequential reaction

This can be explicitly calculated in terms of the R-matrix theory or the theory of Humblet and Rosenfeld[43]. According to Ref.[12] the use of DWBA and non-zero range forces does not materially alter the picture, but may lead to different populations of the magnetic substates of the intermediate system.

As a first step in analysing our data we neglect Coulomb and threshold effects, interferences between levels and coupling between decay channels. Then assuming the non-resonant coefficients with a smoothly varying energy dependence to be constants, the expression for the reaction-matrix element[13] reduces to

$$|M^{seq}_c(E_x, \theta_{BCM})|^2 = \sum_{l=0}^{l_{max}} \left[C + \sum_n \frac{\frac{1}{2}\Gamma'_n B_{ln} + (E_x - E_n)A_{ln}}{(E_x - E_n)^2 + \Gamma'^2_n/4} \right] P_l(\cos\theta_{BCM}) \qquad (2)$$

The sum over l is limited to $l_{max} < 2J$ or $2L$, whichever is smaller; the B_{ln} are zero for odd values of l. The sum over n extends over all resonances of definite J^π. C is a constant non-resonant term, the B coefficients give the intensity of Breit-Wigner single level resonances, and the A coefficients give the intensity of interference between the resonances and the non-resonant background (limited in size so that the cross-section does not become negative).

Actually the data are measured in the laboratory system, and it is the simplest to carry out the fitting in that system also, because of the folding effect of the energy resolution.

We have fitted the spectra for a set of θ^1_2 for each of the reactions with the expression

$$\frac{d^3\sigma/_{exp}}{d\Omega^1_1 d\Omega^1_2 dE^1_1} = F\left\{\left[C(\theta^1_2)+\sum_n \frac{\Gamma_n B_n(\theta^1_2)+(E_x - E_n)A_n(\theta^1_2)}{(E_x - E_n)^2 + \frac{1}{4}\Gamma^2 n}\right]\rho^1(E^1_1)\right\} \qquad (3)$$

Here F denotes the operation of folding the "theoretical" curve with the experimental resolution, taken to have a gaussian form. The coefficients for each resonance n have been rewritten:

$$B_n(\theta^1_2) = \sum_l \tfrac{1}{2} B_{ln} \ P_l \ (\cos \theta_{RCM}) \qquad (4)$$

$$A_n(\theta^1_2) = \sum_l \tfrac{1}{2} A_{ln} \ P_l \ (\cos \theta_{RCM})$$

For the explicit form of $\rho^1(E^1_1)$ see formula (28) in Ref[10].

An automatic fitting program utilising an IBM 360–65 was developed.

In fitting each family, resonance position as well as width parameters are varied in common and the P_n, A_n and C individually for each spectrum so as to minimize χ^2. The resulting fits are drawn as solid curves in the spectra.

As shown in Fig. 4–6 and 9,10 excellent fits are obtained for all spectra. The value of $\chi^2_1 = \chi^2/(M - N)$ (χ^2 divided by the number of data points minus the number of parameters) ranges between 1.05 and 1.18 for the different families, as compared with expected value of 1.

In fitting the data, regions corresponding to excitation up to 5 MeV in ^{5}Li and ^{5}He were omitted, so as to exclude the mass 5 ground state and a possible weak first excited state around 2.6 MeV.

3.3 The ^{4}He$(\alpha, \alpha'd)$D reaction and transformation into the RCM system

Fig. 6 shows a representative set of spectra for the ^{4}He$(\alpha, \alpha'd)$D reaction. The small bump around 24 MeV excitation does not correspond to a resonance, but results from the shape of the projected phase-space distribution. (see Fig. 7). As for the triton decay there is a broad maximum peaking around 28.5 MeV. This peak falls with increasing θ^1_2 and a structure is reached which certainly cannot be fitted with a single Breit–Wigner resonance.

For this reaction no quasielastic process is expected to contribute as the Q-value ($\sim$24 MeV) is rather large compared with the energy available in the centre of mass (52 MeV). Also its maximum at $\theta^1_2 = 23°$, $E_x = 43$ MeV would lie outside the region measured.

There is no evidence for FSI arising from ^{6}Li resonances. They would show up as narrow, rapidly shifting peaks; though for the spectra for the largest values of θ^1_2 a small contribution cannot be excluded.

The simplest assumption to account for the structure is to use two Breit–Wigner resonances. The resulting solid line in Fig. 6 yields an excellent fit for two resonances at 28.7 MeV and 31.9 MeV. At the very least this assumption yields an excellent parametrisation of the data for transformation into the RCM system. To carry out the transformation the "theoretical" spectrum, not folded, is multiplied by the Jacobi factor for transformation from the laboratory to the RCM system. This can be obtained from eq. (10) in Reference 10.

Note that the expression of Ref. 10 has to be inverted! The corresponding spectra for $\theta^1_2 = 17.4°$ and $\theta^1_2 = 46.9°$ are shown in Fig. 7a. Fig. 7b shows three representative RCM spectra for the ^{4}He$(\alpha, \alpha't)^1$H reaction.

Fig. 8 illustrates the result of a complete transformation into the RCM system. It is characteristic of the effect of the transformation for the reactions investigated in this paper. Here σ_{RCM} is plotted as a function of both E_x and θ_{RCM}. With decreasing E_x the angular range of θ_{RCM} widens, reflecting the decrease in the size of the decay cone. Also
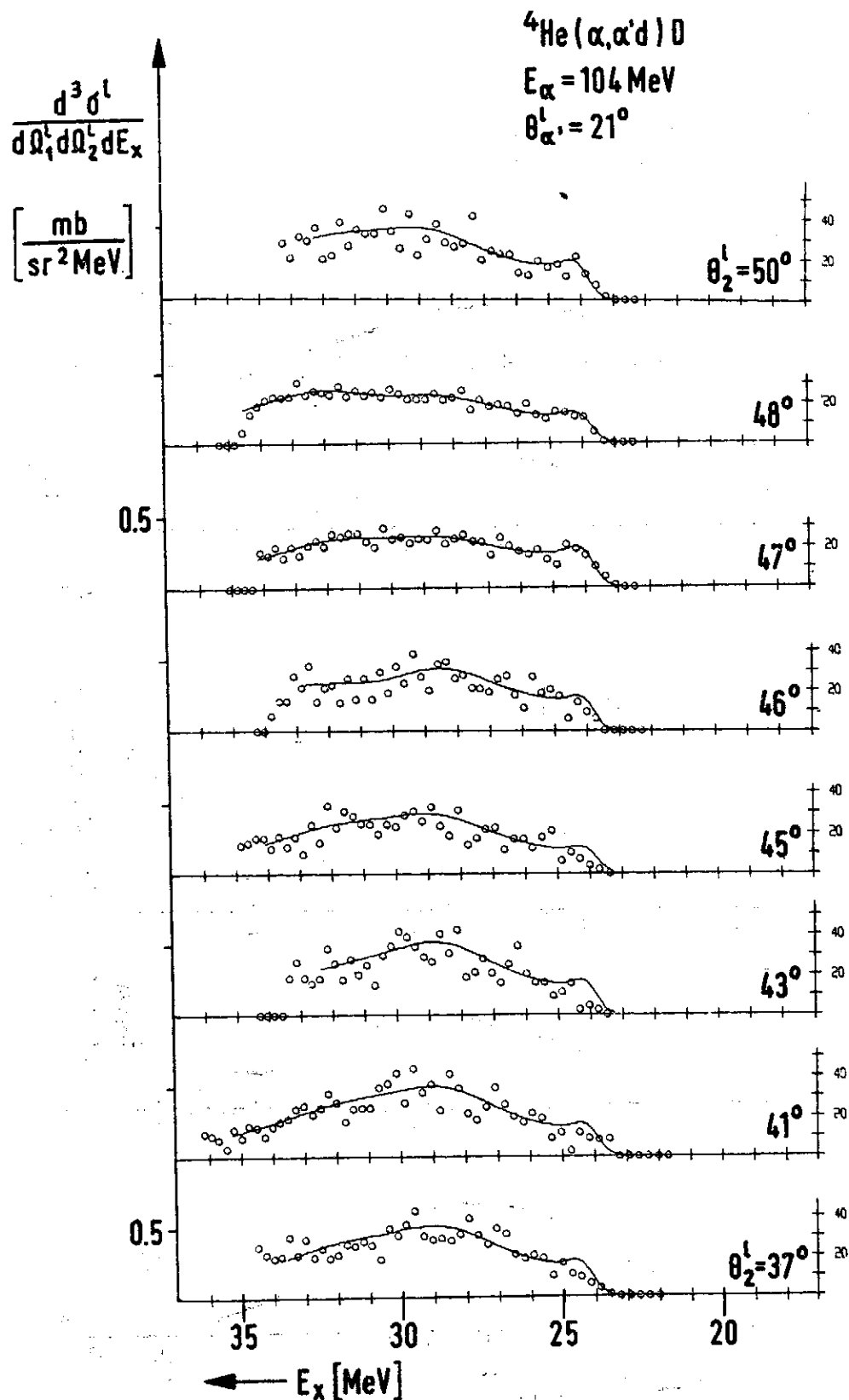
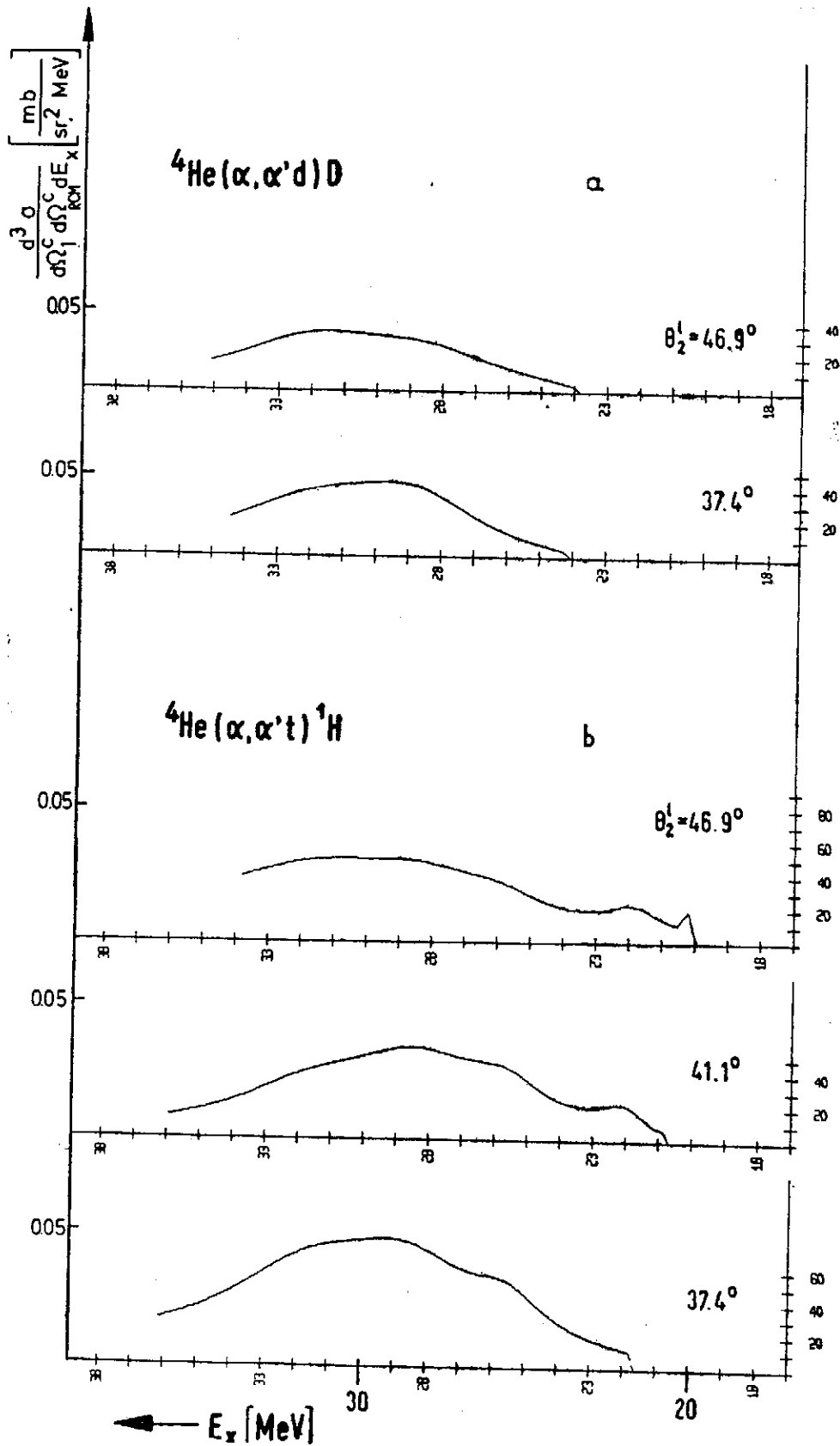Fig. 6. *Representative family of spectra for the* $^4He(\alpha,\alpha'd)D$ *reaction.*

Fig. 7 *Cross section in the RCM system as a function excitation energy,*
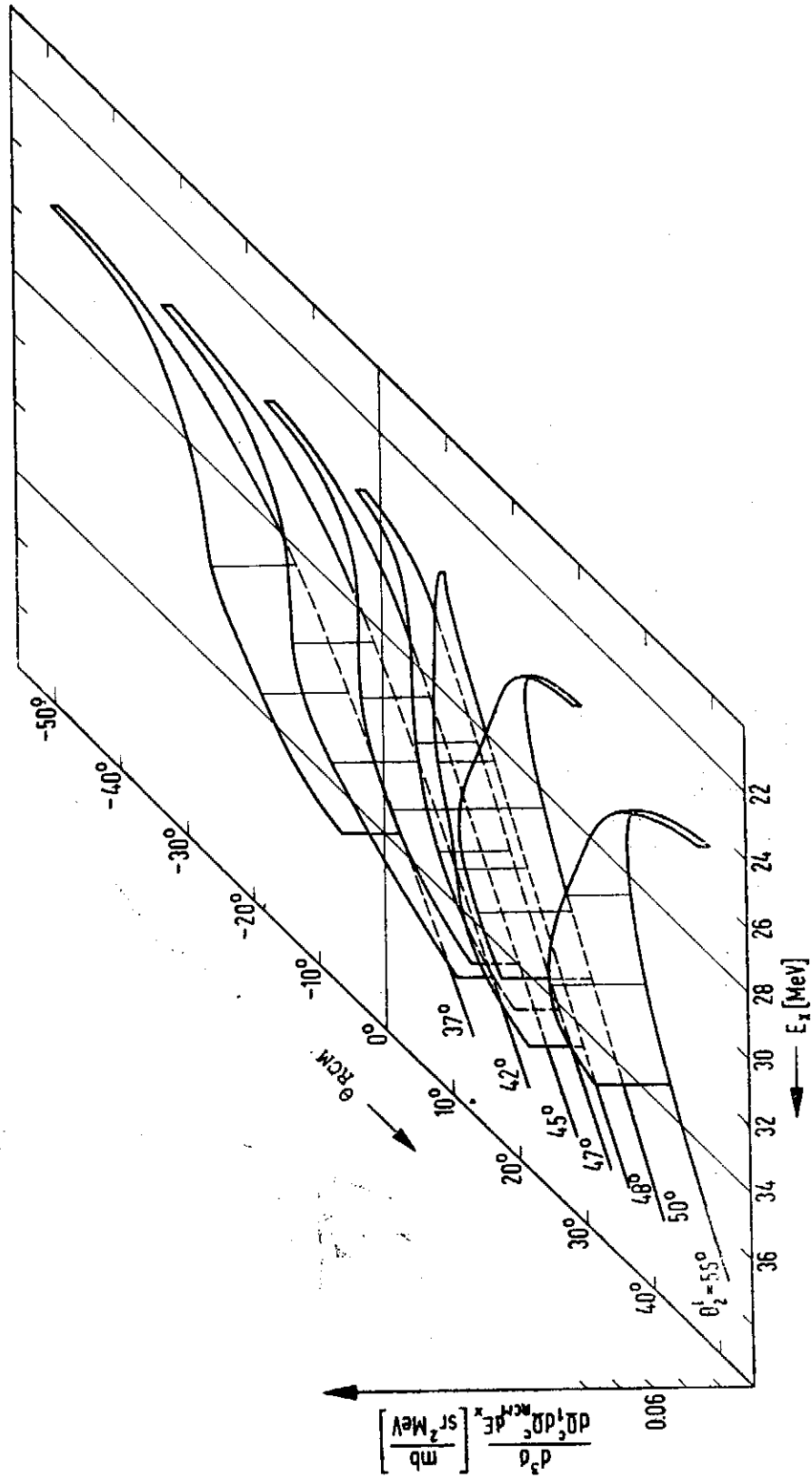*calculated with the parameters of the fits to the experimental data.*

Fig. 8. Cross section in the RCM system, as function of the excitation energy and θ_{RCM}, for the ⁴He(α, α′d)D reaction.
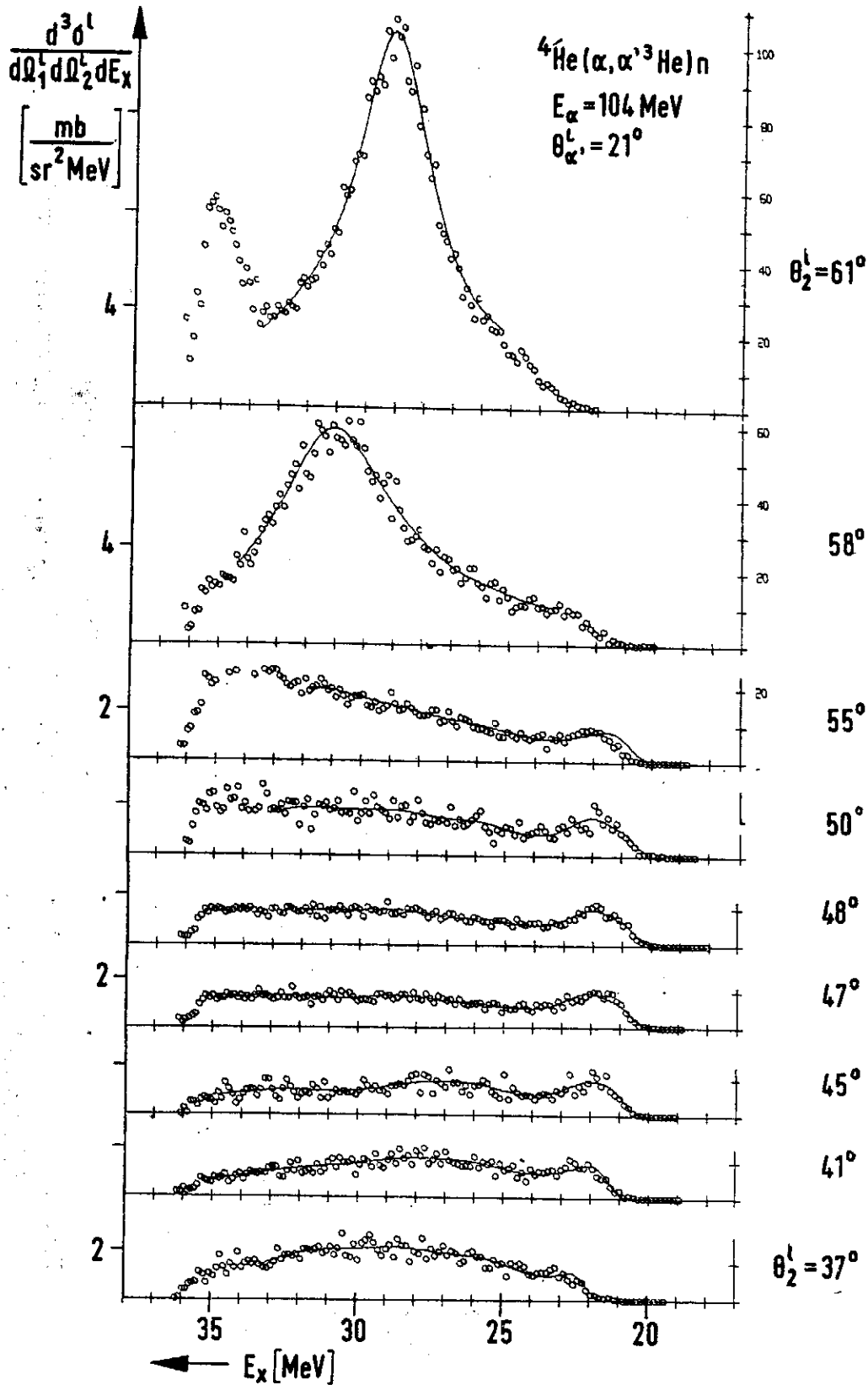
Fig. 9. *Representative set of spectra for the* ^{4}*He*$(\alpha, \alpha'$ ^{3}*He*$)n$ *reaction.*

with increasing E_x the recoil axis ($\theta_{RCM}=0$) moves to smaller values of θ'_2. Note, for increasing θ_{RCM}, that the distribution for the 28.7 MeV resonance drops gradually and that for the 31.9 MeV stays approximately isotropic.

To obtain acceptable fits to the upper and lower branch triton spectra, five resonances have to be assumed. In addition to the obvious ones at 20.2 and 21.9 MeV, a fairly weak one at 25.5 MeV is needed and two more at 28.3 and 31.7 MeV with parameters similar to those of the d,d channel. The values of the resonance parameters for simultaneous fits of the different families of spectra are listed and compared in Table 1, section 3.7.

3.4 The ^{4}He(α,α'^3He)n Reaction

In Fig. 9a representative set of spectra for the ^{4}He(α,α'^3He)n reaction is shown. From a consideration of charge symmetry of nuclear forces they are expected to be identical with the corresponding spectra of the $T+p$ channel, except for the effects associated with the differing C-values. This is indeed the case.

As it is below the threshold, the 20.2 MeV state cannot appear. This makes the 21.9 MeV resonance appear more distinct. A good fit can be obtained, as shown, using for the 21.9, 25.5, 28.3 and 31.7 MeV resonances the parameters determined for the $T+p$ channel.

The ^{5}He ground state appears at large angles more pronounced as it is narrower than the ^{5}Li ground state. The rise near $E_x=35$ MeV in the uppermost spectum stems from the fact that this state also appears twice in the upper and the lower branch but with the role of the $E\alpha'$ and E^3_{He} axis interchanged.

3.5 The ^{4}He(d,d't)^{1}H and ^{4}He (d,d'd)D Reactions

Fig. 10a gives a set of coincidence spectra for the upper branch of the ^{4}He($d,d't$)^{1}H reaction. They are characterized by a single prominent distribution peaking at 21.2 MeV excitation and only weak structure above. The spectra for $\theta'_2=37°$ corresponds to the recoil axis for 20.2 MeV excitation.

The 0$^-$ state at 21.4 MeV[20] is allowed in this reaction. An attempt to fit these spectra with a single Breit-Wigner resonance gave a very poor result. Two fits with different extreme assumptions were carried out; both gave equally acceptable fits:

a) Resonances at 21.9 and 21.1 MeV plus a weak one at 20.2 interfere with a significant non-resonant background,

b) the non-resonant background is assumed to be zero. Then one needs in addition to the ones above further resonances at 25.1, 28.6 and and 31.4 MeV.

These latter fits are shown in Fig. 10a. It is felt that this is more reassonable, as for all other reaction the nonresonant term was negligibly small and in this case the non-resonant term would certainly not be isotropic either. Incidentally the spectrum for $\theta'_2=25°$ is beyond the edge of the decay cone for the 21.1 MeV resonance.
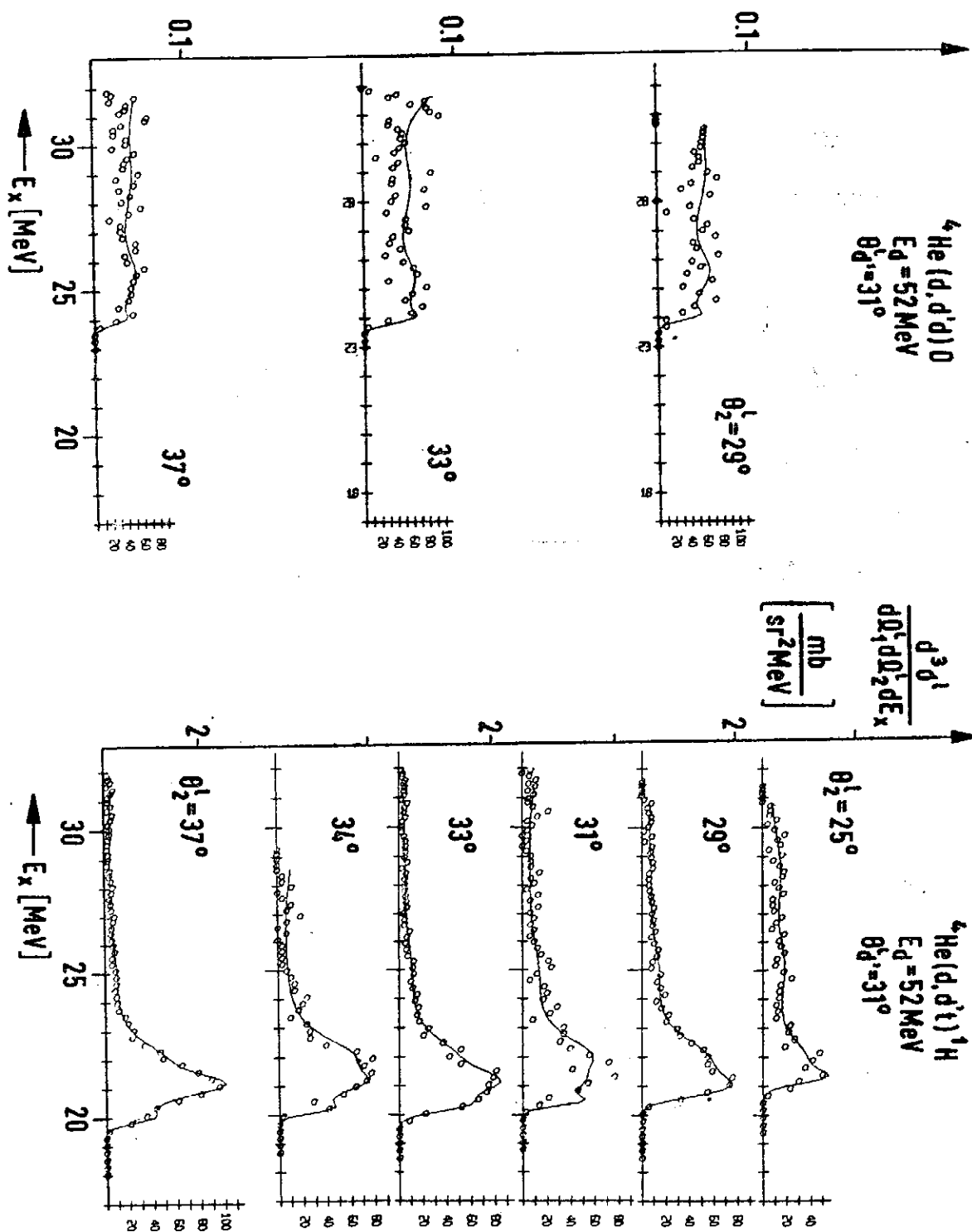
Fig. 10. *Spectra for the ⁴He(d,d't)¹H and ⁴He(d,d'd)D reactions.*

The only interfering reaction would be caused by $T=1/2$ resonances of ³He between 7.5 and 16 MeV excitation, shifting as noted before. However, no evidence was found for such resonances.

The neglect of interference between the 0⁻ and the 2⁻ level might be severe. In a single spectrum there can be no interference between levels of different J^π, as the interference terms drop out upon integration over Ω_{BCM}.
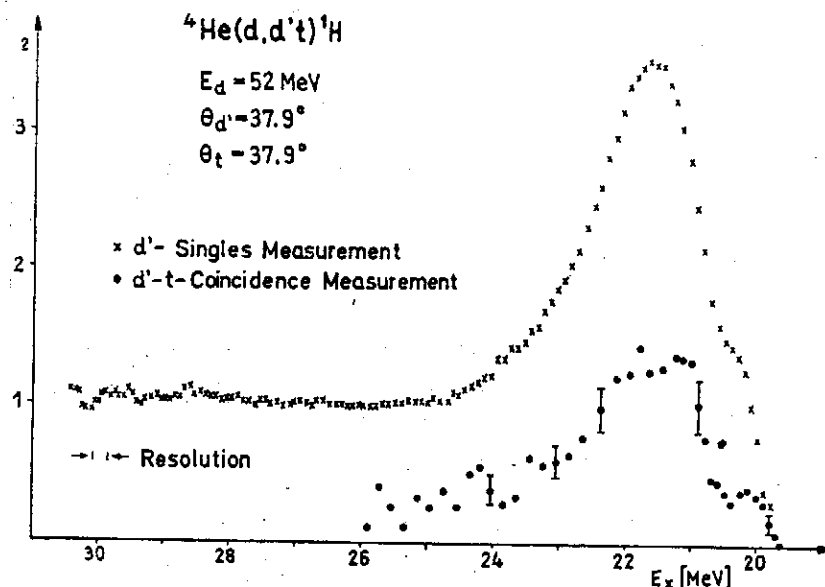

Fig. 11. *Comparison of the ⁴He(d,d′) singles and the ⁴He(d,d′t)¹H coincidence spectra.*

Fig. 11 shows for comparison a single and a coincidence spectrum for $\theta^i_1 = \theta^i_2 = 37.9°$. Here in arbitrary units the square of the matrix element is shown, to eliminate the distortions due to different shape for the phase space space distribution for singles and coincidence spectra. For this pair of angles the 20.2 MeV state is more pronounced, also the sharp drop near $E_* = 21$ MeV. The fit of several singles spectra confirms the parameters obtained from the coincidence spectra.

Three of the simultaneously measured spectra for the ⁴He(d,d′d)D reaction are shown in Fig. 10. They show little structure. These spectra can be adequately fitted with the same resonances. The results are listed for comarison in Table 1 in section 3.7.

3.6 Deuteron induced reaction on ⁶Li

A third possibility to excite the $T=0$ states of ⁴He is by bombarding ⁶Li with deuterons. Recently results on the same reaction at lower energies have been published[14].

A comparison of the results shows the advantage of using higher incident energies, and at the same time demonstrates that even higher energies would be desirable in spite of the positive Q-value. All three decay channels are disturbed by other FSI (⁵He, ⁵Li ⁶Li), so that only limited portions of the angular correlations are clean, as far as ⁴He resonances are concerned.

Fig. 12 shows a spectrum for the ⁶Li(d,α′t)¹H reaction. The fit yields no contribution from the 20.2 and 21.1 MeV states, a very prominent peak for the 21.9 MeV state and a weak indication for a 25.5 MeV state.
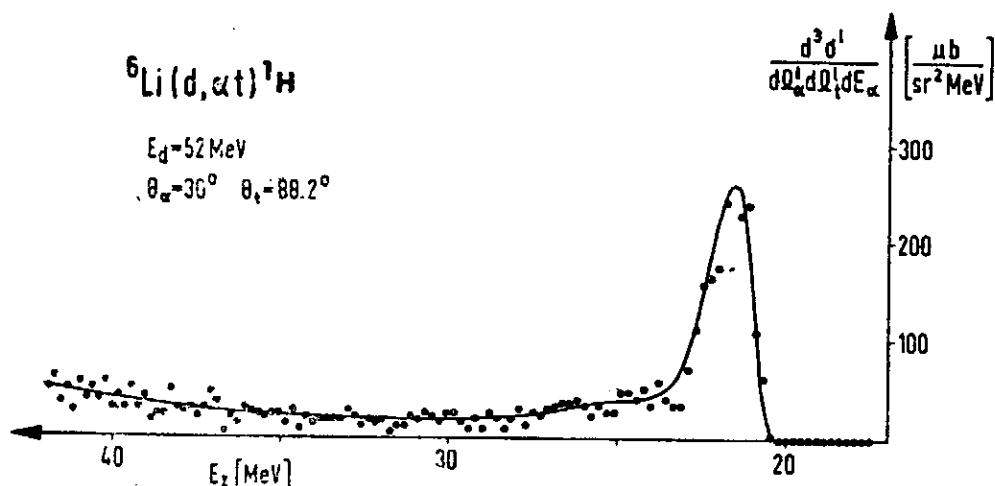
Fig. 12. *Typical spectrum for the $^6Li(d,\alpha t)^1H$ reaction.*

Fig. 13 gives a set of four spectra for the $^6Li(d,d'd)D$ reaction. The bottom two spectra show the 25.5 MeV resonance quite strongly, plus a weaker distribution around 28.5 MeV. The peak at high excitation energies from the 4.57 MeV state of ^6Li. As θ^t_2 decreases the quasielastic peak starts to obscure the FSI peaks.

A narrow 2^+ level 55 keV above the (d,d) threshold has been reported by Franz and Fick[23]. The present reaction should be very suitable to populate such a state, being interpreted as consisting of two deuteron clusters. The proximity to the threshold would cause a significant fraction of the particles decaying into 4π to enter $\Delta\Omega^t_2$ of the second detector. This resonance should show up as a narrow line with the experimental resolution of 2.5 channels just above the threshold for the spectrum at $\theta^t_2 = 93.5°$.

The angle $\theta^t_2 = 104°$ is outside the decay cone. The comparison of these spectra permits us to give an upper limit of 25 nb/sr^2 for the cross section for excitation of such a narrow resonance in this reaction. A corresponding value for the 25.5 MeV resonance is about 4 μb/sr^2.

3.7 Summary of the results on resonance parameters

The data presented in the previous subsections show that for a given reaction only the measurement of an angular correlation θ^t_2 permits one to detect or to exclude, interference from other FSI or the quasielastic scattering. For a fixed θ^t_1 the ^4He resonances are stationary, whereas in general interfering processes shift with changing θ^t_2, and can thus be identified with the help of kinematics.

We have measured eight such correlations for three entrance and three decay channels. For a given correlation those spectra or parts of spectra that are free from interfering reactions were treated as follows:

1) Simultaneous fits minimizing χ^2 were carried out using formula (3). In these fits the positions E_n as well as widths Γ_n for each resonance were varied in common, and the A_n, B_n and C_n were varied indivdually for each spectrum. In fitting, the minimum number of resonances were used that reproduced the data and gave an acceptable fit.

2) The resulting parameters are listed in Table 1.

A subjective estimate for the error in position is $\pm$ 10% of the width, in addition to $\pm$ 60 keV for the uncertainly in the primary energy and θ^t_1, and for the relative error in the widths $\pm$ 15%.
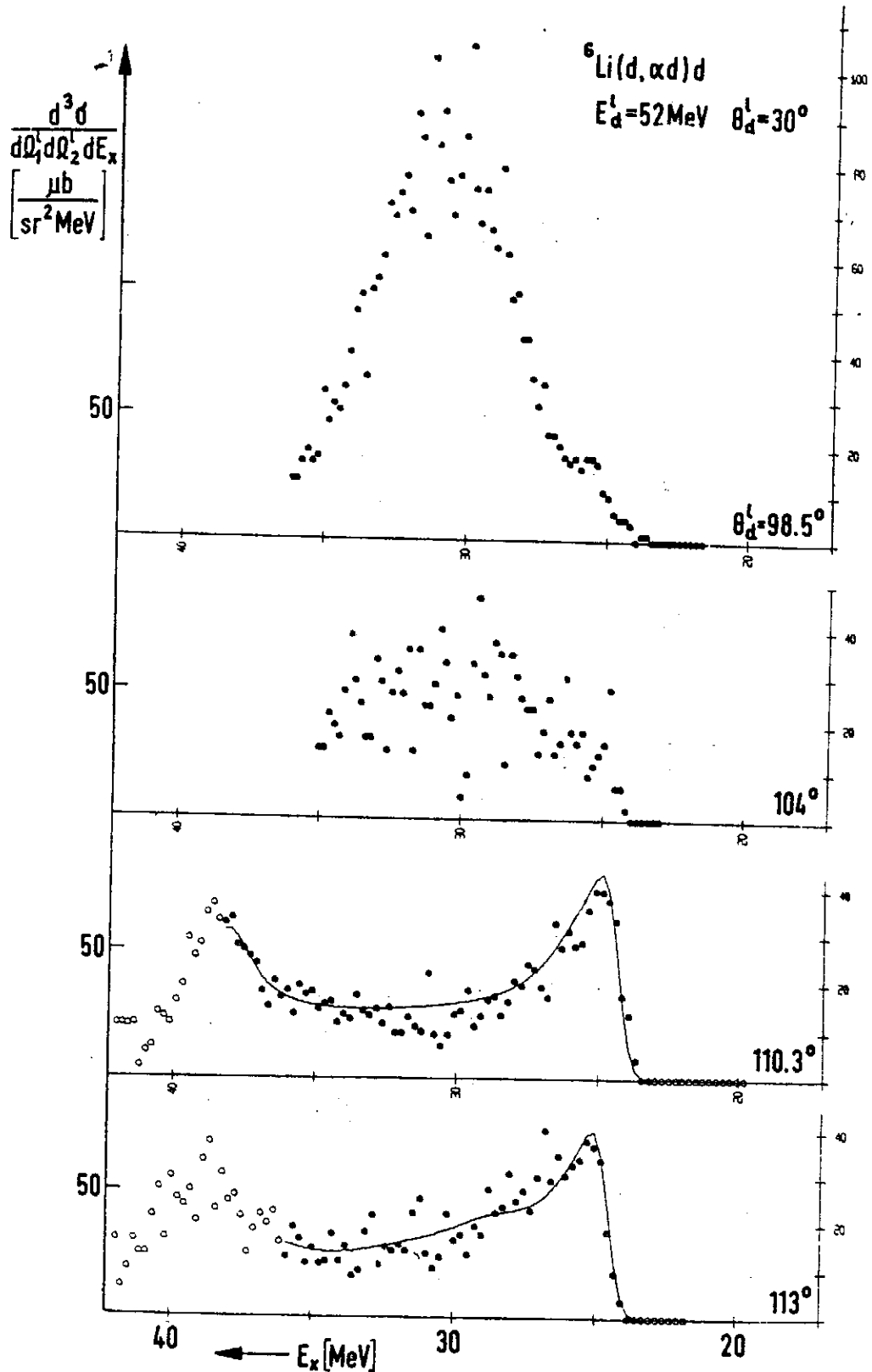
Fig. 13. *spectra for the ⁶Li(d,αd)D reaction showing the 25.5 MeV state. For smaller values of θ^l₄, the quasielastic process dominates.*

$T=0$	^{4}He(α,α')			^{4}He$(d,d'$		^{6}Li$(d,\alpha'$		
	$t)^1$H	^{3}He$)n$	$d)D$	$t)^1$H	$d)D$	$t)^1$H	^{3}He$)n$	$d)D$
20.2 0+	20.2±0.004 $l'=0.2\pm0.006$	—	—	20.2±0.03 0.2±0.01	—	not observed	—	—
21.1 0-	forbidden			21.1±0.02 0.8±0.04	—	not observed		
21.9 2-	21.9±0.017 $l'=1.8\pm0.01$	21.9±0.02 1.9±0.05	weak	22.0±0.03 1.8±0.06	—	21.9±0.04 consistent with other values		
25.5 (0+,1+)	25.5±0.02 $l'=2.9\pm0.01$	25.6±0.06 3.1±0.12	at most	25.1±0.04 2.9±0.2	25.2±0.02 2.2±0.01	weak, consistent		25.5±0.12 3.0±0.22 very weak
28.5 1-	28.3±0.02 $l'=5.3\pm0.01$	28.3±0.03 5.3±0.07	28.7±0.01 5.0±0.13	28.6±0.04 3.8±0.34	28.7±0.03 4.6±0.02	weak, consistent		weak, consistent
31.8	31.7±0.02 $l'=5.6\pm0.01$	31.7±0.05 5.5±0.01	31.9±0.07 5.9±0.02	31.4±0.19 2.8±0.53	31.9±0.04 4.9±0.03	very weak, consistent		very weak
Number of spectra fitted	14+8	13	14	6	3	8	3	2

Comparison of resonance positions and widths obtained in fitting data from 8 reactions. A dash means that the level is below threshold. Errors derived from error matrix, to indicate sensitivity of statistics only.

Table 1

The errors given in Table 1 are the values derived from the diagonal elements of the error matrix. As can be seen the values for E_n, Γ_n agree for all 8 reactions within the errors. Thus the resonance parameters are internally consistent.

They are also in reasonable agreement with those resulting from the phase–shift analyses[8], given in Fig. 14. The 23.5 MeV, 2^+ level shown dashed there is associated with a rise in the d–wave phase, but the interpretation is not unique[22]. For comparison two theoretical
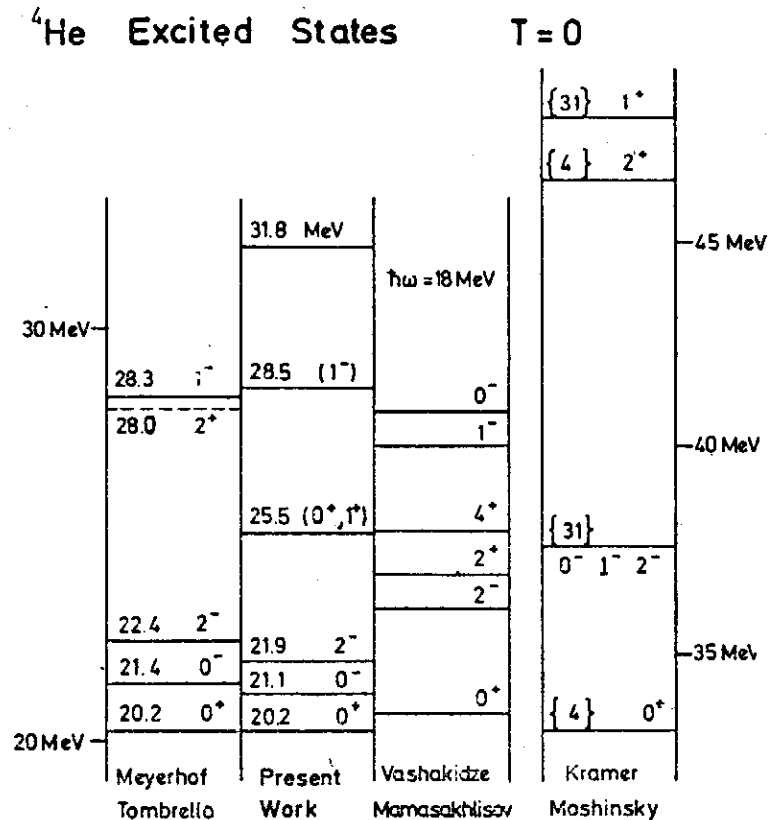
⁴He Excited States T = 0

Meyerhof Tombrello column:
- 28.3 1⁻
- 28.0 2⁺
- 22.4 2⁻
- 21.4 0⁻
- 20.2 0⁺

Present Work column:
- 31.8 MeV
- 28.5 (1⁻)
- 25.5 (0⁺,1⁺)
- 21.9 2⁻
- 21.1 0⁻
- 20.2 0⁺

Vashakidze Mamasakhlisov column (ℏω = 18 MeV):
- 0⁻
- 1⁻
- 4⁺
- 2⁺
- 2⁻
- 0⁺

Kramer Moshinsky column:
- {31} 1⁺
- {4} 2⁺
- {31} 0⁻ 1⁻ 2⁻
- {4} 0⁺

Energy scale: 45 MeV, 40 MeV, 35 MeV, 30 MeV, 20 MeV

Fig. 14. *Energy level diagram for $T=0$ states in ⁴He.*

predictions are also shown. In the work of Kramer and Moshinsky[2] only central forces were used and hence the $l=1$, $S=1$ triplet is degenerate. In the paper by Vashakidze and Mamasakklisov[4] this triplet is split up by spin–orbit forces and gives the Landé $2^-,1^-,0^-$ sequence. To obtain the experimentally observed $0^-,2^-,1^-$ ordering, strong tensor forces are needed[5].

The 25.5 MeV level is new. While it is rather weakly excited in the inelastic scattering off ⁴He, it shows up clearly in the ⁶Li$(d,\alpha'd)$D reaction. There is indication for such a level in the ⁴He(α,α') singles spectra[24]. The 31.8 MeV level is required in fitting most of the spectra, though it does not strongly protrude in any of them. In any case its inclusion permits an excellent parametrisation of the data.

Except possibly for the ⁴He$(d,d't)$¹H reaction we observed that the non–resonant term (coefficient C in eq. (3) was either zero, or contributed only a few percent to the cross–section. Forcing $C=0$, and hence all interference terms $A_n=0$, increased χ^2 by only 10 to 15%, while the number of parameters is reduced by a factor of about two. This further restriction $A_n=C=0$, which cne would not generally expect to hold, has been used in the fo llowing discussion.

4. The angular correlations

Having consistently interpreted our data from eight reactions in terms of a set of six resonances, let us consider the decay angular correlations. We have measured angular correlations of the decay particles from five excited states of ^{4}He.

To simplify as noted we forced the C and hence the A_n coefficients to be zero in the fits. For each family of spectra the resulting fit provided a set of coeffcienfs $B_n(\theta^l_2)$ for each resonance n and angle θ^l_2. The area underneath each resonance is given by $2\pi\ B_n$.

These coefficients, when multiplied by the appropriate Jakobi factor at the centre of the resonance yield the angular correlations in the RCM system as shown in Fig. 15 and 16. The error bars shown are calculated from the diagonal terms of the error–matrix. They give that variation of a given parameter, which increasses the χ^2 value by unity, when all other parameters are held constant.

Figure 15a shows the correlation for the ^{4}He$(\alpha,\alpha' t)^1$H reaction for the 20.2 MeV, 0$^+$ state. If the reaction mechanism is sequential, the distribution for a $J=0$ state must be isotropic, as borne out.
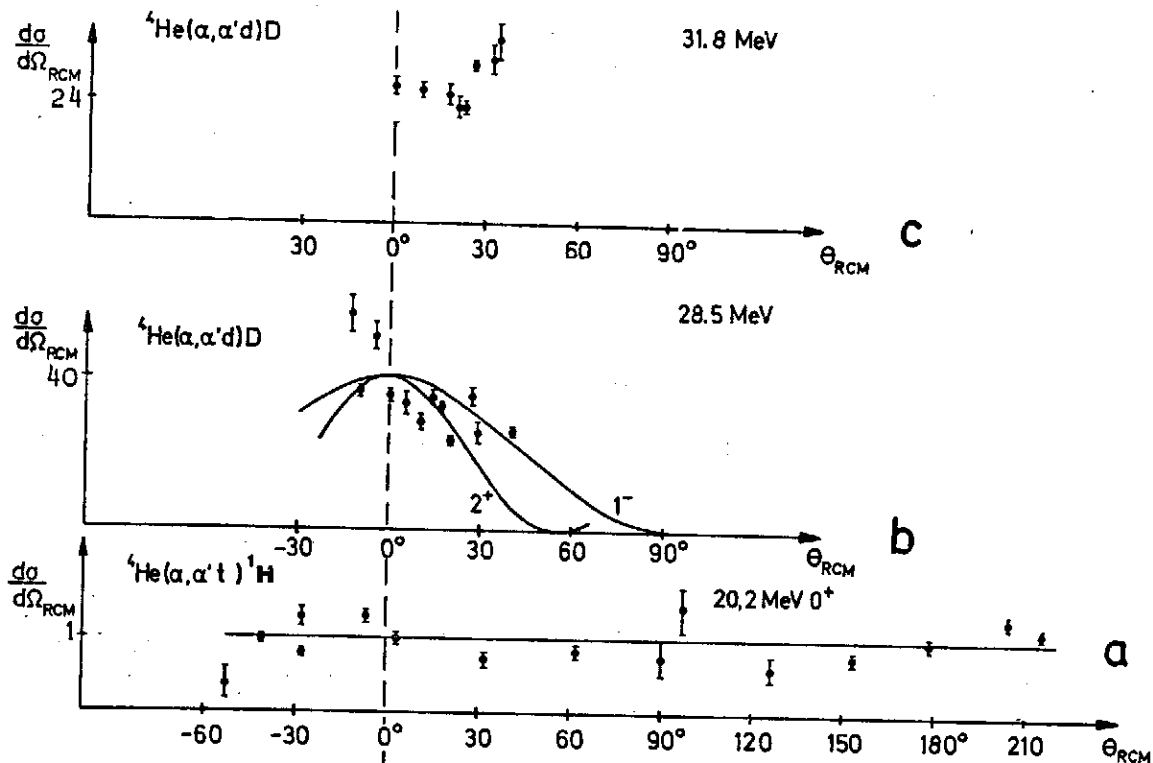

Fig. 15. *Angular Correlations in the RCM system for* $\theta^l_1=21°$. *One unit corresponds to about* 100 $\mu b/sr^2$.

The points around 0° stem from the upper branch, and those around 180° from the lower branch. As the decay cone for this state is rather small, the points near ± 90° carry a correction for the azimuthal angular opening, and the error bars have been doubled.

Fig. 16 shows the anghlar correlations for the 21.9 and the 25.5 MeV resonances, both for the ^{4}He$(\alpha,\alpha' t)^1$H and the ^{4}He$(\alpha,\alpha'^3$He$)$n reactions. As expected from charge symmetry both should yield identical results. The 25.5 MeV resonance is isotropic so far as one can tell. As the channel spin in the exit channel can only be 0 or 1, the $J=0^+$ or 1$^+$ (as 0$^-$ is
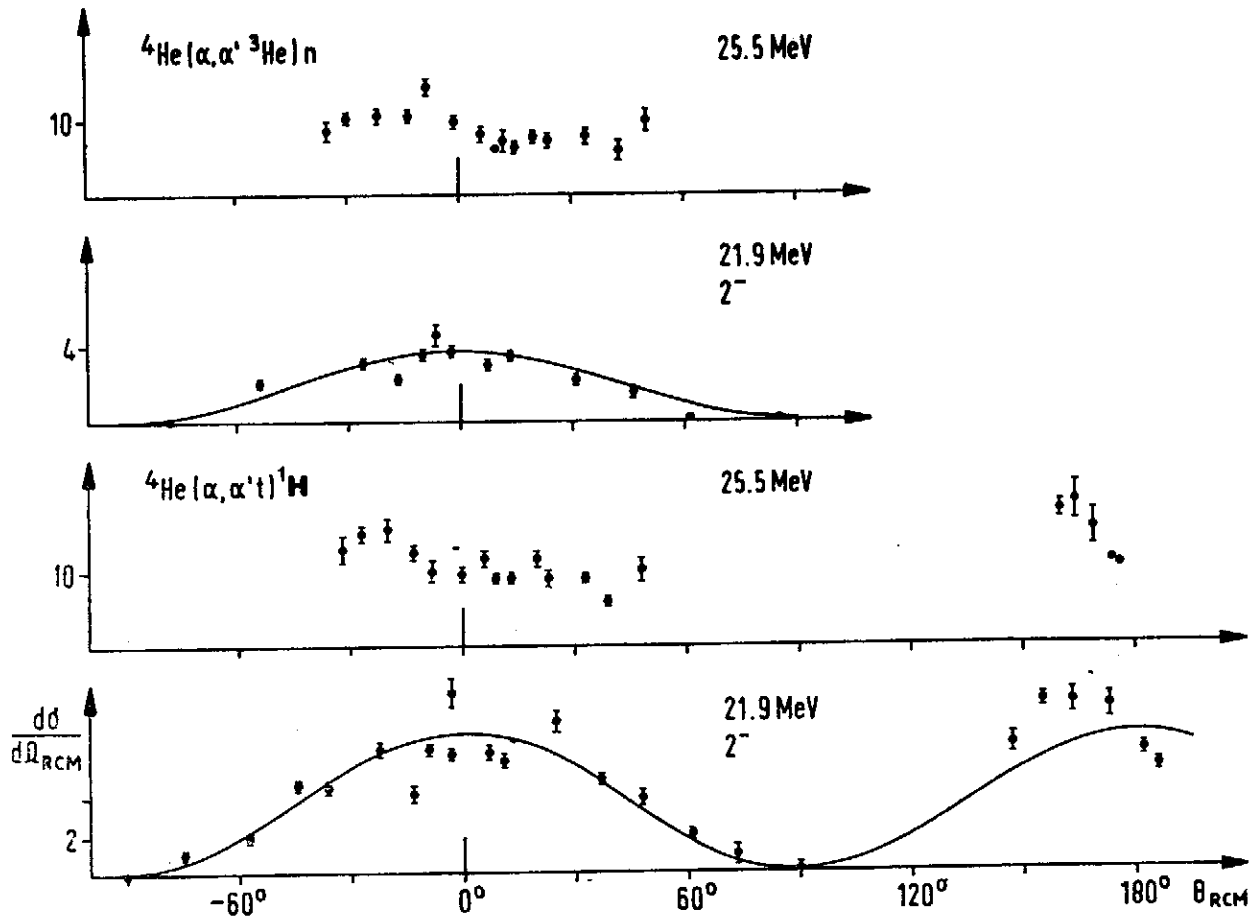
Fig. 16. *Angular correlation in the RCM system for* $\theta^t{}_1=21°$. *One unit corresponds to about* 100 $\mu b/sr^2$.

forbidden) within the validity of our assumptions. A third 0$^+$ state near 25 MeV has recently been predicted by Hutzelmeyer[16].

The 21.9 MeV, 2$^-$ level has non-normal parity, with channel spin S=1. Its excitation is forbidden in the ordinary theories[17] of inelastic α-particle scattering. The PWBA only permits excitation of natural parity states; within the L-S coupling-scheme normal parity S=1 states are also forbidden.

We have calculated the angular correlations using the impulses approximation with the following simplifying assumptions. The projectile interacts with only one cluster component of the target, say a neutron, wheras the ^{3}He-components acts as spectator. The scattering amplitude t is taken to have the same form as in n-α scattering on the energy shell

$$t=a+b\,\vec{\sigma_1}\cdot\vec{n} \tag{5}$$

where $\vec{\sigma}$ is the neutron spin and $\vec{n}$ the normal to the scattering plane and we assume the variations in the functions a and b to be negligible when the spectator momentum varies over the regions of momentum space which make significant contributions to the reaction. With these assumptions and with b vanishing allows the excitation of the same levels and predicts the same angular correlations as the zero range PWBA. With b non-zero S=0 to S=1 transitions are induced. It populates coherently the $m_J=\pm 1$ substates when the quantisation axis is chosen along the recoil axis. The decay into ^{3}He-n or $T+p$ is via L=1, channel spin 1.

For bothe $J=1^-$ and $J=2^-$ states the angular correlation is given by $d\sigma/d\Omega_{RCM}=$const $(\cos^2\theta_{RCM}+\sin^2\theta_{RCM}\sin^2\phi_{RCM})$ where ϕ_{RCM} is measured relative to the reaction plane.

In the reaction plane the experimental points agree well with the $\cos^2\theta_{RCM}$ distribution shown in Fig. 16. Perpendicular to the reaction plane the distribution should be isotropic. A further result of the theory is that interference between 1^- and 2^-, $S=1$ states only effects the amplitude but not the shape of the distribution in the reaction plane.

Also note that the distributions are symmetic about the recoil axis ($\theta_{RCM}=0°$) as predicted by the zero range PWBA, as well as the present theory.

Fig. 15b shows as far as available the distribution for the 23.5 MeV level for the $^4He(\alpha,\alpha'd)D$ reaction. Drawn in are the $\cos^2\theta$ distribution for a $S=1$, $J^\pi=1^-$ state and the PWBA prediction for $L=2$, $S=0$, $J^\pi=2^+$ [25]. The data points favor the 1^- distribution.

Fig. 15c gives the points for the 31.8 MeV resonance. They are consistent with an isotropic distribution. The 23.5 and 31.8 MeV distributions for the ^3He+n and $T+p$ channels have the same shape, but for the largest values of θ_{RCM} they are masked by are the mass 5 resonances.

For the 20.2, 21.9 and 23.5 MeV resonances our results on J^π are consistent with those of Meyerhof and Tombrello [3]. The 25.5 MeV level has not been previously observed. Whether the resonance at 31.8 MeV, which we need to fit our data, is associated with the rise in the d-wave coefficients up to 30 MeV observed in the phase-shift analysis, is not clear. It has been shown [22] that this does not necessarily imply a 2^+ state. There remains the question of the validity of our neglect of interference between resonances. This can be answered only by iteration, as one has to knov J^π and channel spins. If our interpretation of the 21.9 and the 23.5 MeV levels is corret, they do not interfere with each other; also they have $S=1$. The 20.5 and 31.8 MeV resonances all appear to be isotropic. If, as the 20.2 MeV resonance is known to be, all are $S=0$, then interference occurs only between non adjacent resonances, as different channel spins do not interfere.

5. Discussion and conclusions

Resonances arising in FSI lend themselves to a fairly simple interpretation if the reactoin mechanism is that of sequential decay.

Validity of the sequential reaction mechanism is taken to mean that the decay of the intermediate system is independent of its formation. The decay should then proceed according to the same laws that govern the decay of a compound nucleus. In particular the level parameters are a property of the compound system and do not depend on formation or decay. The branching ratios in the decay do not depend on the method of formation. For sequential decay through an isolated level there must also be invariance of the θ_{RCM} dependence of the angular correlation under a rotation by 180° on account of parity conservation [26].

To test the validity of the sequential decay mechanism we have measured angular correlations for three different entrance channels and the three possible exit channels. The following findings support the mechanism of sequential decay:

1) All entrance and exit channels investigated give resonant positions and widths that are consistent within the experimental errors. The resonance parameters are a property of the intermediate system only; no dependence on θ^1_1 or θ^1_2 was observed.

2) Within the experimental errors the three angular correlations checked were found to be invariant under a rotation by 180° about the normal to the reaction plane. $\theta_{RCM} \rightarrow \theta_{RCM}+180°$

3) A further test constitutes the evaluation of the branching ratios for the decay of the intermediate system into the different channels. This has not yet been done; however, the branching ratios do not appear to be crudely out of line.

As regards both positions and widths and information on spin and parity our results are

consistent with what has been previously known about $T=0$ states of ⁴He[8].

The present data facilitate more precise determinations of positions and particularly widths of the resonances. We found evidence for an additional state at 25.5 MeV. The isotropy of its angular correlation suggests $J^\pi = 0^+$ or 1^+. If, as has been predicted by Hutzelmeyer[16], this is a 0^+ state with a strong component of $L=2$, $S=2$, one can understand the fact that it has not been seen in the phase-shift analysis of low energy scattering and reactions.

It is interesting to compare the phase shift analysis method with the one used in the present investigation.

The experimental difficulties of carrying out a coincidence measurement are compensated by the yield of spectra covering a large range of excitation energies starting at the threshold. The added recoil energy makes the simultaneous measurement of the various decay channels readily possible. The present method offers higher selectivity in many cases. It is applicable even when for lack of a stable target the phase-shift analysis cannot be carried out. However, particularly at low incident energies, one does have to concern oneself with possible interference from other FSI and the quasielastic scattering.

The energy spectra show more structure, and so are easier to interpret. See reference[18] for instance. This is attributed to the fact that in the formation of the intermediate system Coulomb and centrifugal forces and more important the non-resonant terms play less of a role. The level widths obtained in the present work are significantly smaller than those used by Meyerhof and Tombrello. This effect has been previously noted[19].

The angular correlations in the RCM system are determined by the population of the magnetic substates of the levels. Except for simple cases such as isotropy, they depend on the reaction mechanism. The symmetry of the angular correlations about the recoil axis ($\theta_{RCM}=0$) is predicted by the zero range PWBA as well as the theory described in section 3.2. It is gratifying to observe that these simple models account for the experimental data. In general this symmetry is not required for a sequential reaction mechanism. It remains to be shown under what conditions such models constitute and adequate description, and permit the use of the method to determine spins and parities. Measurements on heavier nuclei are in progress to test this point.

The authors want to express their gratitude to Prof. A. Citron, Prof. W. Heinz and Prof. H. Schopper for their encouragement and support.

The good cooperation with Dr. G. Schatz and the members of the cyclotron staff is gratefully acknowledged.

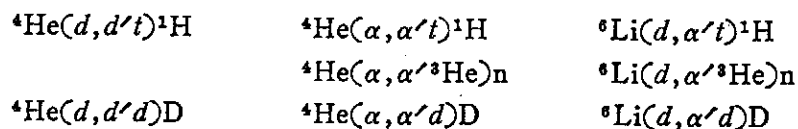We would like to thank Mr. W. Siebert for help with the expriment and the programming.

References

(1) A. de Shalit and T.D. Walecka, *Phys. Rev.* 147,763(1966)

(2) P. Kramer and M. Moshinsky, *Phys. Lett.* 23,574(1966)

(3) B.R. Barrett, *Phys. Rev.* 154,955 (1966)

(4) I. Sh. Vashakidze and V. I. Mamasakhlisov, *Soy. Journ. Nucl. Phys.* 5,532 (1968)

(5) T.T.S. Kuo and J.B. Mc Grory, *Nucl. Phys.* A134,633(1969)

(6) P.P. Szydlik, *Phys. Rev.* C1,146(1970)

(7) E.O. Alt, P. Grassberger and W. Sandhas, *Phys. Rev.* C1,85(1970)

(8) W. E. Meyerhof and T.A. Tombrello, *Nucl. Phys.* A109,1(1968)

(9) E.L. Haase et al., *Proc. Int. Conf. Clustering Phenomena in Nuclei, Bochum IAEA Vienna* 223(1969)

(10) G.G. Ohlsen, *Nucl. Instr. Meth.* 37,240(1965)

(11) M.L. Goldberger and K.M. Watson, *Collision Theory*, Wiley, New York, (1964) p.540 ff

(12) C.A. Levinson and M.K. Banerjee, *Ann. Phys.* 2,471(1957)

(13) J. Humblet and L. Rosenfenfeld, *Nucl. Phys.* 26,529(1961)

(14) J.C. Legg et al. *Nucl. Phys.* A119, 209(1968)

(15) P.A. Assimakopoulos et al., *Nucl. Phys.* A144,272(1970)

(16) H. Hutzelmeyer, *private communicatication*

(17) W.W. Eidson and J.G. Cramer Jr., *Phys. Rey. Lett.* 9,497(1962)

(18) M.D. Goldberg, *Prog. in Fast Neutron Physics*, G.C. Phillips, (J.B. Marisu and J.R. Risser eds.), The University of Chicago Press, Chicago p.3(1963)

(19) V.V. Komarov and H.A. Salman, *Phys. Lett.* 31B,52(1970)

(20) C. Werntz and W.E. Meyerhof, *Nucl. Phys.* A121,38(1968)

(21) ibid, p.60

(22) W.E. Meyerhof et al., *Nucl. Phys.* A148,211(1970)
W.E. Meyerhof et al., *Nucl. Phyt.* A131,489(1969)

(23) H.W. Franz and D. Fick, *Nucl. Phys.* A122,591(1968)

(24) E.E. Gross et al., *Phys. Rev.* 178,1594(1969)

(25) H.B. Willard et al. *Fast Neutron Physics*. (J.B. Marion and J.L. Fowler eds),. Interscience Publishers, New York (1963) p.1217 ff

(26) C. Zupancic, *Few Nucleon Problems (Fed. Nucl. Energy Commission of Yugoslavia, Hercegnovl,* 1964) Vol. II, p.61

利用三粒子反應研究⁴He核之T＝0激能階

本文為以符合測量之實驗技巧完成以能量 52MeV 氘子及能量 104MeV 阿伐粒子引導之下列八種原子核反應，進行對 ⁴He 核之 $T=0$ 受激狀態之研究。

$^4He(d,d't)^1H$	$^4He(\alpha,\alpha't)^1H$	$^6Li(d,\alpha't)^1H$
	$^4He(\alpha,\alpha'^3He)n$	$^6Li(d,\alpha'^3He)n$
$^4He(d,d'd)D$	$^4He(\alpha,\alpha'd)D$	$^6Li(d,\alpha'd)D$

在實驗過程中用二個偵測器以測定相關分佈，一偵測器為固定的，用以測定非彈性散射之阿伐粒子，另一偵測器為可變動的，其位置之變動在一角度範圍內均有利於對 ⁴He 核終態交互作用之研究，所得資料可決定 ⁴He 核六個 $T=0$ 受激能階，分別在 20.2MeV，21.1MeV，21.9MeV，25.5MeV，28.5MeV及 31.8MeV，其能寬分別為 0.2MeV，0.8MeV，1.8MeV，2.9MeV，5.3MeV 及 5.6MeV.

再者以上各反應之角相關結果與用 impulse approximation 理論計算符合，對於 sequential 反應理論應用之有效性在本文中另詳加討論之。

The ^{26}Mg(d, α)^{24}Na Reaction at Low Energies[*]

E. K. LIN (林爾康) , W. N. Wang （王唯農）, G. C. Kiang （江紀成）,

C. C. Hsu, P. S. Song and L. P. Liang （梁靈平）

Tsing Hua University and Academia Sinica

Abstract

The reaction ^{26}Mg (d,α) ^{24}Na was investigated in the incident deuteron energies, ranging from 2.5 to 3.0 MeV. A total of seven alpha-particle groups, corresponding to levels in ^{24}Na up to 1.88 MeV excitation, were observed. Data were taken at thirteen angles from 40° to 160° at E_d=2.5, 2.7, 2.8, 2.9 and 3.0 MeV to obtain angular distributions. Excition functions in 25 keV steps between 2.5 and 3.0 MeV were measured at θ=140° lab. The measured angular distributions of all alpha-particle groups were found to be nearly isotropic, and the measured excitation functions indicate the predominance of the compound nucleas mechanism in the investigated region of deuteron energies.

1. Introduction

The level structure of ^{24}Na has been studied extensively[1] from deuteron stripping reaction and decay-scheme work. A level scheme of the low-lying levels derived from the measurement of the ^{23}Na$(d,p)^{24}$Na reaction[2-5] and from the ^{23}Na(n,γ) thermal-neutron capture gamma rays[6,7] is given in Fig. 1.

Recently Jahr et al[8] reported a new level at 1.51 MeV in ^{24}Na, which was not seen in the above mentioned works, from magnetic analysis of alpha particles from the ^{26}Mg (d,α) ^{24}Na reaction at E_d=11.8 MeV. This level was observed to be rather strongly excited and the peak appeared in the spectrum is about equally prominent as the ground state transition. A high spin value ($e\geq4$) has been suggested [6] to this level, since the excitation of a high-spin state is probably enhanced in the (d,α) reaction[9].

(*) Work performed at the Physics Research Center in Hsinchu and supported by the Academia Sinica and Tsing Hua University.

(1) P.M. Endt and C. van der Leun, *Nucl. Phys.* A105, 1(1967).

(2) C. Daum, *Nucl. Phys.* 45, 273(1963).

(3) C. Daum, *Nucl. Phys.* 51, 244(1964).

(4) A.Z. El-Behay, M.A. Farouk, M.L. Jhingan, M.H. Lassef and I.I. Zaloubovsky, *Nucl. Phys.* 74, 225 (1965).

(5) Ma. Esther O. de Lopez, *Rev. Mex. Fys.* 12, 159(1963).

(6) R. C. Greenwood, *Phys. Lett.* 23, 482(1966).

(7) I. Bergqvist, J.A. Biggerstaff, J.H. Gibbons, and W.M· Good, *Phys. Rev.* 158, 1049 (1967).

(8) R. Jahr, J.A.H. Pfleger and H. Zell, *Phys. Lett.* 25P, 113(1967).

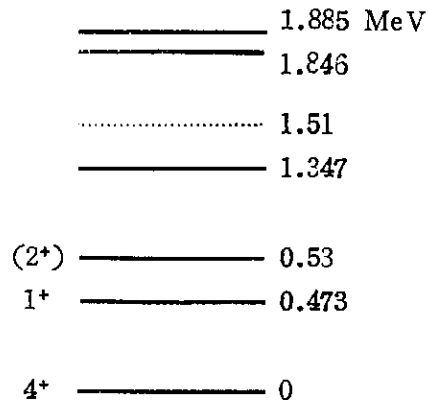(9) N. MacDonald, *Nucl. Phys.* 33, 110(1962).

```
_____ 1.885 MeV
_____ 1.846

................ 1.51

_____ 1.347


(2⁺) _____ 0.53
1⁺  _____ 0.473


4⁺  _____ 0
```

Fig. 1. *Level diagram for low–lying levels of* ^{24}Na. *The dashed line indicates the new level at* 1.51 *MeV observed from the* $^{26}Mg(d,\alpha)^{24}Na$ *reaction at* $E_d = 11.8$ *MeV (see Ref.8).*

The $^{26}Mg(d,\alpha)^{24}Na$ reaction at other energies has been very little investigated. Previously we have made a series measurement of the (d,α) reactions on ^{24}Mg, ^{25}Mg and ^{27}Al in the deuteron energy region 2.0–3.0 MeV (Refs. 10–12). The results shown that the investigated reactions in this range of low energies proceed mainly via a compound nucleus, and the integrated cross sections can be described by the statistical theory[13]. The (d, α) reaction on ^{26}Mg is expected to have some features in common with the (d,α) reaction in the neighboring even–A isotope ^{24}Mg. In present work, we have carried out the measurement of the $^{26}Mg(d,\alpha)^{24}Na$ reaction in the bombarding deuteron energy range from 2.5 to 3.0 MeV. An attempt is made to find the evidence for existence of a new level at 1.51 MeV in ^4Na. Preliminary results on the angular distributions and the excitation functaions for the $^{26}Mg(d,\alpha)^{24}Na$ reaction are given in this report.

2. Experimental Method

A deuteron beam from the 3 MeV Van de Graaff accelerator of the Tsing Hua University was used to bombared a target of ^{26}Mg. To prepare the targets, MgO powder enriched in ^{26}Mg was evaporated under vacuum onto thin carbon foils, and a ^{26}Mg thickness of about 100 $\mu g/cm^2$ was obtained. Monitoring was done with a beam current integrator. The alpha particles produced in the reaction were detected in a pair of the semiconductor surface barrier detector. A detailed description of the experimental method has been given elsewhere. [10-12]

Runs were performed for thirteen values of the laboratory angles in the interval from 40° to 160° to obtain angular distributions at $E_d = 2.5$, 2.7, 2.8, 2.9 and 3.0 MeV. The excitation functions were measured in steps of 25 KeV between 2.5 and 3.0 MeV at an angle of 140°.

3. Results and discussion

Figs. 2–6 show some energy spectra of alpha particles at deuteron energies 2.5–3.0 MeV. We observed seven groups of alpha particles. Impuity groups were observed from the

(10) C.C. Hsu, E.K. Lin and W.N. Wang, *Nuo. Cim.* 56B, 39(1969).

(11) W.N. Wang, E.K. Lin, Ren Chiba, T.J.Lee. Y.C. Yang, C.C. Hsu and T. Chiao, *Nucl. Phys.* A162, 537(1967).

(12) E.K. Lin, W.N. Wang, T. Chiao, T.J. Lee, C.C. Hsu, and Y.C. Yang Chin. *J. Phys.* 4, 6(1966).

(13)T. Ericson, *Adv. Phys*, 9, 425(1960).

^{12}C$(d,\alpha)^{10}$B and ^{16}O$(d,\alpha)^{14}$N reactions. The α_0 group corresponds to the ground state of ^{24}Na excited in the ^{26}Mg(d,α) reaction. The doublet ($\alpha_{1,2}$ group), corresponding to the first and second excited states at 0.473 and 0.53 MeV respectively, was not resolved clearly, and at some angles the impurity group from the ^{16}O$(d,\alpha)^{14}$N reaction seriously obscured the $\alpha_{1,2}$ group. The α_3 group leads to the third excited state of Na^{24} at 1.347 MeV. It is about equally excited at E_d=2.5, 2.7 and 2.8 MeV as the ground state, while the intensity becomes larger at E_d=2.9 and 3.0 MeV. The α_4 group corresponds to a new level of ^{24}Na at 1.51 MeV excited in the present reaction. It appears in the spectrum defintely at several forward angles. The observed intensity decreases approximately to the background as increasing angle to $\theta_{lab}\sim 80°$. At backward angles the peak appears to be rather weak. Checking from the kinematics of the α_4 group, the variation in energy with angles corresponds exactly to the kinemaitcs calculated for a ^{26}Mg$(d,\alpha)^{24}$Na reaction. Also, the obtained energy of this level is in agreement with the value obtained by Jahr et al[6] from the same reaction at higher energy (E_d=11.8 MeV). However, its cross section in the case of our deuteron energies is relatively much smaller as compared to other alpha groups. Accordingly the excitation of this level from the ^{26}Mg$(d,\alpha)^{24}$Na reaction is seen to depend on the incident energy. The $\alpha_{5,6}$ group corresponds to a doublet of the fifth and sixth excited states at 1.846 and 1.885 MeV; it was not resolved in most cases.

The shape of the measured angular distributions is varying with the deuteron energies 2.5–3.0 MeV. From formation of a compound nucleus, the averaged cross sections over a sufficient interval of incident energy are expected to be generally symmetric about 90°. Fig. 7 shows the obtained angular distribution averaged over five deuteron energies 2.5, 2.7, 2.8, 2.9 and 3.0 MeV. It is observed that all excited states are somewhat characterized by an isotropic distribution. Not shown in Fig. 7 is the angular distribution for the 1.51 MeV state. Because statistics are meager for this state, no angular distribution was obtained.
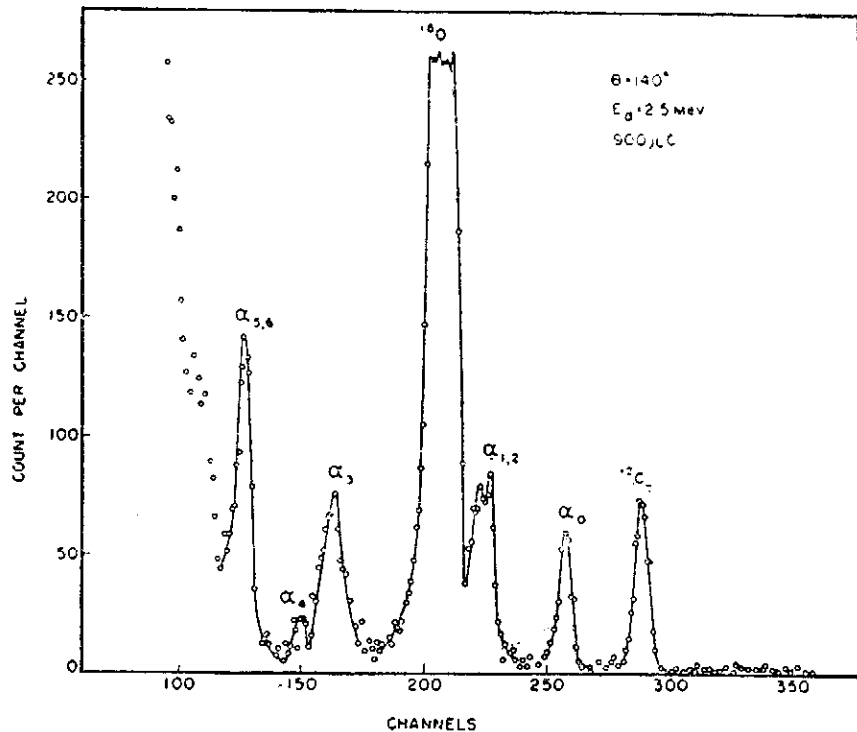

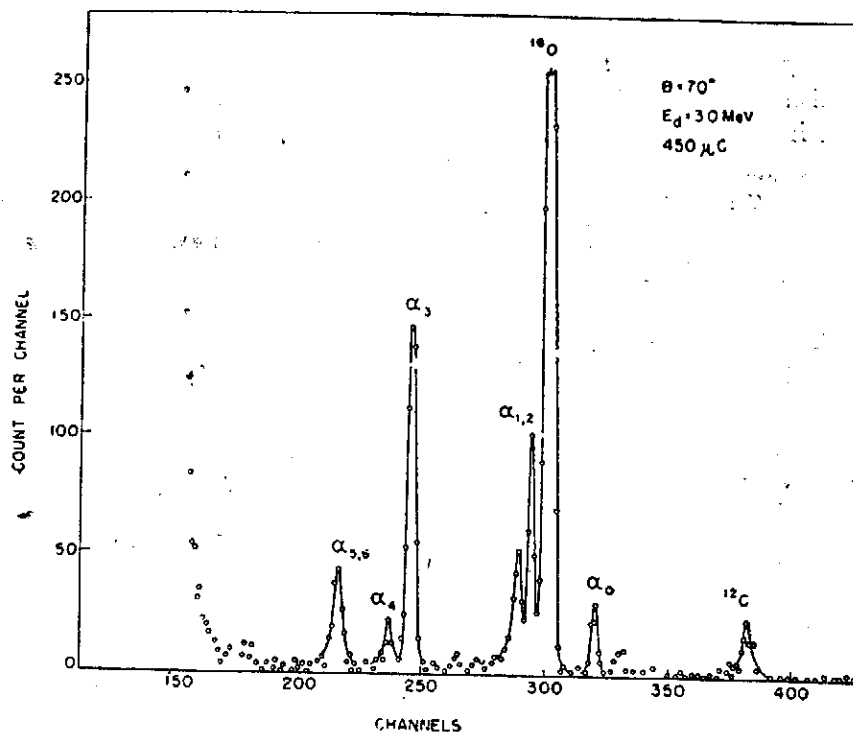Fig.2. *Typical α-particle spectrum for the* ^{26}*Mg*$(d,\alpha)^{24}$*Na reaction at 2.50 MeV deuteron energy*

Fig.3. *Typical α-particle spectrum for the* $^{26}Mg(d,\alpha)^{24}Na$ *reaction at 2.70 MeV deuteron energy*

Fig.4. *Typical α-particle spectrum for the* $^{26}Mg(d,\alpha)^{24}Na$ *reaction at 2.80 MeV deuteron energy*

Fig.5. *Typical α-particle spectrum for the ^{26}Mg$(d,\alpha)^{24}$Na reaction at 2.90 MeV deuteron energy*

Fig.6. *Typical α-particle spectrum for the ^{26}Mg$(d,\alpha)^{24}$Na reaction at 3.00 MeV deuteron energy*

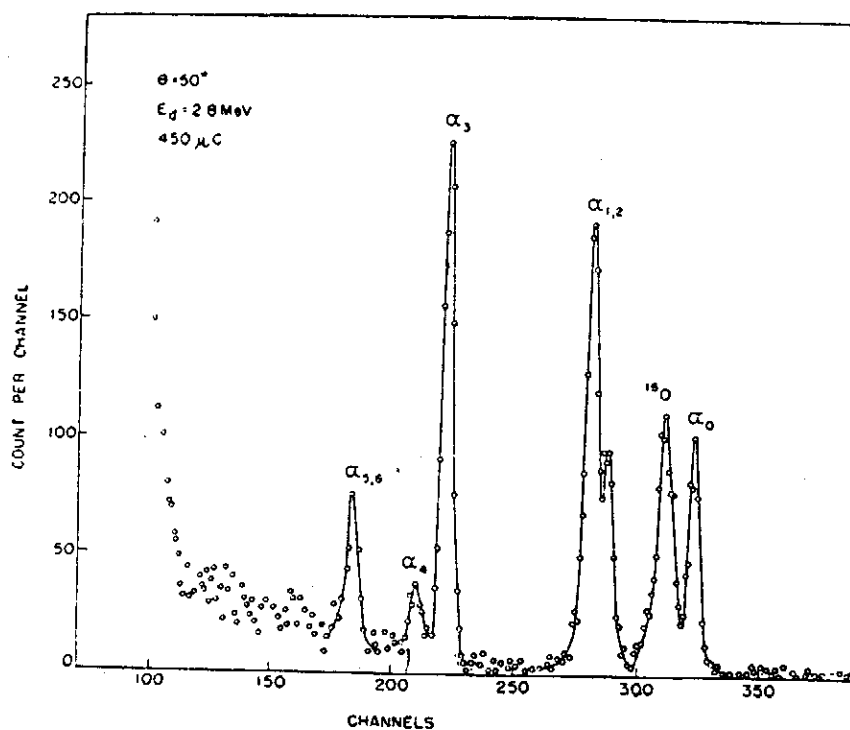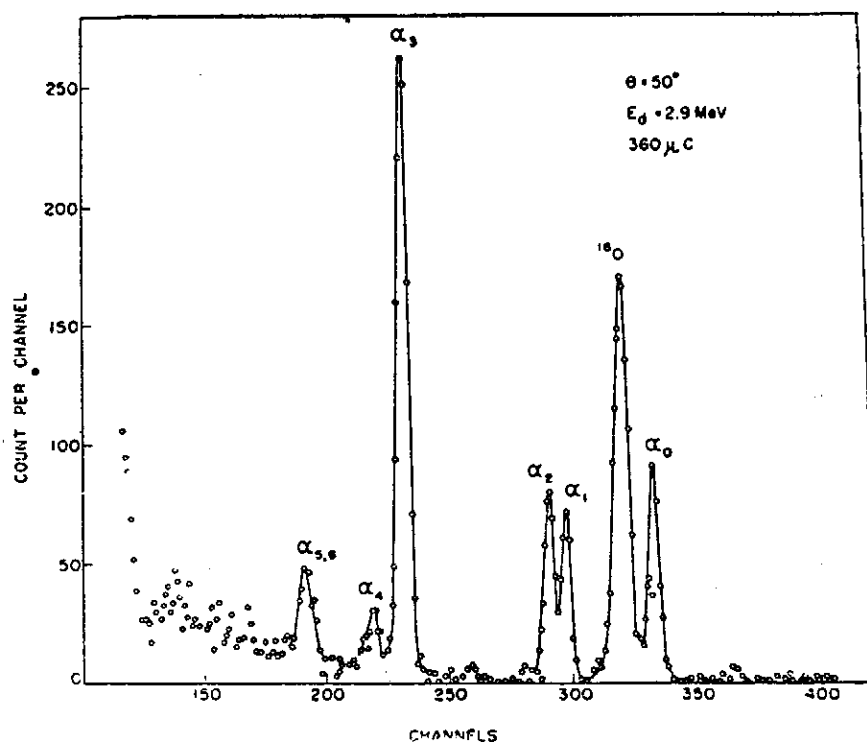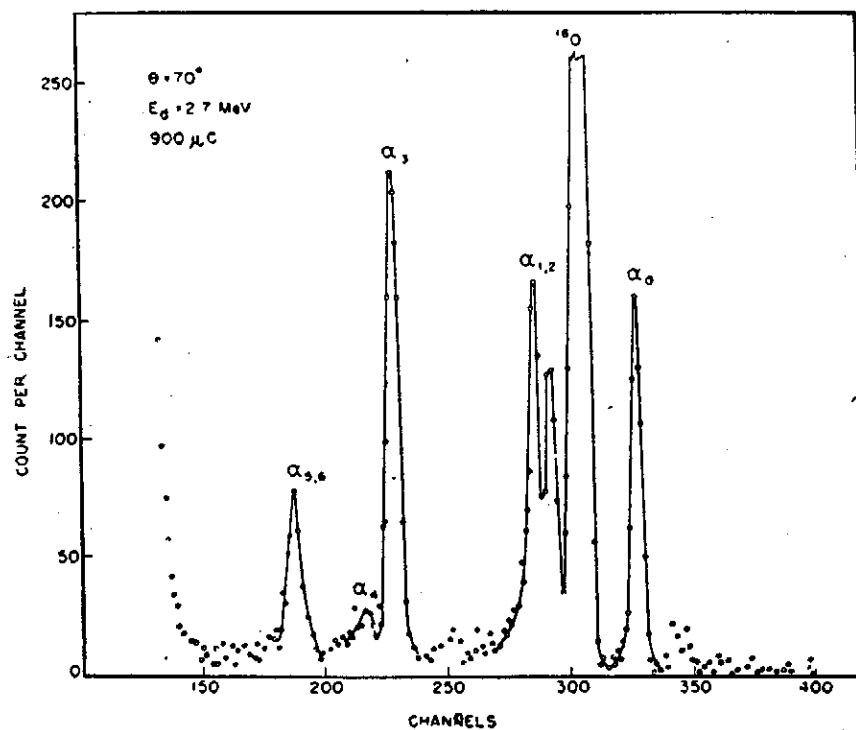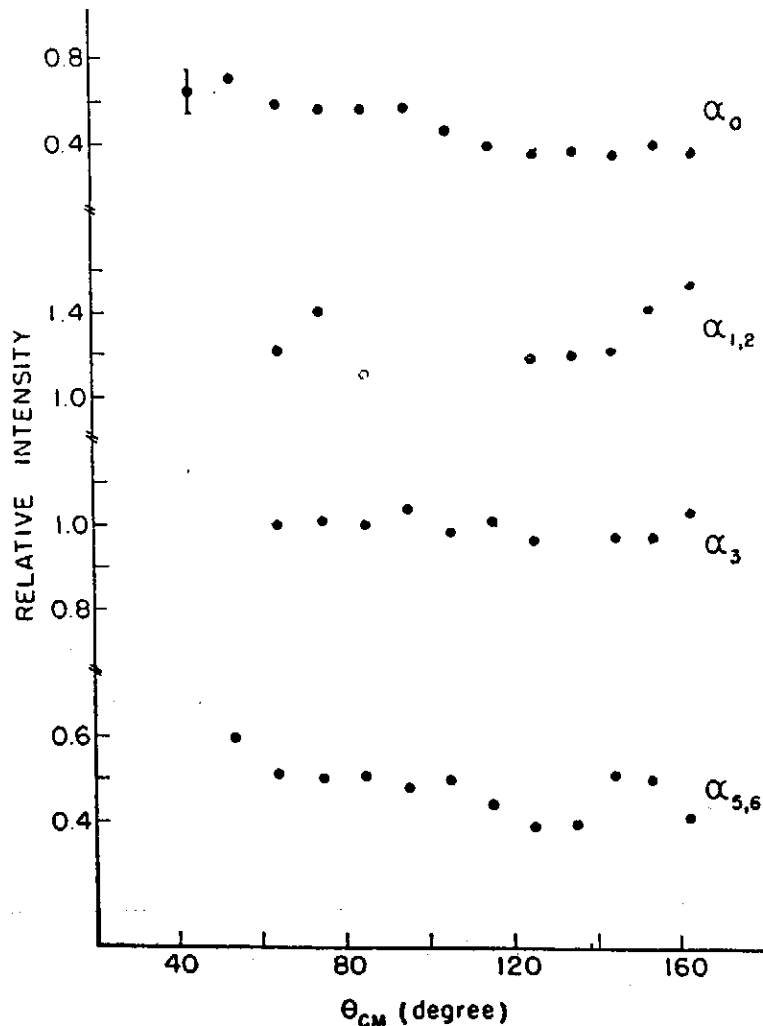Fig.7. *Angular distributions of α-particles from the* $^{26}Mg(d,\alpha)^{24}Na$ *reaction averaged over five deuteron energies 2.5, 2.7, 2.8, 2.9 and 3.0 MeV. The error bar indicates the statistics error.*

The results of the measured excitation functions at $\theta = 140°$ lab. for the present energies $E_d = 2.5 - 3.0$ MeV are presented in Fig. 9. For all alpha groups the excitation functions show more or less marked fluctuations with energy. This behavior has been observed in the previously investigated ^{24}Mg $(d,\alpha)^{22}$ Na reaction [10], where a compound nucleus formation was found to be responsible for the reaction process.

Verification of the $2I+1$ rule has been previously discussed for several (d,α) reactions [11,12]. A large amount of data has been accumulated on the (d,α) reaction on odd-A nuclei. It has been shown that the deviation from proportionality for the high spin values of the final nucleus is attributed to the insufficient energy of the deuterons and to the excitation of region of levels of the compound nucleus. It has been also shown that the cross section for high spin states are much depressed from the $2I+1$ line. The ground state of ^{24}Na has a high spin value ($I=4$). The second and third excited states are known to have spin $I=1$ and 2, respectively. At higher excitation all spins of excited states are unknown. It is apparent that the $^{26}Mg(d,\alpha)^{24}Na$ reaction is not favorable for an examination of the $2I+1$ rule. From
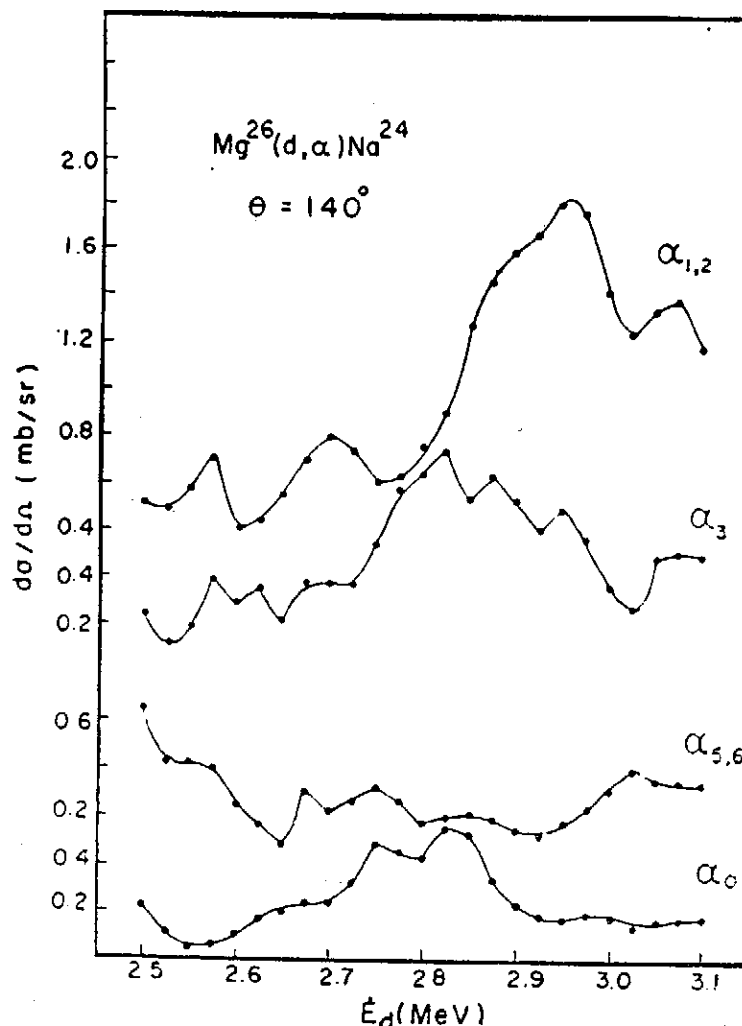
Fig.8. *Excitation functions of the α-particle groups from the ^{26}Mg$(d,\alpha)^{24}$Na reaction at angle 140° lab*

present data, it is not possible to draw some information and get suggestion on the spin of the excited states of ^{24}Na.

Finally we note that the isotropic angular distributions and the fluctuations of the excitation functions, and the analogy with the ^{24}Mg$(d,\alpha)^{22}$Na reaction investigated [12] previously allow us to conclude that the ^{26}Mg$(d,\alpha)^{24}$Na reaction in the investigated region of deuteron energies proceeds via a compound nucleus. In order to extract more information from experimental data, a detailed investigation of the ^{23}Mg$(d,\alpha)^{24}$Na reaction would be required.

Acknowledgements

低能量氘子對 ^{26}Mg$(d,\alpha)^{24}$Na 核反應之研究

此篇主要為研究重子能量自2.5到3.0MeV所引導之 ^{26}Mg$(d,\alpha)^{24}$Na 核反應。觀察到之七組α粒子相應于 ^{24}Na 核能階自0到 1.88 MeV。資料在自 40° 到160°間每10°收集一次，在氘子能量為E_d=2.5, 2.7, 2.8, 2.9, 3.0 MeV處。能量激發函數在140°處自2.5 MeV到3.0MeV每2.5 keV取一點。所測得之α粒子之角分佈均近乎平均分佈，更由能量激發能量函數顯示，在此能量下之氘子引導α反應主要為複合核反應。

Study of ^{27}Al(n,d)^{26}Mg Reaction by 14.1 MeV Neutrons

Wei-Noon Wang (王唯農) and Ming-Chien Wang (王明建)

Institute of Physics, Academia Sinica and
National Tsing Hua University

Adstract

The ^{27}Al$(n,d)^{26}$Mg reaction has been studied at neutron energy of 14.1 MeV by using a counter telescope. Angular distributions corresponding to ^{26}Mg levels at 0, 1.81 and 2.97 MeV are measured and compared with the Distorted Wave Born Approximation theory. The cross sections, l values and spectroscopic factors have been obtained. The experimental results seem to agree with the predictions of the rotational model.

1. Introducticn

In last ten years stripping and pickup reactions with the help of Distored Wave Born Approximation calculation have been extensively used to study the single particle structure of nuclei. There are a great number of experimental results on (d,p), (p,d) and (d,t) reactions which are mainly concerning the investigation of the neutron structure of the nuclei. The proton pickup reactions (n,d) and $(d, ^3$He) are comparably rare. The early ^{27}Al$(n,d)^{26}$Mg reaction reported by Colli et al[1] has measured only one single spectrum at 17°. The angular Pistribution of deuteron groups corresponding to ^{26}Mg levels at 0, 1.83 and 3.6 MeV by (n,d) reaction at 14.8 MeV has been reported by Glover et al[2]. They have analyzed their data with Plane Wave Born Approximation calculation. The ^{27}Al$(d,^3$He$)^{26}$Mg pickup reaction leading to the same final states has been studied by Cujec[3] and by Pellegrini et al[4]. Pellegrini et al have made a comparison between their results with the (n,d) work. A reasonable agreement has been found between these two works on the ground and the 1.83 states.

In the present work (n,d) reaction on ^{27}Al has been studied by using 14.1 MeV neutrons. The angular distributions have been compared with the Distorted Wave Born Approximation calculation.

2. Experimental Method

The counter telescope and associated equipments were described earlier [5,6]. The experiment was carried out and the data were analysed essentially as before[6]. Self supporting Al foil of thickness 3.5mg/cm^2 was used as target. The observed energy resolution at deuteron

(1) L. Colli, F. Cvelbar, S. Micheletti and M. Pignanelli, *Nuovo Cim.* 14, 1120 (1959)

(2) R.N. Glover and E. Weigold, *Nuclear Physics* 24, 630 (1961)

(3) B. Cujec, *Phys. Rev.* 128, 2303 (1962)

(4) F. Pellegrini and S. Wiktor, *Nuclear Physics* 40, 412 (1963)

(5) W.N. Wang, *Chinese Journal of Physics* 3, 75 (1965)

(6) W.N. Wang and E.J. Winhold, *Phys. Rev.* 140, B882 (1965)
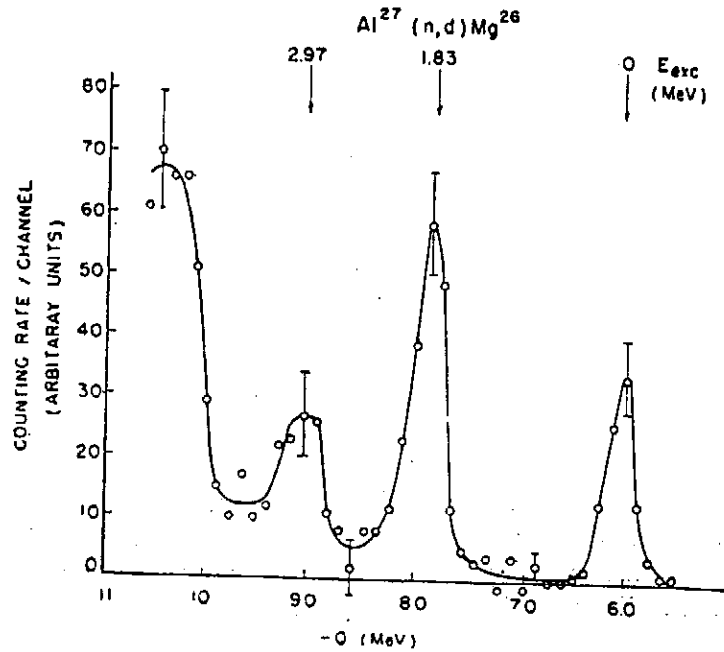
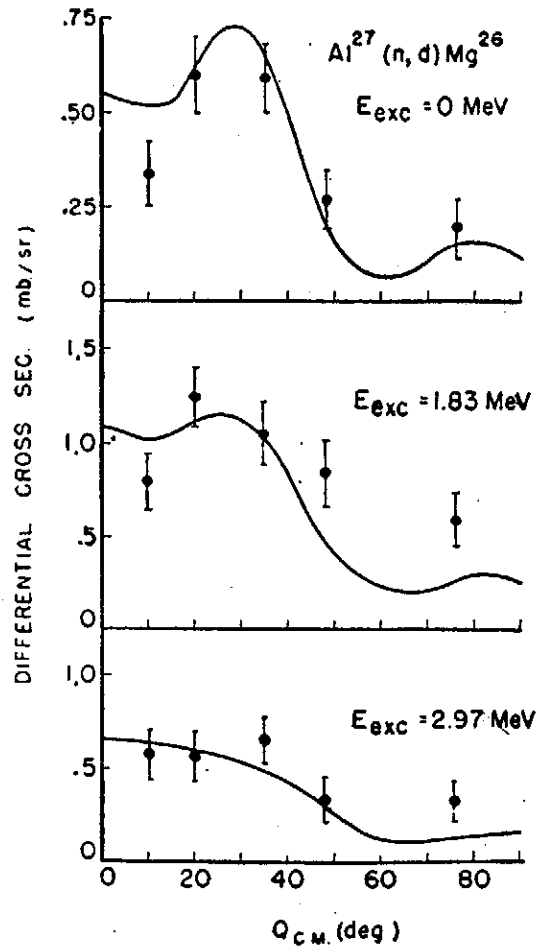Fig. 1. $^{27}Al(n,d)^{26}Mg$ deuteron energy spectrum. Data at angles between 10° and 35° have summed.

Fig. 2. Angular distributions of deuteron groups observed in $^{27}Al(n,d)^{26}Mg$ reaction. The solid curves are calculated DWBA predictions as described in the text.

energy 8 MeV was about 250 keV. The uncertainty of experimentally determined energies is about 50 keV. Owing to the very low counting rates in the present experiment (~2 count/min.), the data were acquired only at five angles in the forward hemisphere which are considered to be the key angles for l value determination.

3. Results and discussions

Energy spectrum obtained by combining data for laboratory angles between 10° and 35° is shown in Fig. 1. The deuteron peaks corresponding to transitions to the ground state and first excited (1.83 MeV) state were identified. The third peak located at Q=−9.0 MeV was corresponding to 2.97 MeV state. Our energy assignments give good agreement with Pellegrini et al[4]. Angular distributions for the three prominent peaks are displayed in Fig. 2. The data were fitted by calculated DWBA curves. The calculations were performed using a computer program due to Smith and Ivash[7], which assumes Woods–Saxon shape for both real and imaginary deuteron and neutron potentials. The deuteron potential was obtained by averaging the parameters acquired by Smith and Ivash[8] in this energy and mass range. The neutron potential was used as before[6]. They are listed in Table I. The computed best fitting angular distribution curves for various transitions are shown in Fig. 2. The errors indicated in all these Figures include only the uncertainties due to the statistics and to the background. Values for orbital angular momentum transfer l obtained from the fits and the spectroscopic factor S are listed in Table II.

Table I

Optical model parameters used in DWBA calculation

Particle	V(MeV)	W(MeV)	r_0(F)	a(F)
Deuteron	95	8	1.4	0.70
Neutron	43	8	1.25	0.50
Proton	55		1.25	0.60

$*Potential = (V + iW)f(r) + V_c$
$f(r) = [1 + \exp(r - R_0)/a]^{-1}; \quad R_0 = r_0 A^{1/3}$
$V_c = Coulomb \; potential.$

Table II

Experimental and theoretical results on low–lying levels of ²⁶Mg

Mg state MeV	Spin J	l_p	Nilsson[a] orbit No.	Spectroscopic factor S absolute	normalized[b]	predicted	$\int_0^{90} \frac{d\sigma}{d\Omega} d\theta$ (mb)[c]
0	0⁺	2	5	1.25	0.36	0.33	1.0
1.83	2⁺	2	5	2.2	0.64	0.62	3.0
2.97	2⁺	2	7	1.14	0.33	0.36	1.6

a) the suggested Nisson orbit[11] fron which the proton picked up.
b) by assuming the total spectroscopic factor from Nilsson orbit No. 5 equal to one.
c) calculated according to DWBA curves.

(7) W.R. Smith and E.V. Ivash. *Phys. Rev.* **128**,1175 (1962)
(8) W.R. Smith and E.V. Ivash, *Phys. Rev.* **131**,304 (1963)
(9) G.R. Satchler, *Ann. Phys.* **3**, 275 (1958)
(10) P.M. Endt and C. Van der Leun, *Nuclear Physics* **34**, 1(1962)
(11) S. Hinds, H. Marchant and R. Middleton, *Nuclear Physics* **67**, 257 (1965)

Fig. 3 shows the ^{27}Al ground state configuration on the Nilsson model[12], in which the odd 13th proton is in the Nilsson orbit No.5 and all orbits below are filled.
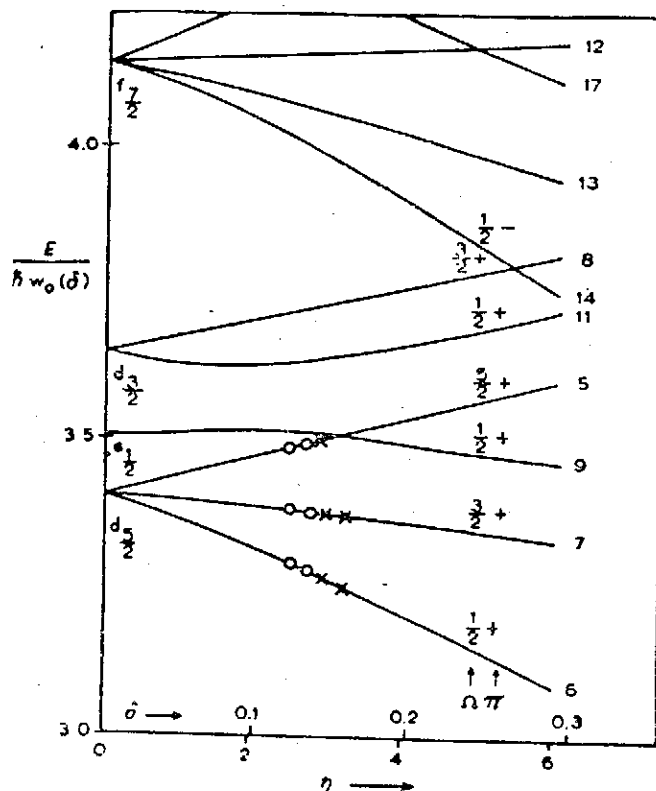

Fig. 3. *Nilsson diagram for ^{27}Al ground state, deformation parameter $\eta \cong 3$.*
The neutrons are denoted by circles and protons by crosses.

All angular distributions correspond with a transition by orbital angular momentum $\ell_p = 2$, which is consistant with the transition to ^{26}Mg states with $0^+, 2^+, 2^+$ spin assigmments [10,11].

The absolute spectroscopic factor is equal to the ratio of the experimental cross section to that obtained from the DWBA calculation. The normalized spectroscopic factor is calculated by assuming that the ground state and the first excited state are in the same rotation band[3,4,11] ($k=0$) excited by picking a proton from the Nilsson orbit No.5 ($\Omega=5/2^+$). This gives the sum of the spectroscopic factor of these two states equal to one.

The spectroscopic factor S for the rotational model is given[3,4,9] in the usual notation by

$$S_{ik} = g^2 \frac{2I_1+1}{2I_2+1} < I_1, j, \pm k, \Omega | I_2 k_2 >^2 < \phi_2 | \phi_1 >^2 C^2_{ij}(\Omega).$$

By assuming the proton pickup from the Nilsson ortital as suggested in Table II, the predicted S values are calculated and also listed in Table II.

The ratio of the spectroscopic factor for transitions to the same rotational band is given by

$$\frac{S'}{S} = \frac{2I'+1}{2I_1+1} \frac{< I'_1, j, k_1, \Omega | \ I_2, k_2 >^2}{< I_1, \ j, k_1, \Omega | \ I_2, k_2 >^2},$$

For transitions to ground and first excited states of ^{26}Mg, the I_1 and I'_1 are 0 and 2 respectively. This ratio is 1.78, which is in good agreement with our experimental value of 1.76. This value is also in agreement with the experimental value of 2.1 by Glover *et al*[3] and the values of 1.87 and 1.53 by $(d, ^3$He$)$ works[3,4].

(12) S.G. Nilsson, *Mat. Fys. Medd. Dan. Vid. Selsk.* 29 No. 16(1955)

The differential cross sections and the angular distributicns for grcund state and first excited state transitions measured by Glover *et al* and by Colli *et al* at 17° are in gocd agreement with the present results. The value of the differential crcss secticn fcr the 2.97 MeV second excited state, which identified as 3.6 MeV state by Glover *et al*, lccates between the two values of the previous measurements.

The 2.97 MeV state with a dcminant $l=2$ transiticn, the protcn was mcst probably picked up frcm the highest filled $d_{5/2}$ Nilsscn crbit No. 7($\Omega=3/2^+$). By assuming a protcn picked up from this orbital, the calculated spectroscopic factor of 0.36 gives gocd agreement with the experimental value (Table II). By assuming a proton removed from the Nilsson orbit No.6 ($\Omega=1/2^+$) as suggested by Pellegrini *et al*, the calculated spectrcscopic factor is abcut three times too small compared with the experimental one.

利用 14.1 MeV 之中子對 Al^{27}(n,d) Mg^{26} 核反應之研究

利用望遠鏡式檢偵器偵察 14.1MeV 中子所引導之 Al^{27}(n,d)Mg^{26} 核反應所產生之重子。對相當於引導 Mg^{26} 之 0，1.81 及 2.97 MeV 能階所產生之重子之角分佈情形用變畸波波恩近似理論來分析。反應至每能階之橫截面大小及角動量值 l 及光譜係數等均獲得數據。

實驗結果認為 Mg^{26} 之能階符合轉動核模型所預測之結果。

Investigation of the ^{26}Mg(d,p)^{27}Mg Reaction below 3 MeV[*]

E.K.Lin (林爾康) , W.N.Wang (王唯農) and J.G.Yu (余建國)

Tsing Hua University and Academia Sinica, Taiwan, China

and

W. C. Tung

Institute of Nuclear Energy Research, Atomic Energy Council, Taiwan, China

Abstract. A study was made for the reaction ^{26}Mg(d,p)^{27}Mg in the deuteron energy range from 2.0 to 3.0 MeV. Angular distributions in the range of $20° \div 140°$ at $E_d = 2.1$, 2.3, 2.5, 2.7, 2.8 and 3.0 MeV were measured. Excitation functions ranged from 2.0 to 3.0 MeV were obtained for the reactions leading to the ground and first excited states of ^{27}Mg. The direct stripping effect was found to give considerable contribution to the P_0' transition, and its significance appears to increase grandually at bombarding energies fron 2.1 to 3.0 MeV. The distorted-wave Born approximation $(DWBA)$ was used to calculate the spectroscopic factor for the ground state. The measured angular distributions of higher proton transitions indicate that the compound nucleus formation becomes more important relative to the stripping process.

1. Introduction.

In recent years a considerable amount of information on the 2s-1d shell nuclei has been obtained from the analysis of the stripping (d,p) reaction. An investigation of the stripping reaction on Mg isotopes (^{24}Mg, ^{25}Mg and ^{26}Mg) has been made by several authors at deuteron energies [1-5] ($E_d = 8 \div 15$ MeV) and also at lower deuteron energies [6-10] ($E_d = 1.5 \div 5.0$ MeV). It was shown that a good agreement between experimental angular distributions ead usthe simple stripping theory can be obtained even at considerably lower deuteron energi (1.5÷2.0MeV). For the (d,p) reaction on ^{26}Mg, previous measurements have been performed at incident energies $E_d = 1.5 \div 2.5$ MeV[9], $E_d = 3.0 \div 5.0$ MeV[10] and $E_d = 8.9 \div 15$ MeV[1,4]. A study of this reaction at bombarding energies[1,4] ($E_d = 8.9 \div 15$ MeV) indicated that the main contribution to the cross-section for many levels of^{27}Mg excited in the reaction comes from stripping. The obtained data were reasonably well explained by the distorted-wave Born approximation $(DWBA)$ analysis. Silverstein *et al.*[10] have measured protons from the ^{26}Mg (d,p) reaction leading to the ground and low-lying states of ^{27}Mg for incident energies from 3.0 to 5.0 MeV. They reported that for these energies, the proton angular distributions for the first three excited states of ^{27}Mg show a characteristic stripping pattern. Using the $DWBA$, absolute spectroscopic factors were calculated and compared qualitatively well with previous determinations. At lower deuteron energies ($E_d = 1.5 \div 2.5$ MeV), Omat *et al*[9] have made measurements for the same reaction and found strong evidence of a predominantly direct stipping reaction mechanism at $E_d = 2.0 \div 2.5$ MeV for the ground and first excited states transitions. They analyzed data by the simple Bulter theory only for the first excited state at an incident energy of $E_d = 2.26$ MeV.

The aim of the present investigation was to extend the study of the ^{26}Mg(d,p)^{27}Mg reaction to the 2.5÷3.0 MeV deuteron energy range, in order to obtain some information on the reaction mechanism and the structure of the energy dependence of differential cross

sections for the $^{26}Mg(d,p)^{27}Mg$ reaction at low bombarding energies. We have measured, for several proton groups leading to the low-lying states of ^{27}Mg, complete angular distributions to investigate the strength of the stripping effects, and also measured excitation functions to ascertain the strength of the compound nuclear effect.

The obtained angular distributions at E_d=2.5 and 3.0 MeV for the ground state of ^{27}Mg were analysed in terms of the *DWBA* and spectroscopic factor extracted. Furthermore, measurements were also made at deuteron energies 2.0÷2.5 MeV; these results were compared with previous measurements of Omar *et al*[9].

2. Experimental method

The experiments were performed using a deuteron beam from the 3 MeV Van de Graaff accelerator of the Tsing Hua University. The target was prepared by an evaporation procedure in which highly enriched ^{26}MgO powder, obtained from Oak Ridge National Laboratory, was mixed with pure zirconium powder in the tantalum heater. The oxide was reduced by the zirconium and the resulting, nearly pure, ^{26}Mg evaporated onto a thin carbon backing. The prepared target contains 99% ^{26}Mg and is approximately 100-200$\mu g/cm^2$ thick. The protons emitted from the reaction were detected by two solid-state detectors, and the proton spectra were recorded on a 1024 channel analyzer. The beam current was collected in the Faraday cup located at a distance of 55 cm from the center of the scattering chamber. In order to remove the elastically scattered deuterons and reaction alpha-particles, a set of aluminum foils (15mg/cm^2 thick) was stacked in front of the detector. The details of the experimental method have been described in a previous paper [11].

Angular distributions were measured at incident deuteron energies of 2.1, 2.3, 2.5, 2.7, 2.8 and 3.0 MeV. The measurements were made at 10° intervals from 20° to 140° lab., with target angle kept at 45° and 135° with respect to the incident deuteron beam. Excitation functions were obtained at angles between 30° and 140°, ranging from 2.0 to 3.0 MeV in steps of 15 keV. The errors in the relative differential cross section which are mainly due to counting statistics vary between 5÷10%. The error in the absolute cross sections is estimated to be 25÷30%.

3. Result and discussion.

Typical proton spectrum of the $^{26}Mg(d,p)^{27}Mg$ reaction is shown in Fig. 1. The peaks are labeled according to the excitation energy of levels in ^{27}Mg, these were identified from their known energies [4,10]. The energy spectra obtained are similar to those observed from the same reaction at higher energies (3÷15MeV) in earlier works[4,10]. Fig. 2 gives the level scheme for ^{27}Mg obtained from the $^{26}Mg(d,p)^{27}Mg$ reaction.

Groups P_0,P_1 and P_2 are well separated in all the spectra, they correspond to the low-lying levels of ^{27}Mg with excitations 0, 0.98 and 1.69 MeV. Group $P_{5,8}$ represents four unresolved levels P_5,P_6,P_7 and P_8 of ^{27}Mg having excitation 3.42, 3.47, 3.48 and 3.56 MeV. Group $P_{9,10}$ leading to the states of ^{27}Mg of the energies 3.76 and 3.78 MeV was not separated in all the spectra. Group P_{12} corresponding to the 4.15 MeV state of ^{27}Mg was observed only in some cases, because it appeared near the end of the spectrum.

Angular distributions measured at deuteron energies between 2.1 and 3.0 MeV are shown in Figs. 3-5. As is seen from Fig. 3, the angular distributions of the P_0 group show a rather regular behavior as function of energy. It indicates that the importance of the stripping effect increases gradually with deuteron energy, and the stripping peak is dominant at E_d-3.0 MeV. The obesrved stripping behavior corresponds to $\ell=0$ assignment for the ground state transition as expected. The angular distributions of the P_1 group have somewhat stripping-like character of $\ell=2$ having maximum at near 50°. Fig. 4 shows the variation of

the P_1 angular distributions with deuteron energy in the range investigated. For groups P_0 and P_1 at deuteron energies 2.5÷3.0 MeV, the magnitude of the cross–section and the shape of the angular distribution are not very different from those measured previously at higher energies 3.0÷5.0 MeV [10].

At deuteron energies 2.0÷2.5 MeV our angular distributions for these two groups are, in general, comparable to those from earlier measurement by Omar et al[9] in the same range of energy. However, there is notable difference concerning the shape of the angular distribution for group P_1 in few cases. Groups $P_2, P_4, P_{5,8}$ and $P_{9,10}$ have somewhat isotropic distributions as shown in Fig. 5. Apparently the main contribution to the cross–section for the transition to the excited states higher than 0.93 MeV state comes from compound nucleus formation. The P_3 group was seriously obscured by the ^{12}C contamination and as a result, its angular distribution could not be obtained.

The direct–effect contribution for groups P_0 and P_1 at E_d=2.5 and 3.0 MeV was calculated by the DWBA stripping theory [12]. The optical–model parameters used in the DWBA calculations with the computer code Julie are given in table I. These are taken from Ref. 10, which were obtained in a study of the ^{26}Mg(d,p) stripping at E_d=3.0÷5.0 MeV. For both deuterons and protons, the real optical potential used is of the Saxon form and the imaginary part is in the form of surface absorption.

The DWBA calculations were carried out with several values of the cutoff radius R_{LC}. The best fit to the experimental data for the P_0 group at E_d=3.0 MeV was found at R_{LC}=4.2F as shown in Fig. 6. The same value of R_{LC} was chosen for the DWBA calculation at E_d=2.5 MeV. The ground state of ^{27}Mg is well known to be 1/2+. As is seen from Fig. 6(left), the calculated angular distribution for ℓ=0 capture and the measured for the P_0 group showed consistently a sharp dip in the vicinity of 37° and a peak at 75°. It is interesting to note that the peak position aod width are very close to the previous result[10] at E_d=3.0÷3.67 MeV. The fit of DWBA calculation for the group P_0 to the experimental data at E_d=2.5 MeV is shown is Fig. 6 (right). The peak is slightly shifted and broadened relative to the DWBA theory. This discrepancy may result from the nonvaried parameters chosen for the analysis at E_d=2.5 MeV. However, it is seen that the direct effect is significantly present at low incident energy of 2.5 MeV. The observed stripping pattern is similar to the angular distribution of the P_0 group from the ^{27}Al $(d,p)^{28}$Al reaction[11] at same deuteron energy.

A comparison of the measured cross–sections with the calculation for ℓ=2 transition proceeding to the first excited state (3/2+) at 0.93 MeV is presented in Fig. 6 (top). The agreement is less satisfactory as compared to the obtained good fit for the ground–state (ℓ=0) transition. At E_d=3.0MeV, the calculated values were found to deviate considerably from the measured cross sections at large angles (from 90° on backward). It seems probable that the interference between stripping and compound process is present and dominate at backward angles.

In view of the generally satisfactory agreement between experiment and theory for the ground–state transition, it is possible to extract the spectroscopic factor in the present work. From the ratio of the experimental cross section, $(d\sigma/d\Omega)_{exp}$, to the calculated from DWBA, $\sigma_{DW}(\theta)$, one can determine the spectroscopic factor for a (d,p) reaction on an even–even target nucleus involving a single value of J as follows:

$$S = \frac{1}{(2J+1)} \cdot \frac{(d\sigma/d\Omega)_{exp}}{\sigma_{DW}(\theta)}$$

The transition strength $(2J+1)S$ and the extracted spectroscopic factor S for the ground state are listed in table II.

E. K. Lin, W. N. Wang, J. G. Yu and W. C. Tung

Also listed in table II is the comparison of the obtained spectroscopic factor with earlier measurement[10]. At $E_d = 3.0$ MeV the measured cross section leads to a spectroscopic factor for the ground state being 0.62 ± 0.20 which agree, within experimental error, with the measured value (0.70 ± 0.35) at $E_d = 3.0 \div 5.0$ MeV[10]. The extracted S-value also agrees reasonably well with the measured value $(S = 0.58)$ for the isotonic nucleus ^{29}Si, obtained from the ^{28}Si$(d,p)^{29}$Si reaction at $E_d = 2\text{-}6$ MeV[11]. The spectroscopic factor for the excited states is not determined, because the presence of considerable compound-nucleus contribution makes it unlikly to yield reliable S-values.

Contribution from the compound nucleus formation to groups P_0 and P_1 was estimated by Hauser-Feshbach calculation[14], and the calculated cross section, shown as the dashed line in Fig. 7, was compared with the results of the measurements of two excitation functions for these two proton groups. The calculation was performed with spin-cutoff parameter $\sigma^2 = 9.0$[13,15] and the required transmission coefficients of reaction particles were calculated from optical potentials with a computer code of Chang[16]. As is seen from Fig. 7, the measured cross sections, which were obtained by numerical integration over the angles $30°$ to $150°$, appear to fluctuate and increase with the deuteron energy. The difference between the experimental points and the calculations is small for the P_1 transition, but is rather large for the P_0 transition, especially at deuteron energies higher than 2.3 MeV. It would indicate that the stripping process is more important for the ground-state transition than for the first-excited transition, and is less important for both transitions at low energies $(E_d = 2.0 \div 2.3 \text{MeV})$, where the compound nuclear effect is dominant. The results of the angular-distribution measurements support the above statement about the relative importance of two reaction mechanism for the P_0 and P_1 transitions.

In summary, the measured angular distributions indicates that $\ell = 0$ and 2 stripping patterns can be identified for the ground and first excited states from the ^{26}Mg$(d,p)^{27}$Mg reaction in the investigated energy range between 2.0 and 3.0MeV. The ground state has the $\ell = 0$ stripping peak which becomes remarkable and predominant with the increasing deuteron energy, and the importance of direct effect is largest at $E_d = 3.0$ MeV. For the first-excited-state transition the compound nuclear effect interferes considerably with the direct stripping, in contrast to the results at $E_d = 3.0 \div 5.0$ MeV[10] where the main contribution to the cross section for the first-excited-state group was found to come from stripping. Qualitative agreement of the extracted spectroscopic factor for the ground state with earlier measurement[10] would give an evidence for the reaction mechanism that the direct effect plays a significant role in the P_0 transition at low deuteron energies $(2.0 \div 3.0 \text{MeV})$. The behavior of our data for the higher proton transitions indicates, however, that the compound nucleus formation becomes more important relative to the stripping process, and it seems probable that the reaction at deuteron energies investigated proceeds essentially through the compound-nucleus formation for the transition to the excited states higher than the 0.98 MeV state.

低於 3.0MeV 能量的氘子所引導之 ^{26}Mg(d,p)^{27}Mg 核反應研究

本篇主要為研究氘子能量自 2.0～3.0MeV 所引導之 ^{26}Mg$(d,p)^{27}$Mg 核反應。角分佈自20°—140°在 $E_d = 2.1$, 2.3, 2.5, 2.7, 2.8, 3.0 處均分別測量。能量激發函數自 2.0～3.0MeV 所引導至 Mg^{27} 之基態及第一激發態均加測量。實驗結束發現對基態 P_0 之反應主要來自直接剝制反應，能量愈高，其作用愈明顯。利用了畸形波波恩近似法計算了基態之光譜係數。所測得之至激勳態之質子其角分佈情形顯示其中複合過程佔較重要之成分。

Table I

Optical-model parameters used

in the DWBA calculations

	Deuteron	Proton
V(MeV)	75.0	50.9
r_0(F)	1.15	1.25
a(F)	0.81	0.65
W_s(MeV)	60.0	25.4
r_s(F)	1.34	1.25
a_s(F)	0.68	0.47

Table II

Spectroscopic factors extracted from the

DWBA fitting to the experiment data

		measured			Spectroscopic factor S			
					E_d=3.0	E_d=3.0-5.0	E_d=2.5	E_d=2-6MeV
E_x(MeV)	l	σ_{max}(mb/sr)	$(2J+1)S$	$J^\cdot$	Present Work	Ref.10	Present Work	^{28}Si$(d,p)^{29}$Si[13]
0	0	3.3	1.24±0.4	$\frac{1}{2}^+$	0.62±0.2	0.70±0.35	0.48±0.15	0.58

References

(1) S. Hinds, R. Middleton and G. Perry: *Proc. Soc.* 71, 49(1958)

(2) E.W. Hamburger and A.G. Blair: *Phys. Rev.* 119, 777(1960).

(3) R. Middleton and S. Hinds: *Nucl. Phys.* 34, 404(1962).

(4) B. Cujec: *Phys. Rev.* 136, B1305(1964).

(5) H. F. Lutz and S.F. Eccles: *Nucl Phys.* 88, 513(1966).

(6) S.A. Cox and R.M. Williamson: *Phys. Rev.* 105, 1799(1957).

(7) Naoyuki Takano: *Journ. Phys. Soc. Japan* 16, 598(1961).

(8) R.B. Weinberg, G.E. Mitchell and L.J. Lidofsky: *Phys. Rev.* 133, B884(1964).

(9) H.M. Omar, I.I. Zaloubovsky, M.H.S. Bakr, R. Zaghloul and V.J. Gontchar: *Nucl. Phys.* 56, 97(1964).

(10) J. Silverstein, L.J. Lidofsky, G.E. Mitchell, and R.B. Weinberg: *Phys. Rev.* 136, B1703(1964).

(11) C.S. Lin and E.K. Lin: *Nuovo Cimento,* 66, 336(1970)

(12) R.H. Bussel, R.M. Drisko and G.R. Satchelr: *Oak Ridge Nat. Lab. Report ORNL-3240(1962).*

(13) U. Strohbusch, W. Bakowsky and H. Lacek: *Nucl. Phys.* A149, 605(1970).

(14) W. Hauser and H. Feshbach: *Phys. Rev.,* 87, 366(1952).

(15) Y.C. Liu and C. Chang; *Journ. Phys. Soc. Japan* 30, 5(1971).

(16) C. Chang (unpublhised).
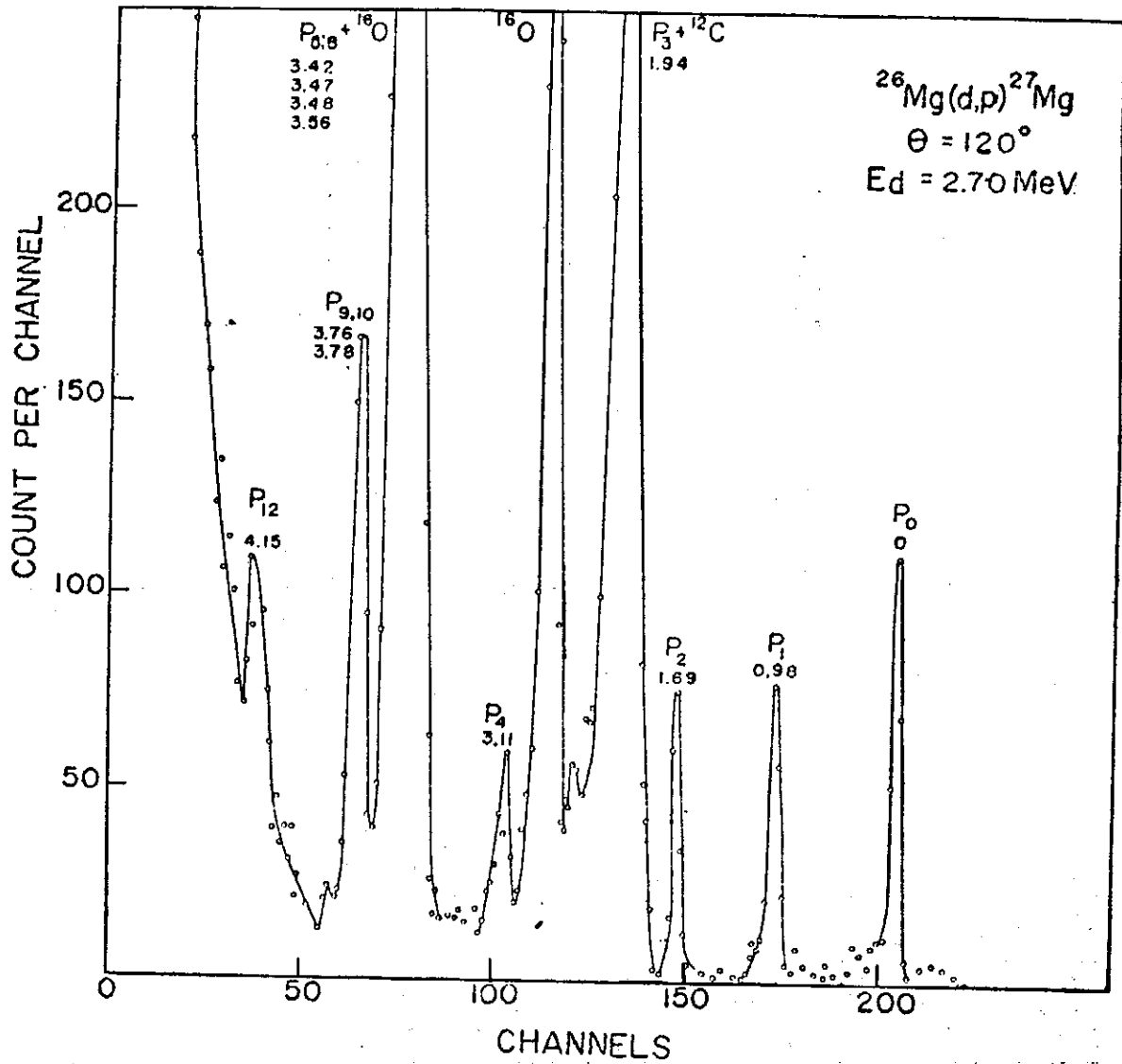
Fig. 1 *Typical proton energy spectrum for the* $^{26}Mg(d,p)^{27}Mg$ *reaction.* *Numbers over peaks refer to excitation energy (in MeV) of levels in* ^{27}Mg. $E_d = 2.7$ *MeV*, $\theta_L = 120°$
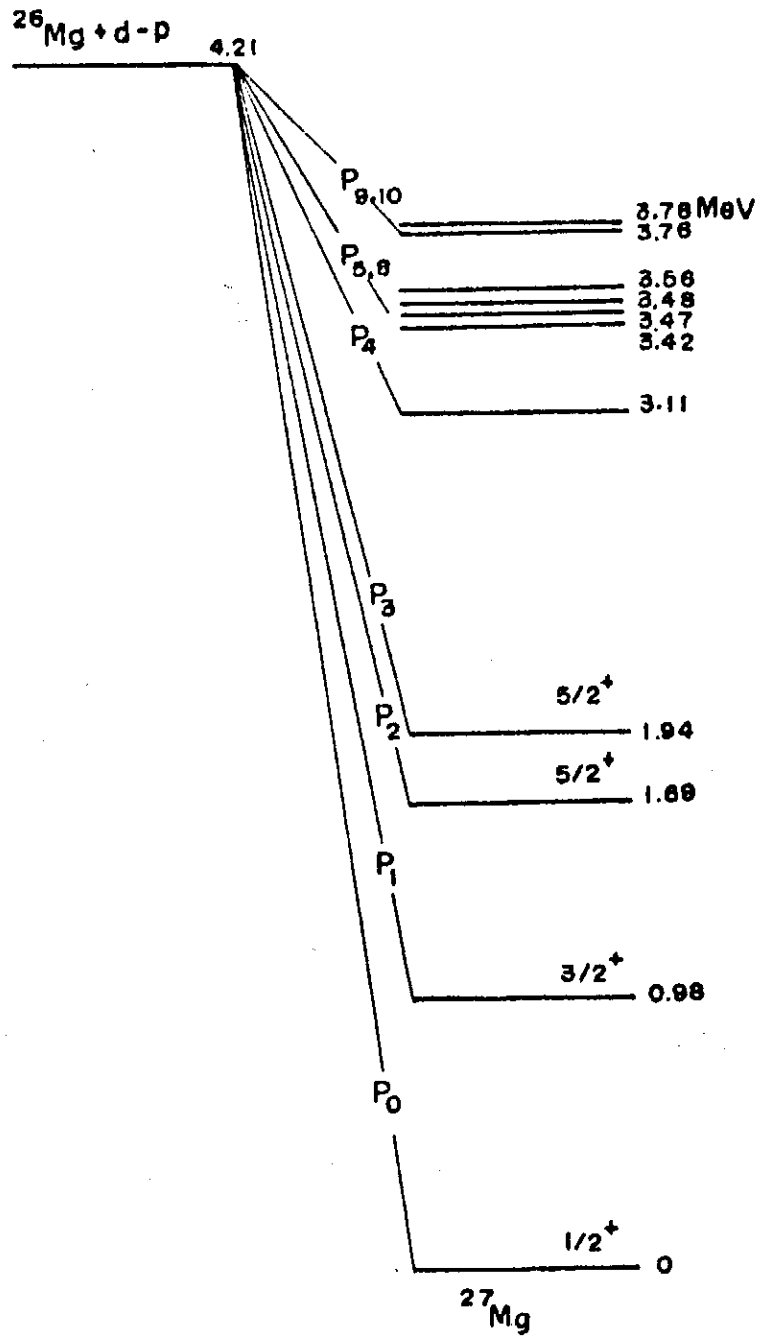
Fig. 2 *Level scheme for the low-lying levels of* ^{27}Mg
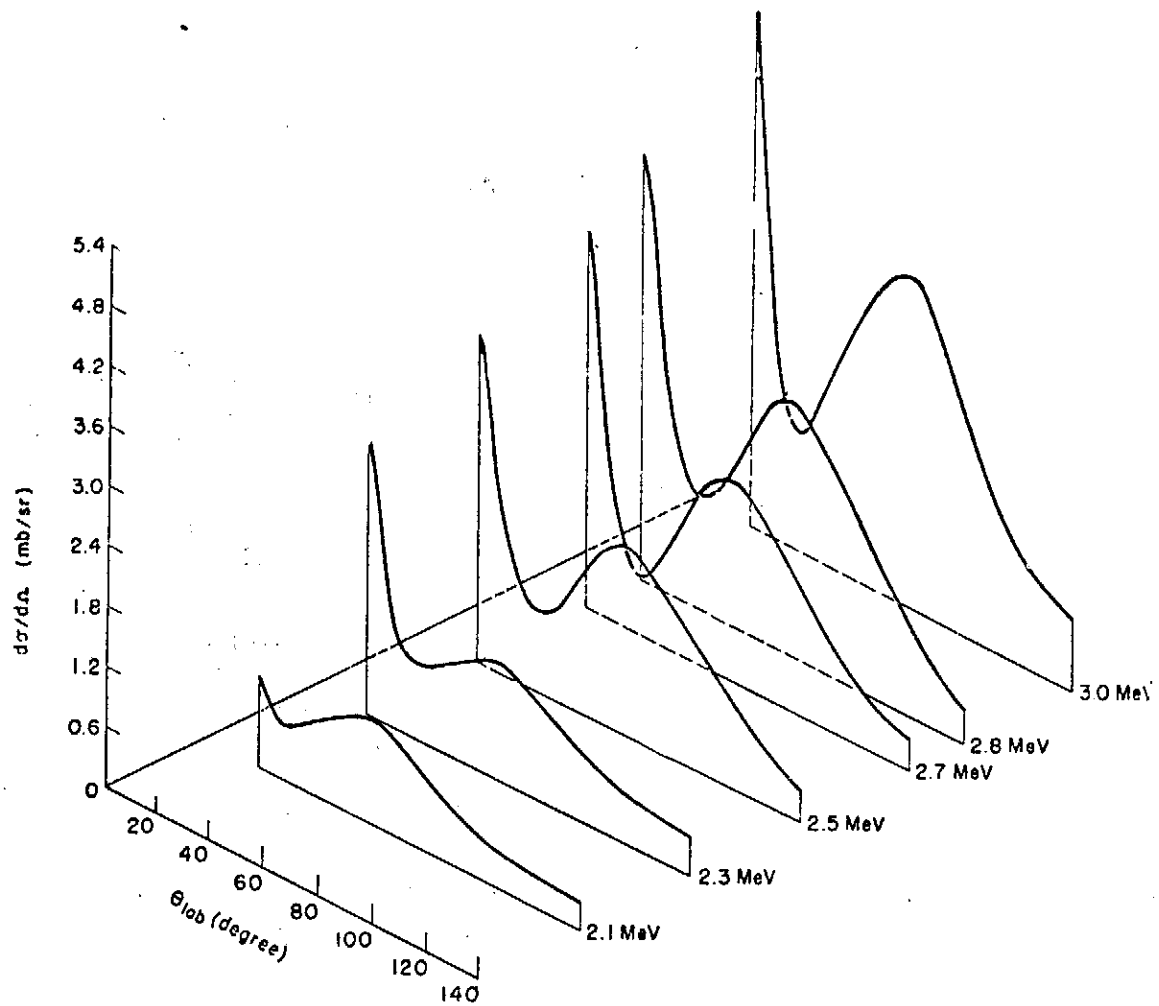
Fig. 3 *Angular distributions for the* $^{26}Mg(d,p_0)^{27}Mg$ *reaction*
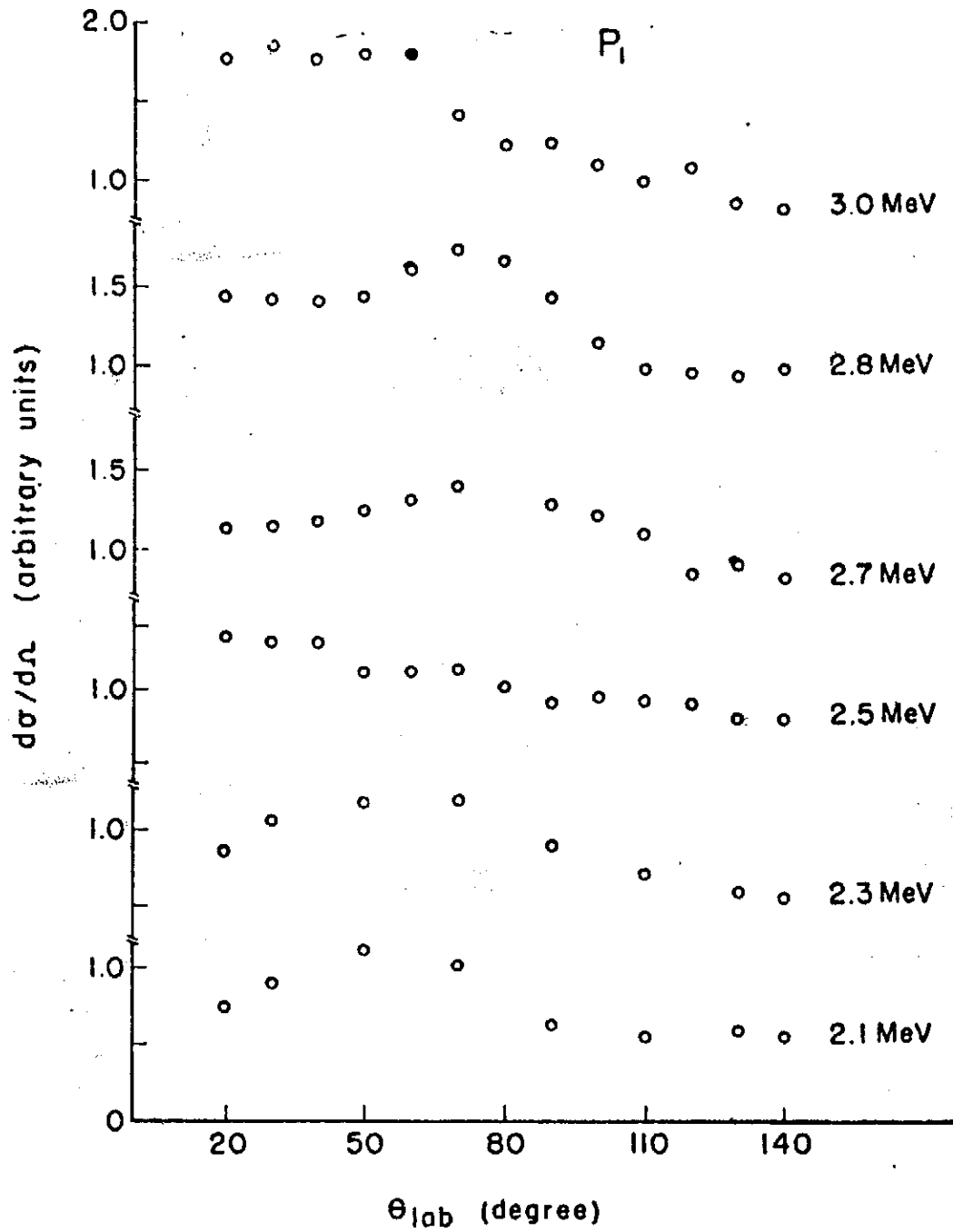
Fig.4 *Angular distributions for the* $^{26}Mg(d,p_1)^{27}Mg$ *reaction*
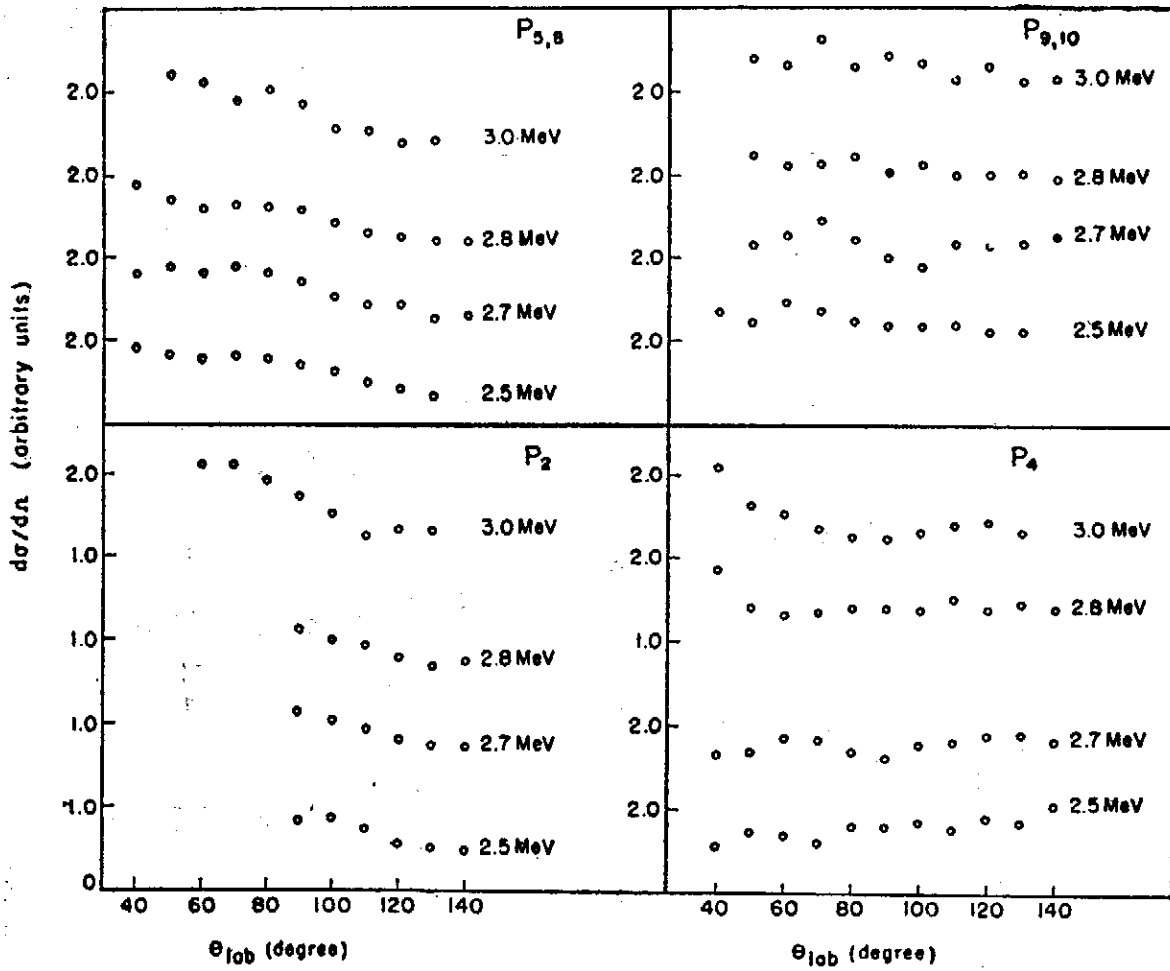
Fig. 5 *Angular distributions of groups* $P_2, P_4, P_{5,8}$ *and* $P_{9,10}$ *from the* $^{26}Mg(d,p)^{27}Mg$ *reaction*
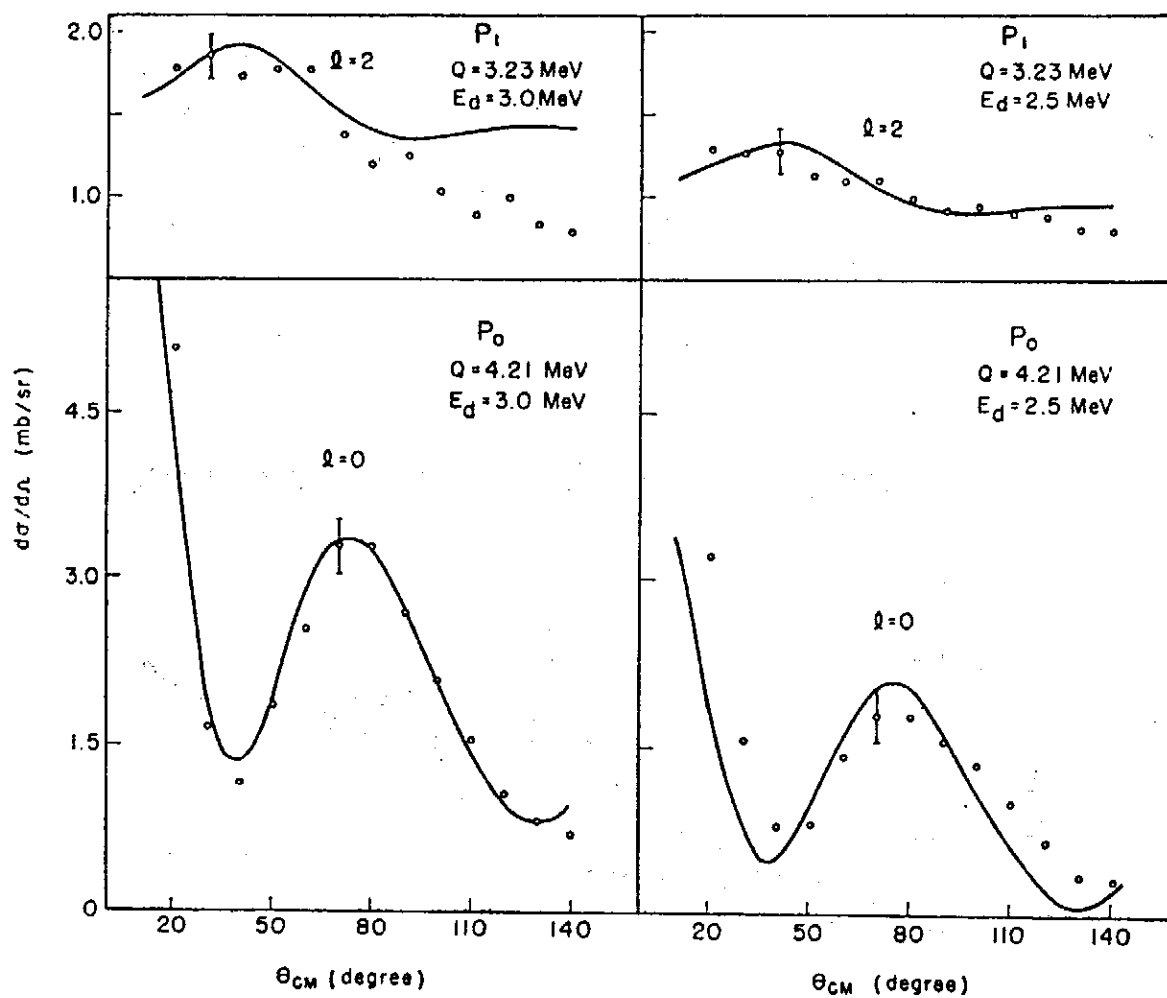
Fig. 6 *Comparison of the angular distributions of two proton groups P_0 and P_1 from the ^{26}Mg$(d,p)^{27}$Mg reaction with the DWBA calculation; for P_0 transition with $\ell=0$, and for P_1 transition with $\ell=2$. The full line represents the calculated σ_{DWBA} with cutoff radius $R_{LO}=4.2F$*

E. K. Lin, W. N. Wang, J. G. Yu and W. C. Tung
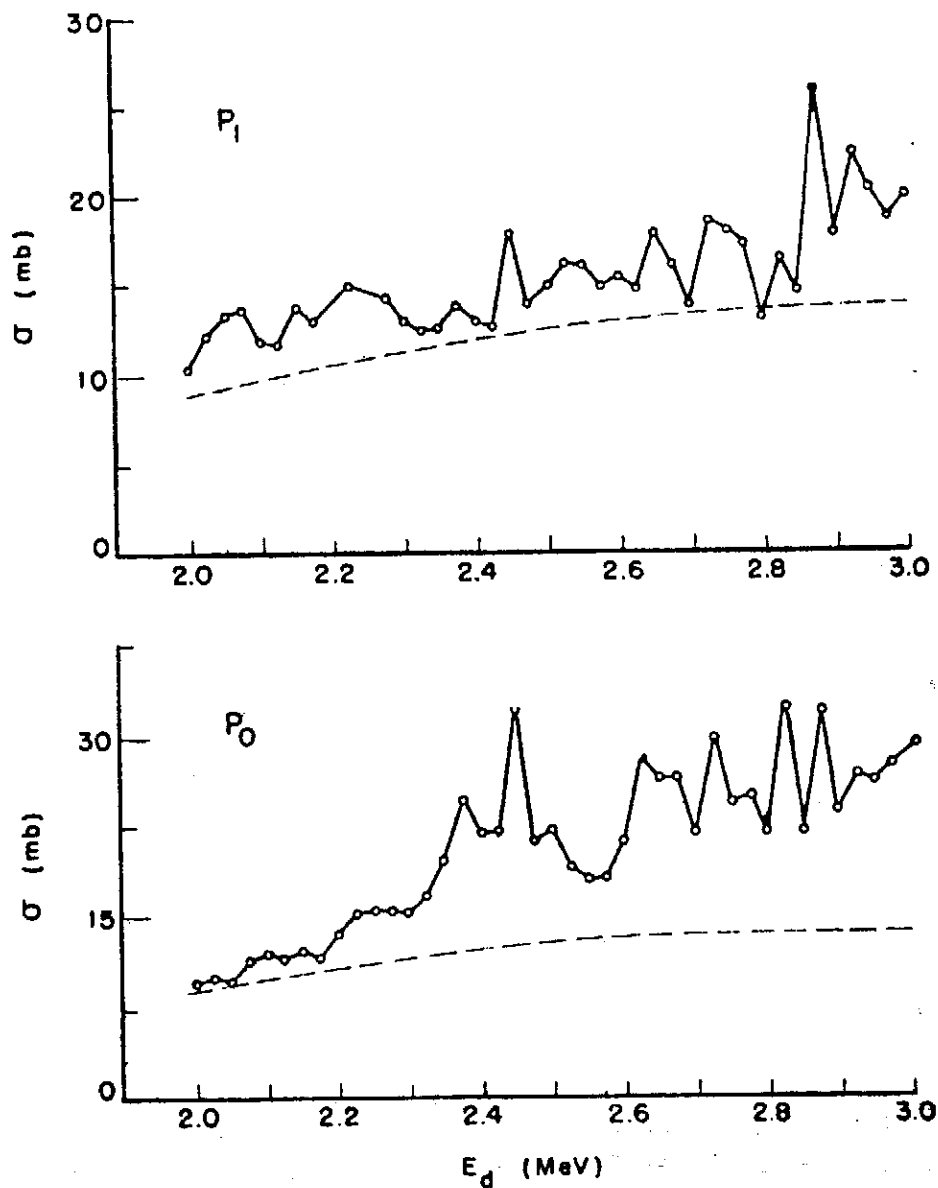
Fig. 7 *Excitation functions of groups P_0 and P_1 from the $^{26}Mg(d,p)^{27}Mg$ reaicton. The dotted line is the Hauser–Feshbach calculation using spin–cutoff parameters $\sigma^2=9$.*

靜 磁 場 引 發 電 阻 突 變

Magnetically Induced Insulator–Conductor Transition in Silicon

Yu–Tung Yang (楊毓東) and Chau–Kun Hu (胡朝坤)

Institute of Physics, Academia Sinica and Tsing Hua University

(*Received April* 1971)

In high electric field, if a gold–silicon junction is biased below the critical voltage, then with the aid of the magnetic energy the insulator–conductor transition can also occur. We find by energy conservation that there is an equivalence between the electric energy and the magnetic energy, $e \triangle V = k\mu H$. $k\mu = \mu^*$ which is the effective magnetic moment. μ^* may exist in high electric field in the gold–silicon junction layer. The value of k is about 1.44×10^4, depending on the condition of the junction layer.

1. 緒　　言

通常在強電場中，不良導體可因某一臨界電場而突然由非導體轉變爲導體，當電場撤銷時則又突然還原爲非導體。此種現象稱之爲電阻突變，發現已有若干時日，（見 *Rev. Mod. Phys.* 40, 1968 全卷）。理論方面有 D.C. Mattis 曾爲解釋（見 *Phy. Rev. Lett.* 22, 936, 1969）。

半導體如矽，鍺之類屬於不良導體。鍺之電阻突變於 1959 年爲 A.L. McWhorter 等所發現而稱爲 Cryosar（見 *Proc. IRE*, 47, 1207, 1959）。它發生於 4.2°K，當時解釋爲材料特性之突變。

在半導體工程學中，有半導體可控制整流子 (SCR) 有此電阻突變特性，是由 PNPN 結合體引起的，應用於室溫，爲 J.J. Ebers 所創製（見 *Proc. IRE*, 40, 136, 1952）。

本文所述者爲電阻突變之新現象，卽在強電場中，如再加靜磁場可以引發電阻突變。材料中之磁能與電能有互相補助之功用，將導電質點 (Charge Carrier) 送上導電帶 (Conduction band)。若質點之磁矩（以 Bohr magneton 爲單位）爲 μ，磁場強度爲 H，則能量爲 μH。若電場中電能爲 eV_c 可使材料中發生電阻突變，則在 V_c 附近可有 $\triangle V$，而吾人發現

$$e \triangle V = K\mu H, \tag{1}$$

或
$$\triangle V = K \frac{\mu}{e} H = K'H. \tag{2}$$

表示磁能與電能可以在某一材料中互換。上式中 K 或 K' 爲試驗常數，例如 $K = 1.44 \times 10^4$ 而能在某一樣品中符合試驗結果。

2. 方 法 與 試 驗

取電阻係數在 10^3 歐姆公分以上之矽半導體加以表面化學處理除去氧化物。洗淨並卽刻以熱結合法以一定壓力將細金線（作導線用，直徑在千分之一英寸）熱結合於矽表面，於是成爲金矽兩極體。以下簡稱兩極體。

將兩極體按照圖 1 接線。吾人使用"兩點測量法"而非四點測量法旨在明瞭接合點物理特性。用於測量兩極體兩金導線間之電位降之電表有五位讀數。表本身輸入端之阻抗爲 10^8 歐姆。在電阻突變前，矽在 77°K 中之電阻測知爲 10^8 歐姆。線路中負荷電阻共爲 11K 歐姆，但與矽之電阻比較則微不足道，故可忽略不計。金線兩端之電壓降亦卽直接測量直流電源輸出端之電壓降，其誤差可以忽略不計。

吾人所用矽材合硼，表面爲 〔111〕，屬 p 類。

電阻突變後，電阻之值約減低 10^6 倍以上。在此試驗中，吾人僅注意電阻突變前之各種狀況，主要注意使突變發生之臨界電壓及磁場，V_c 與 H。

圖 1 所表示，試驗用穩定直流電壓係由本國倍達公司製造之電力供給器供給。其安定性良好，約為每小時 0.5mV。輸出時電力最高 30 瓦特，最高壓 30V，最高電流 1A。

電阻突變與 $\frac{\partial V}{\partial t}$ 極有關。$\frac{\partial V}{\partial t}$ 大者可促成電阻突變在電壓不穩定時發生。為防止 $\frac{\partial V}{\partial t}$ 不定，吾人乃使用電動機控制電力供給器之電壓輸出，吾人所使用者約可使直流電壓每秒增加 0.01 伏特。

吾人又接 F80XY 平面記錄器於金導線之兩端，記錄器之輸入阻抗約為 10^6 歐姆。記錄器之使用目的主於使吾人得知究在何時發生電阻突變。由於記錄器之輸入電位降與兩極體之電位降相同，故讀數電位計所讀者仍為兩極體之電位降。此一電位降應包括金矽接點電位降與矽本身電位降。金矽接合點之電位降佔重要成分可由試驗中看明。

電位降之讀數可有四位有效數，誤差有數個至十個 mV，故記錄每一 $V_c H$ 點均需十次以上至二十次測量，並計算其平均平方誤差。此種誤差發生於試驗裝備之雜音，及液態氮所發生之汽泡。

兩極體放置於液氮瓶中並置於靜磁場中，包以黑紙以防光線引起電阻突變。兩極體在液氮瓶中須冷卻一二小時以達溫度平衡狀態，然後方開始試驗。

靜磁場係由電磁鐵供給。電磁鐵之磁場均勻度約為 1 至 2mG/c.c.，長時間安定性約為 10^{-6}，對本試驗已足敷用。

試驗之初，將電壓調至 V_0 附近，但略小於 V_0。為查驗製成之兩極體有無磁引發電阻突變可以自動方法或手控方法緩慢改變磁場。若在某一磁場強度 H_0，兩極體突然發生電阻減少現象，則該兩極體為可用者。此時再緩慢降低磁場，在某一磁場強度 H_0 時，則發現電阻又會突然升高使導體恢復為非導體。在強電場中此現象常常發生於製成之兩極體中。

以現象而論，在強電場中由磁場引起之電阻突變與純由電場增強引起之電阻突變並無分別。只是電阻突變發生後，若繼續增加電壓則在變成較好導體狀態之樣品中之電流 I 會隨之增加並大致符合歐姆定律。但在電阻突變發生之後，若因增加磁場強度 $H > H_0$，非但不能使電流 I 增加而且有阻凝電流之效果，就性質而言，顯然電阻突變發生電阻降低後再無可供繼續使用之磁能 μH，而另一方面磁阻 (Magnetoresistance) 在材料中繼續隨磁場強度增加而使電流略減弱。

由試驗得知矽有餘電現象，故試驗時以一次完成測定一列系數字為原則。反覆試驗常使 V_0 之測得值不一，雖然誤差不足以影響結查之分析，但仍以一次完成一曲線為佳。若每次將 V 及 H 改變拖長，$\frac{\partial V}{\partial t}$ 及 $\frac{\partial H}{\partial t}$ 為極小，則餘電現象不明顯，但完成一曲線費時甚久，似無必要。

3. 結果及分析

磁場引發電阻突變可分為四種情形：(一)磁場不能引發突變，(二)磁場只在兩極體之一側引發突變，(三)磁場在兩極體之另一側引發突變，(四)磁場在兩極體之兩側均可引發突變。

吾人認為第二第三兩類兩極體可以分析有下列原因：

在試驗中 V_0 與 H 之測量包括(1)接觸點電壓降，(2)矽本身電壓降，(3)因磁場引起電阻改變而引起非突變之電壓降，(4)電阻突變中磁能 μH 之影響。

在磁場引發電阻突變中，可利用只有第二類或第三類特性之兩極體作試驗。這類兩極體之兩面對一定方向 $(\pm)$ 之磁場而言，有一面使測得之電壓降包括(1)，(2)，(3)與(4)，而另一面只有(1)，(2)，(3)。通常(4)之值抵消一部份(1)，(2)與(3)者，故(1)，(2)，(3)之合較(1)，(2)，(3)，(4)之合為大。將正反兩種電壓降之值相減則剩(4)，因此得到相減電壓降 $\triangle V$ 與 H 之關係曲線。由於假定磁能與電能在此兩極體中可以互換，故得

$$e\triangle V = K\mu H, \tag{1}$$

$$\triangle V = K\frac{\mu}{e}H, \tag{2}$$

兩極體本身成為電阻突變現象中磁能轉換為電能之媒介物。

磁場引發電阻突變之四種情形其第一第四兩種不能用來完成磁電關係試驗，因每種情形均缺少其他一種特性，有(1)(2)(3)者無(4)，四者皆有時又無(1)，(2)與(3)之單獨數據不含(4)。

圖二表示試驗之安排。圖中之兩極體有第二或第三類特性如前述者。做試驗時電場方向維持一定，只是改變磁場方向，一次由矽至金（屬第二類或第三類之兩極體均可用）（如 2A 圖），所得試驗結果如圖 3A 曲線。反轉磁場方向由金至矽（如圖 2B 圖）並得試驗結果如圖 3B 之曲線。在某一固定磁場 H 中，使 3B 之點（代表前述包括(1)，(2)，(3)之電壓降）減去 3A 之點（代表前述包括(1)，(2)，(3)，(4)之電壓降）即得與磁有關之電壓降 $\triangle V$。而 $\triangle V$ 與 H 之間之關係見圖 4 所示之曲線。

圖4顯示H在 0.1 至 0.5 weber/m² 之間 $\triangle V$ 與H之關係近一直線當 $H<0.1$ weber/m² 時則由於材料特性使 μ 快速增長，至突變完成後，μH 不再存在於兩極體中，因 $\mu_{av}=0$，故磁能電能互換之作用亦停止。

在圖4中 $0.1<H<0.5$ 可稱為H之窗，在此窗中有明顯磁能電能互換作用發生。若磁場 $H>0.5$（或其他接近數字，單因兩極體製作情形而定，V_e 及H值有大有小），突變現象變為不明顯。主要是由於磁造成之電阻太高，使突變所需時間拉得太長（～一秒或更長）不能再顯出非歐姆式電阻變化與電阻突變之區別。吾人認為此種高磁阻阻止電阻突變發生之現象產生即象徵突變現象之終止。

由不需磁場僅由電場引發突變現象至磁阻高達電阻突變不能發生為止所得之 $\triangle V_e$ 與H之關係，根據兩種能量互換之假設如公式(1)，得知 $K=1.44\times10^4$ 試驗結果頗與(1)式相近。

其他樣品與圖4結果相近者亦有磁能與電能互換之直接關係如圖5及圖6所示。但因兩極體金矽結合點之物理性質不盡相同，故所得 K' 不同。例如樣品 2.3 之K各為 1.45×10^4 與 8.97×10^4。但均由試驗顯示磁能與電能間之線性關係。

圖7為模式電阻突變之交流電場效果。橫座標代表非導體狀態之電壓降。縱座標代表導體狀態之電流性質。圖中顯示微小的餘電現象。若將電壓減至略小於 V_e，並增高磁場，則發生之電阻突變圖形與圖7所示者相近似。

作者等甚為感激高亦涵教授之指教。
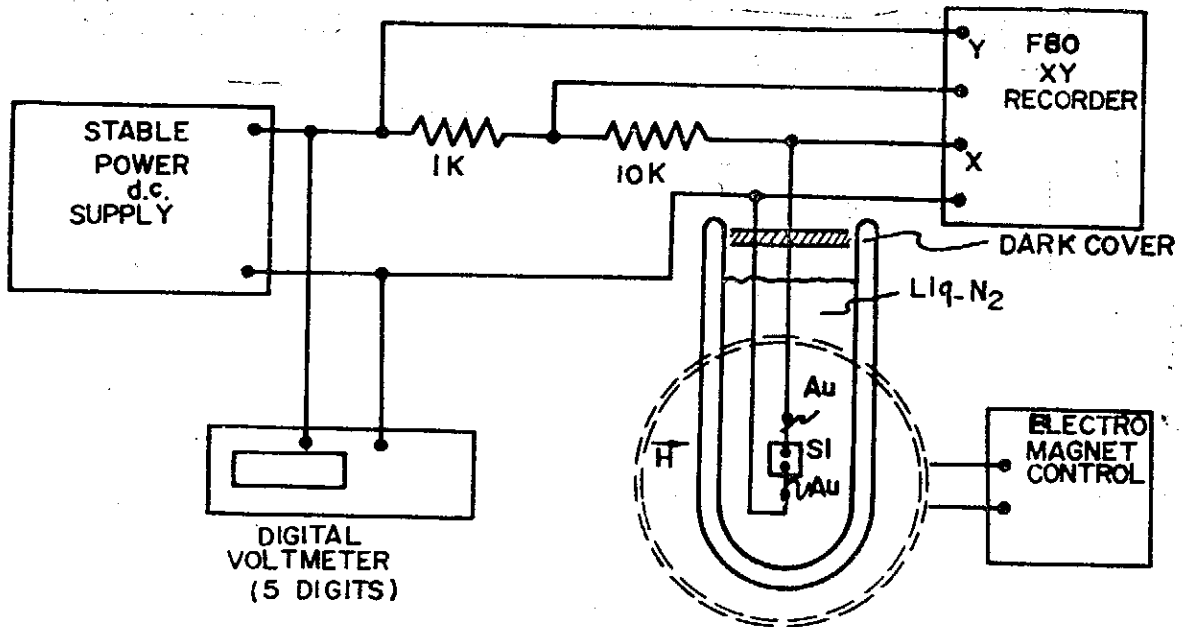
圖1　線路裝置圖。圖中安定直流電源之安定性達 0.5mV 以下。可以連續調節由 0V 至30V，電流最高可達 1A。定速率之電壓改變可由微動電動機控制，例如每秒變百分之一伏特。

(A) 0° H field   **(B) 180° H field**
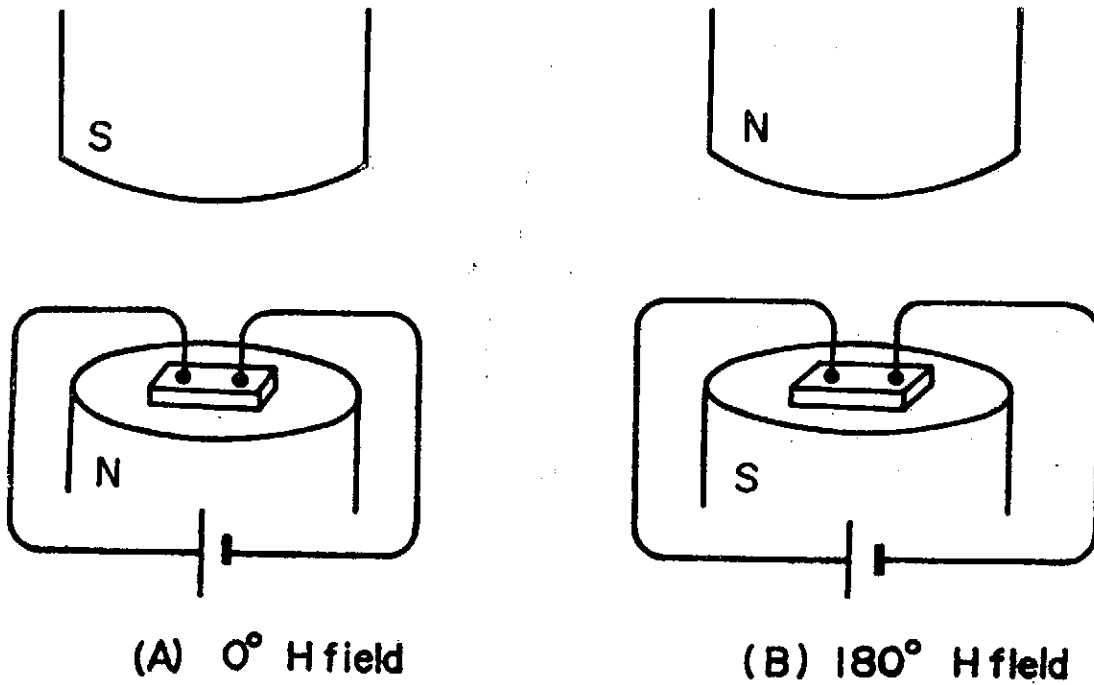
圖 2 磁場相關位置圖。僅有磁場沿一方向可以產生磁誘導之非導體導體電阻突變。反方向則不能。發生此一現象所需電壓約為 26±1 伏特，或在電場為 520 伏特每公分左右，視矽材之電阻係數高低而異。
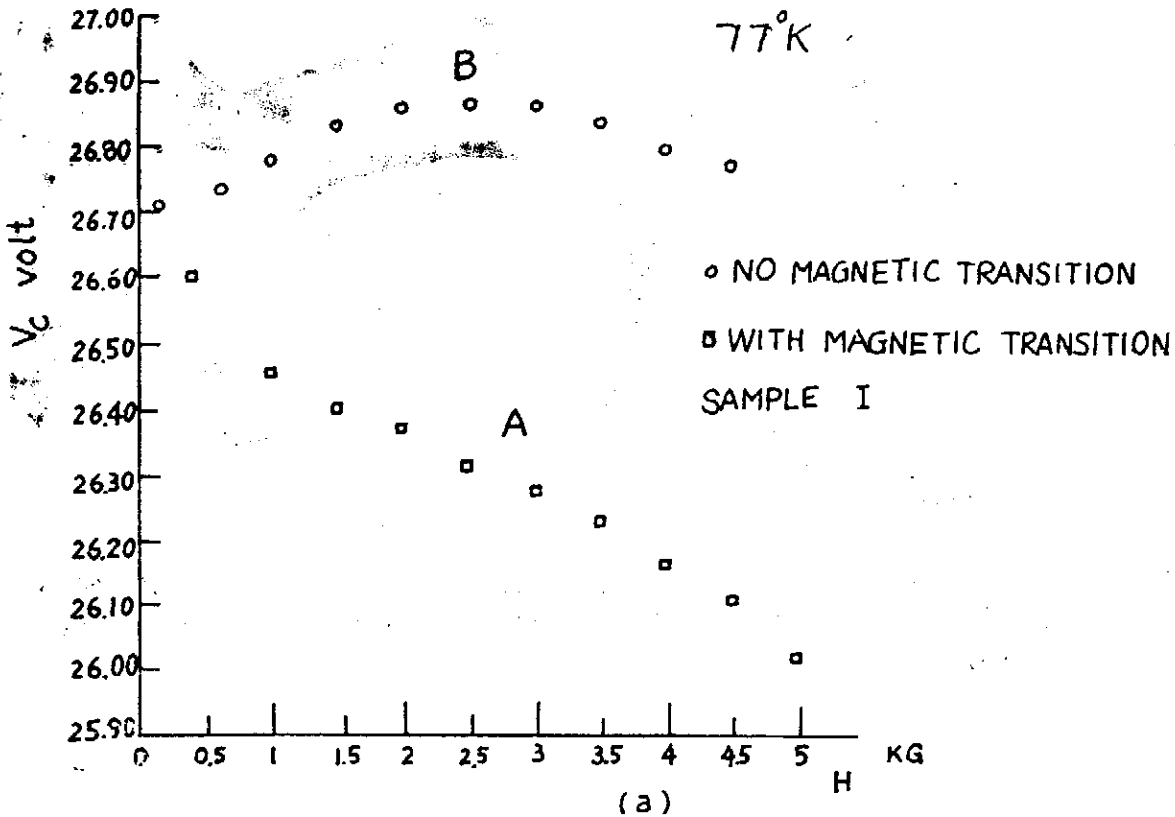
圖 3 V_e 與 H 關係曲線
（A）由有靜磁引發電阻突變之 V_e 與 H 關係，
（B）由無靜磁引發電阻突變之 V_e 與 H 關係。
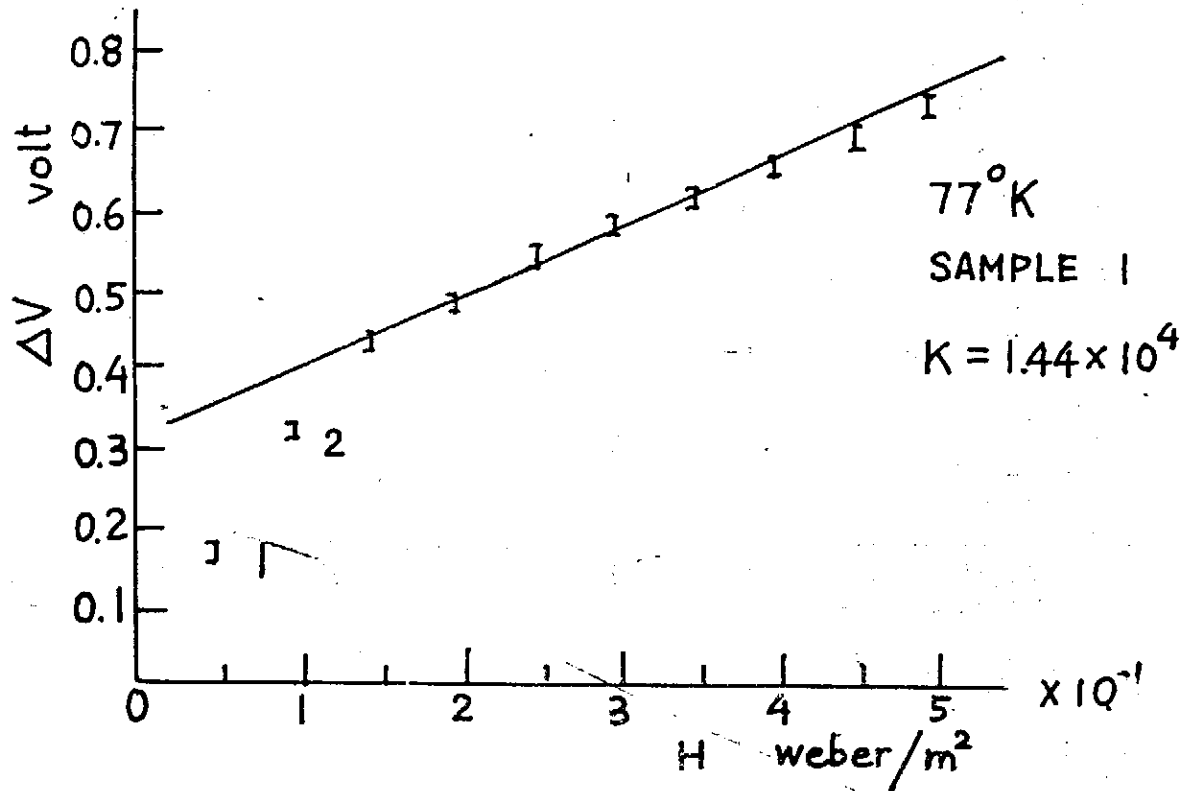
圖 4 試驗與理論比較。圖中每一試驗值均由十至十五記錄以誤差法求得。誤差如圖所示。吾人得知 $\triangle V = K'H, K'$ 為常數為試驗值。又 $K' = K\dfrac{\mu}{e} \cdot K$ 為 1.44×10^4 為試驗值，則 $K' = 0.834$。$\triangle V$ 以伏特計，H 以 weber/m² 計，e 以庫隆計，μ 以焦耳/weber/m² 計。本圖係由圖 3 中 A, B 兩曲線在同一 H 時相減而得，即 $V_B - V_A = \triangle V$。本圖中 1、2 兩點不似因誤差引起，可假設為有效磁偶之迅速增長之結果。

(a)

(b)
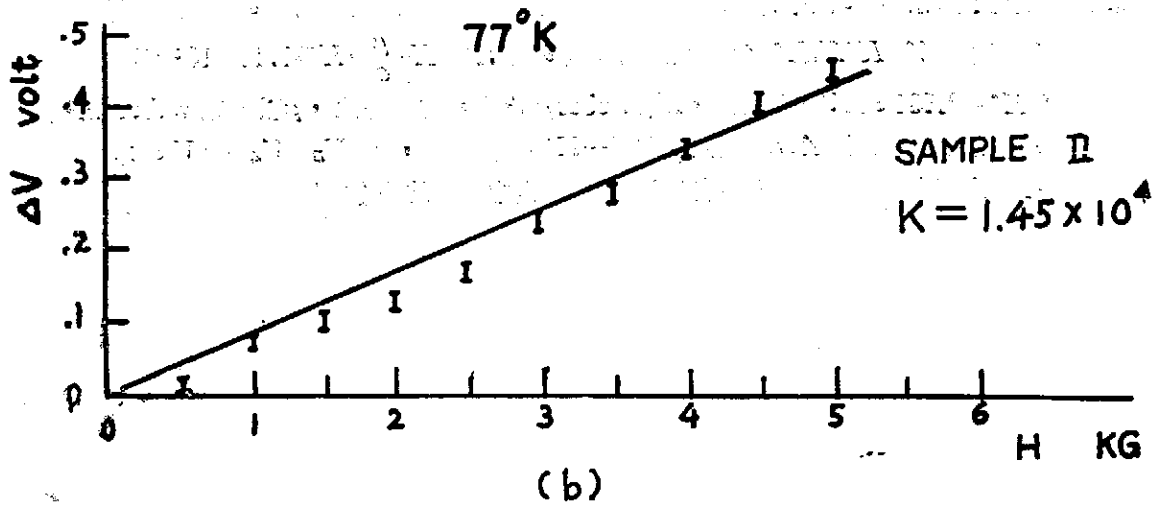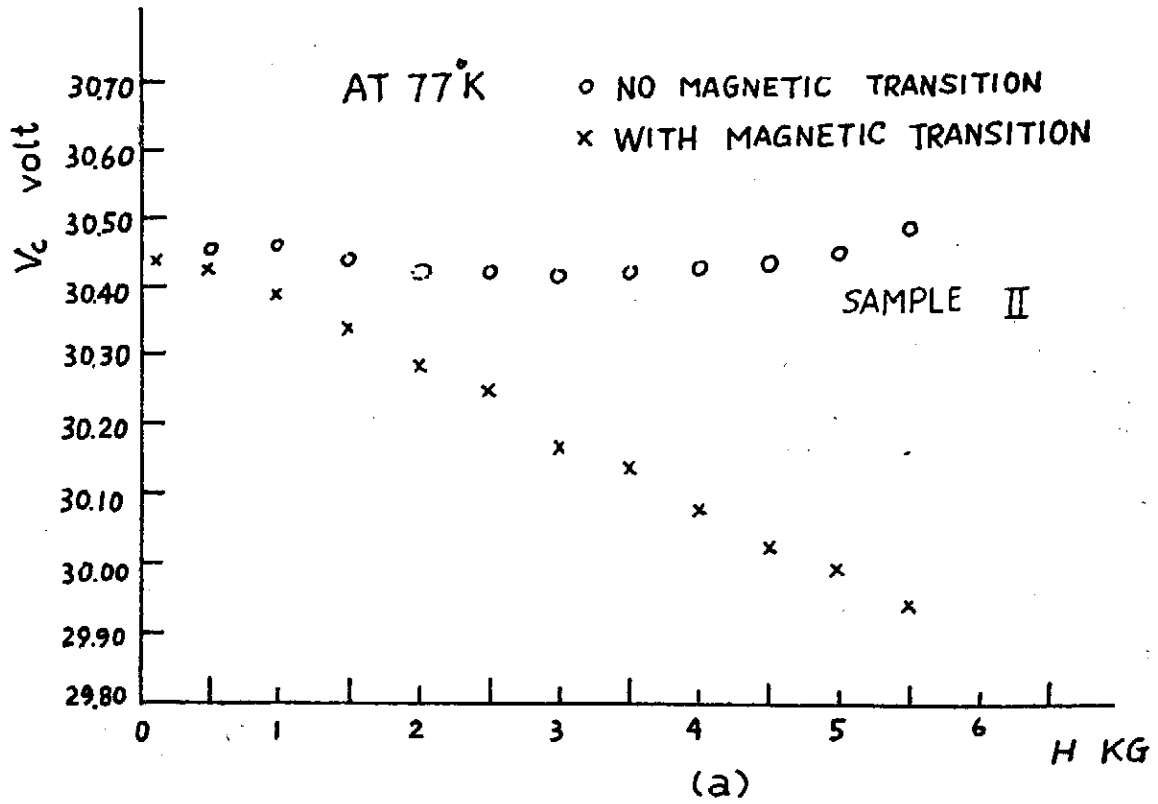
圖 5 樣品 II 之磁引發電阻突變結果
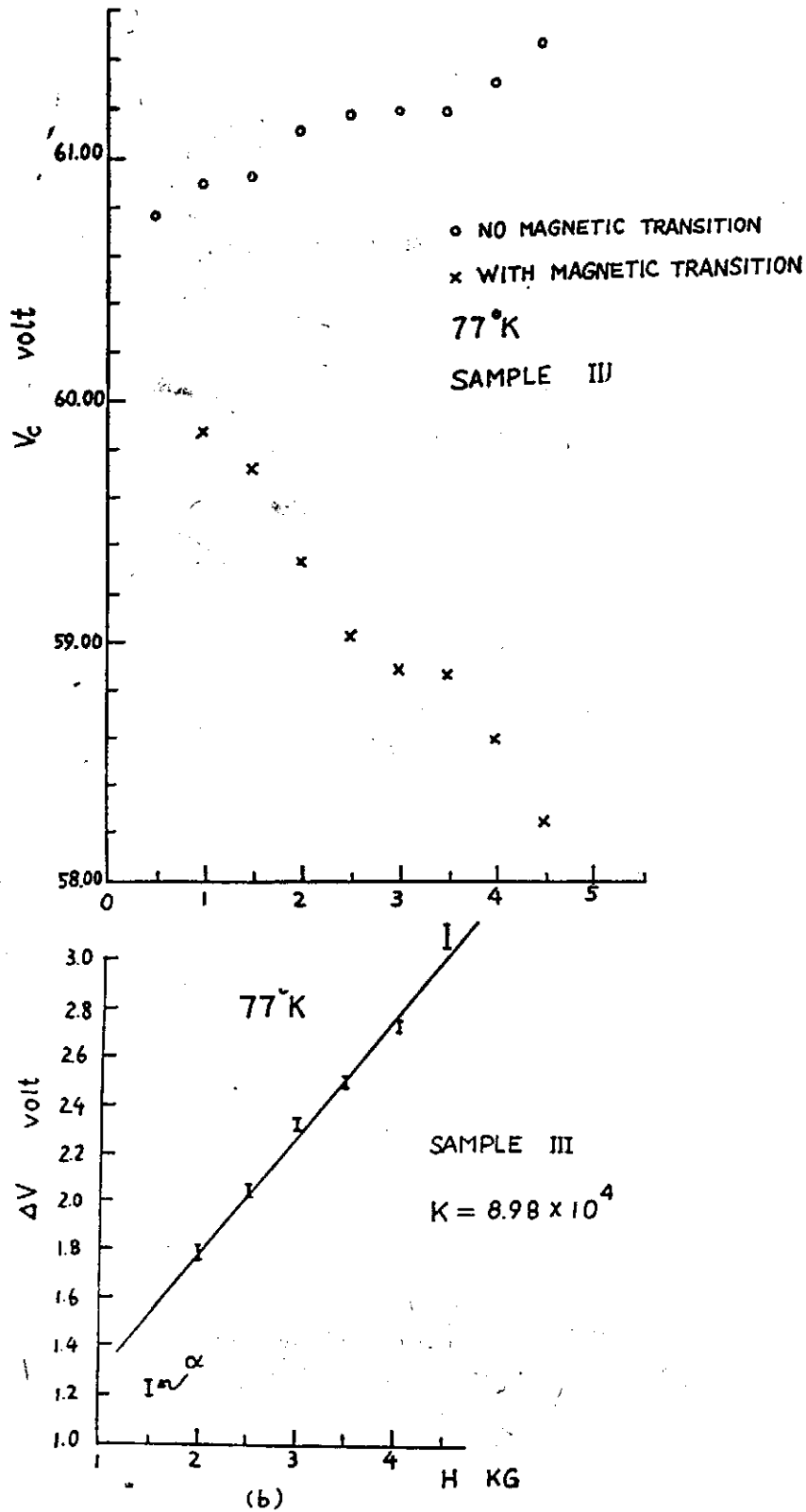
圖6　樣品 III 之磁引發電阻突變結果。

圖中 α 點再度顯示有效磁偶在接近 V_e 時迅速增加。本圖又顯示較高電阻係數之矽
，可用之有效磁偶亦較少，而 μ^*H 遠小於 eV 而K值較大。
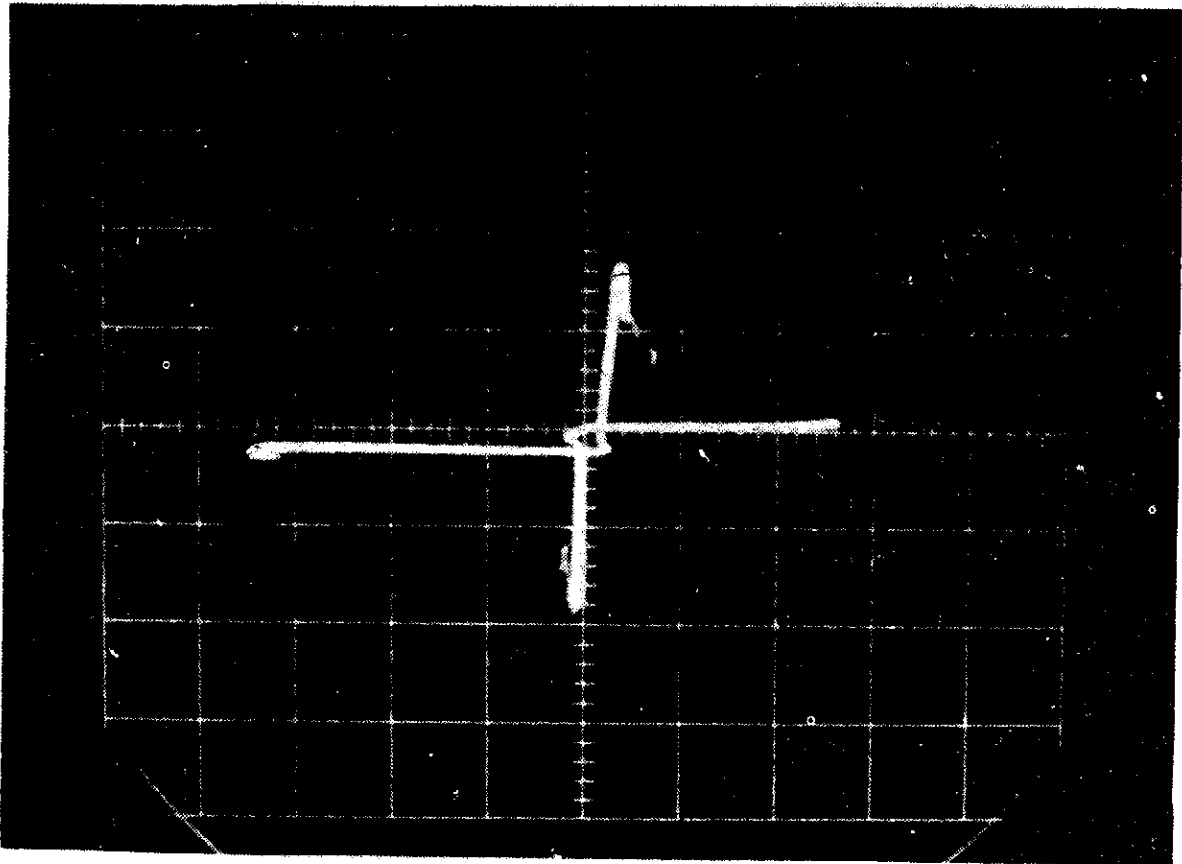
圖 ‹　非導體導體突變之性狀.外加電壓爲交流60周
,V。約爲70伏特.樣品之溫度爲恆溫77°K

Studies of Size Effects in Bi Thin Films

Chih-Chung Chen, Wu-Yi Lai,

Nai-Tsung Liang (梁乃崇) and Yu-Tung Yang (楊毓東)

Institute of Physics, Academia Sinica, Nankang, Taipei, Taiwan

The thin Bi films are made by depositing the pure Bi on mica substrates. The thickness dependence on the resistivity has been studied. The behaviors of films are severely affected by the conditions of sample preparation. By comparing with the results of other workers, our results probably are quantum oscillations at 120°K. It is interesting that the resistivity of the film exhibits a minimum at $d=100$ Å and a maximum at $d=500$Å.

Introduction

In thin metallic films it is possible to observe two kinds of size effects. The classical size effect occurs [1,2] if the thickness d of the film is comparable with the mean free path of electrons l. It leads to an increase of the resistance and to a change of the kinetic characteristics of the film when $d<l$.[2] The other is the quantum size effect (QSE) which arises when the thickness of the film becomes commensurate with the effective de Broglie wavelength λ of the electrons. In the QSE the energy spectrum in the thickness direction becomes discrete, this leads to the appearance of an oscillatory dependence of the kinetic coefficients on the thickness of the film.

In this experiment we wish to study the size effect in bismuth thin films. We also hope to see how the classical boundary scattering processes affect the properties of the film.

In our experiment, the samples were always kept in high vacuum ($\sim 10^{-6}$ torr.), and the resistance was measured by using a Keithley electometer 610B. The samples were all deposited on mica substrates at room temperature. We have attempted three different methods of sample preparations: (1) without annealing and cooling, by using those samples, we have the results as shown in Figs. 1; (2) with annealing at 373°K and then cooling down to room temperature, the results are shown in Fig. 2; and (3) with annealing at 373°K and then cooling down to 120°K, from the last method, we got Fig. 3. The results obtained from these three methods are different. It is clear that the behavior of films is severely affected by the conditions of sample preparation.

1. Classical size effect

Fig. 1A and 1B show the results of two samples. The resistivity has minimum values, one at about 600 Å and the other at 1200 Å. This agrees qualitatively with the results obtained by Chou and Yang.[10] Their samples were taken out of high vacuum for resistivity measurements while ours were not.

---

(1) K. Fuchs, *Proc. Camb. Phil. Soc.* **34**, 100(1938)

(2) E.H. Sondheimer, *Adv. Phys.* **1**, 1(1952)

(3) Yu F. Ogrin, V.N. Lutskii, M.I. Elinson, *JETP* **3**, 71(1966)
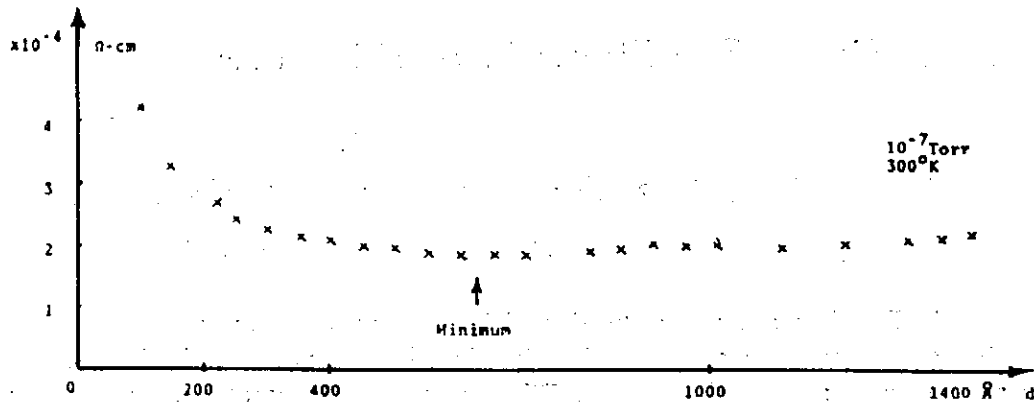
Fig. 1A *It is deposited at room temperature, without annealing and cooling.*
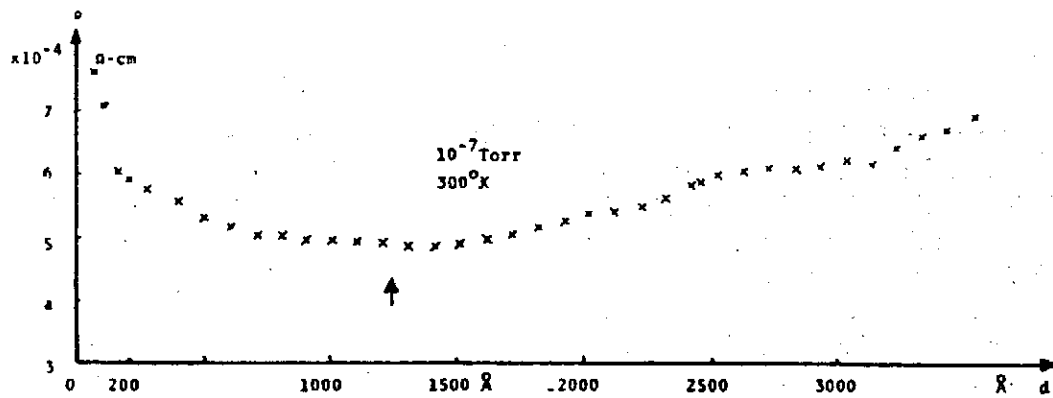
Fig. 1B. *It is deposited at room temperature, without annealing and cooling.*

In Fig. 2 the resistivity decreases monotonically with no minimum point. Similar results were also obtained by Duggal *et al*, Raj Rup[11] and by Garcia.[9] By comparison of the appearance of a resistivity minimum, we may conclude that without annealing the resistivity will show a minimum, and this minimum is more significant at lower temperature of condensation.[3]

There is one more thing we can conclude from the above results: According to Funchs' analysis on classical size effect,[1] the resistivity increase significantly when the film thickness becomes smaller than the mean free path of the carriers. Hence from Fig. 1A we obtained the mean free path $l \doteq 500$ Å and from Fig. 1B, $l \doteq 1000$ Å. Also, in Fig. 2 we have $l \doteq 1000$ Å. Those values are to be compared with the values for bulk sample, i.e., $l \doteq 1$mm at 4.2°K and $l \doteq 10000$ Å at room temperature. In a thin film the effective mean free path is less than that in a bulk sample. Assuming $\dfrac{l(\text{bulk})}{l(\text{film})} = \dfrac{\rho(\text{film})}{\rho(\text{bulk})}$, our l's are consistent with the typical value ρ (bulk) $= 1.2 \times 10^{-4} \Omega$-cm.

In Fig. 3, the resistivity appears to have a minimum at about $d \doteq 100$ Å and a maximum at $d \doteq 500$ Å. Beyond this interesting region, where the resistivity thickness relationship has not been investigated before, the resistivity decreases with small oscillations. We had repeated the experiments, and found the results quite the same. Also, the curves are quite similar for different temperatures in our thickness range. Similar results were obtained by
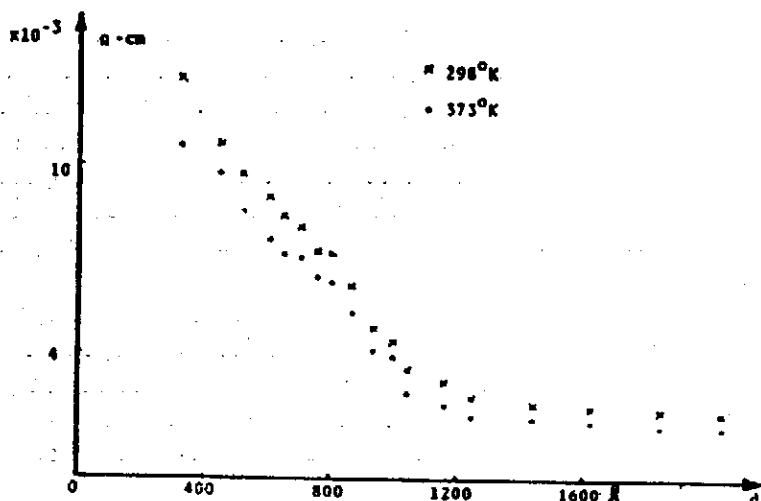
Fig. 2. *It is deposited at room temp., with annealing at* $373°K$.

Garica at $12°K$. It was considered as an intrinsic property of Bi thin films. However, the main difference is that the minimum and maximum were observable at rather high temperatures in our work.
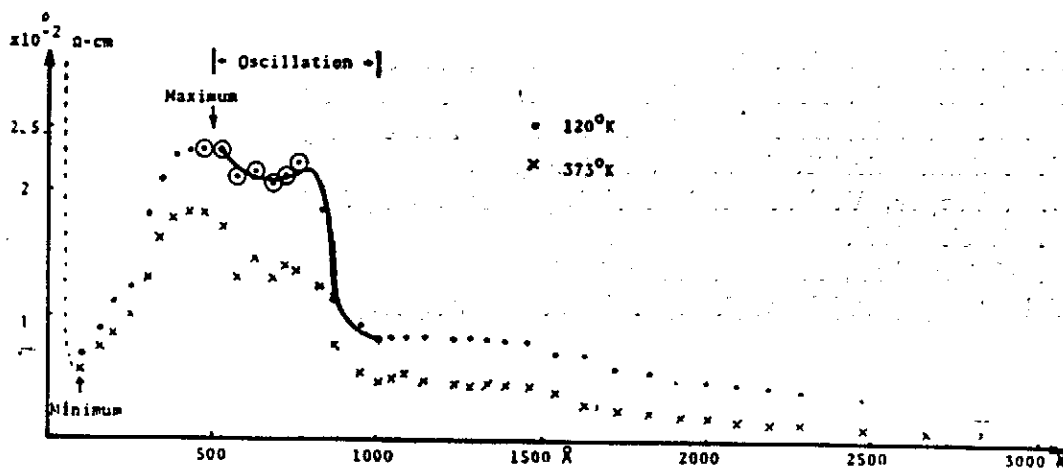
Fig. 3. *It is deposited at room temperature, with annealing at* $373°K$ *and then cooling*

2. Quantum size effect

The QSE has been investigated, both experimentally and theoretically. [2-9] Observation of this effect for electrons and holes in bismuth polycrystalline films was first made by Ogrin et al,[3] Kommik et al.[4] The same effect was also found in some metals other than bismuth, such as antimony[5] and tin[6].

The experimental evidence of the oscillatory dependence on the thickness below $12°K$ has been identified by many workers. However above this temperature the QSE has never been ascertained. [4,5,6,9] We tried to observe QSE, at $77°K$ and at room temperature. Contributing to the appearance of the size effect in non-singlecrystal films of bismuth is the

fact that the structure of bismuth has axial symmetry relative to the trigonal axis. Thus, in all the crystallites, the orientation of the trigonal axis along the normal to the surface of the film is the necessary condition for the appearance of resistivity oscillation.

In Fig. 3, the circles represent maximum experimental errors, we see that there are small oscillations of the resistivity from 500Å to 1200Å. The results of quantum oscillation[4] reported by Komnik et al similar to ours but their results were obtained at 4.2°K, while ours were obtained at 120°K. By this comparison, we may tentatively attribute them to quantum oscillations.

All the films prepared by using these three different methods (Fig. 1,2,3) show a common feature, that is, there is an abrupt decrease of the resistivity as large as 6 order of magnitude at $d \doteq 100$ Å. For comparison, we note the similar behavior was found in gold films but with a much broader range of resistivity change. We also found that annealing at elevated temperatures followed by cooling at low temperatures will tend to make this abrupt change in resistivity more pronounced.

鉍薄膜之體形效應

在眞空裡加熱蒸發純的鉍，使鉍的蒸氣附着於雲母片上，由此方法可製得鉍的薄膜，厚度與薄膜的電阻關係是我們研究的項目，薄膜的性質深受製薄膜時的條件影響（如雲母片的溫度等），我們的結果與其他工作者結果比較後，我們發現在120°K 可能有量子體形效應的存在，另外薄膜的電阻係數在厚度爲 100Å 時有一個極小值在 500Å 時有一個極大值。

(4) Yu. F. Komnik, E.I. Bukhshtab, *JETP* 27, 34(1968)
(5) Yu. F. Komnik, E.I. Bukhshtab, *JETP Lett.* 6, 58(1967)
(6) Yu. F. Komnik, E.I. Bukhshab, *JEPF Lett.* 8, 4(1968)
(7) V.B. Satndomirskii, *JETP* 25, 101(1967)
(8) B.A. Tavger, V. Ya. Demikhovskii, *JETP* 5, 469(1968)
(9) N. Garcia, *Private communication*
(10) Hue-Ming Chou, *Private communication*
(11) V.P. Dugga, Raj Rup, *J. App. Phys.* 40, 492(1969)

The Motion of Vortex Ring in the Presence of a Rigid Sphere

渦環流過剛球的流場分析

Huai-chu Wang (王懷柱)

New York University, New York and Academia Sinica, Taipei

(Received April, 1971)

Abstract 摘要

　　將渦流方程式中以與渦量雷諾數有關的小參量漸近展開所得之解用以渦環流過剛球的流場分析。並按無粘性流動理論分析之。從比較可以看出，若渦量的起始分佈相同，則由於渦量擴散的緣故，在以後的過程中，兩者的結果互有差異。

Solutions of the equation of vorticity constructed as an asymptotic expansion in terms of a small parameter related to the Reynolds number of the vortex are used to analyse the motion of the vortex ring over a rigid sphere. The solution of this analysis is identified with that of a classical inviscid theory with the same initial vorticity distribution for the initial instant. They disagree afterwards because the inviscid theory ignores the diffusion of the vorticity in the core.

1. Introduction

The classical inviscid model of a vortex line moving in an inviscid flow has been employed frequently for the explanation of many fluid dynamics phenomena.[1] Since a real fluid is viscous, the inviscid solutions should be identified as special limiting solutions of the viscous theory and the informations which are either missing or incorrectly provided by the inviscid theory will then be accounted for by the viscous theory.

It is known the inviscid theory yields a flow field with infinite velocity along the vortex line. So the inviscid theory is inadequate to describe the motion of a circular vortex ring or of a curved vortex line. Furthermore, the infinite velocity at the center of the vortex core is not physically realistic. The large velocity will be accompanied by a large velocity gradient. In the neighborhood of the vortex line, i.e., in the vortical core, the viscous force is no longer small as compared to the inertia term and should therefore be included to describe the actual flow in the same manner as in the boundery layer analysis [2,3].

In the present paper the analyses of the motion of vortex ring are briefly reviewed and the results are applied to the analysis of the motion of a vortex ring over a rigid sphere in the following sections.

2. Outer and Inner Solutions

The Naver-Stokes equations for incompressible flow in terms of the stream function ψ and vorticity ζ are

$$\frac{d\zeta}{dt} = \nu \triangle \zeta \tag{1}$$

$$\triangle \psi = -\zeta \tag{2}$$

where $\triangle$ is the Laplacian operator. By use of the boundary layer technique[2,3], the radial distance to the center of the vortex is streched by a factor $\frac{1}{\epsilon}$ which is the square root of

the reference Reynolds number, $Re = |\Gamma'|/\nu$, where ν is the kimematic viscosity and Γ' is the strength of the vortex ring. The solutions for the inner viscous core are expanded:

$$\bar{\psi}(\bar{r},t,\theta,\epsilon) = \bar{\psi}^{(0)}(\bar{r},t) + \epsilon\bar{\psi}^{(1)}(\bar{r},t,\theta) + \cdots\cdots \tag{3}$$

$$\bar{\zeta}(\bar{r},t,\theta,\epsilon) = -[(\bar{\psi}_R/R)_R + \bar{\psi}_{ZZ}]/R$$
$$= \epsilon^{-2}[\bar{\zeta}^{(0)}(\bar{r},t) + \epsilon\bar{\zeta}^{(1)}(\bar{r},t,\theta) + \cdots\cdots] \tag{4}$$

and matched with the solutions of the outer inviscid region which are expanded as:

$$\psi(r,t,\theta,\epsilon) = \psi^{(0)}(r,t,\theta) + \epsilon\psi^{(1)}(r,t,\theta) + \cdots\cdots \tag{5}$$
$$\zeta(r,t,\theta,\epsilon) = \zeta^{(0)}(r,t,\theta) + \epsilon\zeta^{(1)}(r,t,\theta) + \cdots\cdots \tag{6}$$

Two different length scales r and $\bar{r}$ are introduced for the "inner" and "outer" regions, the radius coordinate in the inner region is streched from r to $\bar{r}$ with $\bar{r} = r/\epsilon$.

The viscous effect is limited to the neighborhood of the circular vortex ring. In the er region where the shortest distance r to the vortex ring is not too small as compared with the radius R_0 of the ring, the classical inviscid solution should be valid.

For each region the power series in ϵ are sustituted into (1) and (2) in toroidal coordinates:

$$\frac{\partial\zeta}{\partial t} + u\frac{\partial\zeta}{\partial r} + \frac{v}{r}\frac{\partial\zeta}{\partial\theta} - \frac{w_1\zeta}{\rho} = \nu[\triangle_1\zeta + \frac{1}{\rho}(\cos\theta\frac{\partial\zeta}{\partial r} - \frac{\sin\theta}{r}\frac{\partial\zeta}{\partial\theta}) - \frac{\zeta}{\rho^2}] \tag{7}$$

where
$$\triangle_1 = \frac{\partial^2}{\partial r^2} + \frac{1}{r}\frac{\partial}{\partial r} + \frac{1}{r^2}\frac{\partial^2}{\partial\theta^2}$$

$$\rho = R_0(t) - r\cos\theta$$
$$z = Z_0(t) + r\sin\theta$$

and
$$\zeta = \rho^{-1}\triangle_1\psi - \rho^{-2}[\cos\theta\frac{\partial\psi}{\partial r} - \sin\theta\; r^{-1}\frac{\partial\psi}{\partial\theta}] \tag{8}$$
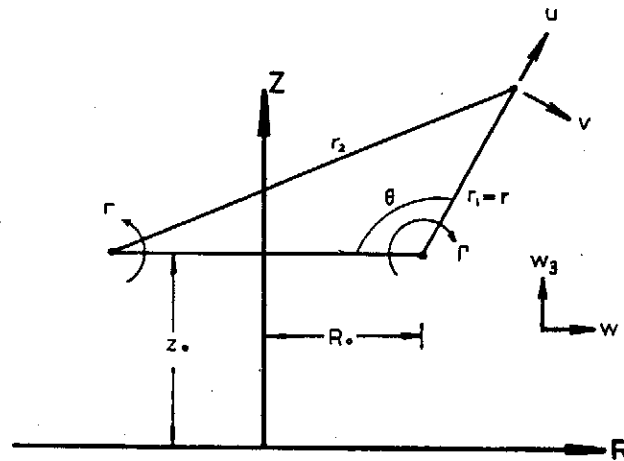
Fig. 1: *Circular vortex ring in axially symmetric stream.*

The flow in the outer region is always a potential flow to any order of approximation if the flow field is initially irrotational, i.e.,

$$\triangle\psi^{(n)} = 0$$
$$\zeta^{(n)} = 0$$

The leading term of the stream function for the outer region is written in terms of toroidal coordinates (r,θ) as

$$\psi^{(0)}(r,\theta) = \psi^*(r,\theta) + \psi_1(r,\theta) \tag{9}$$

where $\psi^*(r,\theta)$ represents an axially symmetric potential flow without the vortex ring and $\psi_1(r,\theta)$ represents the flow due to vortex ring alone defined by[4]

$$\psi_1(r,\theta) = -\frac{\Gamma'}{2\pi}(r_1 + r_2)\left[K\left(\frac{r_2 - r_1}{r_2 + r_1}\right) + E\left(\frac{r_2 - r_1}{r_2 + r_1}\right)\right] \tag{10}$$

K and E are the complete elliptical integrals of the first and second kind respectively.

For the inner solution the governing equations for the leading asymmetric part $\bar{\Psi}^{(1)}$ $(t,\bar{r},\theta)$ in $\bar{\phi}^{(1)}$ $(t,\bar{r},\theta)$ and leading symmetric part $\bar{\phi}^{(0)}$ $(t,\bar{r})$ are

$$\bar{\zeta}_{\bar{r}}^{(0)}\bar{\phi}_{\theta}^{(0)} - \bar{\phi}_{\bar{r}}^{(0)}\bar{\zeta}_{\theta}^{(1)} = [\bar{r}\bar{\zeta}^{(0)}/R_0]\bar{\phi}_{\bar{r}}^{(0)}\sin\theta \tag{11}$$

$$\bar{\zeta}_t^{(0)} - \Gamma'(\bar{r}\bar{\zeta}_{\bar{r}}^{(0)})_{\bar{r}}/\bar{r} = (\dot{R_0}/R_0)(\bar{r}^2\bar{\zeta}^{(0)})_{\bar{r}}/(2\bar{r}) \tag{12}$$

The boundary conditions at $\bar{r}=0$ are

$$\bar{\phi}_{\bar{r}}^{(0)}(t, \bar{r})=0, \qquad \bar{\zeta}^{(0)}(t, \bar{r})=\text{finite} \tag{13}$$

$$\bar{\Psi}_{\bar{r}}^{(1)}(t, \bar{r},\theta)=0, \qquad \bar{\Psi}_{\theta}^{(1)}(t,\bar{r},\theta)/\bar{r}=0 \tag{14}$$

The condition of matching with the outer solution as $\bar{r}\to\infty$ and $r\to0$ yields:

$$\bar{v}^{(0)}=-\bar{\phi}_{\bar{r}}^{(0)}/R_0 \to \Gamma/(2\pi\bar{r}) \tag{15}$$

$$\bar{\Psi}^{(1)}(t,\bar{r},\theta) \to \Gamma'/(4\pi)\bar{r}\cos\theta[\ln(8R/r)-1]+R_0\bar{r}[-(w_1{}^*-\dot{R_0})\sin\theta+(w_3{}^*-\dot{Z})\cos\theta] \tag{16}$$

where $w_1{}^*$ and $w_3{}^*$ are the velocity components along R and Z axes evaluated at (R_0,Z_0) without the contribution of the vortex ring.

The asymmetric part $\bar{\Psi}^{(1)}$ $(t,\bar{r},\theta)$ can be resolved into Fourier components with coefficients $\bar{\Psi}_{j1}^{(1)}$ $(\bar{r},t)$ for $\cos j\theta$ and $\bar{\Psi}_{j2}^{(1)}$ $(\bar{r},t)$ for $\sin j\theta$ and reduced to:

$$\frac{\partial \bar{\Psi}_{11}}{\partial \bar{r}^2}+\frac{1}{\bar{r}}\frac{\partial \bar{\Psi}_{11}^{(1)}}{\partial \bar{r}}-\left\{\frac{1}{\bar{r}^2}-\frac{R_0\bar{\zeta}_{\bar{r}}^{(0)}}{\bar{\phi}_{\bar{r}}^{(0)}}\right\}\bar{\Psi}_{11}^{(1)} = -2\bar{r}\bar{\zeta}^{(0)}-\bar{v}^{(0)} \tag{17}$$

for $j=1$. The boundary condition of $u=v=0$ at $\bar{r}=0$ yields the following conditions for $\bar{\phi}_{jk}^{(1)}$ as $\bar{r}\to0$

$$\bar{\Psi}_{12}^{(1)}=0 \tag{18}$$

$$\bar{\Psi}_{jk}^{(1)}=0 \qquad k=1,2, \qquad j=2,3,4\cdots\cdots \tag{19}$$

The behavior of $\bar{v}^{(0)}$ as $\bar{r}\to\infty$ is

$$\bar{v}^{(0)}=\frac{\Gamma'}{2\pi\bar{r}} \tag{20}$$

Consequently, the asymptotic behavior of $\bar{\Psi}_{11}^{(1)}$ as $\bar{r}\to\infty$ can be given

$$\bar{\Psi}_{11}^{(1)}(t,\bar{r}) \to -\frac{\Gamma}{4\pi}\left\{\bar{r}\ln\bar{r}+C_1(t,\bar{r})+\frac{C_2(t)}{\bar{r}}+0(\bar{r}^{-1})\right\} \tag{21}$$

Coefficients $C_1(t)$ and $C_2(t)$ will be related to the boundary condition at $\bar{r}=0$ after the determination of the vorticity distribution $\bar{\zeta}^{(0)}$. From eq. (18) the matching condition of eq. (15) yields

$$\dot{R_0}(t)=w_1{}^*(t,R_0,Z_0) \tag{22}$$

And the axial velocity is given by

$$\dot{Z}_0(t) = w_3{}^*(t, R_0, Z_0) + \Gamma'(4\pi R_0)^{-1}\left\{\ln\left[\frac{8R}{\epsilon} - 1 + C_1(t)\right]\right\} \tag{23}$$

Equation (17) is an ordinary differential equation in $\bar{r}$ for $\bar{\Psi}_{11}^{(1)}(t, \bar{r})$ with t appearing as a parameter, therefore, for each prescribed vorticity distribution at each instant $\bar{\Psi}_{11}^{(1)}$ can be determined.

3. Motion of the Vortex Ring over Rigid Sphere

If the initial vorticity distribution is that of a rotating disk of radius δ_0, the $\bar{\zeta}^{(0)}$ and $\bar{v}^{(0)}$ distribution at the instant $t = t_0$ is

$$\bar{\zeta}^{(0)} = 2\Omega, \qquad \bar{v}^{(0)} = \Omega\bar{r} \qquad \text{for } \bar{r} < \bar{\delta}_0 \tag{24}$$

$$\bar{\zeta}^{(0)} = 0, \qquad \bar{v}^{(0)} = \frac{\Gamma'}{2\pi\bar{r}} \qquad \text{for } \bar{r} > \bar{\delta}_0 \tag{25}$$

where $\Omega = \Gamma'/(2\pi\delta_0{}^2)$ and $\bar{\delta}_0 = \delta_0/\epsilon$. The solution of equation (17) with the boundary condition at $\bar{r} = 0$ is

$$\bar{\Psi}_{11}^{(1)}(t_0, \bar{r}) = -(5/8)\bar{r}^2\Omega \quad \text{for } 0 \leq \bar{r} \leq \bar{\delta} \tag{26}$$

$$\bar{\Psi}_{11}^{(1)}(t_0, \bar{r}) = -\Gamma'/(4\pi)[\bar{r}\ln\bar{r} + C_1\bar{r} + C_2\bar{r}^{-1}] \quad \text{for } \bar{r} > \bar{\delta} \tag{27}$$

The continuity of $\bar{\Psi}_{11}^{(1)}$ and the jump condition of $\bar{\Psi}_{11,\bar{r}}^{(1)}$ at $\bar{r} = \bar{\delta}$ give

$$C_1(t_0) = \ln\bar{\delta} - \frac{3}{4}$$

$$C_2(t_0) = \frac{1}{2}\bar{\delta}^2$$

Therefore the axial velocity (23) at $t = t_0$ becomes

$$\dot{Z}(t_0) = w_3{}^*(t, R_0, Z_0) + \frac{\Gamma'}{4\pi R_0}\left[\ln\frac{8R}{\delta_0} - \frac{1}{4}\right] \tag{28}$$

Due to the diffusion of vorticity distribution of (12), eqs. (24), (25) and (28) will not be valid for $t > t_0$. A similar solution of eq. (12) can be constructed by change of variable t to τ, with t denoting the life time of the line vortex

$$\tau = \int_0^t R_0(t')dt' / R_0(t) \tag{29}$$

$\bar{\Psi}_{11}^{(1)}(t, \bar{r})$ can thus also be represented by similar solution

$$\bar{\Psi}_{11}^{(1)}(t, \bar{r}) = -(\Gamma'^{3/2}\tau^{1/2}/\pi)f(\eta) \tag{30}$$

The asymptotic behavior of $f(\eta)$ for large η is

$$f(\eta) \to \frac{1}{2}[\eta\ln\eta + 0.442\eta + 1.294\eta^{-1} + 0(\eta^{-1})] \tag{31}$$

By comparison the eq. (23) becomes

$$\dot{Z}_0(t) = w_3{}^*(t, R_0, Z_0) + \Gamma'(4\pi R_0)^{-1}[\ln(8R/\sqrt{4\nu\tau}) - 0.558] \tag{32}$$

Now we can thus analize the motion of the vortex ring over a rigid sphere. By the

method of images[4], the vortex ring is equivalent to a spherical sheet of double-sources of uniform density, concentric with the fixed sphere. The image of this sheet will be another uniform concentric double-sheet, which is, again, equivalent to a vortex ring coaxal with the first. It was found that the circulations (I', I'') are related to the radii (R_0, R_0') of the vortex ring and its image by

$$I'R_0^{-\frac{1}{2}} + I''R_0'^{-\frac{1}{2}} = 0 \tag{33}$$

Therefore at the point (Z_0, R_0) the stream function induced by the image vortex ring is
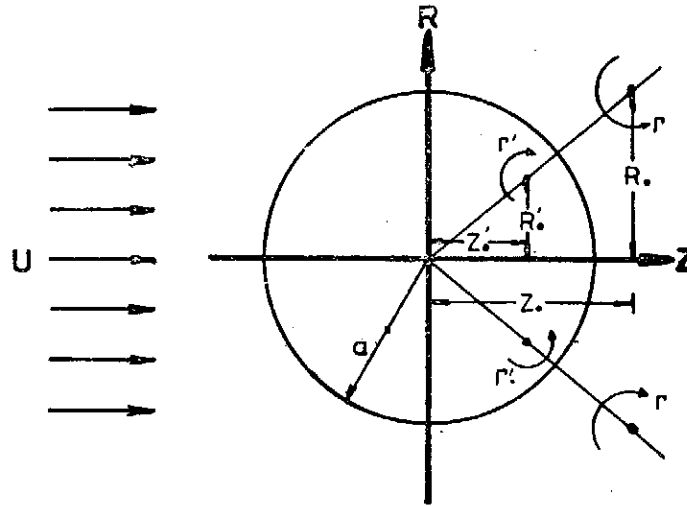
Fig. 2: *The motion of a circular vortex ring in unifom stream and rigid sphere*

$$\psi' = -\frac{I''}{2\pi}(r_1^* + r_2^*)\left[F\left(\frac{r_2^* - r_1^*}{r_2^* + r_1^*}\right) - E\left(\frac{r_2^* - r_1^*}{r_2^* + r_1^*}\right) \right] \tag{34}$$

where
$$I'' = -\frac{\sqrt{R_0^2 + Z_0^2}}{a} I'$$

$$r_1^* = \sqrt{(R_0 - R'_0)^2 + (Z_0 - Z_0')^2}$$

$$r_2^* = \sqrt{(R_0 + R_0')^2 + (Z_0 - Z_0')^2}$$

with a the radius of the sphere.

From the linear combination of the stream functions of a uniform flow, doublet and image

$$\psi(Z_0, R_0) = \psi^*(R_0, Z_0) + \psi'(R_0, Z_0)$$

$$= \frac{1}{2} U R_0^2 \left[1 - \frac{a^3}{(Z_0^2 + R_0^2)^{3/2}} \right] + \psi'(Z_0, R_0) \tag{35}$$

the velocity components along R and Z axes w_1^* and w_3^* are thus calculated by

$$w_1^* = \frac{\partial \psi^*}{\partial Z_0}, \qquad w_3^* = -\frac{1}{R_0} \frac{\partial \psi^*}{\partial R_0} \tag{36}$$

respectively. By substituting (36) into (22) and (28) or (32) we found the trajectories of the vortex ring moving over a rigid sphere in a uniform stream. The Reynolds number Ua/ν is 6.25×10^4. The strength of the vortex ring I' is chosen to be $\frac{Ua}{2}$. The initial condtion at $t = 0$ are

$$Z_0(0) = -10a$$

$$\zeta_0(0) = \Gamma(\pi\delta_0{}^2)^{-1}[\exp-(r/\delta_0)^2]$$

Calculations have been carried out for $\delta_0/a = 10^{-2}, 10^{-3}$ and $R_0(0)/a = 0.5$, 1.

For the viscous theory, the relationship between ζ and t requires the knowledge of the ring since its creation, which is expressed by eq. (29) with $\tau(0) = \delta_0{}^2/4\nu$.

For the inviscid theory, R_0 is also given by eq. (22) and Z_0 is given by eq. (28) with $4\nu\tau$ replaced by $\delta^2(t)$. The relationship between δ and t is given by Helmholtz vortex theorem. From the definition of $\delta(t)$, the radius of the core, it is clear that:

$$\zeta(\delta, t)/\zeta(0, t) = e^{-1}$$

$$\int_0^\delta \zeta(r, t) 2\pi r \, dr = \Gamma(1 - e^{-1}) = \text{const.}$$

The conservation of mass then gives $2\pi R_0(t)\pi\delta^2(t) = \text{const.}$ or

$$\delta(t) = \delta_0 \, [R_0(0)/R_0(t)]^{1/2}$$

The condition fulfills eq. (12) without the diffusion term.

4. Conclusions

Fig. 3 shows the differences between the trajectories of the viscous theory and the inviscid theory. The difference are more pronounced for smaller core size. Fig. 4 shows the variation of the core size $\delta(t) = (4\nu\tau)^{1/2}$. The size in the inviscid theory does not change except during the passage over the sphere. In the viscous theory, the core radius increases due to diffusion at a higher rate for the core with smaller δ_0. The trajectories in the inviscid theory for $\delta_0/a = 10^{-2}$ and 10^{-3} are distinct due to constant differences in core size while the corresponding differences in the viscous theory are much smaller.

References

1. Rrandtl, L., *Essentials of Fluid Dynamics*. Hafner Publ. N.Y. (1952).
2. Ting, L. and Tung, C., Motion and Decay of a Vortex in a Non-uniform Stream, *Phys. Fluids* 8, pp. 1009–1051, (1965).
3. Tung, C. and Ting, L., Motion and Decay of a Vortex Ring, *Phys. Fluids*, 10, pp. 901–910, (1967).
4. Lamb, H., *Hydrodynamics*, 6th ed., Dover, N.Y. (1932).
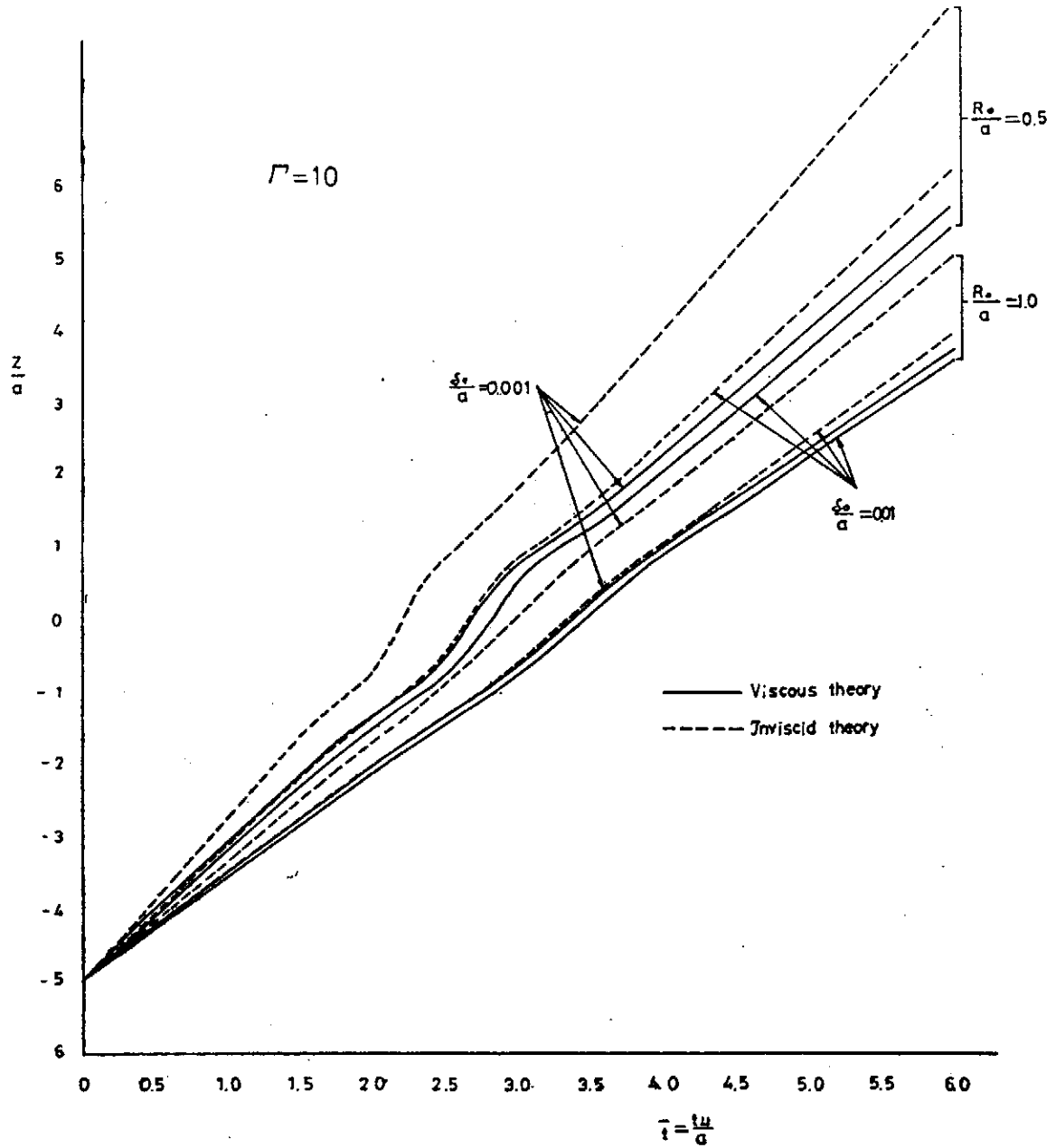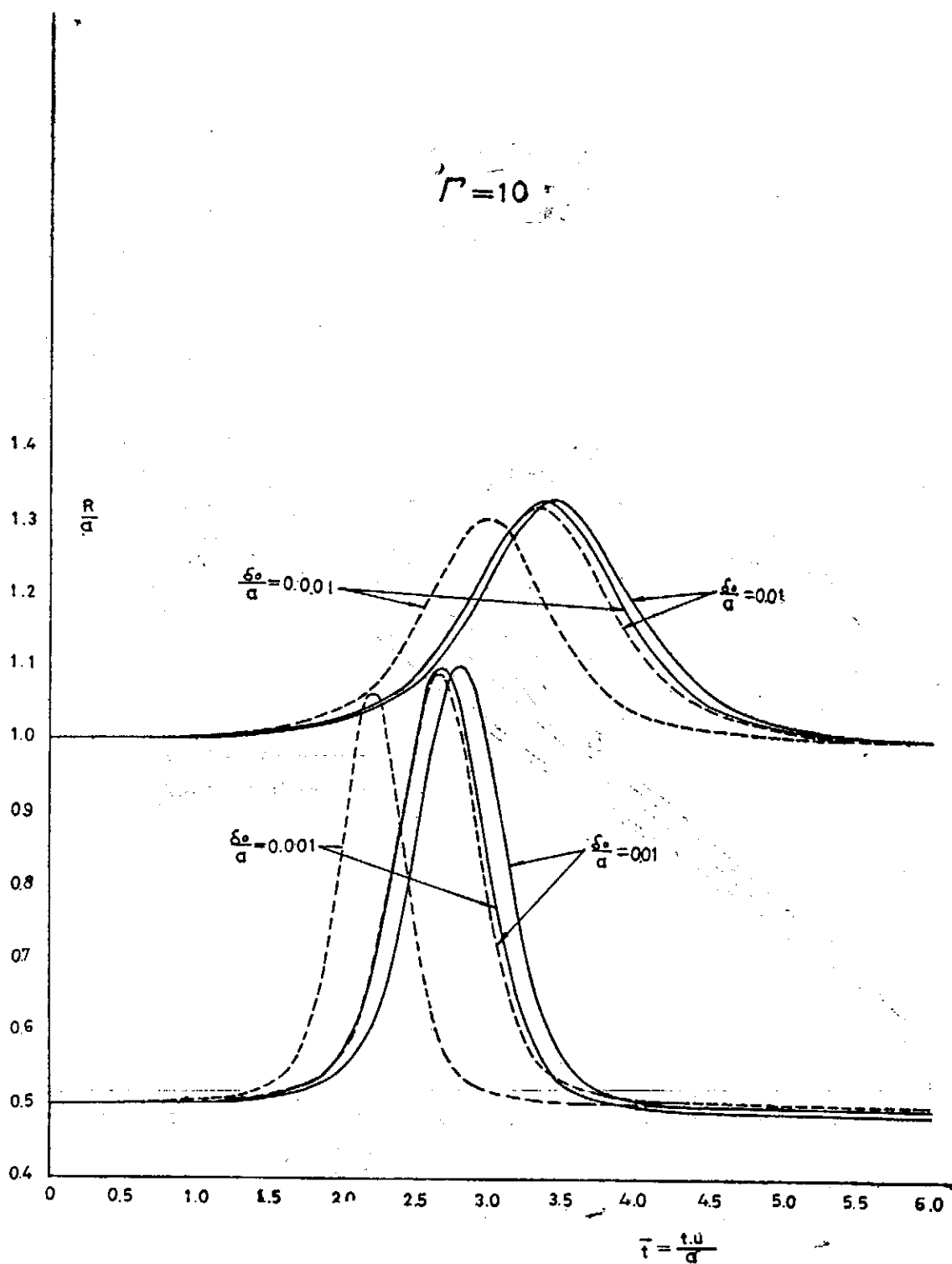
Fig. 3a: *Trajectory of Circular Vortex Ring*

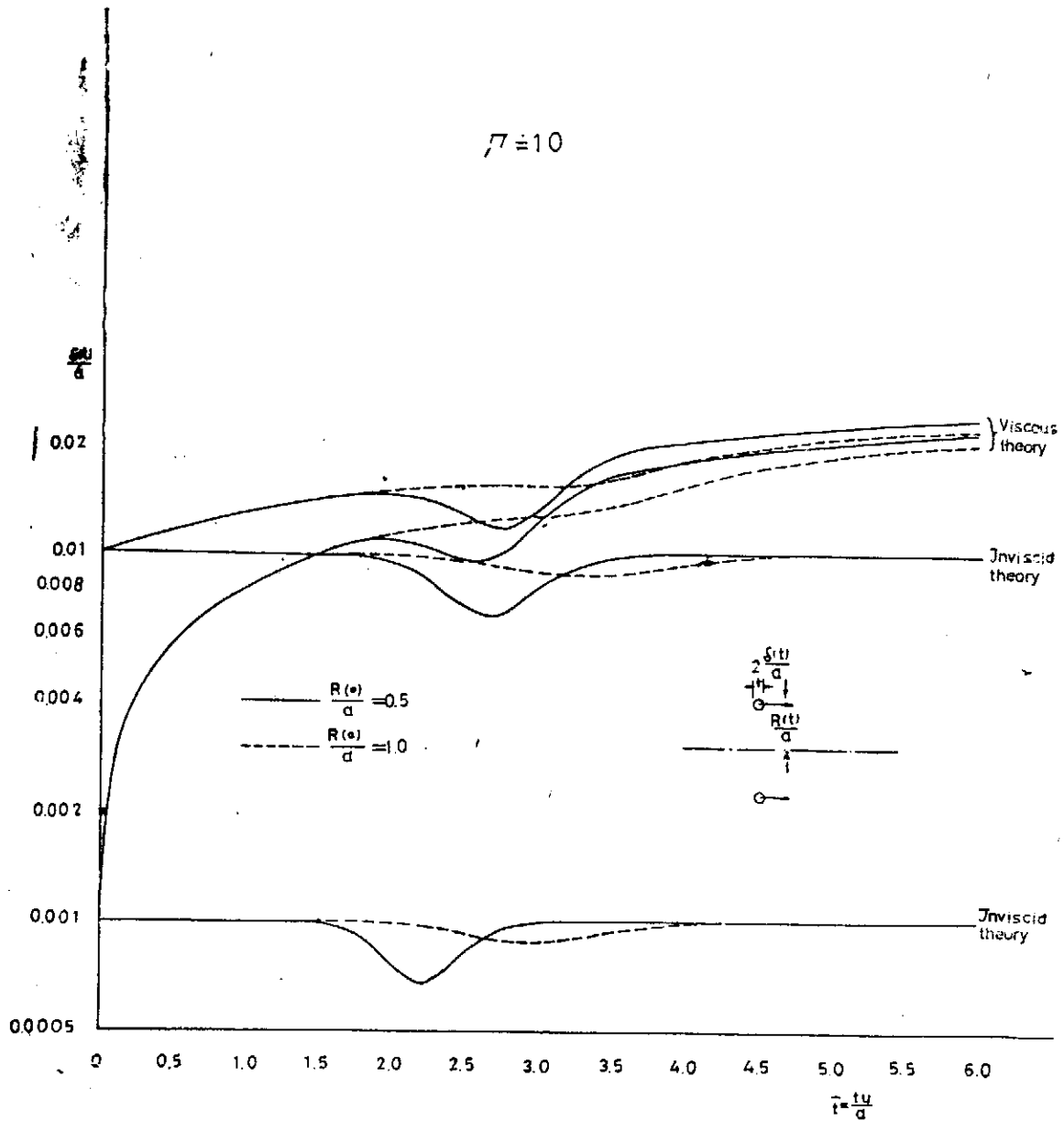Fig. 3b: *Trajectory of Circular Vortex Ring*

Fig. 4: *Variation of the core radius of vortex ring($\Gamma = 10$)*

Expressions for Standing Waves over

a Sloping Beach

by

Hsao-Hsin Chen (陳學信) and Cheng-Yu Wang (王鎮宇)

Academia Sinica and National Taiwan University
(received April 1971)

Abstract

In this paper two-dimensional problem of waves climbing a beach sloping at an angle $\pi/2n$, with n an integer, has been solved by applying Lewy's differential equation. However, different from Stoker's (1947,1955), the singularity at the shore line is assumed to be an infinite series of negative powers of the complex variable. The solution so obtained permits us to construct an incoming progressive wave, in particular, an irregular one, in infinity.

Introduction

The theoretical investigation of the problem of waves on sloping beaches has been made by many authors in the past almost ninety years. Within the scope of linearized theory of small wave amplitude, the solution, from which the progressive waves can be constructed at infinity, can not be found, unless a singular point is assumed to happen at the shore line. Although it is not clear physically what type of singularity most nearly describe the behavior of real waves, most writers, however, have restricted their treatment to the weakest possible singularity, i.e. the logarithmic one. When the beach is sloping at the angle of $\pi/2n$, with n an integer, Stoker (1947, 1965) has applied Lewy's differential equation to continue the fluid region from the sector bounded by the undisturbed water level and the bottom into the whole plane, so that a function related to velocity potential, which is analytic in the entire plane except at the shore line, is obtained. In the present work, we take the singularity at the shore line to be, instead of the weakest possible one, an infinite series of negative powers of the complex variable, and have solved this problem following mainly Stoker's scheme. Incidentally, it is not until almost two years after the present work has been done that Brillouet's (1957) paper which deals with the similar problem was found (thank Professor J.V. Wehausen for his personal copy of Brillouet paper lended to one of the present authors). On the other hand, although the principle used in the present work is same as in Brillouet's, however, it is different in detail procedure, and, thus, suggests another approach to the problem under consideration.

Mathematical Formulation

Let the fluid at rest be contained in the sector of angle $\pi/2n$, with n an integer (see Figure 1). For an inviscid irrotational flow, the velocity potential $\phi(x,y,t)$ exists as a solution of Laplace equation:

$$\nabla^2\phi(x,y,t)=0 \tag{1}$$

If we assume that the velocity potential is taken in the form

$$\phi(x,y,t)=\varphi(x,y)\exp(i\sigma t), \tag{2}$$

where $\varphi(x,y)$ is regular and analytic in the entire sector except possible the origin of

Equation (6) may also be represented in the form

$$h(z)=(\alpha_1 D)\ (\alpha_2 D)\cdots\cdots(\alpha_{2n-1}D)\ (\alpha_2 D-\nu)\cdots\cdots(\alpha_{2n}D-\nu)f(z).$$

Multiplying out the first n parentheses on the right-hand side of this equation, then, integrating it consecutively n times with respect to z, and noting $\alpha_1\alpha_3\cdots\cdots\alpha_{2n-1}=(-1)^n$, we obtain

$$(\alpha_2 D-\nu)(\alpha_4 D-\nu)\cdots\cdots(\alpha_{2n}D-\nu)f(z)=\sum_{p=1}^{\infty}\ \frac{(-1)^{n+1}ia_p}{z^n(2p-1)}.\tag{11}$$

In the process to obtain equation (11), the first $(n-1)$ integration constant must be zero due to the application of (9) successively, while the nth constant must be imaginary in order to satisfy the boundary condition (7), therefore, this constant may be neglected. Further, in equation (11) the constant ia_p is related with b_{2pn} by

$$ia_p=\frac{(-1)^{n+1}b_{2pn}}{(2pn-1)\cdots(2pn-n)},$$

with a_p real.

If one introduces

$$\beta_k=(\alpha_{2k})^{-1}=e^{i\pi(\frac{k}{n}+\frac{1}{2})},\qquad k=1,2\cdots,n,\tag{12}$$

then, $\beta_1\beta_2\cdots\beta_n=(-1)^n i$, and equation (11) may be reduced to

$$(D-\beta_1\nu)(D-\beta_2\nu)\cdots(D-\beta n\nu)f(z)=\sum_{p=1}^{\infty}\ \frac{a_p}{z^n(2p-1)},\tag{13}$$

which forms the basic differential equation for our problem.

Solution of Complex Function $f(z)$

The homogenous solution of the differential equation (13) is

$$f_H=\sum_{k=1}^{n}C_k\ \exp(\nu\beta_k z).\tag{14}$$

To obtain the particular solution f_P we express it by the following series and then verify that it satisfies all conditions, particularly the boundary conditions:

$$f_P=\sum_{p=1}^{\infty}f_p,\tag{15}$$

where f_p is assumed to be

$$f_P=\sum_{k=1}^{n}(-1)^{n(p-1)}d_{pk}\ e^{\nu\beta_k z}{}_C\int_{\infty}^{\beta_k z}\frac{e^{-\nu t}dt}{t^{2n(p-1)+1}}.\tag{16}$$

The path of integration for the complex integrals is shown in Figure 2. We note that since z lies in the sector for which $-\pi/2n\le\arg z\le0$ and the β_k is given by (12) it follows that $\beta_k z$ always lies in the left-plane.

Substituting (15) and (16) into (13) and noting that

$$(D-\nu\beta_k)\left((-1)^{n(p-1)}d_{pk}\ e^{\nu\beta_k z}{}_C\int_{\infty}^{\beta_k z}\frac{e^{-\nu t}dt}{t^{2n(p-1)+1}}\right)=\frac{d_{pk}}{z^{2n(p-1)+1}},$$

one finds

coordinate system. If we further introduce a function $f(z)$ such that

$$f(z) = \varphi(x,y) + i\psi(x,y),\tag{3}$$

with $z = x + iy$ the complex variable, then, $\varphi(x,y)$, thus the velocity potential ϕ, is completely determined through $f(z)$ satisfying the linearized boundary condition at free surface:

$$\text{Re}\left(i\frac{df}{dz} - \nu f\right) = 0, \qquad \nu = \frac{\sigma^2}{g}, \qquad x > 0, \quad y = 0,\tag{4}$$

the condition at bottom:

$$\text{Re}\left\{-i\,\exp\left(-i\,\frac{\pi}{2n}\right)\frac{df}{dz}\right\} = 0, \qquad z = r\,e^{-i\pi/2n},\tag{5}$$

with $r = \sqrt{x^2 + y^2} > 0$, and the condition at infinity where we require $\text{Re}\{f(z)\}$ and $d^k f(z)/dz^k$, $k = 1, 2, \cdots, 2n$, to be uniformly bounded. However, we allow the point at $z = 0$ to be a singular point which is not necessary a logarithmic one.

Following Stoker (1947) we introduce a function $h(z)$ which is related with Lewy's linear operators in the following form:

$$\begin{aligned}h(z) &= L(D)f(z)\\&= L_1(D)L_2(D)\cdots L_{2n}(D)f(z),\end{aligned}\tag{6}$$

where

$$L_k(D) = \begin{cases}\alpha_k\dfrac{d}{dz}, & k = \text{odd},\\[2mm]\alpha_k\dfrac{d}{dz} - \nu, & k = \text{even},\end{cases}$$

$$\alpha_k = \exp\left\{-i\pi\left(\frac{k}{2n} + \frac{1}{2}\right)\right\}, \qquad k = 1, 2\cdots, 2n,$$

and the symbol D represents d/dz.

The substitution of (6) into (4) and (5) yields respectively

$$\text{Re}\{h(z)\} = 0, \qquad x > 0, \ y = 0,\tag{7}$$

and

$$\text{Re}\{h(z)\} = 0, \qquad \text{on } z = re^{-i\pi/2n}.\tag{8}$$

At infinity $|h(z)|$ is uniformly bounded due to the definition (6) of $h(z)$ and the condition at infinity imposed for the function $f(z)$. Consequently,

$$\left|\frac{d^k h(z)}{dz^k}\right| \to 0, \qquad k = 1, 2\cdots, 2n,\tag{9}$$

along any rays not parallel to the sides of the sector when $|z| \to \infty$, as shown by Stoker. The condition (7), (8) and the bounds for $h(z)$ at infinity enable us to continue $h(z)$ analytically by reflection into the entire plane where it possesses a single-valued regular solution bounded at $|z| \to \infty$, except at $z = 0$. Thus, $h(z)$ may be represented by Laurent's expansion in the neighborhood of $z = 0$ as

$$h(z) = \sum_{s=-\infty}^{\infty} b_s (x + iy)^s.$$

In order to satisfy the conditions at free surface and at the bottom, the coefficients b_s of Laurent's expansion must be imaginaries, and $s = 2pn$, with p the integer. On the other hand, $h(z)$ must satisfy the condition at far field. Therefore,

$$h(z) = \sum_{p=-\infty}^{-1} b_{2pn}\, z^{2pn}, \qquad b_{2pn} \text{ are imaginaries.}\tag{10}$$

Equation (6) may also be represented in the form

$$h(z) = (\alpha_1 D)\ (\alpha_3 D)\cdots\cdots(\alpha_{2n-1} D)\ (\alpha_2 D - \nu)\cdots\cdots(\alpha_{2n} D - \nu)f(z).$$

Multiplying out the first n parentheses on the right-hand side of this equation, then, integrating it consecutively n times with respect to z, and noting $\alpha_1\alpha_3\cdots\cdots\alpha_{2n-1}=(-1)^n$, we obtain

$$(\alpha_2 D - \nu)(\alpha_4 D - \nu)\cdots\cdots(\alpha_{2n} D - \nu)f(z) = \sum_{p=1}^{\infty} \frac{(-1)^{n+1} i a_p}{z^{n(2p-1)}}. \tag{11}$$

In the process to obtain equation (11), the first $(n-1)$ integration constant must be zero due to the application of (9) successively, while the nth constant must be imaginary in order to satisfy the boundary condition (7), therefore, this constant may be neglected. Further, in equation (11) the constant $i a_p$ is related with b_{2pn} by

$$i a_p = \frac{(-1)^{n+1} b_{2pn}}{(2pn-1)\cdots(2pn-n)},$$

with a_p real.

If one introduces

$$\beta_k = (\alpha_{2k})^{-1} = e^{i\pi(\frac{k}{n}+\frac{1}{2})}, \qquad k=1,2\cdots,n, \tag{12}$$

then, $\beta_1\beta_2\cdots\beta_n=(-1)^n i$, and equation (11) may be reduced to

$$(D-\beta_1\nu)(D-\beta_2\nu)\cdots(D-\beta_n\nu)f(z) = \sum_{p=1}^{\infty} \frac{a_p}{z^{n(2p-1)}}, \tag{13}$$

which forms the basic differential equation for our problem.

Solution of Complex Function f(z)

The homogenous solution of the differential equation (13) is

$$f_H = \sum_{k=1}^{n} C_k\ \exp(\nu\beta_k z). \tag{14}$$

To obtain the particular solution f_P we express it by the following series and then verify that it satisfies all conditions, particularly the boundary conditions:

$$f_P = \sum_{p=1}^{\infty} f_p, \tag{15}$$

where f_p is assumed to be

$$f_P = \sum_{k=1}^{n} (-1)^{n(p-1)} d_{pk}\ e^{\nu\beta_k z} \int_{C\ \infty}^{\beta_k z} \frac{e^{-\nu t}dt}{t^{2n(p-1)+1}}. \tag{16}$$

The path of integration for the complex integrals is shown in Figure 2. We note that since z lies in the sector for which $-\pi/2n \le \arg z \le 0$ and the β_k is given by (12) it follows that $\beta_k z$ always lies in the left-plane.

Substituting (15) and (16) into (13) and noting that

$$(D-\nu\beta_k)\left((-1)^{n(p-1)} d_{pk}\ e^{\nu\beta_k z} \int_{C\ \infty}^{\beta_k z} \frac{e^{-\nu t}dt}{t^{2n(p-1)+1}}\right) = \frac{d_{pk}}{z^{2n(p-1)+1}},$$

one finds

$$\sum_{k=1}^{n} \prod_{i \neq k}^{n} (D - \nu \beta_i) \frac{d_{pk}}{2^{2n(p-1)+1}} = \frac{a_p}{2^n(2p-1)}, \tag{17}$$

or

$$\left\{ \sum_{k=1}^{n} d_{pk} D^{n-1} + (-\nu) \sum_{k=1}^{n} d_{pk} \left(\sum_{i \neq k}^{n} \beta_i \right) D^{n-2} + (-\nu)^2 \sum_{k=1}^{n} d_{pk} \left(\sum_{i<j}^{n} \beta_i \beta_j \right) D^{n-3} \right.$$
$$i, j \neq k$$

$$\left. + \cdots + (-\nu)^{n-1} \sum_{k=1}^{n} d_{pk} \left(\prod_{i \neq k}^{n} \beta_i \right) \right\} \frac{1}{2^{2n(p-1)+1}} = \frac{a_p}{2^n(2p-1)}. \tag{18}$$

The symbol Π means, as usual, a continued product. However,

$$D^{n-1} \frac{1}{2^{2n(p-1)+1}} = (-1)^{n-1} \frac{[n(2p-1)-1]!}{[2n(p-1)]!} \frac{1}{2^{n(2p-1)}},$$

by comparing both sides of (18), we obtain

$$(-1)^{n-1} \left(\sum_{k=1}^{n} d_{pk} \right) \frac{[n(2p-1)-1]!}{[2n(p-1)]!} = a_p, \tag{19}$$

and

$$\sum_{k=1}^{n-1} d_{pk} \left(\sum_{i \neq k}^{n} \beta_i \right) = -d_{pn} \sum_{i \neq n}^{n} \beta_i,$$

$$\sum_{k=1}^{n-1} d_{pk} \left(\sum_{i<j}^{n} \beta_i \beta_j \right) = -d_{pn} \left(\sum_{i<j}^{n} \beta_i \beta_j \right),$$
$$i, j \neq k \qquad\qquad\qquad i, j \neq n$$

$$\cdots\cdots\cdots,$$

$$\sum_{k=1}^{n-1} d_{pk} \left(\sum_{i<j<\ldots<r}^{n} \beta_i \beta_j \cdots \beta_r \right) = -d_{pn} \left(\sum_{i<j<\ldots<r}^{n} \beta_i \beta_j \cdots \beta_r \right),$$
$$i, j \ldots, r \neq k \qquad\qquad\qquad i, j \ldots, r \neq n$$

$$\cdots\cdots\cdots,$$

$$\sum_{k=1}^{n-1} d_{pk} (\beta_1 \beta_2 \cdots \beta_{k-1} \beta_{k+1} \cdots \beta_{n-1}) = -d_{pn} (\beta_1 \beta_2 \cdots \beta_{n-1}), \tag{20}$$

where there are $(n-1)$ equations, by which the constants d_{pk}, $k \neq n$, may be expressed in terms of d_{pn} in the following manner:

Let us denote by $\det[\beta_{ij}]$ the determinant of the matrix whose elements are the multipliers of the constants d_{pk}, $k \neq n$, on the left–hand side of equation (20), by $\det[\beta_{ij}]_{k=n}$ the determinant of the matrix whose elements are exactly the same as $[\beta_{ij}]$ except the kth colum which is replaced by the array, the elements of which are the multipliers of $-d_{pn}$ on the right–hand side of (20). Thus, if $\det[\beta_{ij}] \neq 0$, we have

$$d_{pk} = -d_{pn} \frac{\det[\beta_{ij}]_{k=n}}{\det[\beta_{ij}]}. \tag{21}$$

The $\det[\beta_{ij}]_{k=n}$ may be simplified by firstly factoring out β_k from the $(n-1)$th row. Then, substracting the $(n-1)$th row from $(n-2)$th row, and replacing by this new row the $(n-2)$th row. For this time we may again factor out another β_k from $(n-2)$th row. Continuing this process for $(n-3)$th, $(n-4)$th, $\cdots$rows, we will end up to a position that $\det[\beta_{ij}]_{k=n}$ becomes β_k^{n-1} times a determinant whose elements of the first row would be all unity and those of the other rows would not contain β_k. Afterwards, substract the 2nd column from

the first one, and use this array so obtained to replace the first column of the determinant just mentioned. Continuing this process for the 2rd, 3rd,·· columns, i.e. replacing the second column by an array obtained by subtracting the 3rd from the 2rd column, and so on, we obtain easily

$$\det[\beta_{ij}]_{k=n} = (-1)^{n+k-1} \beta_k^{n-1} \prod_{\substack{i<j \\ i,j \neq n}}^{n} (\beta_i - \beta_j).$$

Similarly, we find

$$\det[\beta_{ij}] = \beta_n^{n-1} \prod_{\substack{i<j \\ i,j \neq n}}^{n} (\beta_i - \beta_j).$$

Hence, substituting the last two results into (21), one may verify that

$$d_{pk} = -d_{pn} \frac{\beta_k^{n-1} \prod_{\substack{i=1 \\ i \neq k}}^{n-1} (\beta_n - \beta_i)}{\beta_n^{n-1} \prod_{\substack{i=1 \\ i \neq k}}^{n-1} (\beta_k - \beta_i)}, \tag{22}$$

with $k=1,2,\cdots,n-1$. If the index k in (22) is replaced by $(n-k)$, its conjugate becomes

$$\overline{d}_{p(n-k)} = -\overline{d}_{pn} \frac{(\overline{\beta}_{n-k})^{n-1} \prod_{\substack{i=1 \\ i \neq n-k}}^{n-1} (\overline{\beta}_n - \overline{\beta}_i)}{(\overline{\beta}_n)^{n-1} \prod_{\substack{i=1 \\ i \neq n-k}}^{n-1} (\overline{\beta}_{n-k} - \overline{\beta}_i)}$$

Since

$$\beta_k = \overline{\beta}_{n-k} , \quad \overline{\beta}_n = -\beta_n, \tag{22a}$$

the last equation may be written, after the index $(n-i)$ has been changed to i, as

$$\overline{d}_{p(n-k)} = -\overline{d}_{pn} \frac{\beta_k^{n-1} \prod_{\substack{i=1 \\ i \neq k}}^{n-1} (-\beta_n - \beta_i)}{(-\beta_n)^{n-1} \prod_{\substack{i=1 \\ i \neq k}}^{n-1} (\beta_k - \beta_i).} \tag{23}$$

The division of equations (22) by (23) yields

$$\frac{d_{pk}}{\overline{d}_{p(n-k)}} = (-1)^{n-1} \frac{d_{pn}}{\overline{d}_{pn}} \frac{\prod_{i=1}^{n-1} (\beta_n - \beta_i) (-\beta_n - \beta_k)}{\prod_{i=1}^{n-1} (-\beta_n - \beta_i) (\beta_n - \beta_k)}.$$

However. as may be seen from (12),

$$\frac{-\beta_n - \beta_k}{\beta_n - \beta_k} = i \tan \frac{k\pi}{2n},$$

and

$$\frac{\prod\limits_{k=1}^{n-1}(\beta_n-\beta_k)}{\prod\limits_{k=1}^{n-1}(-\beta_n-\beta_k)}=(-i)^{n-1}\prod\limits_{k=1}^{n-1}\cot\frac{k\pi}{2n}=(-i)^{n-1}. \tag{23a}$$

Consequently,

$$\frac{d_{pk}}{\overline{d_{p(n-k)}}}=(i)^n\tan\frac{k\pi}{2n}\frac{d_{pn}}{\overline{d_{pn}}},\quad k=1,2\cdots,n-1 \tag{24}$$

Another relation which is similar with (24) may be deduced from (22) by firstly replacing the index k in (22) by $(n-k+1)$, then, taking its conjugate and using (22a). This relation is

$$\overline{d_{p(n-k+1)}}=-\overline{d_{pn}}\ \frac{(\beta_{k-1})^{n-1}\prod\limits_{\substack{t=1\\t\neq k-1}}^{n-1}(-\beta_n-\beta_t)}{(-\beta_n)^{n-1}\prod\limits_{\substack{t=1\\t\neq k-1}}^{n-1}(\beta_{k-1}-\beta_t)} \tag{25}$$

But

$$\beta_{k-1}=\beta_k e^{-i\pi/n},$$

and

$$\beta_{k-1}-\beta_t=e^{-i\pi/n}(\beta_k-\beta_{t+1}),$$

equation (25) may be reduced to

$$\overline{d_{p(n-k+1)}}=-\overline{d_{pn}}\ \frac{(-1)^{n-1}\,e^{-i\pi/n}(\beta_k)^{n-1}\prod\limits_{\substack{t=1\\t\neq k-1}}^{n-1}(-\beta_n-\beta_t)}{(\beta_n)^{n-1}\prod\limits_{\substack{t=2\\t\neq k}}^{n}(\beta_k-\beta_t)}. \tag{26}$$

Similarly, we divide (22) by (26), and obtain

$$\frac{d_{pk}}{\overline{d_{p(n-k+1)}}}=\frac{d_{pn}}{\overline{d_{pn}}}(-1)^{n-1}\ e^{i\pi/n}\ \frac{(\beta_k-\beta_n)(-\beta_n-\beta_{k-1})}{(\beta_k-\beta_1)(\beta_n-\beta_k)}\frac{\prod\limits_{t=1}^{n-1}(\beta_n-\beta_t)}{\prod\limits_{t=1}^{n-1}(-\beta_n-\beta_t)}. \tag{27}$$

We note

$$-(\beta_n+\beta_{k-1})=-e^{-i\pi/n}(\beta_k-\beta_1).$$

The substitution of (23a) into (27) yields

$$\frac{d_{pk}}{\overline{d_{p(n-k+1)}}}=(i)^{n-1}\frac{d_{pn}}{\overline{d_{pn}}},\quad k=1,2,\cdots,n. \tag{28}$$

If we further assume

$$d_{pn}=R_p\,e^{i(\theta-\frac{n-1}{4}\pi)}, \tag{29}$$

where R_p is real. Then, equations (24) and (28) become respectively

$$\frac{d_{pk}}{\overline{d_{p(n-k)}}} = i\tan\frac{k\pi}{2n}\, e^{i2\theta}, \qquad k=1,2,\cdots,n-1, \tag{30}$$

$$\frac{d_{pk}}{\overline{d_{p(n-k+1)}}} = e^{i2\theta}, \qquad k=1,2,\cdots,n. \tag{31}$$

From (30) and (31) we easily obtain the following recurrence relation by taking conjugates and eliminating $\overline{d_{pk}}$:

$$d_{p(n-k)} = i\, d_{p(n-k+1)}\cot\frac{k\pi}{2n}, \qquad k=1,2,\cdots,n-1,$$

which may also be expressed in the form

$$d_{p(n-k)} = (i)^k d_{pn}\cot\frac{\pi}{2n}\cot\frac{2\pi}{2n}\cdots\cot\frac{k\pi}{2n}, \tag{32}$$

$k=1,2,\cdots n-1$. If we set $k=n-1$ in (32) the cotangents cancel each other and the following relation results:

$$d_{p1} = (i)^{n-1}d_{pn}. \tag{33}$$

For $k=n$ we have, from (31), the additional relation

$$d_{pn} = e^{i2\theta}\,\overline{d_{p1}}. \tag{34}$$

Combining (30) and (32), noting afterwards that the relation holds for $k=n$, and using (33),(34), and (29) consecutively, we obtain

$$d_{pk} = R_p\, e^{i\theta}\, e^{i\pi[(n+1)/4-k/2]}\cot\frac{\pi}{2n}\cot\frac{2\pi}{2n}\cdots\cot\frac{(k-1)\pi}{2n}, \tag{35}$$

which is valid for $k=2,3\cdots n$. In particular,

$$d_{p1} = R_p\, e^{i\theta}\, e^{i(n-1)\pi/4}. \tag{36}$$

Substituting (35) and (36) into (19) and noting that

$$e^{i(n-1)\pi/4} + e^{i(n+1)\pi/4}\sum_{k=2}^{n} e^{-ik\pi/2}\cot\frac{\pi}{2n}\cot\frac{2\pi}{2n}\cdots\cot\frac{(k-1)\pi}{2n} = \sqrt{n},$$

We obtain

$$a_p = (-1)^{n-1}\frac{[n(2p-1)-1]!}{[2n(p-1)]!}\sqrt{n}R_p e^{i\theta}.$$

It followe that $\theta=0$ since both a_p and R_p are reals.
Consequently,

$$d_{p1} = R_p\, e^{i(n-1)\pi/4},$$

$$d_{pk} = R_p\, e^{i\pi[(n+1)/4-k/2]}\cot\frac{\pi}{2n}\cot\frac{2\pi}{2n}\cdots\cot\frac{(k-1)\pi}{2n},$$

$$k=2,3,\cdots,n. \tag{37}$$

Hence, the combination of (14),(15), and (16), with the substitution of (37),results

$$f(z) = \sum_{p=1}^{\infty}\, \sum_{k=1}^{n} d_{pk}\left(C_{pk} + (-1)^{n(p-1)}C\int_{\infty}^{\beta_{pk}}\frac{e^{-\nu t}dt}{t^{2n(p-1)+1}}\right)e^{\nu\beta_k z}, \tag{38}$$

where d_{pk}, $k=1,2,\cdots,n$, are given by (37), while C_{pk} is related with the constant C_k in (14) by the following relation:

$$C_k = \sum_{p=1}^{\infty} d_{pk} C_{pk}. \tag{39}$$

The constants in (38) are to be determined in such a way that the solution $f(z)$ satisfies the boundary conditions (4) and (5).

To satisfy the condition (4) we shall write

$$H(z) = (iD - 1)f(z), \tag{40}$$

and require that

$$H(z) = -\overline{H(\bar{z})}, \quad \text{for } z = x. \tag{41}$$

We note

$$\overline{d_{pk}} = - i \tan \frac{k\pi}{2n} d_{p(n-k)}, \quad k = 1, 2 \cdots, (n-1), \tag{42}$$

as may be obtained from (30) by setting $\theta = 0$, and $\beta_k = \overline{\beta_{n-k}}$, as seen from the definition (12).

Also $\sum_{k=1}^{n} d_{pk}$ is real, as given by (19).

Substituting the solution given by (38) into (41), one encounters to evaluate the conjugate of the integral:

$$_C\!\!\int_{\infty}^{\overline{\beta_k z}} \frac{e^{-\nu t}\, dt}{t^{2n(p-1)+1}},$$

which, by evaluating the residue of $\oint e^{-\nu t} dt / [t^{2n(p-1)+1}]$ at the origin, becomes

$$_{\overline{C}}\!\!\int_{\infty}^{\overline{\beta_k}\bar{z}} \frac{e^{-\nu t}\, dt}{t^{2n(p-1)+1}} - i2\pi \frac{\nu^{2n(p-1)}}{[2n(p-1)]!}, \tag{43}$$

in which the integral is taken along a path symmetrical to the path C, coming from $+\infty$ along the real axis, then going along a circular arc with the center at the origin (leaving the origin to the left), and finally along a ray from the origin to the point $\overline{\beta_k}\bar{z}$ (see Fig 2). It is clear that the integral in (43) is the conjugate of the integral along the path conjugate to C.

The direct substitution of the solution $f(z)$, together with (42) and (43), and using the facts that

$$\tan \frac{n-k}{2n} = \cot \frac{k\pi}{2n},$$

and

$$\frac{i\beta_k - 1}{i\beta_k + 1} = - i \cot \frac{k\pi}{2n},$$

equation (41) yields

$$C_{pk} = \overline{C}_{p(n-k)} + i2\pi \frac{(-1)^{n(p-1)}\nu^{2n(p-1)}}{[2n(p-1)]!}, \tag{44}$$

for $k = 1, 2, \cdots, n-1$.

To satisfy the condition (5) we write

$$K(z) = - i\exp\left(-\frac{i\pi}{2n}\right)\frac{df(z)}{dz},$$

with f given by (38), and require

$$K(z) = -\overline{K(\bar{z})}, \quad \text{for } z = r\exp\left(-\frac{i\pi}{2n}\right).\tag{45}$$

Using (43) and

$$d_{pk} = \overline{d}_{p(n-k-1)}, \quad k=1, 2, \cdots, n,$$

one may similarly obtain from (45) the following relation:

$$C_{pk} = \overline{C}_{p(n-k+1)} + i2\pi \frac{(-1)^{n(p-1)} \nu^{2n(p-1)}}{[2n(p-1)]!},\tag{46}$$

for $k=1,2,\cdots,n$.

From the relations (44) and (46) one can readily verify

$$C_{p1} = C_{p2} = \cdots = C_{pn} = \overline{C}_{pn} + i2\pi \frac{(-1)^{n(p-1)} \nu^{2n(p-1)}}{[2n(p-1)]!}.$$

Thus, if we write

$$C_{pk} = C_{pk}' + iC_{pk}'', \quad k=1,2,\cdots,n,$$

where C_{pk}' and C_{pk}'' are reals, then,

$$C_{pk}' = C_p, \quad \text{say},$$

and

$$C_{pk}'' = \pi \frac{(-1)^{n(p-1)} \nu^{2n(p-)}}{[2n(p-1)]!}$$

for all k. Hence,

$$C_{pk} = C_p + i\pi \frac{(-1)^{n(p-1)} \nu^{2n(p-1)}}{[2n(p-1)]!}, \quad k=1, 2,\cdots,n.\tag{47}$$

Substituting (47) into (38), we find

$$f(z) = \sum_{p=1}^{\infty}\sum_{k=1}^{n} d_{pk} \left(C_p + i\pi \frac{(-1)^{n(p-1)} \nu^{2n(p-1)}}{[2n(p-1)]!} \right.$$

$$\left. +(-1)^{n(p-1)} \ _C\!\!\int_{\infty}^{\beta_k z} \frac{e^{-\nu t}dt}{t^{2n(p-1)+1}} \right) e^{\nu\beta_k z}.\tag{48}$$

Two simple cases can be readily deduced from this result: (1) when $k=n=1$, this reduces to solution for the standing waves in front of a cliff; and (2) when $p=1$, by taking the difference in the path of integration into account, one obtains the case of waves over a sloping beach, the solution of which has a logarithmic singularity at the shore line (see Stoker [1947,1965]).

As $|z| \to \infty$ in the sector $-\pi/2n \leq \arg z \leq 0$ the function $\exp(\beta_k z)$ dies out exponentially except the case for $k=n$ which is $\exp(-iz)$, since all β_k's except β_n have negative real parts. On the other hand, it is not hard to show that the integrals in (48) behave saymptotically as

$$_C\!\!\int_{\infty}^{\beta_k z} \frac{e^{-\nu t}dt}{t^{2n(p-1)+1}} \sim \begin{cases} -i2\pi - \dfrac{1}{\nu} \dfrac{\exp(-\beta_k z)}{\beta_k^{2n(p-1)+1}}\left(\dfrac{1}{z}+\cdots\right)^{2n(p-1)+1}, \\ \qquad \text{for } \pi/2 < \arg\beta_k z \leq \pi; \\ -\dfrac{1}{\nu}\dfrac{\exp(-\beta_k z)}{\beta_k^{2n(p-1)+1}}\left(\dfrac{1}{z}+\cdots\right)^{2n(q-1)+1}, \end{cases}\tag{49}$$

$$\text{for } \pi < \arg\beta_k z \leq 3\pi/2.$$

Thus, using (29) where $\theta=0$, the asymptotic expression of (48) as $x\to\infty$ and for $y=0$ is given by

$$f(x) \sim \sum_{p=1}^{\infty} R_p \left(C_p + (-1)^{n(p-1)} \frac{i\pi\nu^{2n(p-1)}}{[2n(p-1)]!} \right) \exp\left[-i\left(\nu x + \frac{n-1}{4}\pi\right) \right], \quad (50)$$

or

$$\phi(x,0,t) \sim \sum_{p=1}^{\infty} e^{i\sigma t} R_p \mathrm{Re}\left\{ \left[C_p + (-1)^{n(p-1)} \frac{i\pi\nu^{2n(p-1)}}{[2n(p-1)]!} \right] \times \right.$$

$$\left. \exp\left[-i\left(\nu x + \frac{n-1}{4}\pi\right) \right] \right\}, \quad (51)$$

From the asymptotic expression as $x \to \infty$ one sees that it is possible to construct, through the equation (2), an incoming progressive wave by proper choice of the constant C_p, which behaves like either $\cos[\nu x + \sigma t + (n-1)\pi/4]$ or $\sin[\nu x + \sigma t + (n-1)\pi/4]$.

We note that, if we replace σ in (2) by σ_p, thus, ν by ν_p, the solution given by (48), as (50) and (51), is still valid, except σ and ν have to be written in σ_p and ν_p, respectively. For this case, the incoming progressive wave at $x = \infty$ becomes an irregular one.

References

Brillouet, G. and Villat, Préface de M.H. Etude de quelques problèmes sur les ondes liquides de gravité, *Publications Scientifiques et Techniques*, du Ministére de L'Air, Paris. (1957)

Stoker, J. J. Surface waves in water of variable depth, *Quarterly of Applied Mathematics*, 5, No. 2.(1947)

Stoker, J. J. *Water waves, the mathematical theory with applications*, Second printing, Interscience Publishers, New York.(1965)

Free Surface

$\omega = \dfrac{\pi}{2n}$

Bottom
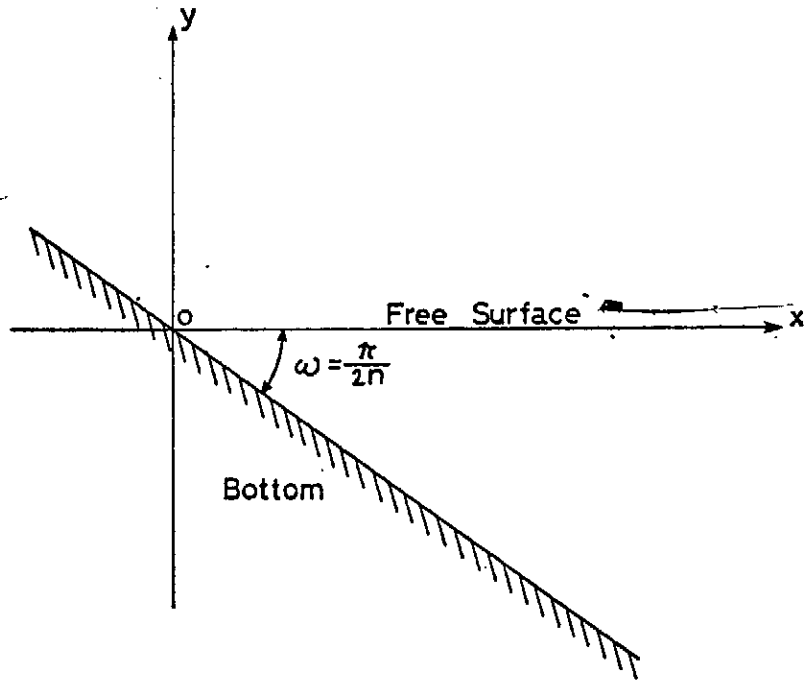
Figure 1 — Physical Problem and
Coordinate System

$\bar{\beta}_k \bar{\delta}$

$\bar{C}$

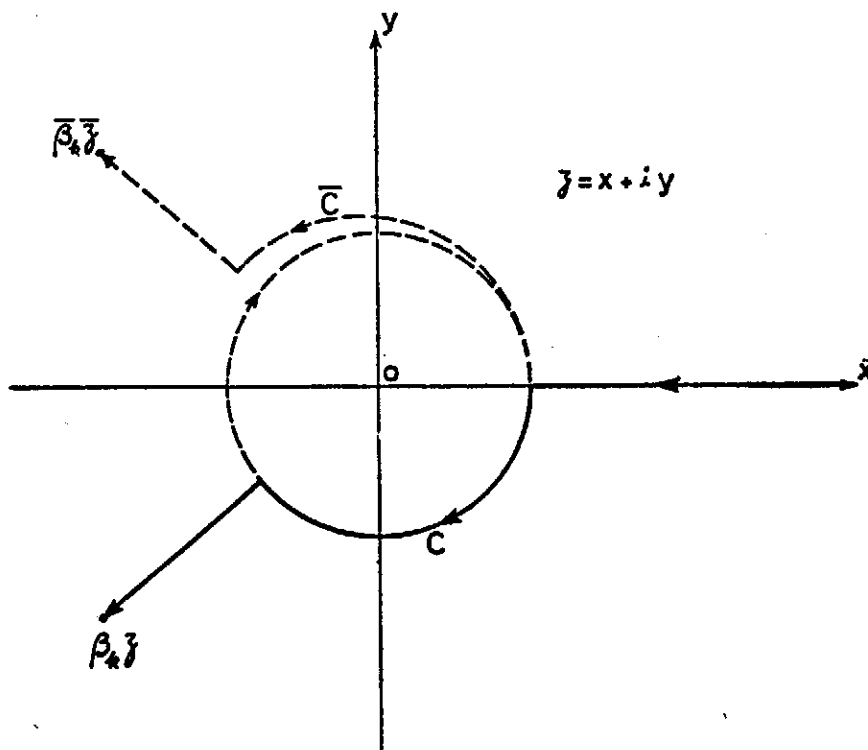$\tilde{\jmath} = x + iy$

o

$\beta_k \delta$

C

Figure 2 — Path of Integration

Drop–Water Impact

Chun-Tsung Wang (汪軍從)

Institute of Physics, Academia Sinica
(Received April 1971)

摘　　要

此文研究水滴撞擊水面後之現象。以合成單元流體法（Synthetic–Cell–Fluid Scheme）控制流體之運動，解含有表面張力為邊界值之那維爾史托克方程式而得最大撞擊壓力模式、壓力分佈、界面阻力及表面張力效應等。同時以不同撞擊速度之各種大小水滴撞擊水面所得撞擊壓力之實驗數值亦與理論值相符合。

Introduction

The raindrop impact process is closely related to the rainfall–runoff process in urban areas and the soil erosion process as well. The relative raindrop impact effect decreases as the flow depth increases, and is generally neglected in studying open–channel flow problems. However, in analyzing overland flow problems where the depth of flow is small, this effect of drop impact on the flow may be significant. The general approach to this problem has been to solve the one–dimensional spatially varied flow equations, treating rainfall as lateral flow[16] and including raindrop impact effect in the form of a boundary shear resistance coefficient[29] or overpressure[2].

Another approach is a detailed investigation of the flow near the drop impact point. Worthington[30] and Mutchler[23] conducted photographic studies. Palmer[24] made a series of tests on pressure–drop mass relations for various water layer depths. Harlow & Shannon[11] analytically studied the drop splashing problem with a Marker–And–Cell technique. Neglecting viscous and surface tension effects, numerical results of pressure and velocities for some arbitrary impact conditions were shown.

This study extends Palmer's measurements and Harlow's analytical work to provide a better understanding of the mechanics after a single drop strikes a stagnant thin water layer. The drops studied correspond to those which most frequently occur during a natural rainfall intensity of one to six inches per hour[18], while acquiring an impact velocity of the magnitude of their respective terminal velocities.

Analytical approach

Governing Equations–In order to develop a one–phase fluid model, it is assumed that no interfacial tension exists when a drop strikes the water surface, and that no air entrainment is produced by drop splashing. The fluid density, air and fluid temperatures are further assumed to remain unchanged and the entire phenomenon is assumed to be axisymmetric. Under these assumptions the continuity equation and the equations of motion which govern the phenomenon are

$$\frac{1}{r}\frac{\partial rv_r}{\partial r} + \frac{\partial v_z}{\partial z} = 0 \qquad (1)$$

$$\frac{\partial \overset{*}{v_r}}{\partial \overset{*}{t}} + \frac{1}{\overset{*}{r}}\frac{\partial \overset{**}{rv_r}{}^2}{\partial \overset{*}{r}} + \frac{\partial \overset{**}{v_r v_s}}{\partial \overset{*}{z}} = -\frac{1}{\rho}\frac{\partial p}{\partial \overset{*}{r}} + \nu\frac{\partial}{\partial \overset{*}{z}}\left(\frac{\partial \overset{*}{v_r}}{\partial \overset{*}{z}} - \frac{\partial \overset{*}{v_s}}{\partial \overset{*}{r}}\right) \tag{2}$$

$$\frac{\partial \overset{*}{v_s}}{\partial \overset{*}{t}} + \frac{1}{\overset{*}{r}}\frac{\partial \overset{*}{r}\,\overset{**}{v_r v_s}}{\partial \overset{*}{r}} + \frac{\partial \overset{*}{v_s}{}^2}{\partial \overset{*}{z}} = -g - \frac{1}{\rho}\frac{\partial p}{\partial \overset{*}{z}} - \frac{\nu}{\overset{*}{r}}\frac{\partial}{\partial \overset{*}{r}}\left[\overset{*}{r}\left(\frac{\partial \overset{*}{v_r}}{\partial \overset{*}{z}} - \frac{\partial \overset{*}{v_s}}{\partial \overset{*}{r}}\right)\right] \tag{3}$$

where $\overset{*}{v_r}$ and $\overset{*}{v_s}$ are the radial and axial velocity components respectively in cylindrical polar coordinates$(\overset{*}{r}, \overset{*}{z})$, p is the pressure taken here as the gage pressure, ρ is the density of the fluid, g is the gravitational acceleration, $\overset{*}{t}$ is the time variable, and ν is the kinematic viscosity of the fluid which is assumed constant.

It is convenient to introduce the following dimensionless variables and parameters.

$$
\begin{array}{lll}
r = \overset{*}{r}/L & z = \overset{*}{z}/L, & t = \overset{*}{t}v_0/L \\
v_r = \overset{*}{v_r}/v_0, & v_s = \overset{*}{v_s}/v_0, & \varphi = p/\rho v_0{}^2 \\
N_B = v_0 L/\nu, & F = v_0{}^2/gL, & W = \rho L v_0{}^2/\Gamma
\end{array} \tag{4}
$$

Where L is an arbitrary length parameter taken as the cell size dimension in the numerical computation, v_0 is the drop impact velocity, and Γ is the surface tension force per unit length between air and water. The governing equations therefore take the form

$$\frac{1}{r}\frac{\partial r v_r}{\partial r} + \frac{\partial v_s}{\partial z} = 0 \tag{5}$$

$$\frac{\partial v_r}{\partial t} + \frac{1}{r}\frac{\partial r v_r{}^2}{\partial r} + \frac{\partial v_r v_s}{\partial z} = -\frac{\partial \varphi}{\partial r} + \frac{1}{N_B}\frac{\partial}{\partial z}\left(\frac{\partial v_r}{\partial z} - \frac{\partial v_s}{\partial r}\right) \tag{6}$$

$$\frac{\partial v_s}{\partial t} + \frac{1}{r}\frac{\partial r v_r v_s}{\partial r} + \frac{\partial v_s{}^2}{\partial z} = -\frac{1}{F} - \frac{\partial \varphi}{\partial z} - \frac{1}{N_B}\frac{1}{r}\frac{\partial}{\partial r}\left[r\left(\frac{\partial v_r}{\partial z} - \frac{\partial v_s}{\partial r}\right)\right] \tag{7}$$

With given initial and boundary conditions, these equations can be solved by a two-step numerical scheme. In the first step, Eqs. 6 and 7 are combined to yield

$$\frac{\partial^2 \varphi}{\partial z^2} + \frac{1}{r}\frac{\partial}{\partial r}\left(r\frac{\partial \varphi}{\partial r}\right) = -\frac{\partial D}{\partial t} - \frac{1}{r}\frac{\partial^2 r v_r{}^2}{\partial r^2} - \frac{2}{r}\frac{\partial^2 (r v_r v_s)}{\partial r \partial z} - \frac{\partial^2 v_s{}^2}{\partial z^2} \tag{8}$$

where $D = \frac{1}{r}\frac{\partial r v_r}{\partial r} + \frac{\partial v_z}{\partial z}$, from which the pressure field, φ, can be evaluated by an iteration procedure if the velocity field, v_r and v_s, is known. In the second step, the velocity field at an advance stage (timewise) can be calculated by solving any two of Eqs. 5,6 or 7 if the mass and momentum are rigorously conserved.

Boundary Conditions–Since the drop–liquid impact phenomenon is assumed to be axisymmetric, only half of the (r, z) plane is considered. The origin of the coordinate system is located at the bottom of the water layer under the drop impact point.

Along the axisymmetric (z) axis the symmetry of fluid motion requires

$$\frac{\partial \varphi}{\partial r} = 0, \qquad \frac{\partial v_s}{\partial r} = 0, \qquad v_r = 0 \tag{9}$$

Along the bottom of the water layer, two cases are considered[18]. A no slip condition in which a solid boundary is assumed at the bottom of the water layer and the fluid in contact with the boundary has zero velocity. Thus, for $z=0$ Eq. 7 yields

$$\frac{\partial \varphi}{\partial z} = -\frac{1}{F} - \frac{1}{N_B}\cdot\frac{\partial}{r\partial r}\left(r\frac{\partial v_r}{\partial z}\right) \tag{10-a}$$

and the mathematical statement of the no slip condition is

$$v_r = 0, \qquad v_z = 0$$

A free slip condition assumes that the fluid slips freely along the wall provided the boundary layer developed there is thinner than that of a single cell size used in the numerical computations. In this case for $z = 0$

$$v_r \neq 0, \qquad v_z = 0, \qquad \frac{\partial v_r}{\partial z} = 0, \qquad \frac{\partial \varphi}{\partial z} = -\frac{1}{F} \tag{10-b}$$

Along the radial edge of the domain of interest $(\overset{*}{r} = R)$, a solid circular wall is imposed, since an infinitely wide computational field is not practical. The boundary conditions are:

$$\frac{\partial \varphi}{\partial r} = -\frac{1}{N_R} \frac{\partial^2 v_z}{\partial r \partial z}, \qquad v_r = 0, \qquad v_z = 0 \tag{11-a}$$

if the fluid in contact with the boundary has zero velocity, and

$$v_r = 0, \qquad v_z \neq 0, \qquad \frac{\partial v_z}{\partial r} = 0, \qquad \frac{\partial \varphi}{\partial r} = 0 \tag{11-b}$$

if the fluid is assumed to slip freely along the wall.

At the free surface the rapid change of the free surface shape is one of the most interesting parts of the drop splashing phenomenon. However, the question of employing a dynamic or static expression for surface tension is a difficult one since both approaches have been employed. [1,8,19].

Therefore in this study the dynamic free surface tension is assumed to be equal to that of the static case for the same free surface configuration. At the free surface, the only net force exerted on it is the surface tension force. In differential form this condition is expressed as [14,16]

$$\Gamma \left(\frac{1}{\overset{*}{R_1}} + \frac{1}{\overset{*}{R_2}} \right) n_i = -\sigma_{i,j} n_j = p n_i - \sigma_i^1, j n_j \quad (i,j = 1,2) \tag{13}$$

where $\sigma_{i,j}$ and $\sigma_i^1,_j$ are the tensor and deviatoric tensor stresses respectively, n is the unit outward normal, and $\overset{*}{R_1}$ and $\overset{*}{R_2}$ are the principal radii of curvature of the surface, assumed positive when the corresponding centers of curvature lie on the fluid side.

In Fig. 1, $\overset{*}{R_1}$ denotes the local radius of curvature of a surface curve formed in the $\overset{*}{r}-\overset{*}{z}$ plane. While $\overset{*}{R_2}$ in the axisymmetric case is the radius of curvature of a curve formed by the intersection of the plane with a cone which is tangent to the surface at the surface and has symmetry about the $\overset{*}{z}$ axis. For a free surface, $z = \eta(\overset{*}{r}, t)$ as shown, the unit outward normal vector n is

$$n_r = -\frac{\partial \eta}{\partial \overset{*}{r}} [1 + \frac{\partial \eta}{\partial \overset{*}{r}})^2]^{-1/2}$$

$$n_z = [1 + (\frac{\partial \eta}{\partial \overset{*}{r}})^2]^{-1/2}$$

where subscripts r and z refer to unit vector in $\overset{*}{r}$ and $\overset{*}{z}$ directions respectively.

After substituting the stress tensor components, $\sigma_{i,j}$ [26], where μ is the absolute viscosity of the fluid, into Eq.(12), the free surface boundary conditions take the dimensionless form

$$\varphi = \frac{1}{W} \left(\frac{1}{R_1} + \frac{1}{R_2} \right) + \frac{2}{N_R} \left[n_r^2 \frac{\partial v_r}{\partial r} + n_r n_z \left(\frac{\partial v_r}{\partial z} + \frac{\partial v_z}{\partial r} \right) + n_z^2 \frac{\partial v_z}{\partial z} \right] \tag{14}$$

$$\varphi = \frac{1}{W} \left(\frac{1}{R_1} + \frac{1}{R_2} \right) + \frac{2}{N_R} (n_r^2 \frac{\partial v_r}{\partial r} - n_z^2 \frac{\partial v_z}{\partial z}) / (n_r^2 - n_z^2) \quad \text{if } n_r^2 \neq n_z^2 \tag{15}$$

$$\frac{1}{N_B}\left[2n_r\,n_s\left(\frac{\partial v_r}{\partial r}-\frac{\partial v_s}{\partial z}\right)+(n_s{}^2-n_r{}^2)\left(\frac{\partial v_r}{\partial z}+\frac{\partial v_s}{\partial r}\right)\right]=0 \tag{16}$$

where $R_1=\dot{R}_1/L$ and $R_2=\dot{R}_2/L$.

Initial Conditions-The initial conditions needed in the two-step computation outlined earlier are drop shape and drop velocity at the moment of impact. In this study the drop shapes obtained experimentally by McDonald[22] and Mutchler[23] are used.

The required impact velocity can be obtained from the equation of motion for a drop. Neglecting minor forces, the balance between drag forces, buoyant force, and gravity force, for a freely falling drop gives

$$\frac{\pi d^3}{6}(\rho-\rho_a)g-0.5\rho_a\,v_D{}^2\frac{\pi d^2}{4}C_D=\frac{\pi\rho d^3}{12}\cdot\frac{dv_D{}^2}{dy} \tag{17}$$

where ρ_a is the air density, d is the equivalent drop diameter (the diameter of an equivalent sphere having the same volume as that of the drop), y is the direction of fall, v_D is the fall velocity, and C_D is the drag coefficient based on a projected area of an equivalent sphere. Based on data obtained from the fall height versus fall velocity relations measured by Gunn & Kinzer[7] and by Laws[17] for drop diameters of 0.1mm to 6.1mm, drag coefficients were calculated and plotted against $N_{RA}=\rho_aV_Dd/\mu_a$ in Fig. 2. The resulting drag coefficient relationship deviates increasingly from that of a solid sphere for $N_{RA}>1000$, indicating that the drop is flattening and therefore the drag force is increasing with N_{RA}. Eq.17 can be rearranged as

$$Y=\int dy=0.5\int\left[(1-\frac{\rho_a}{\rho})g-\frac{3\rho_aC_D}{4\rho d}v_D{}^2\right]^{-1}dv_D{}^2 \tag{18}$$

With the initial condition $v_D=0$ at $Y=0$, Eq. 18 can be integrated numerically and the result used with Gunn and Kinzer's drag coefficient data to determine the impact velocity of a drop falling a specific distance. Test runs for three drop sizes of equivalent drop diameter of 2.3mm, 3.0mm, and 3.92mm (at 68°F) displaying the relation between fall velocity and fall height are plotted in Fig. 3. Values predicted are in general agreement with Laws' data.

Numerical scheme

The two-step numerical scheme is shown schematically in Fig. 4. With a given fluid domain, defined as the fluid field under consideration at a specific moment, and velocity field at time t, the pressure field based on Eq. 8 can be evaluated. The fluid is then moved by utilizing a Synthetic-Cell-Fluid method, and the fluid domain at an advanced stage is defined by preserving the total fluid mass. Eq(3). (6) and(7) then yield the new velocity field and the whole computational cycle starts again.

The computational field is divided into rectangular cells as shown in Fig. 5. The cell pressure is located at the center of each individual cell. While velocities in r-direction are centered on the left and right side of the cell, and velocities in z-direction are centered on the upper and lower side of the cell to satisfy the equation of continuity, Eq. (5), at each individual cell.

Pressure Field -In simple explicit difference form, (8) becomes

$$f(\varphi)=\frac{L^t-L^{t+\varDelta t}}{\varDelta t}-g(v) \tag{19}$$

where

$$f(\varphi)=\frac{\partial^2\varphi}{\partial z^2}+\frac{1}{r}\,\frac{\partial}{\partial r}\left(r\,\frac{\partial\varphi}{\partial r}\right)$$

$$=\frac{1}{\varDelta z^2}\left[\varphi_{i,j+1}+\varphi_{i,j-1}-2\varphi_{i,j}\right]+\frac{1}{(i-0.5)\varDelta r^2}\left[i(\varphi_{i+1,j}-\varphi_{i,j})\right.$$

$$\left.-(i-1)(\varphi_{i,j}-\varphi_{i-1,j})\right] \tag{19-a}$$

$$g(v) = \frac{2}{r}\frac{\partial^2(rv_r v_z)}{\partial r\partial z} + \frac{\partial^2 v_z^2}{\partial z^2} + \frac{1}{r}\frac{\partial^2 rv_r^2}{\partial r^2}$$

$$= \frac{1}{(2i-1)\Delta r\Delta z}[i(v_{r_{i+1,j}} + v_{r_{i+1,j+1}})(v_{z_{i,j+1}} + v_{z_{i+1,j+1}}) - (i-1)$$

$$(v_{r_{i,j}} + v_{r_{i,j+1}})(v_{z_{i,j+1}} + v_{z_{i-1,j+1}}) - i(v_{r_{i+1,j}} + v_{r_{i+1,j-1}})$$

$$(v_{z_{i,j}} + v_{z_{i+1,j}}) + (i-1)(v_{r_{i,j}} + v_{r_{i,j-1}})(v_{z_{i,j}} + v_{z_{i-1,j}})] +$$

$$\frac{1}{4\Delta z^2}[(v_{z_{i,j+1}} + v_{z_{i,j+2}})^2 + (v_{z_{i,j}} + v_{z_{i,j-1}})^2 - 2(v_{z_{i,j}} + v_{z_{i,j+1}})^2]$$

$$+ \frac{1}{(4i-2)\Delta r^2}[(i+0.5)(v_{r_{i+1,j}} + v_{r_{i+2,j}})^2 + (i-1.5)(v_{r_{i,j}} + v_{r_{i-1,j}})^2$$

$$- (2i-1)(v_{r_{i,j}} + v_{r_{i+1,j}})^2] \tag{19-b}$$

and all variables without superscript refer to time t. With a known fluid domain and velocity field at time t and assuming $D^{t+\Delta t}$ is zero, an iteration procedure satisfying the proper boundary conditions is used to evaluate $\varphi_{i,j}$ in terms of its neighboring values at four adjacent cells such that the following criteria in the entire fluid domain are satisfied:

$$\frac{|\varphi_{i,j}^{k+1} - \varphi_{i,j}^k|}{|\varphi_{i,j}^{k+1} + \varphi_{i,j}^k + v_{r_{i,j}}^2 + v_{z_{i,j}}^2 + 2h/F|} < \varepsilon \tag{20}$$

$$\left|\frac{|\sum f(\varphi)|}{|\sum g(v)|} - 1.0\right| < \varepsilon \tag{21}$$

where h is the water layer depth, superscripts k and $k+1$ stand for two successful φ values in iteration process and ε is an arbitrary small value chosen to yield an allowable small D value, although theoretically $D=0$. The carry-over error is calculated as

$$D^{t+\Delta t} = D^t - \Delta t[f(\varphi) + g(v)] \tag{22}$$

which is then taken as the new D value for advance stage computations. This avoids the accumulation error after many cycles of time advancement[9,12] and permits the use of a larger cell size.

Fluid and empty cells are designated as cells filled or not filled with fluid and surface and interior cells refer to fluid cells adjoining or not adjoining empty cells. In evaluating the pressure in the surface cells the centers of the surface cells are regarded as the discrete surface elements to approximate the surface curvature and unit normal at each surface cell. The first principal radius, R_1, of a surface element centered at (r, z) is taken as the radius of a circle, R, passing through the centers of three neighboring surface cells (r_k, z_k), $k=1$, 2,3 (Fig. 1). Hence

$$R_* = [(r_1 - r_0)^2 + (z_1 - z_0)^2]^{1/2} \quad \text{if } \Delta \neq 0 \tag{23}$$

where (r_0, z_0) is the center of the circle. The image (r_c, z_c) of (r_0, z_0) along the line connecting points (r, z) and (r_0, z_0) and with a distance Δr from (r, z) is defined as

$$r_c = r + (r_0 - r)\Delta r/R_*$$

$$z_c = z + (z_0 - z)\Delta r/R_* \tag{24}$$

When the point (r_c, z_c) is located in a fluid cell, the free surface is regarded as concave inward at (r, z) and the principal radius $R_1 = R_*$, otherwise $R_1 = -R_*$ if point (r_c, z_c) is located in an empty cell. The second principal radius, R_2 is defined as the length of a line drawn perpendicular to the local surface profile from the center of the surface cell to the axisymmetric axis.

$$|R_2| = r[1 + (\frac{n_z}{n_r})^2]^{\frac{1}{2}} \tag{25}$$

It is regarded as positive if the free surface is concave inward with respect to the symmetric axis, i.e. $R_2 = |R_2|$ if $n_r \geq 0$ and $R_2 = -|R_2|$ if $n_r < 0$.

After the two principal radii R_1 and R_2 are determined, the pressure in the surface cell can be evaluated from Eqs. (14) or (15). And the interior pressure field from Eq. 19 via a simple iteration scheme based on the Cross-Jacden technique. A set of trial $\varphi_{i,j}$ values designated as $\varphi^k_{i,j}$ are formed by the iteration procedure

$$\varphi^{k+1}_{i,j} = \varphi^k_{i,j} - \frac{f(\varphi_{i,j})}{\partial f(\varphi_{i,j})/\partial \varphi_{i,j}}$$

$$= \frac{\frac{\varphi^{k+1}_{i,j+1} + \varphi^k_{i,j-1}}{\Delta z^2} + \frac{i\varphi^{k+1}_{i+1,j} + (i-1)\varphi^{k+1}_{i-1,j}}{(i-0.5)\Delta r^2} - \frac{D^t}{\Delta t} + g(v)}{\frac{2}{\Delta r^2} + \frac{2}{\Delta z^2}} \tag{26}$$

where $k = 1, 2, \ldots$, and stands for the successive trial steps, and the first trial value, $\varphi^1_{i,j}$, is assumed equal to the true $\varphi_{i,j}$ value at its previous stage, since the time increment Δt is small. This implies that $\varphi_{i,j}$, $\varphi_{i-1,j}$ and $\varphi_{i,j+1}$ are allowed to relax while $\varphi_{i+1,j}$ and $\varphi_{i,j-1}$ are held firm as hinge points when the iteration process is centered at $\varphi_{i,j}$ value. In two successive trial steps if the criterion

$$\frac{\varphi^{k+1}_{i,j} - \varphi^k_{i,j+1}}{\Delta z^2} + \frac{(i-1)(\varphi^{k+1}_{i-1,j} - \varphi^k_{i-1,j})}{(i-0.5)\Delta r^2} < (\varphi^{k+1}_{i,j} - \varphi^k_{i,j})(\frac{2}{\Delta r^2} + \frac{2}{\Delta z^2}) \tag{27}$$

is satisfied, Eq.(26) yields a set of converging $\varphi^k_{i,j}$ values which converge to the true $\varphi_{i,j}$ value at time t. When the difference between the two successive group of trial values is small enough to satisfy Eqs.(20) and (21), the trial $\varphi^k_{i,j}$ value is taken as the true $\varphi_{i,j}$ value at time t and yields the pressure at the interior cells.

Fluid Movement-The 'synthetic cell fluid' physically represents the fractional part of the cell which is occupied by the fluid, f_i. Its variation is traced as an indication of the fluid movement. The general equation of continuity in finite difference form for the compressible fluid flow

$$\rho^{t+\Delta t}_{S_{i,j}} = \rho^t_{S_{i,j}} - \Delta t \{ \frac{1}{(i-0.5)\Delta r}[iv_{r_{i+1,j}}\rho_{SA} - (i-1)v_{r_{i,j}}\rho_{SB}] \tag{28}$$

$$+ \frac{1}{\Delta z}(v_{z_{i,j+1}}\rho_{SC} - v_{z_{i,j}}\rho_{SD}) \}$$

where

$$\rho_{SA} = \begin{vmatrix} \rho_{S_{i,j}} & \text{if} & v_{r_{i+1,j}} & \geq 0 \\ \rho_{S_{i+1,j}} & & v_{r_{i+1,j}} & < 0 \end{vmatrix} \qquad \rho_{SC} = \begin{vmatrix} \rho_{S_{i,j}} & \text{if} & v_{z_{i,j+1}} & \geq 0 \\ \rho_{S_{i,j+1}} & & v_{z_{i,j+1}} & < 0 \end{vmatrix}$$

$$\rho_{SB} = \begin{vmatrix} \rho_{S_{i,j}} & \text{if} & v_{r_{i,j}} & \leq 0 \\ \rho_{S_{i-1,j}} & & v_{r_{i,j}} & > 0 \end{vmatrix} \qquad \rho_{SD} = \begin{vmatrix} \rho_{S_{i,j}} & \text{if} & v_{z_{i,j}} & \leq 0 \\ \rho_{S_{i,j-1}} & & v_{z_{i,j}} & > 0 \end{vmatrix} \tag{29}$$

is assumed to govern the movement of the synthetic cell fluid, and the fluid which flows from cell to cell is assumed to be directly proportional to the density of the cell from which the fluid is flowing[5].

In the velocity and pressure computations, a cell must be classified as either being filled with incompressible fluid or empty. Thus, cells whose synthetic cell fluid is greater than certain value $\zeta(t)$ are defined as fluid cells at that specific instant. The value of $\zeta(t)$ is

determined when

$$\sum_{\rho_{S_{i,j}} > \xi(t)} \rho_{S_{i,j}} \, \Delta \forall_{i,j} \cong \text{Initial total fluid volumn} \tag{30}$$

is staisfied, where $\Delta \forall_{i,j}$ is the volume of cell$_{i,j}$.

Velocity Field–After evaluating the pressure field at time t and classifying the fluid domain at an advance stege $t+\Delta t$, Eqs.5,6 and 7 in their simple explicit difference forms [28] are used to compute the velocity field at the advance stage.

When the fluid cell considered is an interior cell, the new velocity field is directly calculated from Eqs.(6) and (7). When the fluid cell under consideration is a surface cell, the equation of continuity, Eq.(16) and equations of motion, Eqs.(6) and(7), together with the free surface boundary condition, Eq.(16), define the new velocity field [17].

Time Increment-In choosing time increment in time-dependent computations, numerical instability must be avoided. However, the non-linear characters of the equations of motion, Eqs.(6) and(7) make a rigorous stability analysis unavailable. Therefore, the time increment satisfying all the following heuristic stability criteria [25,28] is employed in the present study

$$\Delta t < \text{Minimum} \frac{\Delta r}{||v_r| + |v_z||}, \text{ when } \Delta r = \Delta z \tag{31}$$

which is also the von Neumann necessary condition which must be satisfied upon introducing the vorticity function, $\omega = \dfrac{\partial v_r}{\partial z} - \dfrac{\partial v_z}{\partial r}$, into the equation of motion to reach a linearized stability criterion.

$$\Delta t < 0.5 \Delta z^2 N_R, \text{ when } \Delta r = \Delta z \tag{32}$$

which is the Courant condition restricting the distance a wave can travel in one time increment to be less than one space interval.

$$\Delta t < \Delta r \sqrt{F/h}, \text{ when } \Delta r = \Delta z \tag{33}$$

which is the Courant condition for gravity waves with small wave number.

Experimental program

In order to establish experimentally the relation between maximum impact pressure and water layer depth as a function of drop size and drop impact velocity, an experimental program was carried out to measure the pressure pulse at the boundary immediately beneath the impact point of a single drop as it strikes a stagnant thin water layer. The apparatus arrangement is schematically shown in Fig. 6. It consisted of a drop former placed at specific elevations above a thin water layer. By varying the elevation of the drop former, the impact velocity of the drop was varied. The water layer was contained in a smooth plexiglass tray 2 ft. square with 6 in. high sides. At the center of the tray a Kistler 606A quartz pressure transducer was mounted flush with the tray bottom. The pressure signal from the transducer passed through a Model 504 Kistler charge amplifier containing a Model 548A8 plug-in filter for resonance attenuation, and was displayed on a Tektronix type 564 storage oscilloscope.

Test conditions for this study are ------ rized below in Table 1.

Table 1. Test Conditions	
	Range
Drop diameter, d(mm)	2.7~3.7
Height of fall, H(ft)	4.25~33
Water depth, h(in.)	0.0~0.82
Temperature (°F)	64~75

Different sizes of drops were produced by using capillary tubes of various diameters in the drop former. Drop formation data are tabulated in Table 2.

Table 2. Relation Between Tube Size and Drop Size		
Tube OD d_o (in.)	Tube ID d_i (in.)	Equivalent drop dia. d (mm)
0.024	0.011	2.62~2.73
0.038	0.023	3.09~3.13
0.062	0.045	3.60~3.74

The drop impact velocity for drops falling various distances is calculated from Eq.18 with $\rho_a = 0.00234$ and $\rho = 1.935$ lb-sec^2/ft^4 and tabulated in Table 3.

Table 3. Fall Height Versus Drop Impact Velocity		
Drop size d (mm)	Fall Height H (ft)	Drop Impact Velocity v_a (fps)
2.70	33.0	25.25
2.70	12.0	21.10
2.70	7.5	18.30
2.70	4.67	15.40
3.12	33.0	26.80
3.12	12.0	21.80
3.12	7.50	18.80
3.12	4.67	15.80
3.70	33.0	28.41
3.70	12.0	22.60
3.70	7.5	19.30
3.70	4.67	15.90

Results and discussion

Impact Pressure Model-At the bottom of the water layer directly below the drop impact point, the maximum impact pressure occurs approximately 0.1 to 0.5 msec after drop-liquid impact. During that period of time the non-linear terms in the governing equations do not affect the maximum impact pressure. After the governing equations are solved numerically, the magnitude of the dimensionless point peak impact pressure, φ_c, is related to the water layer depth as shown in Fig. 7.

$$\varphi_c = = 0.2(h/d)^{-1.825} \tag{34}$$

for $0.8 < h/d < 4.0$, where d is the equivalent drop diameter. The pressure distribution along the water layer bottom when φ_c occurs is (Fig.8)

$$\varphi/\varphi_c = \exp\left[-\sum_{i=0}^{4} C_i \, (2\overset{*}{r}/h)^i\right] \tag{35}$$

in which $c_0 = -0.00942$, $c_1 = 0.01365$, $c_2 = 0.34312$, $c_3 = -0.04565$, and $c_4 = 0.00082$.

In order to compare the numerical results with experimental data, the pressure along the water layer bottom is averaged over an effective area equal to the sensing element of the transducer used[27].

This averaged maximum impact pressure p_{max} plotted against the water layer depth h for $d = 3.2mm$ is shown in Fig. 9. Excellent correlation between the numerical results and the experimental data are observed. Drop sizes of 2.7mm and 3.7mm were also investigated with equally good correlation.

Vertical Pressure Distribution—In Fig. 10, the vertical pressure distribution at four vertical cross sections, $r = 1, 5, 10$, and 20, are plotted at three time stages: one before, one near, the one after the time when maximum impact pressure occurs at the bottom of the water layer. The hydrostatic point pressure distributions are also displayed at $r = 20$.

Near the drop impact point, the point pressure increases sharply to its maximum value below the free water surface and then decreases toward the bottom. Due to the direct impact of the impinging drop, the pressure magnitude is substantially higher than that of the corresponding hydrostatic pressure. For example, the peak pressure in Fig. 10 is about 600 times its corresponding hydrostatic pressure. Although this is the case near drop impact point, the pressure distribution has the general shape of the hydrostatic distribution far away from that point. At $r = 20$, which is approximately one half inch from the drop impact point, the pressure value differs little from its corresponding hydrostatic pressure.

In analyzing shallow overland flow problems, an overpressure concept which assumes an additional dynamic prsesure in analyzing the flow problem was mathematically introduced to account for the drop impact effect by some researchers[2,6]. This study points out that the pressure away from drop impact point remains hydrostatically distributed during the drop splashing process. Even under the drop impact point, the high dynamic pressure only lasts 1 to 2 msec before it falls to a value of the same order of magnitude as the initial hydrostatic pressure. This time interval is rather short as compared with the time interval between successive drops in natural rainfall. For the drop pattern used by Wenzel et al.[29], the interval between drop impacts is approximately 0.42 sec. for a 10 in./hr. rainfall. Thus, it suggests that the overpressure concept does not prsent a theoretically accurate description under the condition of a series of single drops striking one point.

Velocity Field and Shearing Stress—In overland flow with rainfall, drops after striking the surface water layer distribute into it and generate a local disturbance which results in high resistance to flow. Thus, the velocity field after drop-liquid impact is one of the important factors in studying the drop-liquid impact process. In Fig. 11 sequences of velocity vector fields are displayed from initial impact up to the time when the crater approximately reaches its maximum size. Lines radiating from the center of each computational cell indicate both the direction and magnitude of the velocity and constitute the instantaneous velocity vector field. Fluid below the drop impact point tends to flow downward and outward, while fluid around it tends to flow outward and upward. These motions combine to form a crater below and a crown around the drop impact point. Of those drops studied, the fluid field was significantly disturbed by the impinging drop in a diameter approximately 1-inch below the drop impact point. This result is in agreement with the high resistance force reported by Wenzel et al.[29] caused by drops spaced 1-inch apart impinging on sheet flow less than one inch deep.

The spatial shear stress distribution along the bottom of the water layer as well as the shear stress time variation at a specific distance from the drop impact point is shown in Fig. 12. This figure shows a relatively high shear stress whose magnitude increases as the crater size increases. For example, the permissible unit tractive force for canals in noncohesive

material reported by U.S. Bureau of Reclamation[3] is approximately 0.04 lb/ft² for particles of average diameter of 1mm. Whereas the maximum shear stress below a 0.083 in. deep water layer is 0.18 lb/ft² with no rainfall present. Thus, the rainfall in this case increases the boundary shear by a factor of approximately 42.

When the crater reaches its maximum size, the kinetic energy of the fluid reaches a minimum. Thereafter, the fluid around the crater flows radially inward to the crater center to form a Rayleigh jet[19,30]. This back flow phase was not studied because of the large amount of computer time required. This backward fluid motion caused a radially inward shearing force which together with the initial outward shearing force could loosen any soil particles in the impact region, thus initiating the soil erosion process. The maximum shearing force occurs around the edge of the maximum crater directed radially outward suggesting that the soil erosion there is the strongest.

Free Surface Behavior—The disturbance generated by an impinging drop can best be visualized by observing the free surface configuration as a function of time.

In Fig. 13 a schematic drawing of the free surface at a specific instant after drop-liquid impact is shown. The concave surface below the drop impact point is called the crater, while the portion of fluid rising above the original water surface is the crown, and the far-reaching point of the crown in the radial direction is called the crown tip.

The time history of the behavior of the crater radius a crown tip b and the center position of the crater c after a 2.7mm drop strikes a 0.241 in. deep water layer with an impact speed 15.4 fps is shown is Fig.14. Some characteristic information are given below:

maximum crater radius=0.194 in.
maximum crater depth>0.241 in.
time to reach maximum crater radius≅15msec

For purposes of comparison experimental data obtained by Engel[4] for a 2.76mm drop striking a large water pool wth an impact speed of 13.1 fps is given below:

maximum crater radius=0.223 in.
maximum crater depth=0.286 in.
time to reach maximum crater radius=13.9msec.

The analytical results show qualitative agreement with Engel's experimental work. The difference between the two crater radii could be due to the finite boundary wall superimposed at a radius 0.506 in. from the drop impact point[31]. The bottom of the tray was exposed in the analytical study, therefore the maximum crater depth could be greater than 0.241 in. should the water layer depth be greater than 0.241 in.[30]. The crown tip behavior also shows a qualitative agreement with the photographic data obtained by Mutchler[27] of a 2.9mm drop striking a 0.114 in. water layer with a speed of 25.6 fps.

The surface disturbance can also be described by indicating variations in water depth. The depth variation at four points, r=0.016, 0.148, 0.313, and 0.616 in. from the drop impact point respectively, are shown in Fig.15. The depth varies rapidly near the drop impact point while remaining nearly unchanged at a distance of 0.5 in. The small depth variation at this radius suggests that depth measurements taken away from the drop impact point can serve as an indication of the average water depth in studying overland flow problems. The first two points are inside the crater where depth decreases rapidly. Toward the end of the sequence shown, a head between the crater center and the surrounding fluid is built which later forces the fluid to flow back into the crater center.

Surface Tension Effect—Surface tension force plays an important role in the drop impact process. In general, it stabilizes or damps free surface movement. The dimensionless impact pressure pulse at the bottom of the water layer under drop impact point is shown in Fig. 16. When surface tension force is considered, the dimensionless pressure pulse has a high peak

which occurs later in time than is the case if surface tension is excluded. Essentially, this is because the surface tension force tends to retard the radially outward fluid motion of the drop after it strikes. The same effect can be verified by examining the fluid movement. At the end of the sequences shown, the axial velocity components near the surface and the bottom of the water layer under the drop impact point are 21.45 fps and 2.19 fps respectively when surface tension force is included. The corresponding velocities excluding surface tension are 21.65 fps and 2.23 fps. At an even later stage, $t^* = 10.6$ msec, the radial velocity component at the crown tip is 4.72 fps when surface tension force is considered. Its corresponding velocity without surface tension force is 5.58 fps. Figure 16 also shows that 5.3% error will be introduced in estimating the dimensionless peak pressure value should the surface tension force be neglected in the analysis in this case.

REFERENCES

1. Boussinesq, J. Vitesse de la chute lente, devenue uniform, d'une goutte liquid spherique, dans un fluide visquex de poids specifique moindre. *Ann. Chim. Phys.*, 29, 364,(1913).
2. Chen, C.L. An analysis of overland flow, *Ph.D. thesis. Michigan State Uni.*, (1962).
3. Chow, V.T. *Open-Channel Hydraulics*. McGraw-Hill Book Company, Inc,, N.Y., (1959).
4. Engel, O.G. Crater depth in fluid impacts. *J. Appl. Phys.*, 37, 1798, (1966)
5. Gentry, R.A., Mbrtin, R.E. and Daly, B.J. An Eulerian differencing method for unsteady compressible flow problems. *J. Compu. Physics*, 1, 87,(1966).
6. Grace, R.A., and Eagleson, P.S. The modeling of overland flow. *Water Resources Res.*, 2, 393,(1966).
7. Gunn, R., and Kinzer, G.D. The terminal velocity of fall for water droplets in stagnant air. *J. Meteor.* 6, 243, (1949).
8. Haberman, W.L. and Morton, R.K. An experimental investigation of the drag and shape of air bubbles rising in various liquids. *Navy Dept. Rept.* 802, *David Taylor Model Basin, Washington, D.C.*, (1953).
9. Harlow, F.H., and Welch, J.E. Numerical calculation of time-dependent viscous, incompressible flow of fluid with free surface. *Phys. Eluids*, 8, 2182,(1965).
10. Harlow, F.H., and Shannon, J.P. Distortion of a splashing liquid drop. *Science*, 157, 547,(1967).
11. Harlow, F.H., and Shannon, J.P. The splash of a liquid drop. *J. Appl. Phys.*, 38, 3855, (1967).
12. Hirt, C.W., and Harlow, F.H. A general corrective procedure for the numerical solution of initial-value problems. *J. Compu. Phys.*, 2, 114,(1967).
13. Hirt, C.W. Heuristic stability theory for finite difference equations. *J. Compu. Phys.*, 2, 339,(1968).
14. Hirt, C.W., and Shannon, J.P. Free-surface stress conditions for incompressible-flow calculations. *J. Compu. Phys.*, 2, 403,(1968).
15. Keulegan, G.K. Spatially variable discharhe over a sloping plane. *Trans. AGU*, 25, 956, (1944).
16. Landau, L.D., and Lifshitz, E.M. *Fluid Mechanics*. Pergamon Press, London,(1959).
17. Laws, J.O. Measurements of the fall velocity of water-drops and raindrops. *Trans. AGU*, 22, 709, (1941).
18. Laws, J.O., and Farsons, D.A. The relation of raindrop-size to intensity. *Trans. AGU*, 24, 452, (1943).
19. Levich, V.G. *Physicochemical Hydrodynamics*. Prentice Hall, Englewood Gliffs, N.J., (1962).

20. Macklin, W.C., and Hobbs, P.V. Subsurface phencmena and the splashing cf drops cn shallow ljquids. *Science*, **166**, 107, (1969).
21. May, A. The influence of the proximity cf tank walls cn the waterenergy behavior of models. *NAVORD Rept.* 2240, Naval Ordance Lab., White Oak, Maryland, (1951).
22. McDcrald, J.E. The shape and aerpdynamics of large raindrops, *J. Meteo.* **11**, 478, (1954).
23. Mutchler, C.K. Parameters for describing raindrop splash. *J. Soil and Water Conservation*, **22**, 91, (1967).
24. Palmer, R.S. Waterdrop impact forces. *Paper No. 63-727, presented at the Winter Meeting of ASAE*, Chicago, Illinois, (1963).
25. Richtmyer, R.D., and Morton, K.W. *Difference Methcds for Initial Value Problems.* Interscience Publishers, N.Y., (1967).
26. Schlichting, H. *Bcundary Layer Theory*. 4th ed., McGraw-Hill Bcok Company, N.Y., (1960)
27. Wang, R.C.T. The methcanics of a drop after striking a stagnant water layer. *Ph.D. Thesis, Univ. of Illinois*, (1970).
28. Welch, J.E. et al. The MAC method-a computing technique for solving viscous, incompressible, transient fluid-flow problems involving free surfaces. *Los Alamos Sci. Lab.*, Los Alamos, New Mexico, LA-3425, (1965).
29. Wenzel, H.G., Jr., Ycon, Y.N. and Wang, R.C.T. The effect of rainfall on sheet flow. *Presented at the 50th Annual Meeting of AGU*, April 2125, (1969).
30. Worthington, A.M. *A Study of Splashes.* MacMillan Co., N.Y., (1963)·
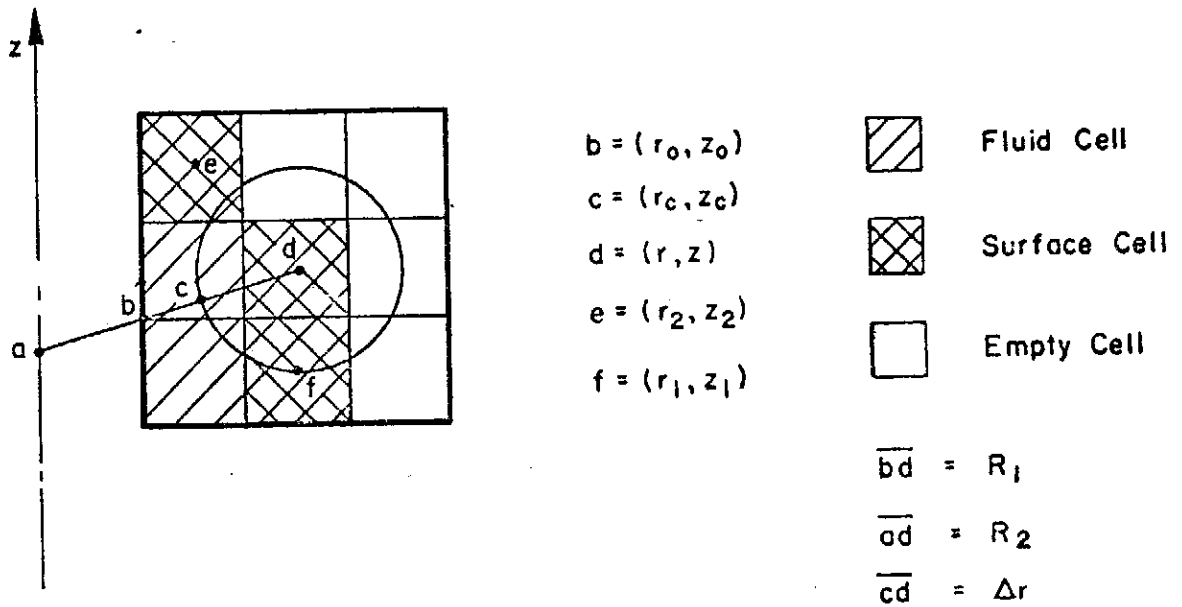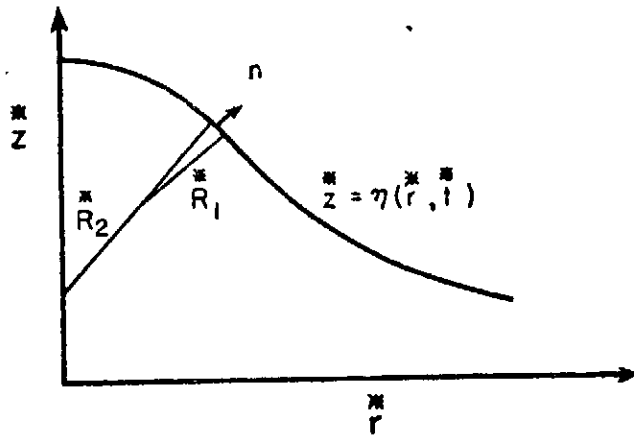
FIG. 1.-PRINCIPAL RADII OF CURVATURE

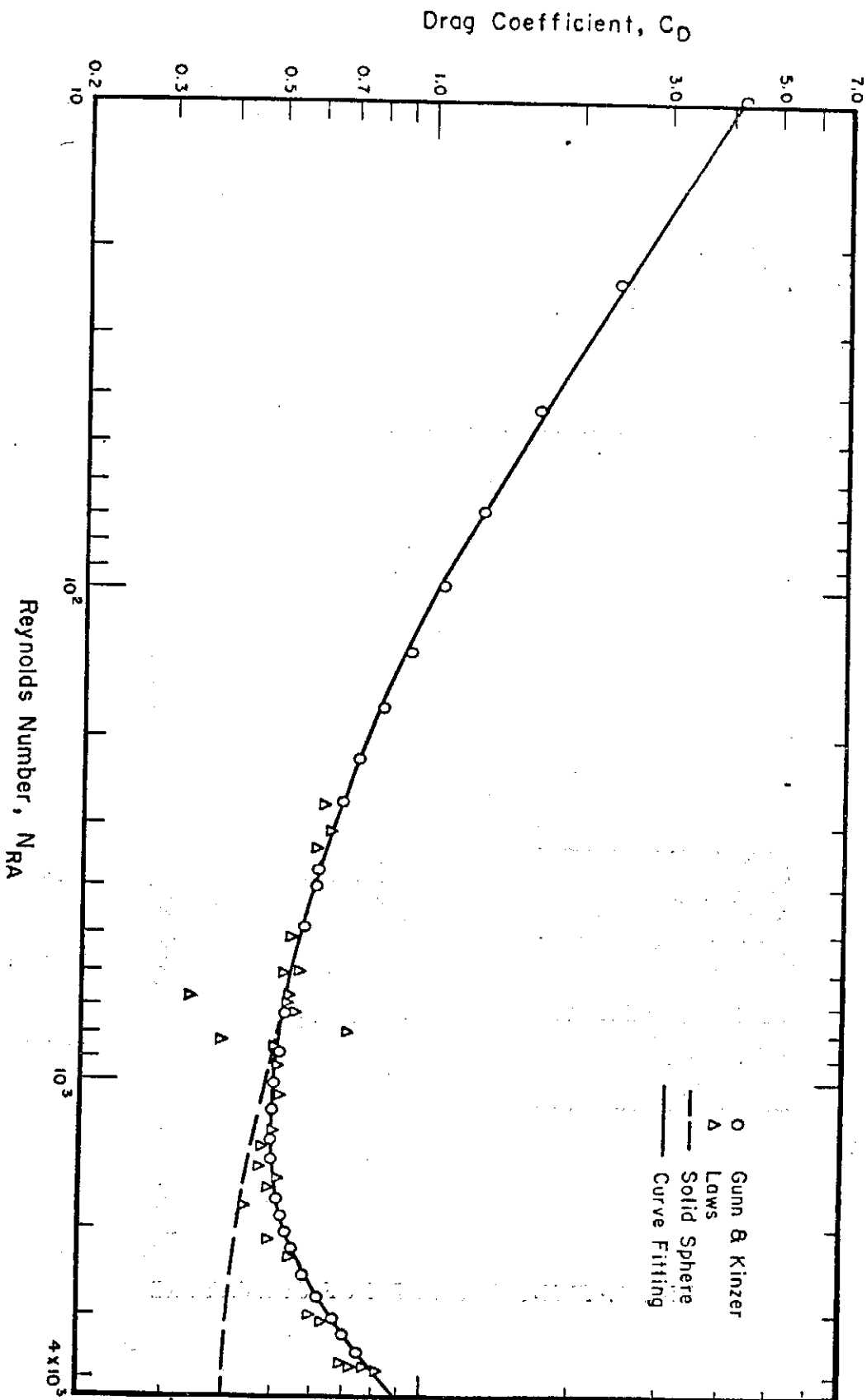FIG. 2.–DRAG COEFFICIENT VERSUS REYNOLDS NUMBER
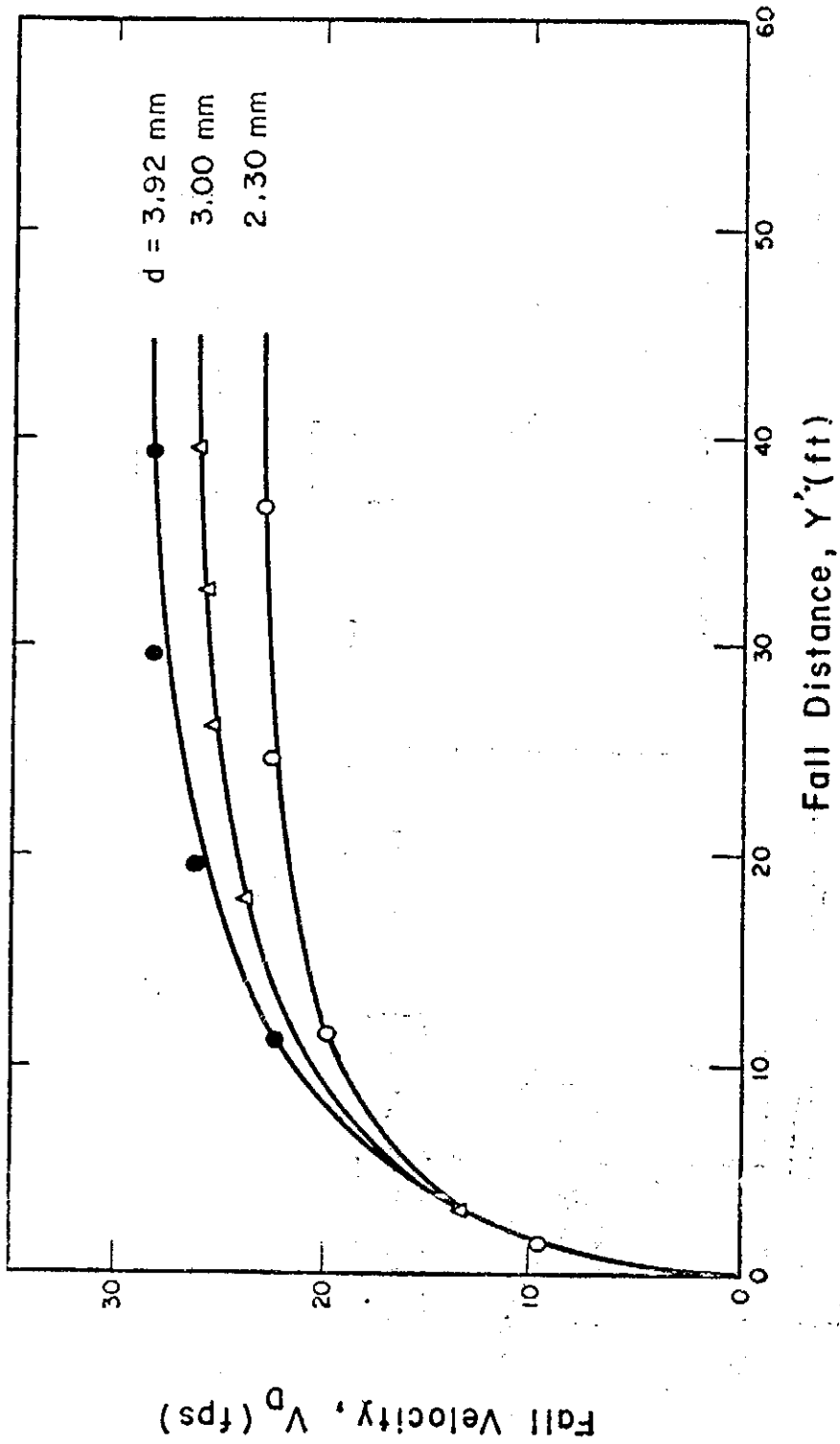
FIG. 3.-FALL VELOCITY VERSUS FALL DISTANCE

FIG. 4.–COMPUTATION CYCLE
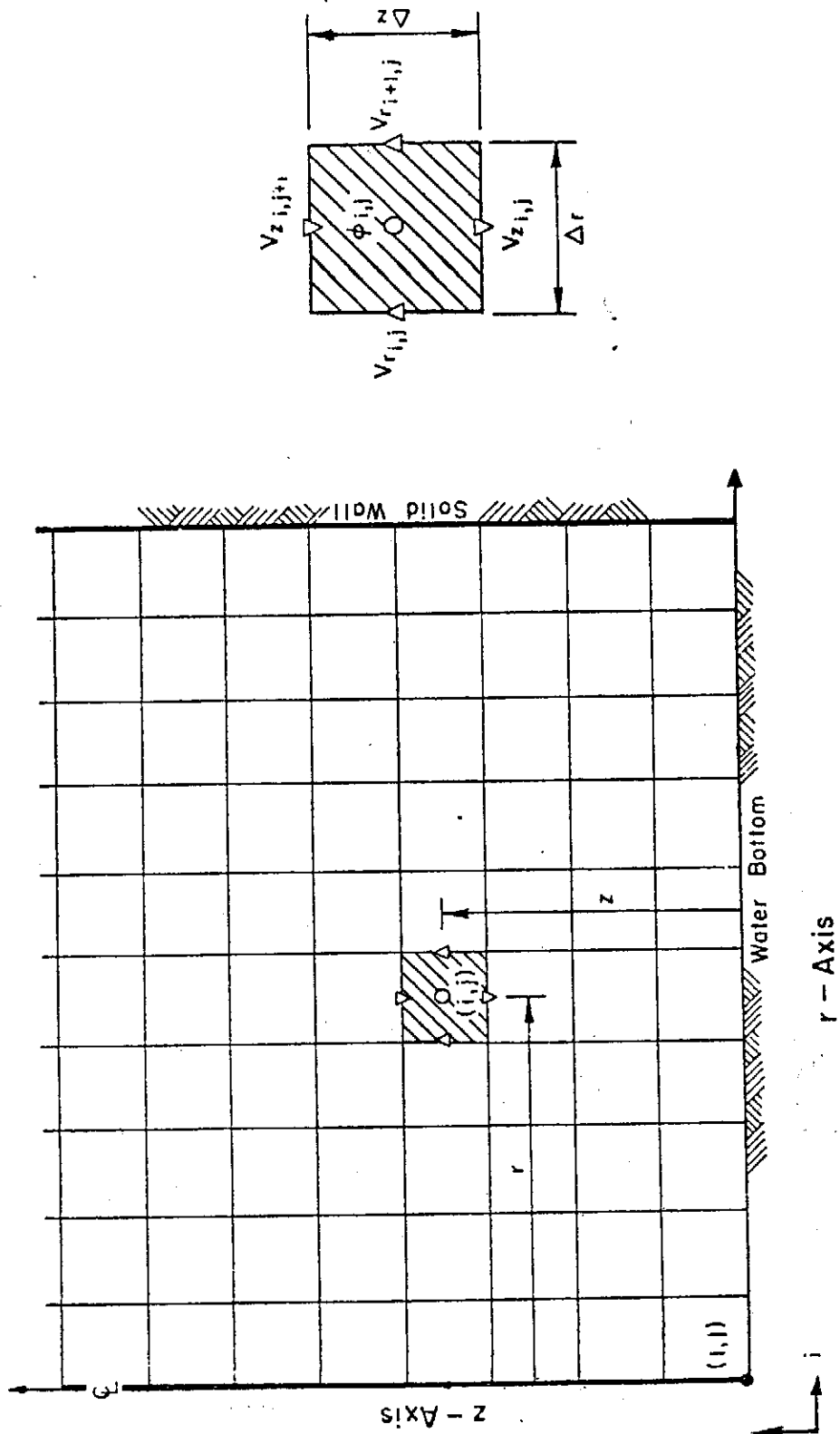
FIG. 5.–CELL CONFIGURATION
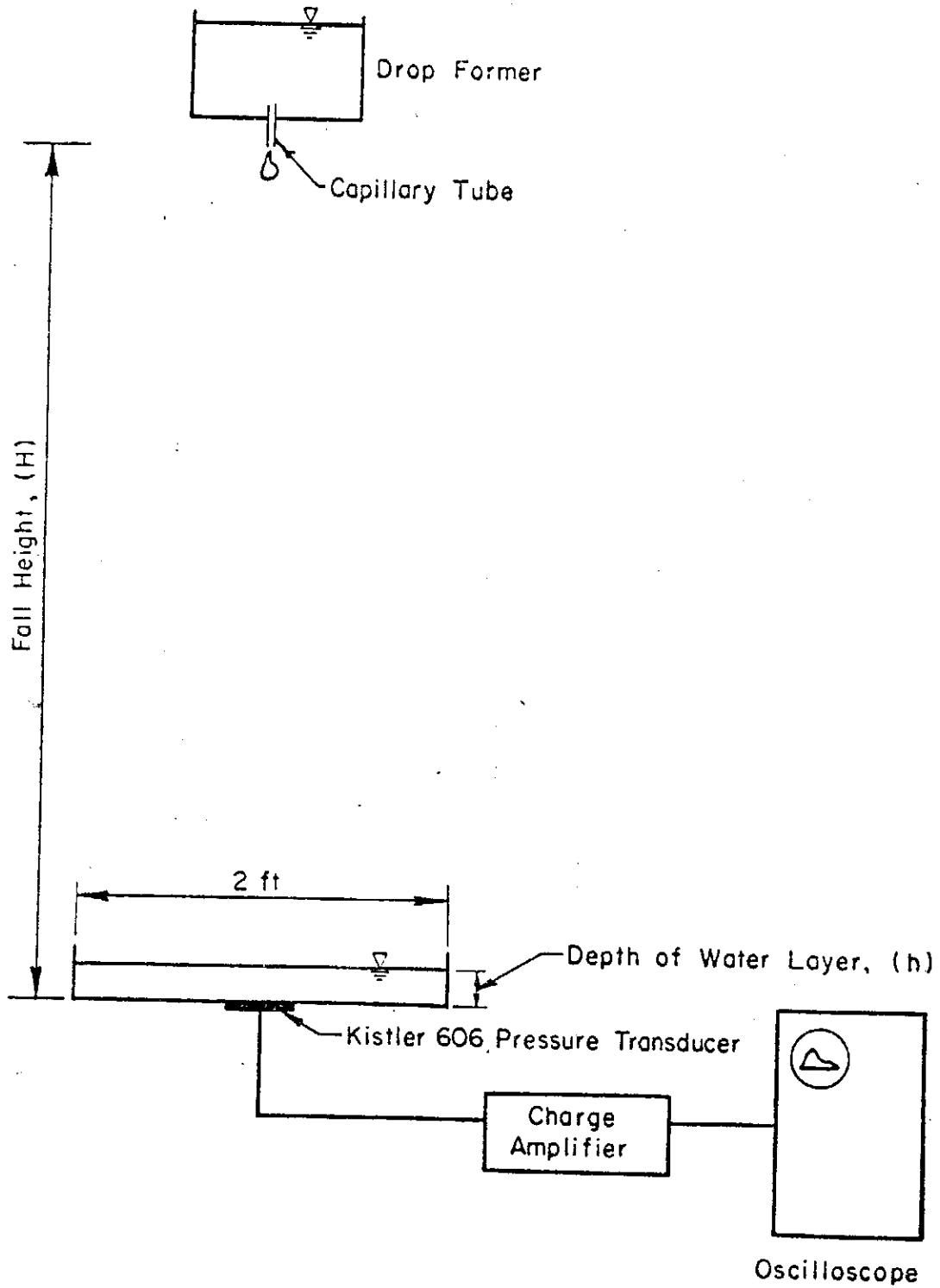
FIG. 6.–APPARATUS ARRANGEMENT
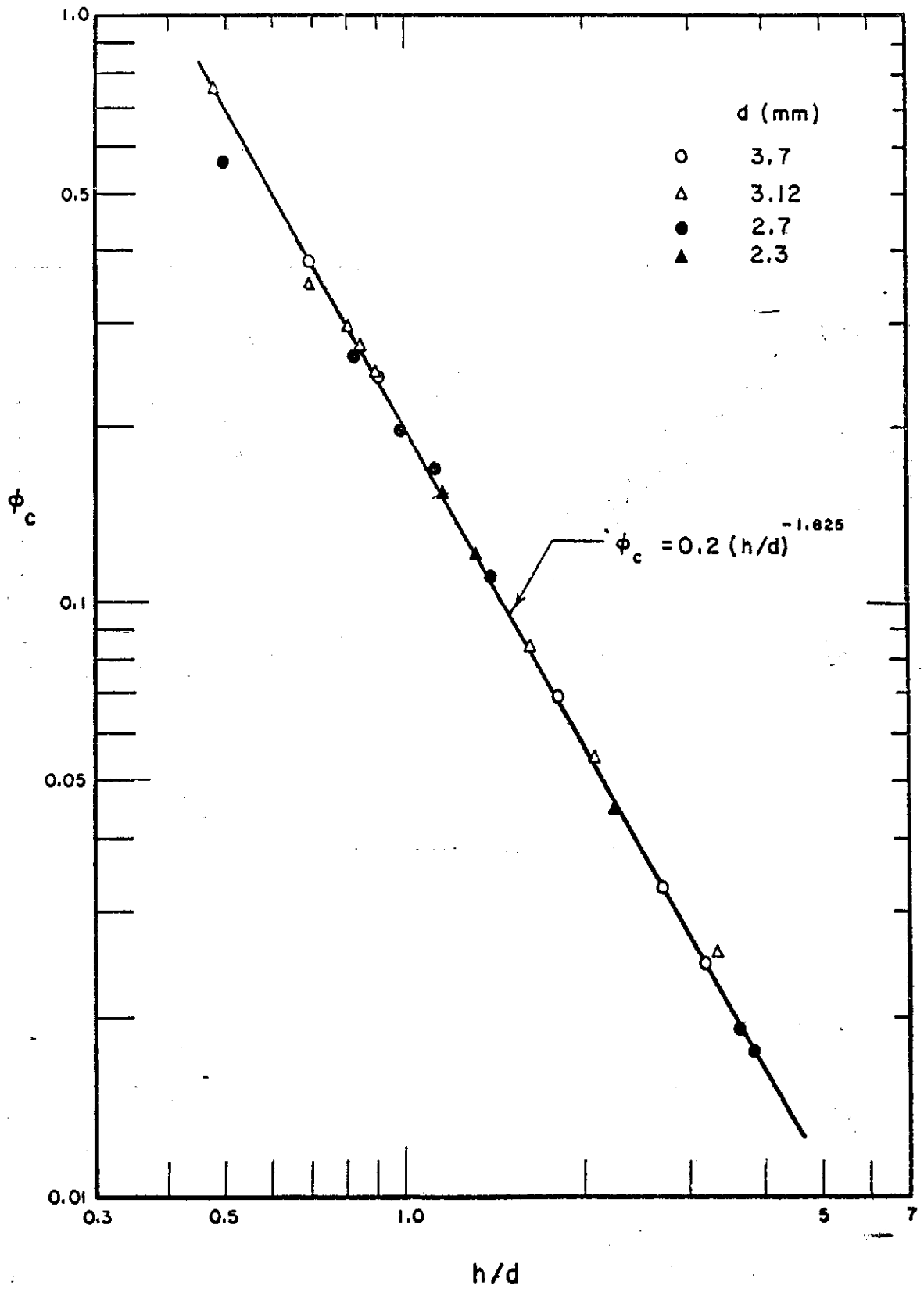
FIG. 7.–ϕ_c VERSUS h/d
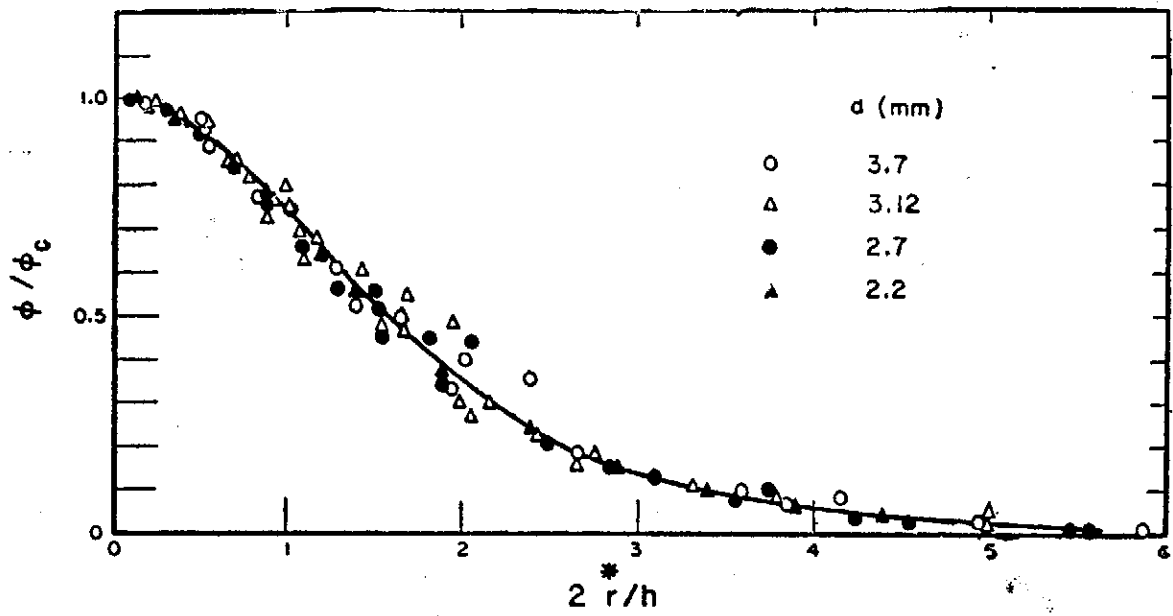
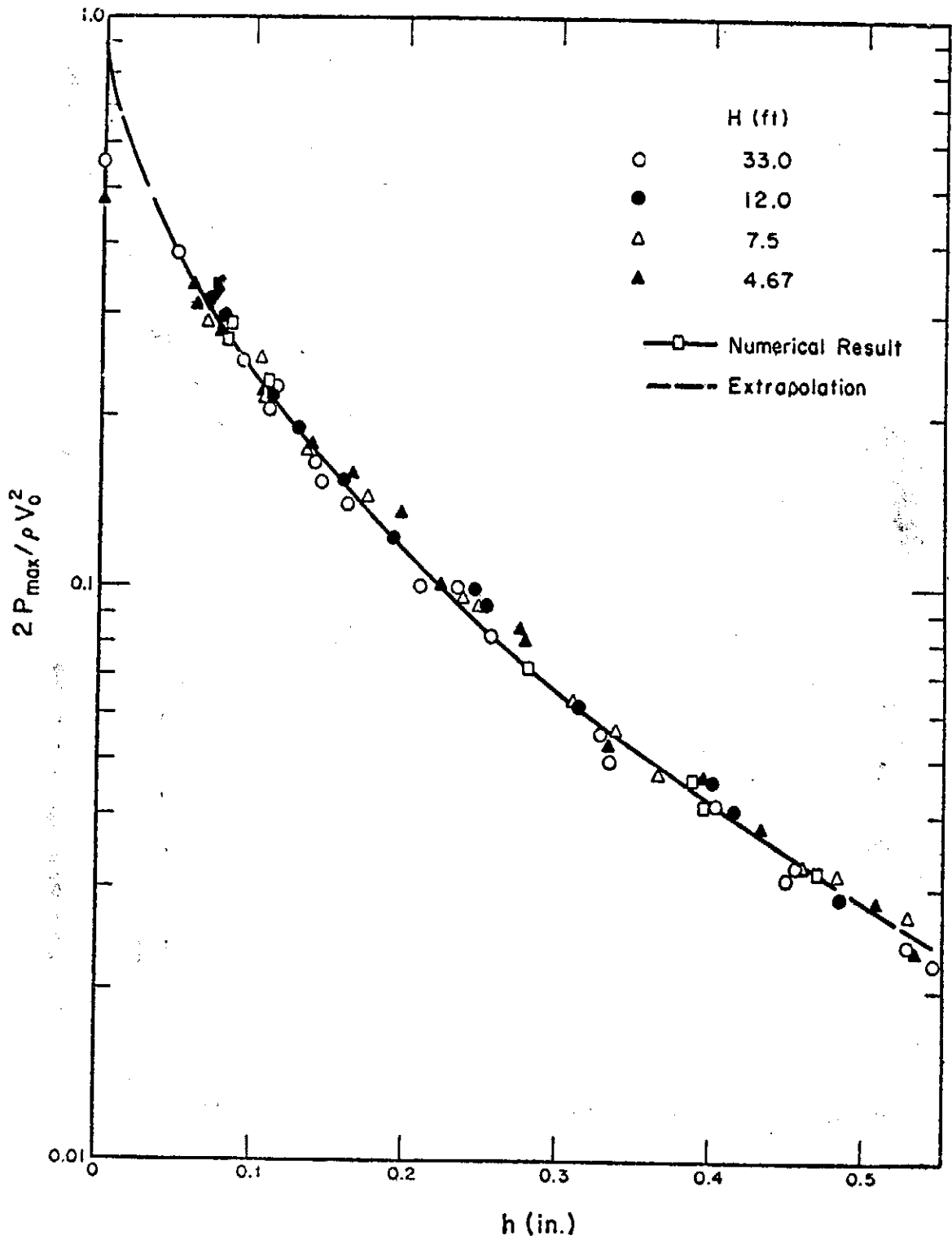FIG. 8. ϕ/ϕ_c VERSUS $2\overset{*}{r}/h$

FIG. 8.ϕ/ϕ_c VERSUS $2r/h$

FIG. 9.–DIMENSIONLESS MAXIMUM IMPACT PRESSURE VERSUS WATER
DEPTH FOR $d=3.12$mm
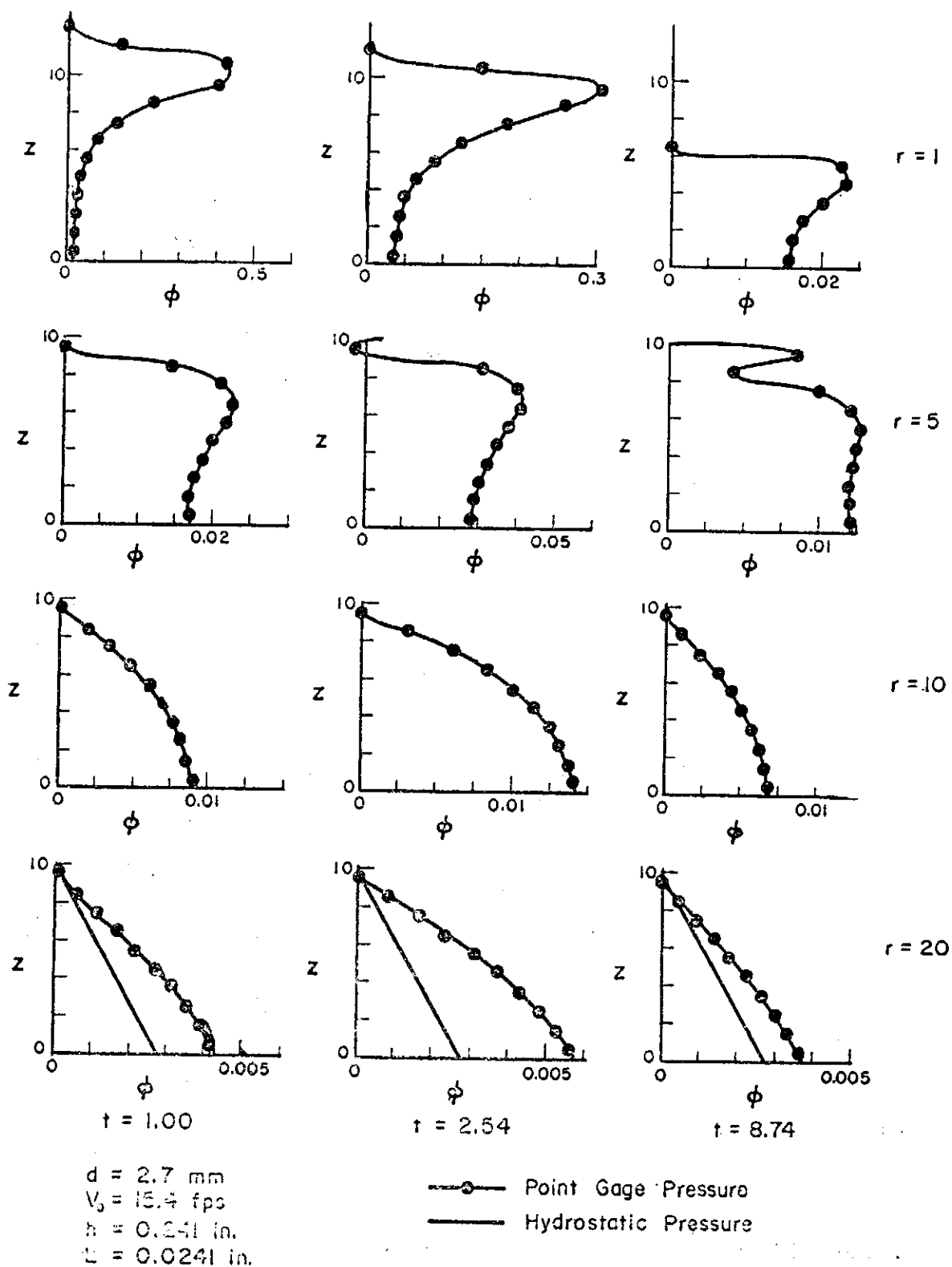
FIG. 10.–VERTICAL PRESSURE DISTRIBUTION

FIG. 11.–VELOCITY VECTOR FIELD
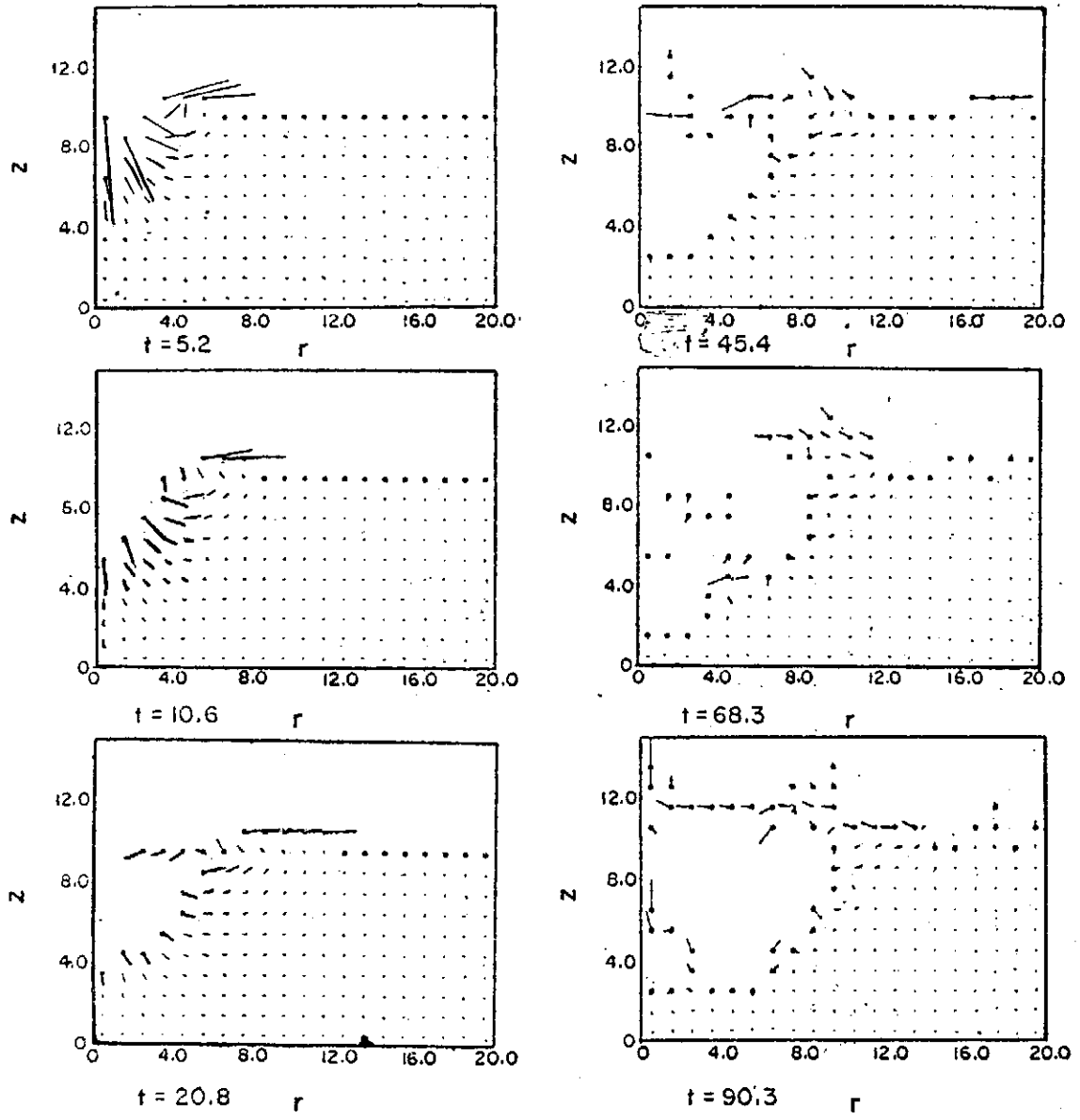
d = 2.7 mm   h = 0.241 in.
V_o = 15.4 fps   R = 0.506 in.
                 L = 0.0241 in.

V_o

Scale
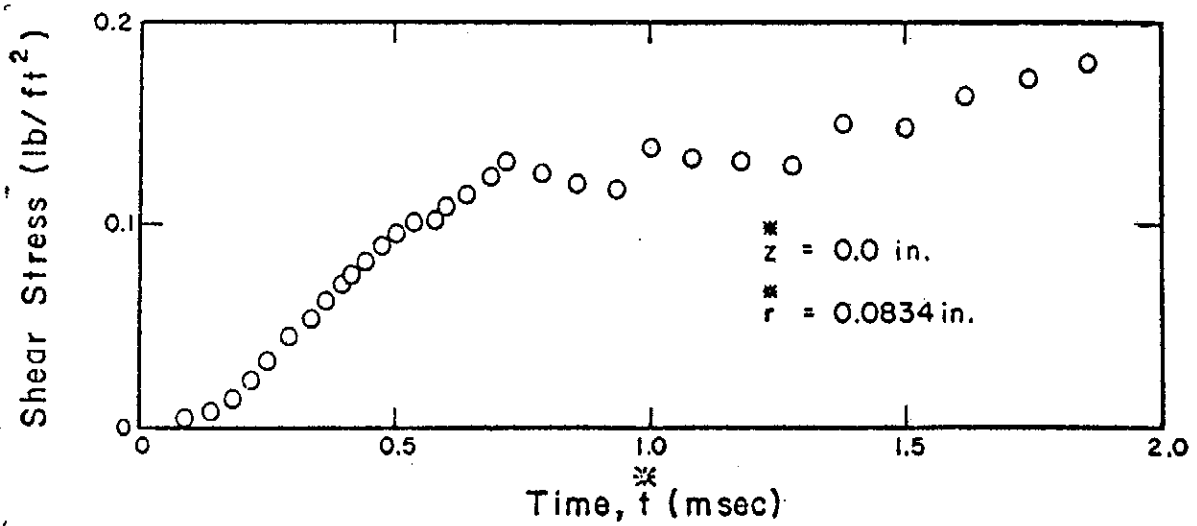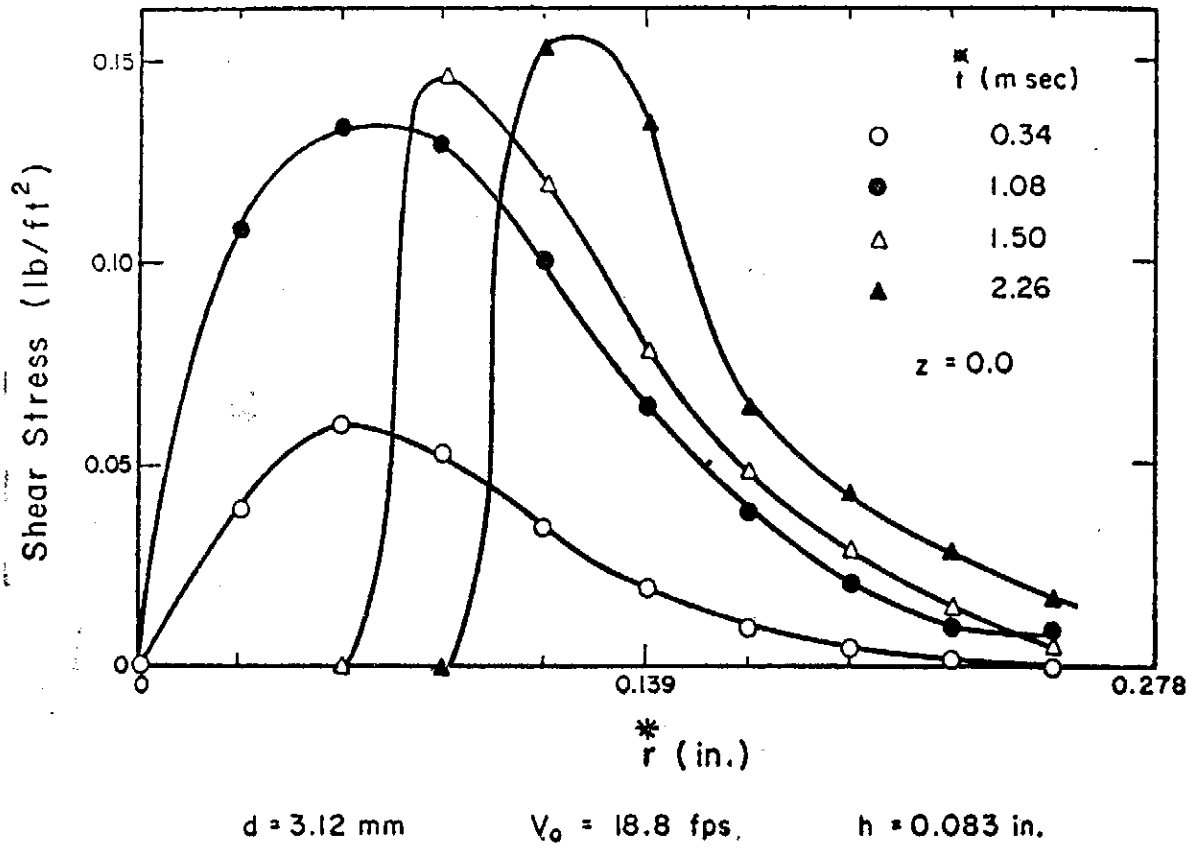
FIG. 12.–SHEARING STRESS FIELD
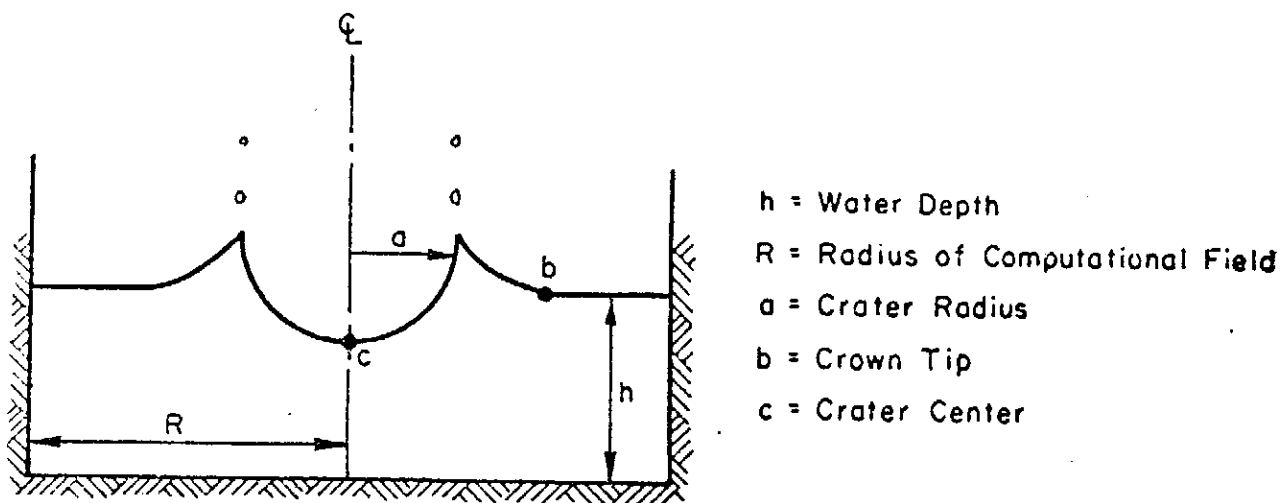
FIG. 13.-FLUID PATTERN

h = Water Depth

R = Radius of Computational Field

a = Crater Radius

b = Crown Tip

c = Crater Center

FIG. 14.–FLUID MOVEMENT

FIG. 15.–DEPTH VARIATION

Einfluss des Turbulenzgrades auf den Sog

紊流度對推力減少影響之研究

戴　堯　天 (Yau-Tien Dai)

Institute of Physics, Academia Sinica

摘　　要

德國 Blohm u. Voss 船廠所造 Pioneer 型船以其異於一般船型之直板遶接而能在巡航速度下達到0.78~0.82 之推進效率實屬難能可貴，究其原因，實由於該種船型之推力減少值（t=0.1）較一般船隻為低所致，然何以其推力減少值能減至如此低值，據作者推測有以下四種因素：

①由於球形船艏之影響。

②由於船艉紊流之影響。

③由於該船俥葉與船艉間空間較大。

④由於相對增大之俥葉直徑。

一般航行於實際流體中之船隻，由於邊界層之存在而改變了船艉之似長和形狀加上俥葉之作用更影響了壓力之分佈，亦即在艉部產生一較艏為低之壓力而使船體受一壓差阻力，如能使船艉之低壓減少或降低推力減少值，當可減少船隻之阻力，而增加船之推進效率。

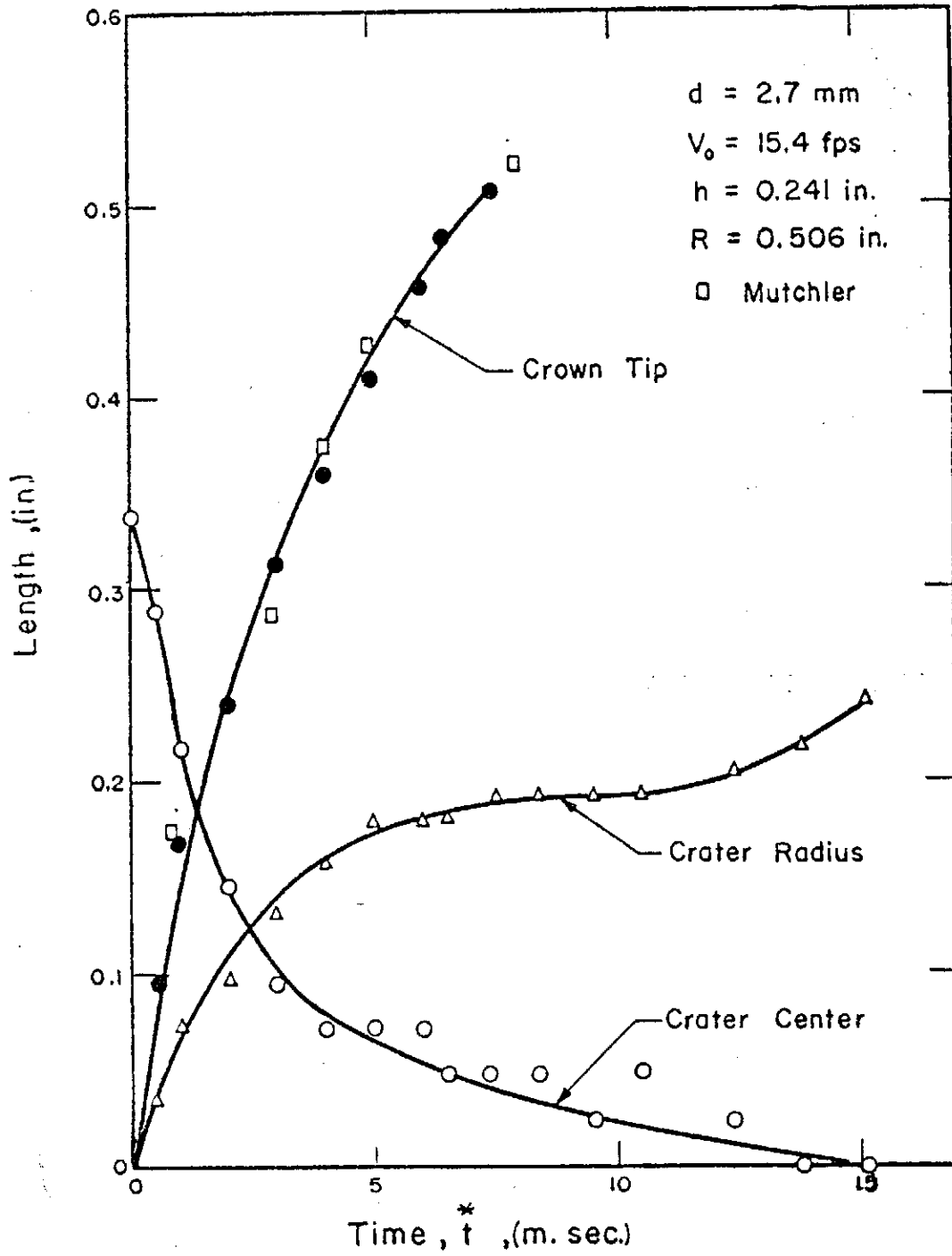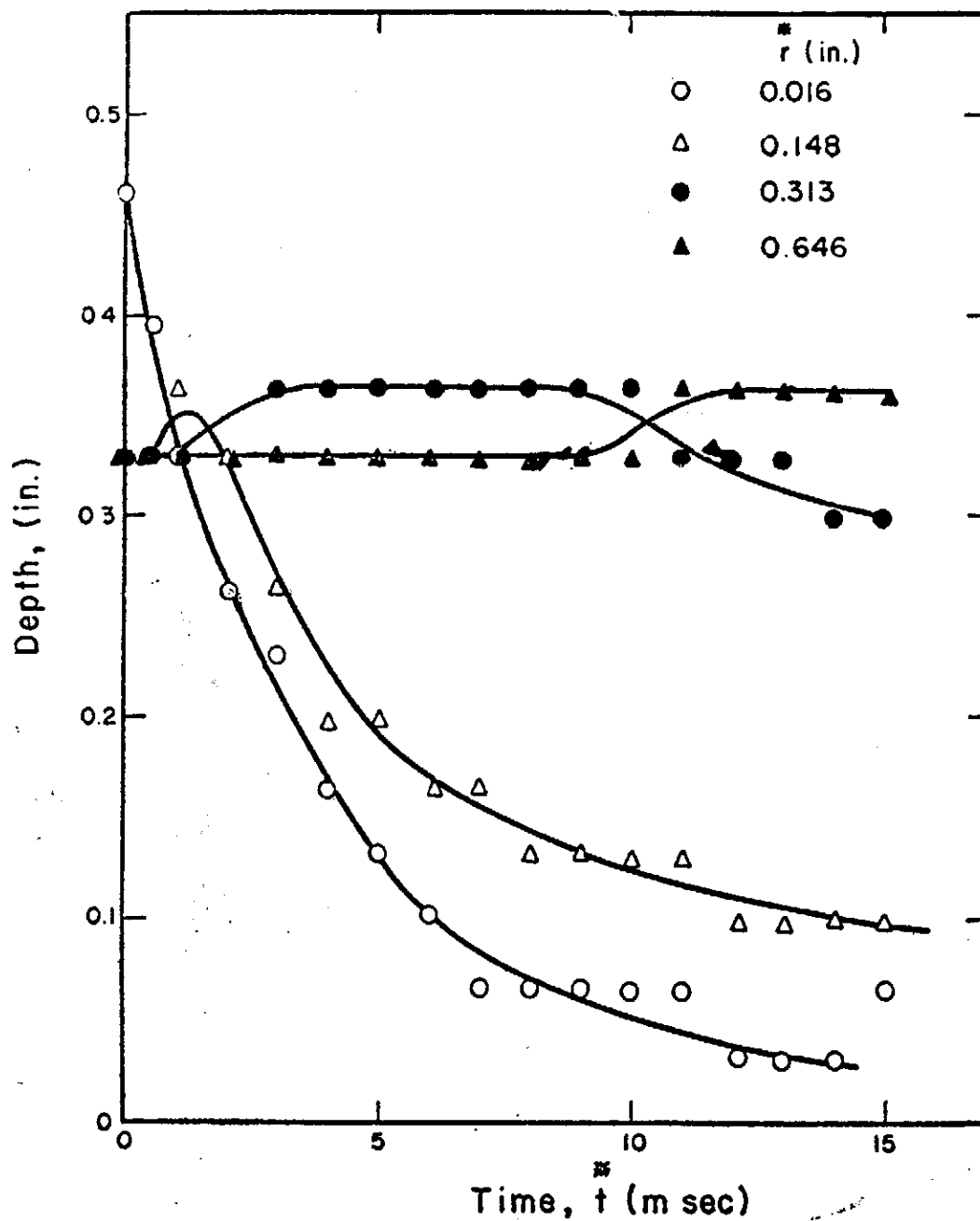由於 Pioneer 型船之啓示，作者試以各種不同之紊流增強器置於船模 M-611-Göteborg 距後垂標1/20船長處，在西德杜伊斯堡船模試驗室 (Versuchsanstalt Für Binnenschiffbau E. V. Duisburg) 作阻力及推進試驗，其結果雖由於加了紊流產生器後阻力均略有增加，但在推力減少上，由於加了某種紊流增強器（如試驗四），當 $F_n < 0,28$ 時確可使之減低，而增加船之推進效率幾達 6%。

這種由於紊流增強器使船艉流體之分離點後移，減少跡流範圍而使船艉低壓部分之面積減小，以及使推力減少值降低的現象確可使瘦狹船隻產生良好的影響，惟如運用於實際船舶是否能獲同樣效果，有無其他更好的紊流增強器及安裝位置，以及其適用於何種船舶，則尚有待進一步之研討。

1. Einleitung

Die nachfolgend durchgeführten und beschriebenen Versuch stellen insofern ein Novum dar, als Zusammenhänge zwischen Sog und Turbulenzgrad bisher m. W. nicht behandelt wurden. Die Anregung zu dieser Untersuchung lieferten die Versuche mit dem "PIONEER"-Typ von Blohm u. Voss[1]. Dieses Schiff mit vereinfachter Außenhautform—die mit Ausnahme des Bug- und Heckwulstes aus ebenen Flächen zusammengesetzt ist—erreicht bei Konstruktionsgeschwindigkeit einen Propulsionsgütegrad von $\eta_D = 0,78\sim0,82$.

Dieser hohe Propulsionsgütegrad ist vor allem auf eine für Frachtschiffverhältnisse außerordentlich geringe Sogziffer zurückzuführen. Für das Pioneerschiff " JAG DEV " (Pioneer-Variante II/III) gelten folgende Daten[4]

L_{pp} = 151,45　　m

B　 = 22,80　　m

T　 = 10,38　　m

$\triangle$　 = 27850　　t

D_p　 = 6,3　　m

δ_{pp}　 = 0,745

β　 = 0,995

φ　 = 0,748

α　 = 0,88

P_D = 8640 PS
V = 16,6 kn
F_n = 0,222
t = 0,1
w = 0,285

Die Werte t und w sind der Veröffentlichung über das Pioneer-System[1] entnommen; sie können auch für "*JAG DEV*" als gültig angesehen werden, da die Schiffsdaten nur geringfügig geändert wurden.

Wie ungewöhnlich niedrig diese Sogziffer ist, zeigt ein Vergleich mit Überschlagsformeln und allgemeingültigen Diagrammen:

1) Heckscher t = $0,5\varphi - 0,12$ = 0,254
2) Schoenherr t = $k \cdot w = 0,7 \cdot 0,285$ = 0,20
3) Göteborg t = $w(1,57 - 2,3\dfrac{\delta}{\alpha} + 1,5\delta)$ = 0,214
4) Harvald   n.Diagr.[4] S.430 t = 0,250
5) Schiffbaukalender 1942, S. 214 t = 0,223

Arithmetisches Mittel $\bar{t}$ = 0,228

Die im Tank gemessene Sogziffer für den Pioneer liegt also um mehr als 0.1 (oder 56%) niedriger als der o.a. Mittelwert.

Die Nachstromziffer liegt mit $w = 0,285$ nur wenig unter dem üblichen Rahmen, wie nachfolgende Aufstellung von Normwerten zeigt.

1) Taylor w = $0,05 + 0,5$ = 0,323
2) Papmehl w = $0,22\delta \sqrt{\dfrac{\sqrt[3]{V}}{D_p}}$ = 0,359
3) Heckscher w = $0,7\varphi - 0,18$ = 0,345
4) Harvald   n.Diagr.[4] S. 426 w = 0,34
5) Schiffbaukalender 1942, S. 214 w = 0,32

Arithmetisches Mittel $\bar{w}$ = 0,337

Dadurch ergeben sich folgende Relationen:

	w/t	$\dfrac{1-t}{1-w}$
"JAG DEV"	2,85	1,26
Mittel der Normalwerte	1,48	1,165

Die etwas geringere als normale Nachstromziffer beim Pioneer bedeutet nicht unbedingt, daß der Energieinhalt des Nachstroms auch geringer als normal ist. Im Falle starker Turbulenz—wie hier als Folge der kantigen Schiffsform anzunehmen ist—kann der Inhalt an kinetischer Energie trotzdem größer als im Normalfall sein.

Es ergibt sich die Frage: Warum ist bei den Pioneer-Schiffen die Sogziffer in einem solchen Maße niedriger als der Durchschnitt?
Naheliegende Gründe dafür sind:

1. der in den letzten Jahren ständig vergrößerte Freischlag zwischen Propeller und Propellersteven,
2. der relativ große Propellerdurchmesser,
3. die Wulstheckform.

Eine persönliche Vermutung, daß auch die sehr niedrige Sogziffer eine Funktion des Turbulenzgrades sein könnte[5], sollte mit den unter 3. beschriebenen Versuchen geprüft werden. Die Turbulenzerzeuger wurden nach folgenden Gesichtspunkten installiert:

1. Abstand vom Propeller so groß, daß sich der Propellersog wenig auswirkt, (Abstand der suf Spant 1 angeordneten Turbulenzerzeuger vom Propeller ist größer als ein Propellerdurchmesser),

2. Ausdehnung in der Spantebene so, daß der turbulente strömungsquerschnitt nicht oder nur wenig über den Propellerkreis hinausreicht,

3. Kleiner Widerstand des Turbulenzerzeugers im Verhältnis zum Turbulenzgrad.

Es wurden folgende Turbulenzerzeuger untersucht:

a) Zylinderkörper (Stäbe aus Rundnägeln ohne Kopf),

b) Zylinderkörper mit "Fähnchen" aus 8 mm breiter rauher Kunststoff-Folie,

c) rechteckige Leitflächen in verschiedener Zahl und Anordnung.

2. Diskussion und Bewertung der Versuchsergebnisse

Die Vorversuche zur Auswahl der leistungsgünstigsten Anordnung ergaben die Aussicht auf eine Reduktion der erforderlichen Antriebsleistung bel den Varianten mit zwei schräg zur Strömung gestellten Blechen als Turbulenzerzeuger anf K—Spant 1.

Die Ergebnisse dieser Anordnungen werden unter 3.2 diskutiert und mit der Anordnung 3 Reihen zylindrische Turbulenzerzeuger" sowie mit dem ursprünglichen Modell verglichen.

Die Turbulenzerzeuger hatten in jedem Fall eine Widerstandserhöhung zur Folge, die sich für jede einzelne Anordnung in ihrer absoluten Größe nur wenig über der Geschwindigkeit änderte. Bei höheren Geschwindigkeiten macht sich offensichtich der Grenzschichteinfluß stärker bemerkbar.

Die Nachstromziffer lag bei den Versuchen mit zylindrischen Turbulenzerzeugern (3 Reihen Nägel) etwas über den Werten für das nackte Modell. Bei Verwendung von nur 2 schräg zur Strömung gestellten Blechen lag die Nachstromziffer im unteren Geschwindigkeitsbereich ($F_n < 0,25$) unterhalb des Wertes für das nackte Modell, im hohen Geschwindigkeitsbereich darüber.

Die Sogziffer war bei Verwendung zylindrischer Turbulenzerzeuger im gesamten Geschwindigkeitsbereich höher als die des nackten Modells. Bei den schräggestellten Blechen lag die Sogziffer im unteren Geschwindigkeitsbereich ($F_n < 0,26$ bzw. 0,28) z.T. erheblich unter der des nackten Modells, bei hohen Geschwindigkeiten darüber. Der vermutete Sogminderungseffekt ist damit für einen großen Bereich festgestellt worden.

Der Propulsionsgütegrad war bei den zylindrischen Turbulenzerzeugern über den gesametn Geschwindigkeitsbereich schlechter als der des ursprünglichen Modells. Die schräggestellten Bleche erzielten dagegen im Bereich unterhalb der Froudeschen Zahl 0,26 bzw. 0,28 erhebliche Verbesserungen.

Der Leistungsbedarf liegt im allgemeinen höher als für das ursprüngliche Modell. Jedoch konnten mit den schräggestellten Blechen im Bereich unter $F_n = 0,26$ Gewinne erzielt werden, die unterhalb $F_n = 0,25$ den Wert von 6% überschritten.

Eine eindeutige physikalische Erklärung ist mit den Ergebnissen dieser Versuche noch nicht möglich. Die Wirkung ist so, als übertrüge stark verwirbeltes Wasser den Druckabfall in geringerem Maße als weniger verwirbeltes Wasser.

Offene Fragen sind dabei:

1.) Die Übertragbarkeit der Versuche anf die Großausführung,

2.) die physikalische Erklarung des Effekts,

3.) die Optimierung der Turbulenzerzeuger,

4.) die Auswahl geeigneter Schiffstypen.

Zu 1.)

Da eine Abhängigkeit der Ergebnisse von der Reynolds'schen Zahl zu erwarten ist, sind zur Prüfung der Übertragbarkeit Geosimversuche angebracht, bei denen zunächst auf die Untersuchung der Großausführung verzichtet werden soll.

Zu 2.)

Zur physikalischen Erklärung des Effekts wäre es zweckmäßig, den Sog direkt zu messen. Be den vorliegenden Versuchen wurde der Sog aus dem Propellerschub-Widerstandsverhältnis errechnet. Besser wäre es, auch den Turbulenzgrad in weitem Bereich zu messen. (Druckdifferenzmessung an der Außenhaut mit Hilfe neuartiger Pitrans und Hot-f:lm Probe).

Zu .3)

Zur Optimierung der Turbulenzerzeuger wären Form und Anbringungsart zu variieren.

Zu 4.)

Inzwischen sind bei der Hamburgischen Schiffbauversuchsanstalt-im Auftrag des Forschungszentrum des deutschen Schiffbaus und bei der VBD-Versuche mit Turbulenzerzeugern an Tankermodellen großer Völligkeit durchgeführt worden.

In beiden Fällen waren die erforderlichen Leistungen um 1-3% höher als für das nackte Modell.

Als Turbulenzerzeuger wurden in beiden Fällen die optimalen der beschriebenen Versuche verwendet. (Beide Versuchsserien sind noch nicht veröffentlicht worden).

Diess Versuche lassen erkennen, daß Turbulenzerzeuger bei völligen Schiffen keinen Sogminderungseffekt zeigen. Hingegen scheint eine Fortführung der Versuche bei Schiffen kleiner Völligkeit sinnvoll zu sein.

3. Modellversuche

3.1 Versuchsvorbereitung

Das für die Untersuchunng verwedete Schiffsmodell wurde aus der Göteborg-Serie 1 ausgewählt. Besonders geeignet schien die Nr. 835 mit einem Völligkeitsgrad von 0,597. Die Schiffs-, Propeller- und Ruderabmessungen sind der folgenden Tabelle, der Spantenriß der Anlage 1 zuentnehmen.

1. Modell

VBD-Modell Nr.			M 611
Maßstab		—	25
Länge zw. de. Loten	$L_{pp(m)}$	m	4,800
Breite auf Spant	$B_{a,Spt,(m)}$	m	0,680
Tiefgang	$T_{(m)}$	m	0,2833
Länge i. d. WL	$L_{WL(m)}$	m	4,920
Verdrängung a. Spant	$V_{a,Spt,}$	dm³	552,32
Benetzte Oberfläche	$S_{(m)}$	dm²	419,90
Völligkeitsgrad	δ_{WL}	—	0,583
	δ_{pp}	—	0,597

2. Ruder

Ruder–Nr.			301
Fläch	A_r	dm^2	2,251
Seitenverhältnis	C/h	—	0,557
Streckung	h^2/A_r	—	1,800
Dickenverhältnis	t/C	—	0,1786

3. Propeller

Propeller–Nr.			130 r
Typ			B 455/Wageningen
Durchmesser	D	mm	180,0
Steigung	P	mm	180,0
Steigungsverhältnis	P/D	—	1,0
Flächenverhältnis	A_o/A_o	—	0,55
Dickenverhältnis	t/D	—	0,045
Blattlänge	$C_{0,7r}$	mm	53,05
Flügelzahl	z	—	4

Nach den Erläuterungen in Abschnitt 1 schien für den Anbringungsort der Turbulenzerzeuger der Spant 1 am sinnvollsten.

Als Turbulenzerzeuger dienten horizontal und rechtwinklig zur Schiffsachse stehende Rundstäbe (in Form von kopflosen Nägeln) bzw. Flachstäbe im Dickenverhältnis 1:10 mit Anstellwinkeln von 10° und 25°. Art und Anordnung sind der Reihenfolge nach den Anlagen 2 bis 6 zu entnehmen.

Da bei diesen ersten grundsätzlichen Untersuchungen der Ungewißheit des Erfolges wegen keine speziellen Meßanlagen mit sehr hohen Aufwendungen geplant waren, kam es auf besonders exakte Erfassung der Meßwerte auf herkömmlichem Wege an.

Infolgedessen mußte eines der Kempf- und Remmers-Drehmomentdynamometer sorgfältig hergerichtet und vor jedem neuen Versuch geeicht werden. Darüber hinaus wurde die Empfindlichkeit des Meßpendels am Schleppwagen erhöht. Die für die Errechnung der Sog–und Nachstromziffer notwendigen Komponenten

Widerstand	R_T	[kp]
Drehmoment	Q	[mkp]
Drehzahl	n	[Upm]
Schub	T	[kp]

in Abhängigkeit von der Geschwindigkeit sowie die Grundwerte des freifahrenden Propellers sind also mechanisch ermittelt, und die Genauigkeit ist durch zweimalige Wiederholung jeder einzelnen Fahrt weiter gesteigers worden.

Der große Schlepptank der VBD hat eine Seitenhöhe von 1,2m. Um während der Versuchsfahrten Wasserverluste durch am Tankrand und am Tankende überschlagende Wellen zu vermeiden, wurde die Wasserhöhe auf 1000mm einreguliert und das Modell auf Kunstruktionstiefgang von 283,3mm mit $\forall$ =552,3dm^3 gefahren.

Um die Meßwerte nach den bekannten Verfahren auszustraken, wurden spezielle Meßblätter und Diagrammformulare vorbereitet. Aus diesen sind ann die Rechenwerte in 2 bzw. 1 kn Staffelung ausgewählt und in Form der am Schluß des Textes angeordneten Tabellen zusammengefaßt worden.

3.2 Vorversuche

Bei Beginn der Untersuchungen mit den notwendigen zeitlichen Unterbrechungen zweck

Auswertung der Meßergebnisse zeigte sich, daß schon durch kleine Unterschiede in der Oberflächenrauhigkeit Differenzen auftreten können, die letztlich trotz größter Sorgfalt eine Schwankung der Sogziffer um ± 20 % ausmachen können. Später wurden die in den Anlagen 2 bis 6 gezeigten Varianten der Turbulenzerzeuger zn den Vorversuchen gezählt und erst nach Auswertung und Diskussion der Ergebnisse die jenigen Formen und Anordnungen weiterverfolgt, die den günstigsten Effekt versprachen. Als Hauptversuche ohne Unterbrechnung bei annähernd gleicher Tankwassertemperatur und gleichen äußeren Bedingungen ausgeführt, erlaubten sie den gewünschten echten spezifischen Vergleich!

Im Rahmen der Vorversuche wnrde auch die Propellerfreifahrt, deren Ergebnisse in Anlage 7 dargestellt sind, ansgeführt.

Die nach der herkömmlichen Propulsionsrechnung gewonnenen Werte für

Widerstand	P_z	[EPS]
Leistung	P_D	[WPS]
Nachstrom	w	[—]
und Sog	t	[—]

werden zu Vergleichsdiagrammen zusammengefaßt und in den Anlagen 8, 9 und 10 dargestellt. Die nachfolgende Tabelle stellt nun zum Abschluß der Vorversuche den Vergleich des Leistungsverhaltens, bezogen auf das Modell ohne künstliche Turbulenzerzeuger dar, damit der Weg für die Wahl weiterer Turbulenzerzeuger (T.E.) der Hauptversuche gewiesen ist.

Leistungsverhalten der Vorversuchs-Varianten (Strakwerte)

v_s	ohne T.E.	3 Rheihen Nägel	5 Bleche	1 Rheine Nägel	3 Bleche	2 Bleche
[kn]	P_D	P_D	P_D	P_D	P_D	P_D
16	3720	4280	4062	4253	4240	4060
17	5250	5800	5347	5495	5400	5230
17.5	6220	6750	6200	6295	6180	6030
18	7300	7800	7204	7310	7080	6980
18.5	9050	9050	8620	8377		

3.3 Hauptversuche

Nach Kenntnis der Vorversuchs-Ergebnisse sind nunmehr die Hauptversuche vorbereitet worden, die ohne Unterbrechung hintereinander gefahren werden mußten. Es wurden folgende vier Modellzustände vergleichend geprüft:

Haupt.Vers.-Nr	Turbulenzerzeuger	Darstellung
1	ohne	Anlage 1
2	3 Reihen Nägel an BB und StB auf Spt. 1, Nägel von 2,5mm und 40mm Länge	Anlage 2
3	2 Bleche von 40mm × 10mm × 1mm an BB u. StB an Spt. 1; 25° Anstellung gegenüber Basis: Öffnungswinkel konvergierend, Kanten gut gerundet	Anlage 7

4	2 Bleche von 40mm×10mm×1mm an BB u. StB an Spt. 1; 25° Anstellung gegenüber Basis; Öffnungswinkel divergierend, Vorkanten gut gerundet	Anlage 3

3.4 Zusammenfassung

In dem Göteborg-Modell Nr.835 (VBD-Nr.611) im Maßstab 1:25, $\delta = 0,597$, sind bei Spant 1 symmetrisch zur Propellerachse verschiedenartige Turbulenzerzeuger angebracht worden, um zu prüfen, ob eine Verbesserung der Sogziffer und damit des Propulsionsgütegrades zu erzielen ist. Diese Turbulenzerzeuger sollten den jenigen der aerodynamischen Untersuchungen an Tragflügeln ähneln, jedoch auf die hydrodynamischen Bedingungen des Schiffes und des Propellers abgestimmt sein. Jede Variante ist durch eine Zeichnung belegt, und die Versuchsergebnisse sind in zwei Gruppen den Vorversuchen und den Hauptversuchen dargestellt. Die aus versuchstechnischen Gründen an einem Tag hintereinander ausgeführten Hauptversuche geben klare Auskunft über die günstigste Form und Anordnung solcher Turbulenzerzeuger und lassen auch quantitativ erkennen, welcher Verbesserung die Gütegrade bei einem solchem Seeschiff unterliegen.
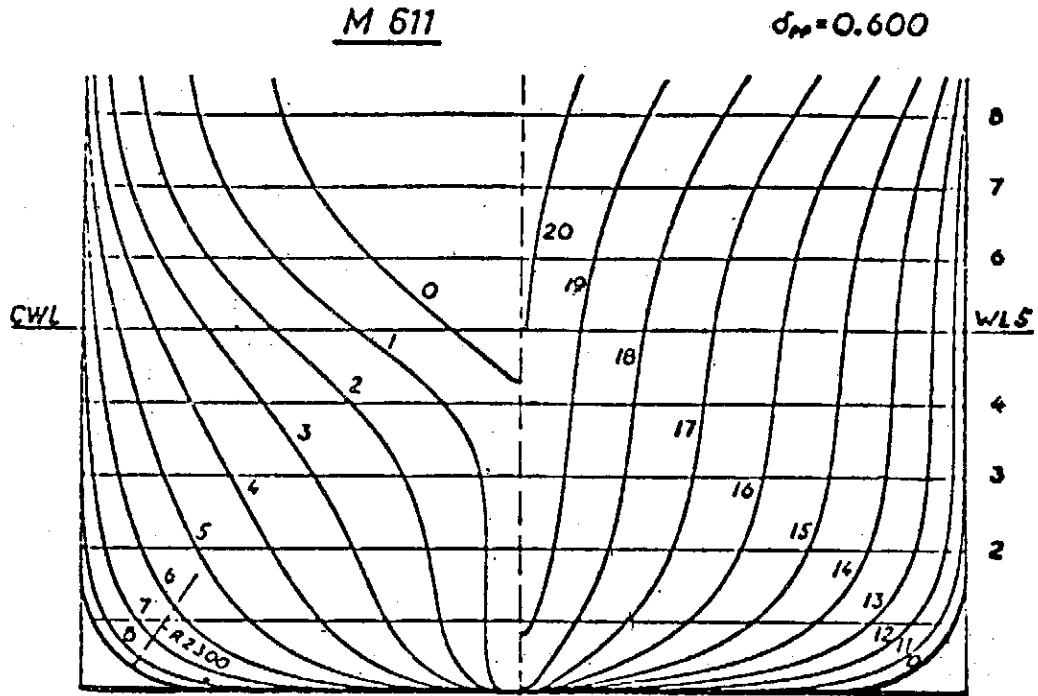
4. Literatur

(1) Gallin und Sandmann: Das Blohm u. Voss-multicarrier-System, *Schiff und Hafen* 4, 241 (1957)

(2) Gallin: Neue Versuchsergebnisse mit dem "PIONEER' von Blohm u. Voss, *Hansa* 11, 1874 (1957)

(3) Das erste Pioneer-Schiff, *Schiff und Hafen*, 11, 785 (1968)

(4) *Die Neubauten*, 235 (1957)

(5) Henschke: *Schiffbautechnisches Handbuch*, 1, 2. Auflage.

(6) *Schiffbaukalender* (1942)

(7) J.O. Hinze: *Turbulenz an Indroduction*, Mc Graw-Hill, (1959)

(8) Prandtl: *Strömungslehre*

(9) Harold E. Saunders: Hydrodynamics in Ship Design

(10) G.K. Batchelor: *The Theory of Homogeneous Turbulence*, Cambridge (1956)

(11) Schlichting: *Grenzschicht-Theorie*

(12) E. Freimanis and H. Lindgren: *Göteborg Nr.* 44

(13) *VBD-Bericht Nr.* 513

(14) E. Freimanis u. H. Lindgren: Systematic Tests with Ship Models with $\delta_{pp} = 0,600\text{-}0,750$. 44. *Mitteilung der Schwedischen Schiffbauversuchsanstalt*, Göteborg.
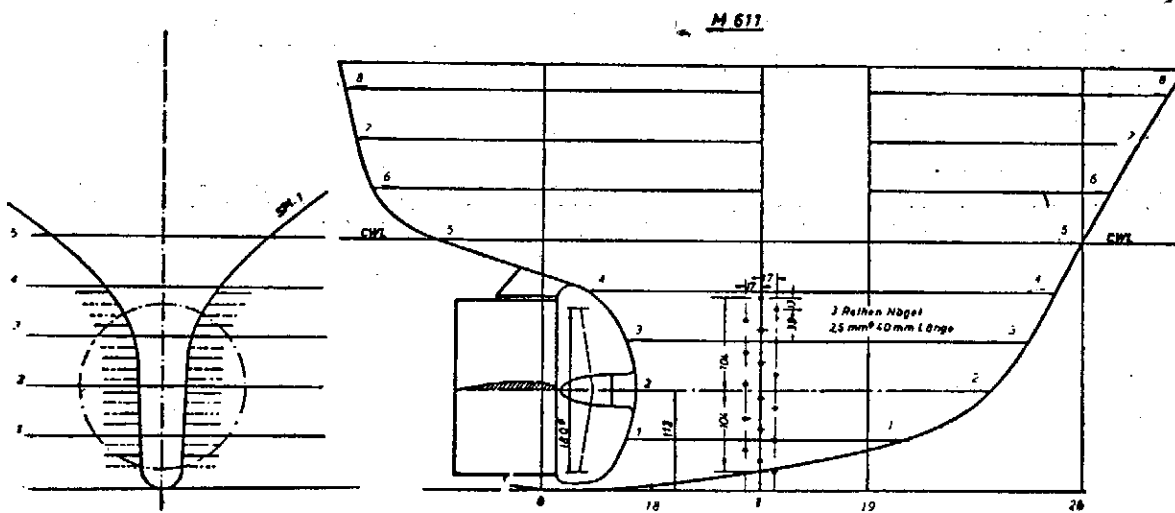
Verwendetes Modelle (nach Göteborg-Bericht Nr.44)
Daten siehe 3.1

Anl. 1

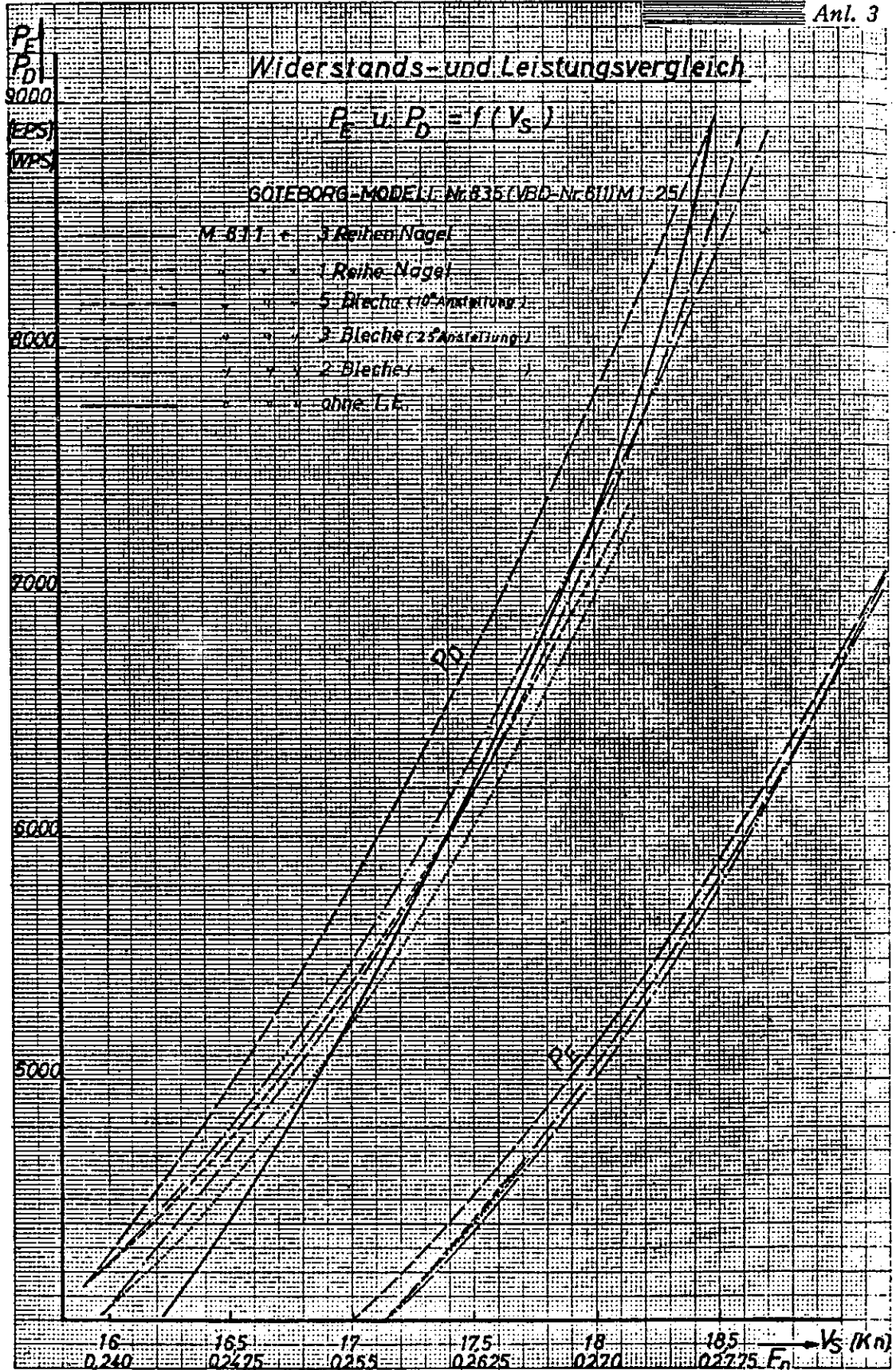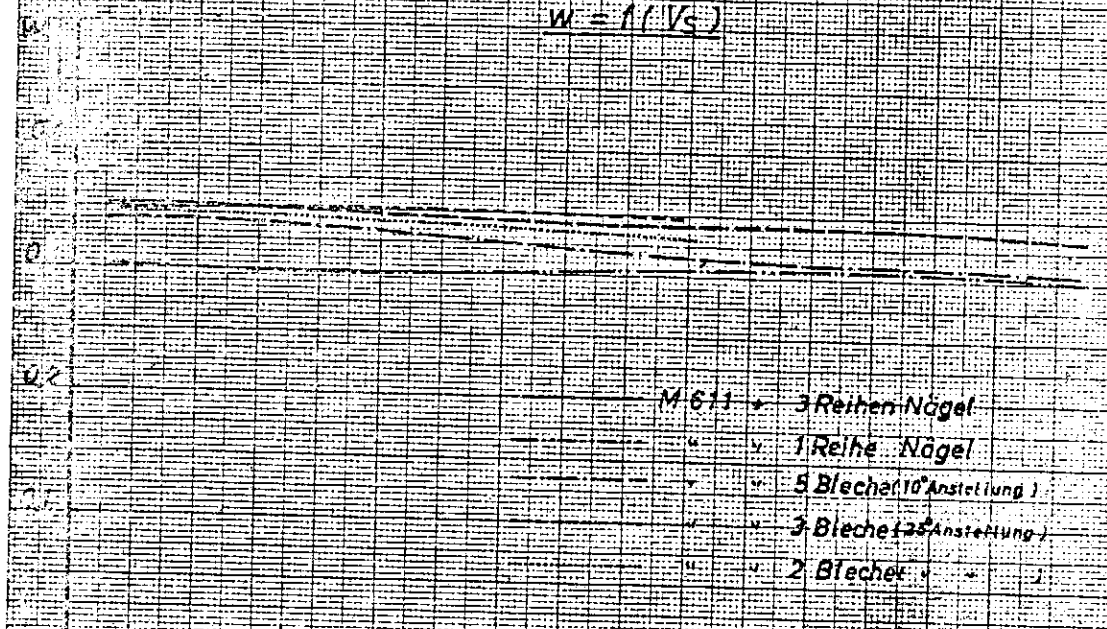M 611 $\delta_M = 0.600$

Anl. 2

M 611

Anl· 4

Vergleich der Nachstromziffer

$w = f(V_s)$

M 611 * 3 Reihen Nägel
" " 1 Reihe Nägel
" " 5 Bleche (10° Anstellung)
" " 3 Bleche (25° Anstellung)
" " 2 Bleche

16   16,5   17   17,5   18   18,5 V_s (Kn)

Vergleich der Sogziffer

$t = f(V_s)$

0,3

0,2

0,1

16   16,5   17   17,5   18   18,5 V_s (Kn)
0,24 02475 0,255 02625 027 02575 F₀

Anl. 5

$\eta_H = f(V_S)$ $\eta_H = \frac{1-t}{1-w}$

M.611 + 3 Reihen Nägel
1 Reihe Nägel
5 Bleche (10° Anstellung)
3 Bleche (25° Anstellung)
2 Bleche

$\eta_D = f(V_S)$ $\eta_D = \frac{P_E}{P_D}$

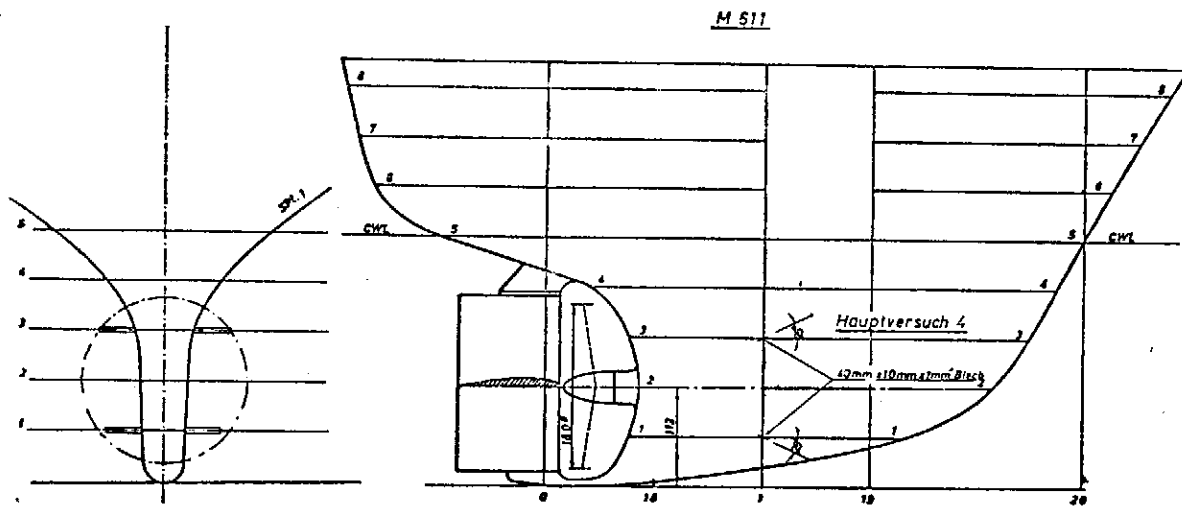| 16 | 16,5 | 17 | 17,5 | 18 | 18,5 | V_S [Kn] |
| 0,24 | 0,2475 | 0,255 | 0,2625 | 0,27 | 0,2775 | F_n |
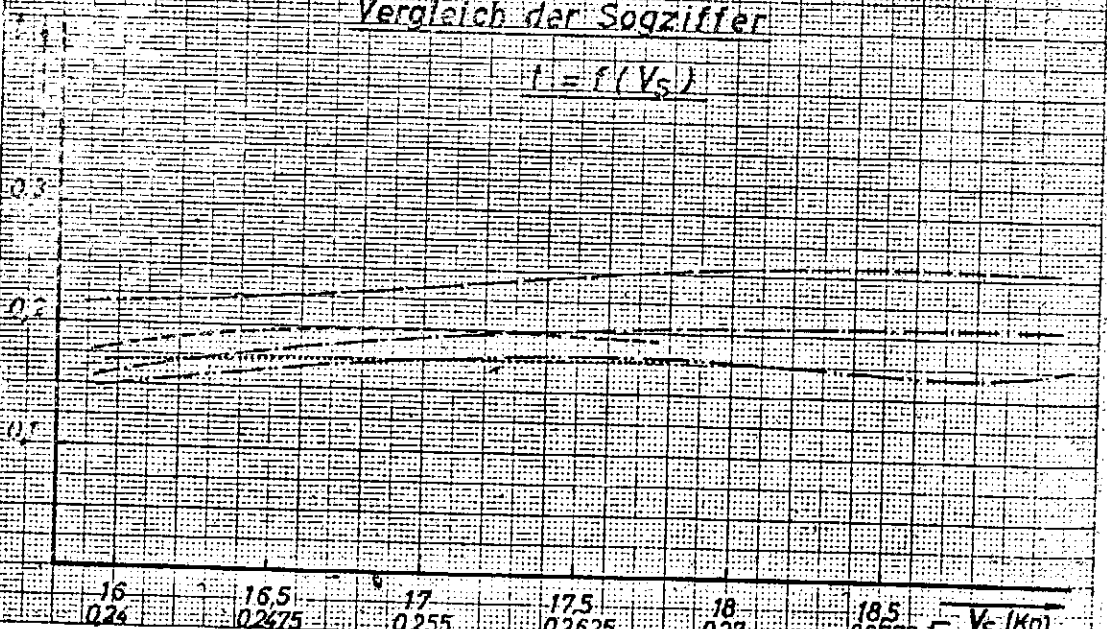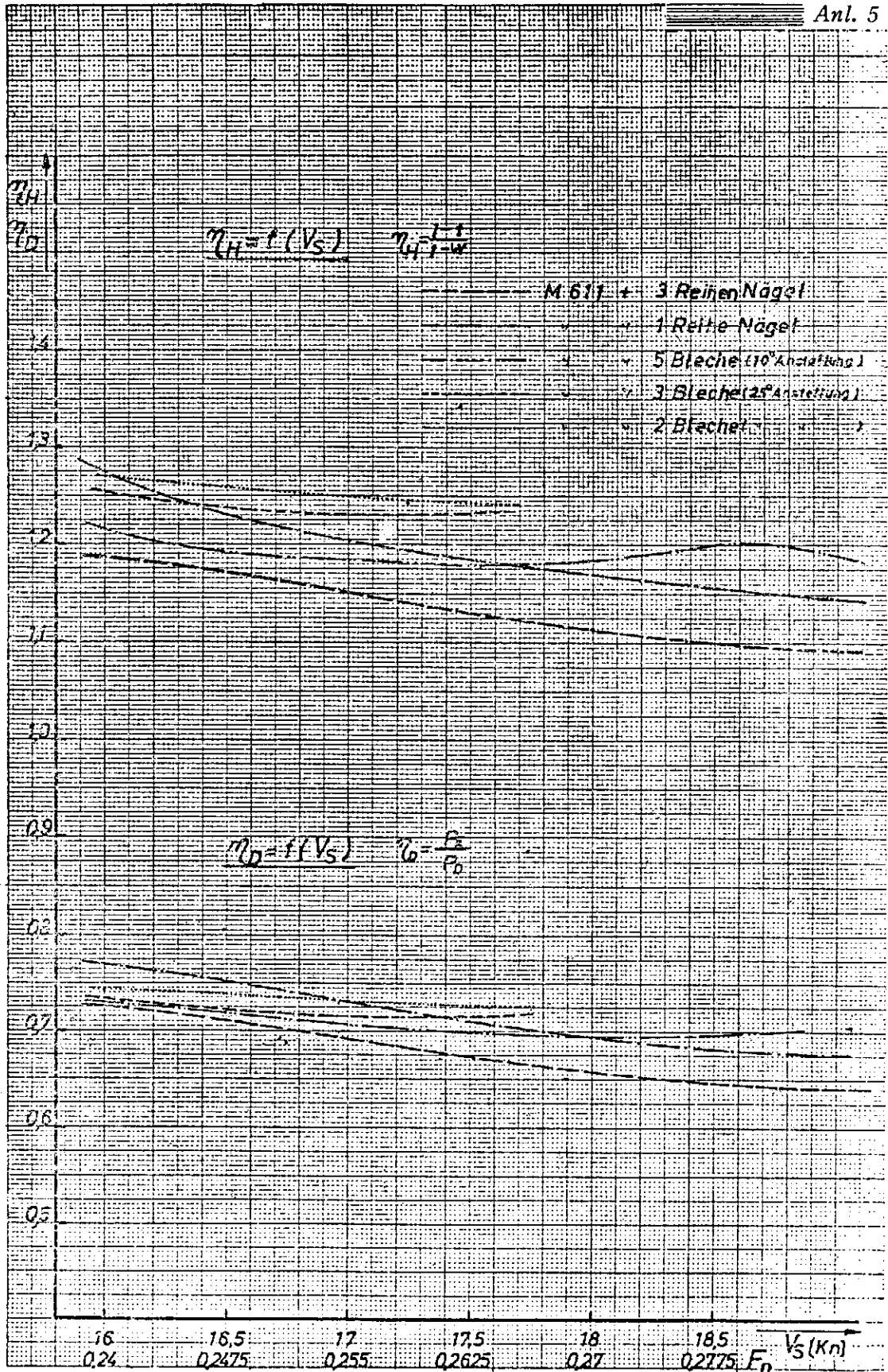
Verwendetes Modell (nach Göteborg-Bericht Nr.44)

Anl. 6

M 611

Hauptversuch 3

40mm x10mm x1mm Blech

Anl. 7

M 511

Hauptversuch 4

40mm x10mm x1mm Blech
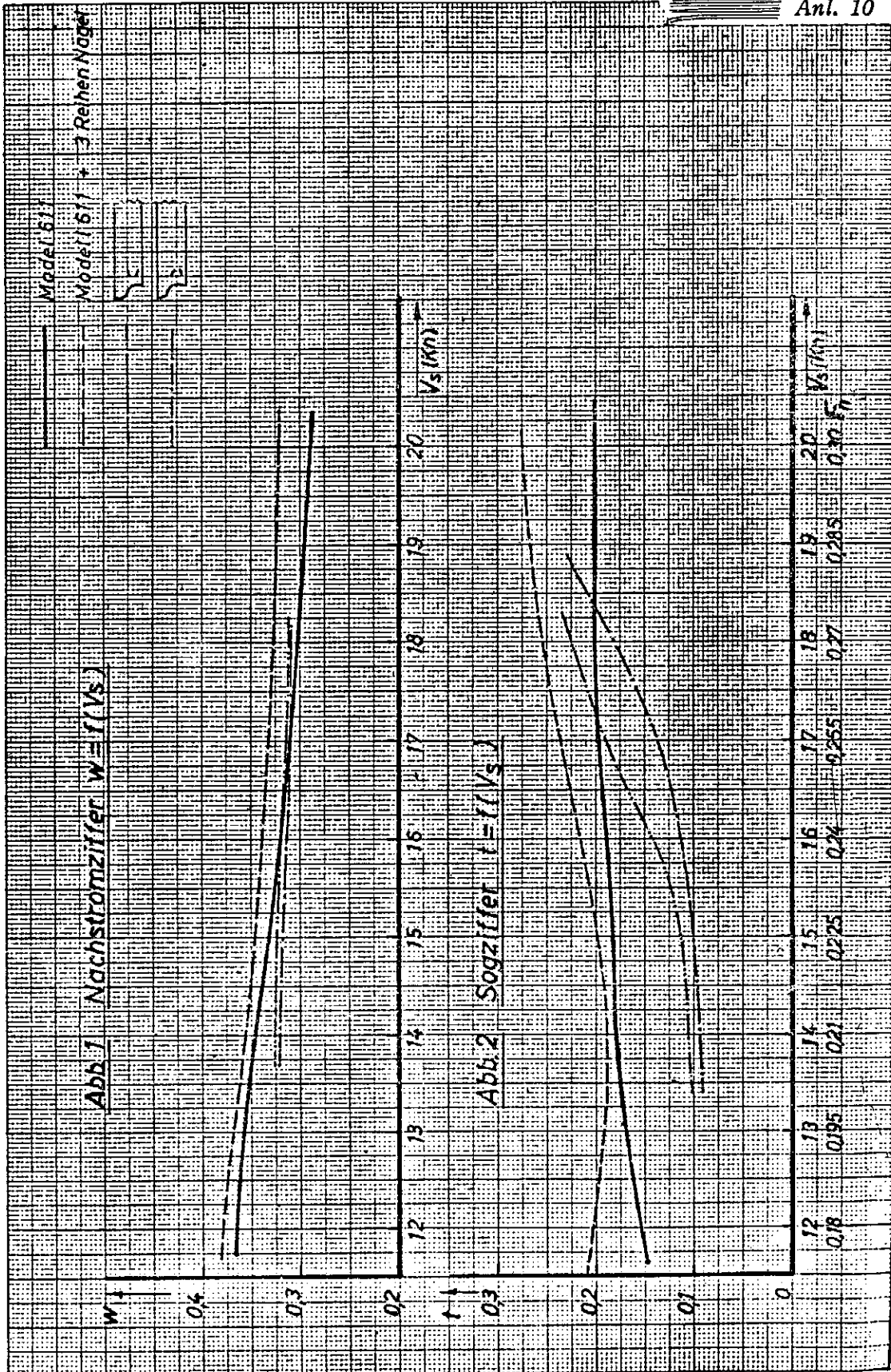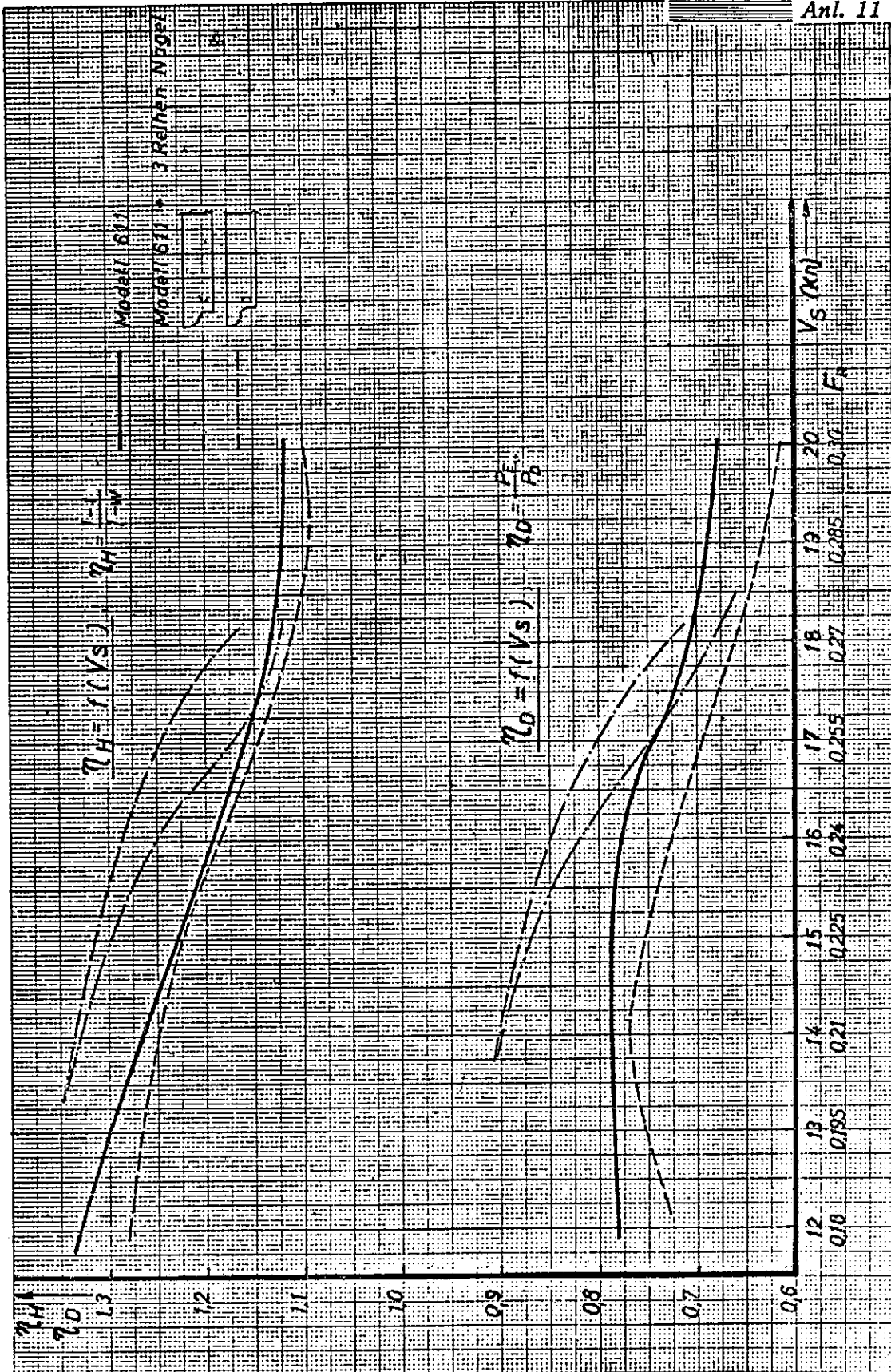
P_D [WPS] = f(Vs)

P_E [EPS] = f(Vs)

Modell 611

Modell 611 + 3 Reihen Nägel

Anl. 11
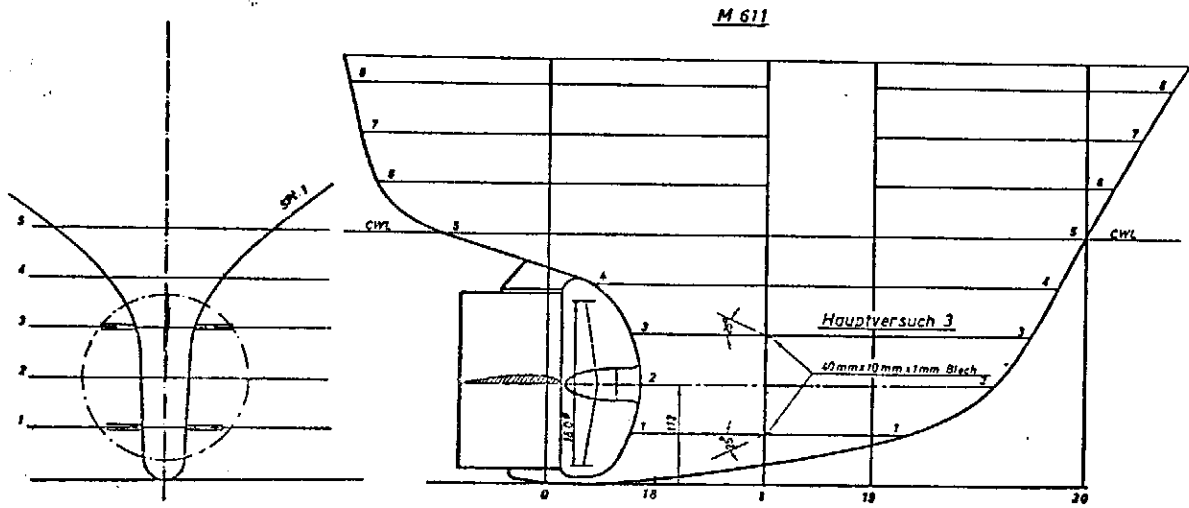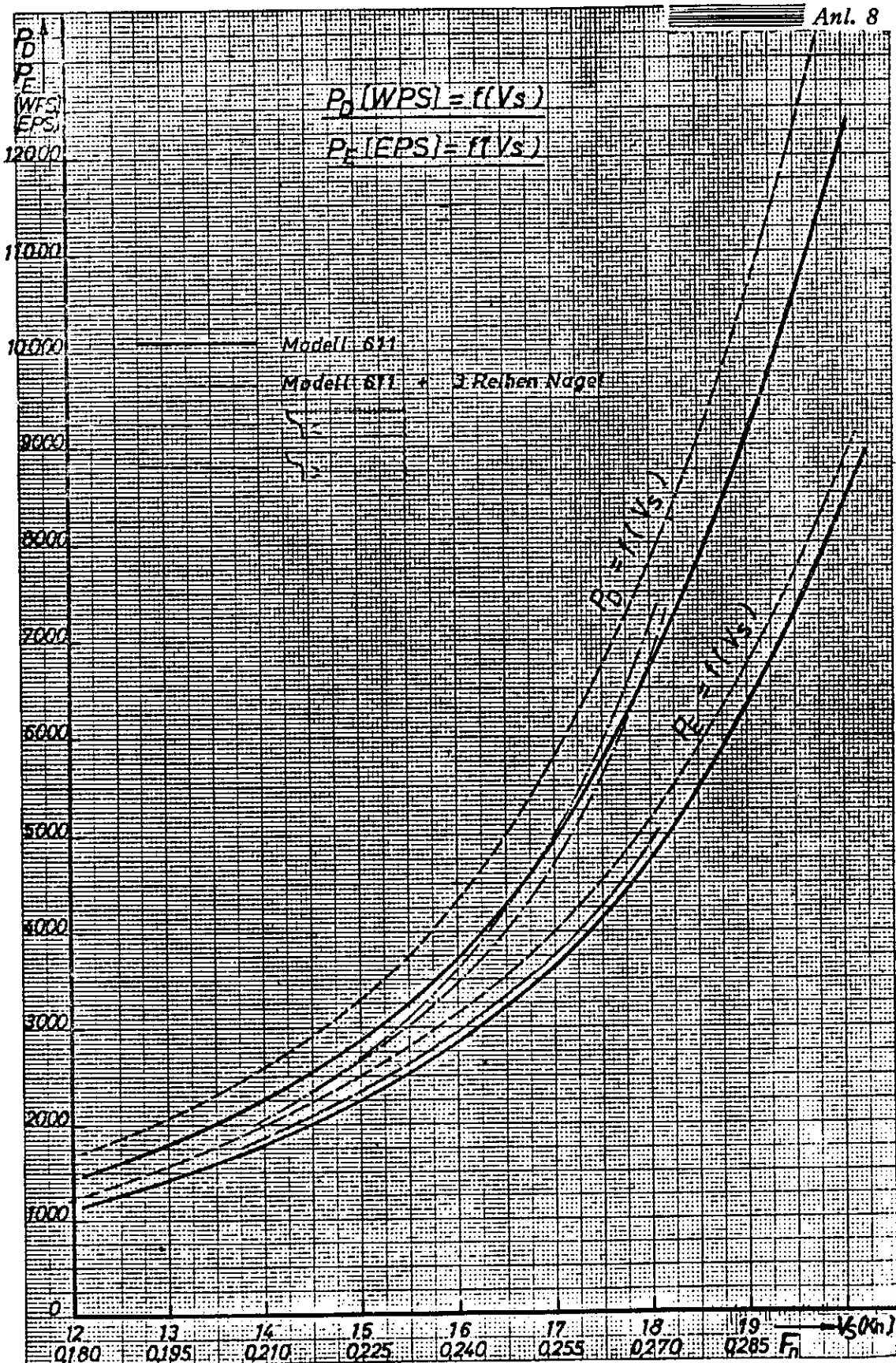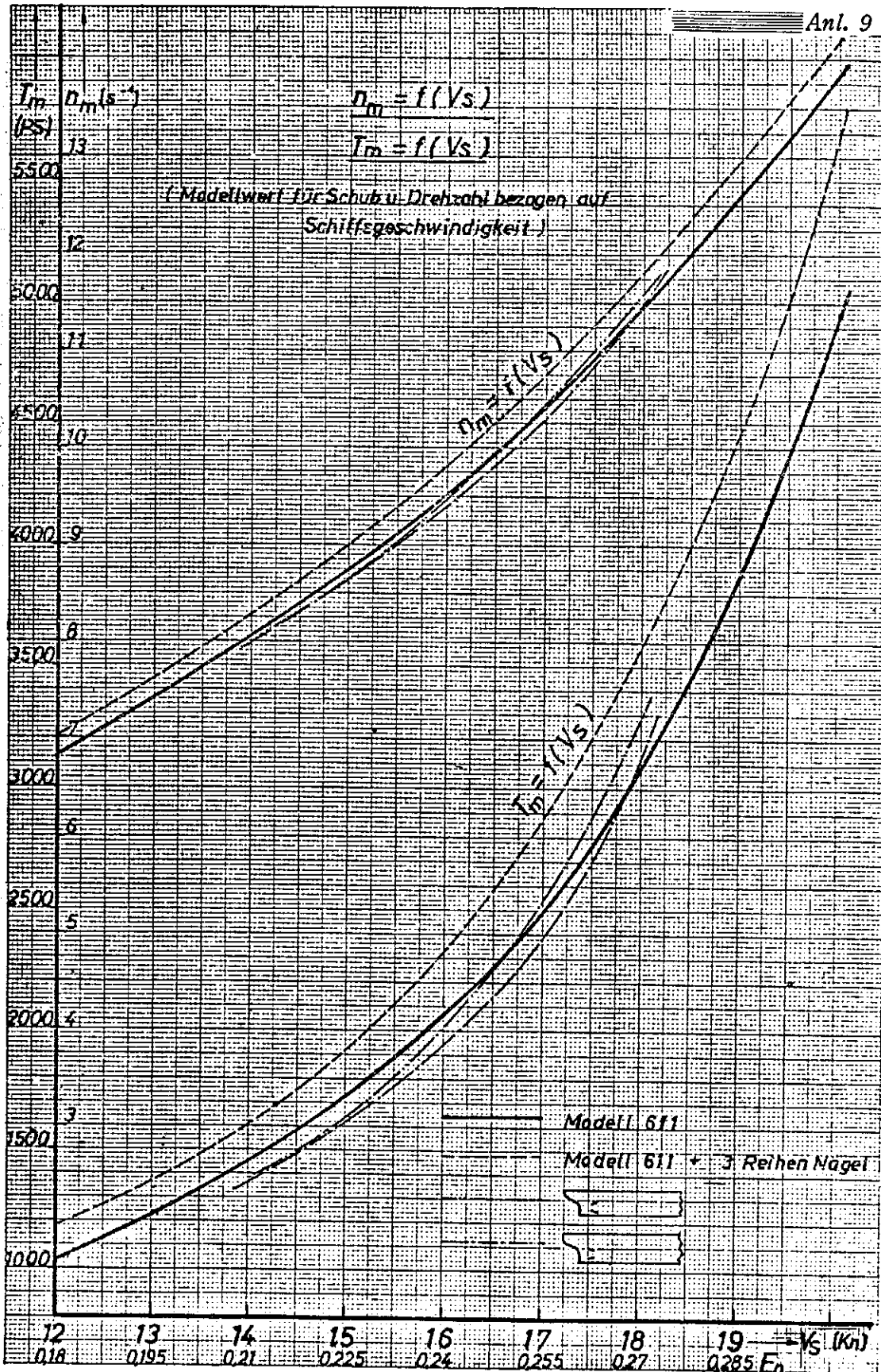
橢圓形厚機翼靠近直固壁時之二維運動

## Two–dimensional Motion of Thick Elliptical Wing near a Solid Boundary

曾忠一 (Chung Yi Tseng)

Institute of Physics, Academia Sinica

橢圓形機翼在理想流體中在直固壁附近的二維定常無旋流動問題可用保角映象(Conformal Mapping) 來考慮。我們可以用

$$z = f(\zeta) \qquad\qquad \zeta = re^{i\theta} \qquad\qquad (0.1)$$

的保角映成把橢圓形的周界轉換爲 ζ 平面上 $r=1$ 的圓，把直固壁即 x 軸轉換爲 ζ 平面上 $r=r_2$ 的圓，而且讓 z 平面上的無窮遠點相當於 ζ 平面上 $\theta=0$ 直線的一點。也就是說，z 平面上流體充滿的區域映到 ζ 平面上由 $r=1$ 的圓和 $r=r_2$ 的圓所圍成的環形區域內。z 平面（即物理平面）與 ζ 平面如下圖所示。

Z 平面 ζ 平面
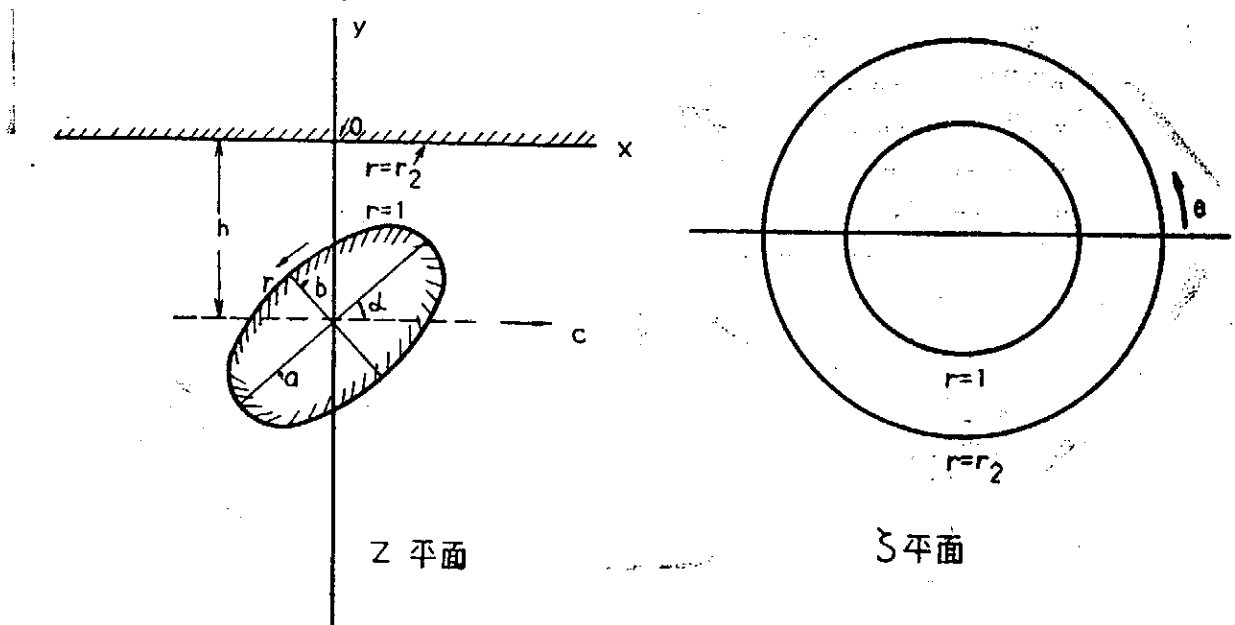
1. 由於 ζ 平面上速度勢函數 ϕ 的拉普拉斯方程式與極座標平面上的拉普拉斯方程式有相同的形式，因此我們可以寫爲：

$$\nabla^2\phi = \frac{1}{r}\frac{\partial}{\partial r}\left(r\frac{\partial\phi}{\partial r}\right) + \frac{1}{r^2}\frac{\partial^2\phi}{\partial\theta^2} = 0 \qquad\qquad (1.1)$$

我們可以得到下面的解[1][2]

$$\phi = \frac{\Gamma}{2\pi}\theta + \sum_{m=1}^{\infty}(A_m r^m + A_{-m}r^{-m})\cos m\theta + \sum_{m=1}^{\infty}(B_m r^m + B_{-m}r^{-m})\sin m\theta \qquad (1.2)$$

這裏 Γ 是環繞機翼周圍的環量，其方向若與 θ 的方向相同時爲正。

2. 我們假設機翼沿着正 x 方向以 c 的速度運動，邊界條件可以寫爲：

$$\frac{\partial\phi}{\partial n} = 0 \qquad\qquad\qquad 當\ r = r_2\ 時$$

$$\qquad\qquad\qquad\qquad\qquad\qquad\qquad (2.1)$$

$$\frac{\partial\phi}{\partial n} = c\,\cos(n,x) \qquad\qquad 當\ r = 1\ 時$$

(2.1) 可以寫為

$$\left(\frac{\partial \phi}{\partial r}\right)_{r=r_2}=0$$

$$\left(\frac{\partial \phi}{\partial r}\right)_{r=1}=c\ \frac{\partial y}{\partial \theta}=\sum_{m=1}^{\infty}(\alpha_m \cos m\theta + \beta_m \sin m\theta) \tag{2.2}$$

上式的參數 α_m, β_m 要由映成函數 (0.1) 決定，而 (1.2) 式中的常數 A_m, A_{-m}, B_m，和 B_{-m} 要由邊界條件 (2.2) 式解出。

3.將 (1.2) 式代入 (2.2) 式，我們分別可以得到下列二式：

$$\sum_{m=1}^{\infty}(mA_m r_2^{m-1}-mA_{-m}r_2^{-m-1})\cos m\theta + \sum_{m=1}^{\infty}(mB_m r_2^{m-1}-mB_{-m}r_2^{-m-1})\sin m\theta=0$$

及

$$\sum_{m=1}^{\infty}(mA_m-mA_{-m})\cos m\theta + \sum_{m=1}^{\infty}(mB_m-mB_{-m})\sin m\theta=\sum_{m=1}^{\infty}(\alpha_m \cos m\theta + \beta_m \sin m\theta)$$

比較上二式中 $\sin m\theta$ 與 $\cos m\theta$ 的係數，我們分別可以得到下列四式：

$$mA_m r_2^{m-1}-mA_{-m}r_2^{-m-1}=0$$
$$mB_m r_2^{m-1}-mB_{-m}r_2^{-m-1}=0$$
$$mA_m-mA_{-m}=\alpha_m$$
$$mB_m-mB_{-m}=\beta_m$$

解出上列四式，可以求得 A_m, A_{-m}, B_m 和 B_{-m} 之值如下：

$$A_m=\frac{\alpha_m}{m(1-r_2^{2m})}$$

$$A_{-m}=\frac{\alpha_m r_2^{2m}}{m(1-r_2^{2m})}$$

$$B_m=\frac{\beta_m}{m(1-r_2^{2m})}$$

$$B_{-m}=\frac{\beta_m r_2^{2m}}{m(1-r_2^{2m})} \tag{3.1}$$

將上列四式代入 (1.2)，我們得到速度勢函數如下：

$$\phi=\frac{\Gamma\theta}{2\pi}+\sum_{m=1}^{\infty}\frac{\alpha_m}{m(1-r_2^{2m})}(r^m+r_2^{2m}r^{-m})\cos m\theta + \sum_{m=1}^{\infty}\frac{\beta_m}{m(1-r_2^{2m})}(r^m+r_2^{2m}r^{-m})\sin m\theta \tag{3.2}$$

已經求出 $\phi(r,\theta)$，我們可以由柯喜黎曼條件 (Cauchy-Riemann condition) 求出流線函數 $\psi(r,\theta)$，因此複數勢函數 (Complex potential) 可以寫為：

$$w=\phi(r,\theta)+i\psi(r,\theta)$$

$$=\frac{\Gamma}{2\pi}\ln\zeta + \sum_{m=1}^{\infty}[(A_m-iB_m)\zeta^m+(A_{-m}+iB_{-m})\zeta^{-m}] \tag{3.3}$$

其中 A_m, A_{-m}, B_m 和 B_{-m} 由 (3.1) 式表示。(3.3) 式中本有虛常數，可以略去。

4.現在我們必須證明 z 平面上無窮遠點之速度為零，即 $v_{x\infty}=0$ 與 $v_{y\infty}=0$。我們知道，函數 $f(\zeta)$ 的極點 (Pole) 決定反函數 (Inverse function) 之無窮遠點 [1]，因此

$$\frac{d\zeta}{dz}=\frac{1}{f'(\zeta)}=0$$

或者

$$\frac{\partial r}{\partial x}=\frac{\partial r}{\partial y}=\frac{\partial \theta}{\partial x}=\frac{\partial \theta}{\partial y}=0 \qquad \text{當 } |z|=\infty \text{ 時}$$

由 (3.2)，很明顯的，當 $\theta=0$ 而且 $1<r<r_2$ 時，導數 $\partial\phi/\partial r$ 和 $\partial\phi/\partial\theta$ 是有界的 (Bounded)，因此

$$v_{x\infty}=\frac{\partial\phi}{\partial x}=\frac{\partial\phi}{\partial r}\frac{\partial r}{\partial x}+\frac{\partial\phi}{\partial\theta}\frac{\partial\theta}{\partial x}=0$$

$$v_{y\infty}=\frac{\partial\phi}{\partial y}=\frac{\partial\phi}{\partial r}\frac{\partial r}{\partial y}+\frac{\partial\phi}{\partial\theta}\frac{\partial\theta}{\partial y}=0 \qquad (4.1)$$

5.把圓環形保角映成到已知的區域有下列的形式：[1,2]

$$z=f(\zeta)=\frac{iB}{1-\kappa\zeta}+A-\frac{iB}{2}+(Q+iP)\sum_{m=1}^{\infty}\kappa^{3m}\zeta^m+(Q-iP)\sum_{m=1}^{\infty}\kappa^m\zeta^{-m} \qquad (5.1)$$

這裏 A,B,Q,P,κ 是要由機翼的幾何性質和固壁決定的實參數，而且 $0<\kappa<1$。我們要把直固壁，即 x 軸，映到 ζ 平面 $r=r_2$ 的圓。我們可以發現，在 (5.1) 式中若 $r=\kappa^{-1}$ 時，$y=\text{Im}f(\zeta)=0$。因此 $r_2=\kappa^{-1}$。

在機翼的周界 $\zeta=e^{i\theta}=\sigma$ 上，因為 $|\kappa\sigma|>1$，所以映成函數可以展開為勞倫數列 (Laurent series)：

$$f(\sigma)=iB\sum_{m=1}^{\infty}\kappa^m\sigma^m+A+\frac{iB}{2}+(Q+iP)\sum_{m=1}^{\infty}\kappa^{3m}\sigma^m+(Q-iP)\sum_{m=1}^{\infty}\kappa^m\sigma^{-m} \qquad (5.2)$$

或寫為

$$f(\sigma)=\frac{iB}{1-\kappa\sigma}-\frac{iB}{2}+A+(Q+iP)\frac{\kappa^3\sigma}{1-\kappa^3\sigma}+(Q-iP)\frac{\kappa}{\sigma-\kappa}$$

為了求 A,B,P,Q,κ，我們可以假設

$$f(\sigma)\simeq f_1(\sigma)=A-\frac{iB}{2}+\frac{iB}{1-\kappa\sigma}+(Q-iP)\frac{\kappa}{\sigma-\kappa}=A+\frac{iB}{2}+iB\sum_{m=1}^{\infty}\kappa^m\sigma^m+(Q-iP)\sum_{m=1}^{\infty}\kappa^m\sigma^{-m} \qquad (5.3)$$

這個假設將在後面導出來。把 (5.3) 式的實數部份和虛數部份分開來，我們可以得到機翼周界的近似參數方程式如下：

$$x\simeq x_1=-(B+P)S_2+QS_1+A$$

$$y\simeq y_1=(B-P)S_1-QS_2+\frac{B}{2} \qquad (5.4)$$

此處

$$S_1=\sum_{m=1}^{\infty}\kappa^m\cos m\theta, \qquad S_2=\sum_{m=1}^{\infty}\kappa^m\sin m\theta$$

現在證明 (5.4) 式是橢圓參數方程式如下：

因為

$$S_1+iS_2=\frac{\kappa\sigma}{1-\kappa\sigma}=\frac{\kappa\cos\theta-\kappa^2-i\kappa\sin\theta}{1+\kappa^2-2\kappa\cos\theta}$$

故

$$S_1=\frac{\kappa\cos\theta-\kappa^2}{1+\kappa^2-2\kappa\cos\theta} \qquad (5.5)$$

又

$$S_1^2+S_2^2=|S_1+iS_2|^2=\frac{\kappa^2}{1+\kappa^2-2\kappa\cos\theta} \qquad (5.6)$$

因此
$$(S_1 - \frac{\kappa^2}{1-\kappa^2})^2 + S_2{}^2 = S_1{}^2 + S_2{}^2 - 2S_1\frac{\kappa^2}{1-\kappa^2} + \frac{\kappa^4}{(1-\kappa^2)^2}$$

$$= \frac{\kappa^2}{1+\kappa^2-2\kappa\cos\theta} - 2\frac{\kappa\cos\theta-\kappa^2}{1+\kappa^2-2\kappa\cos\theta}\frac{\kappa^2}{1-\kappa^2} + \frac{\kappa^4}{(1-\kappa^2)^2}$$

$$= \frac{\kappa^2}{(1-\kappa^2)^2}$$

上式演算中曾利用 (5.5) 式與 (5.6) 式。把上式的結果重寫一遍：

$$(S_1 - \frac{\kappa^2}{1-\kappa^2})^2 + S_2{}^2 = \frac{\kappa^4}{(1-\kappa^2)^2} \quad\text{------} \tag{5.7}$$

現在 (5.4) 由的兩個方程式解出 S_1 與 S_2，我們得到：

$$S_1 = \frac{(x_1-A)Q - (y_1-B/2)(B+P)}{Q^2+P^2-B^2}$$

$$S_2 = \frac{(x_1-A)(B-P) - (y_1-B/2)Q}{Q^2+P^2-B^2} \tag{5.8}$$

(5.8) 式代入 (5.7) 式，我們可以得到下面的橢圓方程式：

$$[\frac{(x_1-A)Q - (y_1-B/2)(B+P)}{Q^2+P^2-B^2} - \frac{\kappa^2}{1-y^2}]^2 + [\frac{(x_1-A)(B-P) - (y_1-B/2)Q}{Q^2+P^2-B^2}]^2 = \frac{\kappa^2}{(1-\kappa^2)^2} \tag{5.9}$$

假如橢圓形機翼的長軸與 z 軸之夾角為 α，而其中心的座標為 $(0, -h)$，如圖所示我們可以求得下列之關係：

$$A = -\frac{Q\kappa^2}{1-\kappa^2}$$

$$\frac{B}{2} - \frac{\kappa^2(P-B)}{1-\kappa^2} + h = 0$$

$$\tan2\alpha = \frac{Q}{P} \tag{5.10}$$

已知橢圓形的標準式為

$$\frac{x^2}{a^2} + \frac{y^2}{b^2} = 1$$

我們可以求得

$$a^2 = \frac{\kappa^2}{(1-\kappa^2)^2}\frac{(Q^2+P^2-B^2)^2}{Q^2+P^2+B^2-2\sqrt{Q^2B^2+P^2B^2}}$$

$$b^2 = \frac{\kappa^2}{(1-\kappa^2)^2}\frac{(Q^2+P^2-B^2)}{Q^2+P^2+B^2+2\sqrt{Q^2B^2+P^2B^2}} \tag{5.11}$$

B, P, Q, κ 可以由 (5.10) 式和 (5.11) 式求得 B, P, Q 的符號要由 $0<\kappa<1$ 的條件成立來決定。對於 $a/b>5$ 而且 $a<15°$ 的橢圓形機翼，我們得到

$$B = \frac{1-\kappa^2}{2\kappa}(a+b) = -2h + \kappa[a+b-(a-b)\cos2\alpha] \tag{5.12}$$

$$A = \frac{Q\kappa^2}{1-\kappa^2} = \frac{\kappa}{2}(a-b)\sin2\alpha \tag{5.13}$$

$$Q = -\frac{1-\kappa^2}{2\kappa}(a-b)\sin2\alpha \tag{5.14}$$

$$P = -\frac{1-\kappa^2}{2\kappa}(a-b)\cos2\alpha \tag{5.15}$$

$$\kappa = \frac{-2h + \sqrt{4h^2 + 2(a^2 - b^2)\cos2\alpha - (a+b)^2}}{2(a-b)\cos2\alpha - (a+b)} \tag{5.16}$$

此處 h 是橢圓中心到直固壁的距離，a 是長軸之半，b 是短軸之半，α 是橢圓機翼之攻角 (Angle of attack)，因此 κ, A, B, P, Q 可以用已知的橢圓形幾何性質表示。由 (5.16) 式我們可以發現，當 h 增加時，參數 κ 之值減少。我們把 (5.12) 到 (5.16) 之值代回 (5.1)，我們就得到映成函數 $f(\zeta)$。

下面的表計算出相同的 $h/2a$，a/b 和 α 值時參數 κ 之值。

$h/2a$	$\alpha = 0°$			$\alpha = 15°$		
	1.0	1.5	2.0	1.0	1.5	2.0
$a/b = 5$	0.153	0.105	0.075	0.162	0.108	0.098
$a/b = 10$	0.136	0.089	0.071	0.138	0.091	0.076
$a/b = 15$	0.132	0.087	0.069	0.133	0.089	0.073

上表是由 (5.16) 式計算的。

6. 現在要證明 (5.3) 式近似假設的合理性。

$$f(\sigma) = \frac{iB}{1 - \kappa\sigma} - \frac{iB}{2} + A + (O + iP)\frac{\kappa^3\sigma}{1 - \kappa^3\sigma} + (Q - iP)\frac{\kappa}{\sigma - \kappa}$$

與 (5.3)，我們得到

$$f(\sigma) = f_1(\sigma) + \triangle f(\sigma)$$

$$\triangle f(\sigma) = \frac{\kappa^3\sigma}{1 - \kappa^3\sigma}(Q + iP) \tag{6.1}$$

此處 $z_1 = f_1(\sigma)$ 是橢圓方程式的複數形式 (Complex form)。

我們由 (5.14) 式，(5.15) 與 (6.1) 式估計 $\triangle f(\sigma)$ 之絕對值，我們可以得到下列的不等式：

$$|\triangle f(\sigma)| = \frac{\kappa^2(1 - \kappa^2)}{2\sqrt{1 - 2\kappa^3\cos\theta + \kappa^6}}(a - b) < \frac{\kappa^2}{2}(a - b) \tag{6.2}$$

當 $h/2a > 1$ 且 $5 < a/b < 15$ 時，我們得到 $|\triangle f(\sigma)| < 0.12b$，即 $x + iy = f(\sigma)$ 的周界相當接近於 $x_1 + iy_1 = f_1(\sigma)$ 的周界。這個結論是根據本頁的表和 (5.16) 式得到的。

7. 現在把 (5.2) 式的實數和虛數部份分開，我們得到：

$$y(1, \theta) = -\frac{B}{2} + (B - P)\sum_{m=1}^{\infty}\kappa^m\cos m\theta + P\sum_{m=1}^{\infty}\kappa^{3m}\cos m\theta - Q\sum_{m=1}^{\infty}\kappa^m(1 - \kappa^{2m})\sin m\theta \tag{7.1}$$

從 (2.2) 式，我們可以求出 α_m 與 β_m

$$\alpha_m = cmQ\kappa^m(\kappa^{2m} - 1)$$

$$\beta_m = cm\kappa^m(P - B - P\kappa^{2m}) \tag{7.2}$$

把 (7.2) 式代入 (3.2) 式，並且記住 $r_2 = \kappa^{-1}$，我們可以求得速度勢函數 ϕ 如下：

$$\phi = \frac{\Gamma\theta}{2\pi} + cQ\sum_{m=1}^{\infty}\kappa^m(\kappa^{2m}r^m + r^{-m})\cos m\theta + c\sum_{m=1}^{\infty}\frac{\kappa^m(P - B - P\kappa^{2m})}{\kappa^{2m} - 1}(\kappa^{2m}r^m + r^{-m})\sin m\theta \tag{7.3}$$

求出 ϕ 之後，我們也可以求出流線函數 ψ 如下：

$$\psi(r, \theta) = \frac{\Gamma}{2\pi i}\ln\zeta + c\sum_{m=1}^{\infty}(Q\kappa^{3m} - i\frac{P - B - P\kappa^{2m}}{\kappa^{2m} - 1})\zeta^m + c\sum_{m=1}^{\infty}(Q\kappa^m + i\frac{P - B - P\kappa^{2m}}{\kappa^{2m} - 1})\zeta^{-m} \tag{7.4}$$

8.現在我們要求出橢圓形機翼所受的升力。這個問題可以先求 ζ 平面上 $r=1$ 的圓（卽對應於平面上精圓形的周界）上所受的力。

由 (7.3) 式可以求得 Γ 方向的速度

$$v_r(1,\theta)=\frac{\partial\phi}{\partial r}(1,\theta)=cQ\sum_{m=1}^{\infty}m\kappa^m(\kappa^{2m}-1)\cos m\theta+c\sum_{m=1}^{\infty}m\kappa^m(P-B-P\kappa^{2m})\sin m\theta \tag{8.1}$$

$$v_\theta(1,\theta)=(\frac{1}{r}\frac{\partial\phi}{\partial\theta})_{r=1}=\frac{\Gamma}{2\pi}-cQ\sum_{m=1}^{\infty}m(\kappa^{2m}+1)\kappa^m\sin m\theta$$

$$+c\sum_{m=1}^{\infty}\frac{m\kappa^m(P-B-P\kappa^{2m})(\kappa^{2m}+1)}{\kappa^{2m}-1}\cos m\theta. \tag{8.2}$$

因爲

$$v^2=v_r^2+v_\theta^2 \tag{8.3}$$

把 (8.1) 式與 (8.2) 式代入 (8.3) 式，可以得到 $v^2(\theta)$。

ζ 平面上 $r=1$ 之圓上的壓力分佈爲

$$p=\text{const}+\frac{1}{2}\rho v^2=\text{const.}-\frac{1}{2}\rho(v_r^2+v_\theta^2) \tag{8.4}$$

其中 ρ 爲流體的密度，我們假設流體爲不可壓縮。因此平行 $\theta=0$ 直線的分力爲：

$$X=\frac{1}{2}\rho\int_0^{2\pi}(v_r^2+v_\theta^2)\cos\theta\ d\theta \tag{8.5}$$

同時垂直於 $\theta=0$ 直線的分力爲

$$Y=\frac{\rho}{2}\int_0^{2\pi}(v_r^2+v_\theta^2)\sin\theta\ d\theta \tag{8.6}$$

將 (8.1) 式與 (8.2) 式代入 (8.5) 式可以把 (8.5) 式積出得：

$$x=\rho\Gamma c+\frac{1}{2}\rho\{\frac{\Gamma c[\kappa(P-B-P\kappa^2)(\kappa^2+1)-2(\kappa^2-1)}{\kappa^2-1}+2\pi c^2\kappa\sum_{m=1}^{\infty}m(m+1)\kappa^{2m}(\kappa^{4m+2}+1)$$

$$\times[Q^2+\frac{(P-B-P\kappa^{2m})(P-B-P\kappa^{2m+2})}{(\kappa^{2m}-1)(\kappa^{2m+2}-1)}]\}$$

上式可以寫爲

$$X=\rho\Gamma c+F(a,b,\alpha,h,\rho,c,\Gamma) \tag{8.7}$$

此處

$$F(a,b,\alpha,h,\rho,c,\Gamma)$$

$$=\frac{1}{2}\rho\{\frac{\Gamma c[\kappa(P-B-P\kappa^2)(\kappa^2+1)-2(\kappa^2-1)]}{\kappa^2-1}+2\pi c^2\kappa\sum_{m=1}^{\infty}m(m+1)\kappa^{2m}(\kappa^{4m+2}+1)$$

$$\times[Q+\frac{(P-B-P^{2m})(P-B-P^{2m+2})}{(\kappa^{2m}-1)(\kappa^{2m+2}-1)}]\}$$

因爲 P,B,Q 皆爲 a,b,α,h 的函數。

將 (8.1) 式與 (8.2) 式代入 (8.6) 式，我們可以求出 Y：

$$Y=-\rho\Gamma c+\frac{1}{2}\{-\Gamma c[Q\kappa(\kappa^2+1)-2]+\pi c^2Q\kappa B(\kappa^2-1)\sum_{m=1}^{\infty}m(m+1)\kappa^4[1+\frac{(\kappa^{2m}+1)^2}{(\kappa^{2m+2}-1)(\kappa^{2m}-1)}]\}$$

與 (8.7) 相似，上式也可以寫爲：

$$Y=-\rho\Gamma c+G(a,b,c,\alpha,h,\rho,\Gamma) \tag{8.8}$$

此處

$$G = \frac{1}{2}\rho\{-\Gamma'c[Q\kappa(\kappa^2+1)-2]+\pi c^2 Q\kappa B(\kappa^2-1)\sum_{m=1}^{\infty}m(m+1)\kappa^{4m}[1+\frac{(\kappa^{2m}+1)^2}{(\kappa^{2m+2}-1)(\kappa^{2m}-1)}]\}$$

因此合力爲

$$F=\sqrt{X^2+Y^2}$$

$$=\rho\Gamma'c\sqrt{2+\frac{2(F-G)}{\rho\Gamma'c}+\frac{F^2+G^2}{\rho\Gamma'c}}$$

$$\therefore \quad =\rho\Gamma c\ H(a,b,\alpha,h,c,\Gamma',\rho) \tag{8.9}$$

此處

$$H(a,b,\alpha,h,c,\Gamma',\rho)=\sqrt{2+\frac{2(F-G)}{\rho\Gamma c}+\frac{F^2+G^2}{\rho\Gamma c}}$$

9. 結論

由流體動力學的理論[3] 知道，物體平行直固壁運動，而且該物體具有環量時，並且流體是理想不可壓縮流體，直固壁將物體所產生的拒斥力或吸引力僅限於垂直固壁的方向，也就是說平行直固壁方向物體不受到任何阻力。在本文的情形下椭圓形機翼不會受到阻力，只會受到升力的作用。上節在 ζ 平面上求到的合力因爲與映成函數沒有關係，只與椭圓形的幾何性質，流體的密度，機翼的速度以及環繞機翼周圍的環量有關，而這些量與映成函數無關，因此 F 就是 z 平面上機翼的升力。假如沒有直固壁存在，也就是機翼在無窮流體中運循時升力應該是 $\rho\Gamma c$. (8.9) 中 H 函數是因爲直固壁存在時的修正值，即當 $h\to\infty$ 時 $H=1$.

參 考 文 獻

(1) Kurdiumova: On the solution of plane irrotational hydrodynamical problems for doubly-connected regions. *PMM* **25**,(1961)

(2) Kurdiumova: On the two-dimensional motion of a thick elliptical wing under a free boundary *PMM* **26**,(1962)

(3) Milne-Thomson: *Theoretical Hydrodynamics*, MacMillan (1960)

(4) Streeter: *Fluid Dynamics*, (Reproduced in Taiwan)

(5) Kochin, Kibel and Roze: *Theoretical Hydromechanics*, Interscience Publishers (1964)

船 模 試 驗 理 論 簡 介

An Introduction to Ship Model Testing Theory

陳 學 信 (Hsao-Hsin Chen)

戴 堯 天 (Yau-Tien Dai)

Academia Sinica and National Taiwan University

一、船模試驗室計劃之經過

近年以來，國內造船工業之發展蒸蒸日上，建造能量已到達十萬噸油輪 (Oil Tanker) ，唯目前此類船舶之基本設計尚多仰仗外人（見參考文獻，王〔1939〕）。小型船舶之結構部份雖可自行設計建造，但對於流體動力學之基本性能，如船阻及船速之預計，尚不能準確計算，雖然此類試驗資料甚多（如美國造船工程學會所出版之試驗資料），唯因小型船舶受當地天候及水域之不同而多具地域特徵，故而如將國外現有之此種資料直接採用於國內設計，尚不盡如理想；至於軍用船舶，以其性能之要求尤高於商用船舶，如本國造船工業無法自製而向國外購置，則無論在國防機密抑或時效之配合均不相宜。由於以上各種原因，國內造船學術界多年來一直爲成立造船研究機構而努力，迄至四年之前，作者之一甫自美國柏克萊加州大學來物理所任職，因受敦促擬訂籌建船模試驗室計劃，當時雖對船模試驗室之興建並無經驗，唯感責無旁貸乃毅然自任。

船模試驗室在國內尙係首見之是類研究設施，故在計劃擬訂之始，對試驗室應包括何種設備，試驗室規模之大小，成立試驗室之目的，目前國內造船人才分佈情形，試驗室建造費用以及日後維持費用之來源等問題頗爲困惑，深感應有愼重考慮之必要。所幸中國造船工程學會以往對船模試驗室研究之資料由交通大學楊珍教授賜下，美國加州大學 J. R. Paulling 教授提供試驗室裝備之最新資料，又得國內外造船工業家、航業家及造船學者之支持與建議，復經中國造船工程學會第十六屆理監事會就上述諸問題廣泛而愼重之研究討論，認爲以首先建立小型船模試驗槽（以下簡稱爲船槽）着重培養人才及研究爲主而以協助解決造船實用工程技術爲輔，然後再逐漸發展，較爲適宜亦切合實際。在此原則下，試驗室計劃經一年研究完成之後，本所所長科導會主任委員吳大猷先生邀請有關專家與學者，研討並徵詢彼等對此一計劃之意見，復由中國造船工程學會，臺灣造船公司，臺灣機械公司，中國驗船協會及臺大聯合建議，計劃始於民國五十七年十二月經科導會及國科會核准在臺灣大學成立，分兩階段並納入科學發展計劃中實施。

船模試驗室自籌備核定至目前業已二年又半，工作人員大部均由各有關單位借用，本所汪羣從先生曾忠一先生及作者亦參加籌建工作，第一階段研究計劃已於五十九年四月完成，所需設備與儀器亦設計及訂購完畢，惟因試驗室受到土地問題的困擾，故延遲至六十年元月廿四日方始正式開工，預計六十一年上旬可以在本所人員支援下建造完成開始作試驗研究工作，本所研究人員並擬利用船模試驗室從事流體力學方面之研究工作。

船模試驗室自開始之時，本所所長吳大猷先生即對此一研究計劃全力支持，科導會與國科會亦均積極推動與配合。作者甚望藉此向吳主任委員及科導會與國科會表示個人由衷之感謝；同時，亦向以下有關人士在計劃擬定期間所給予作者之支持、鼓勵及建議致謝：造船實業家周茂柏先生、王先登先生、楊珍先生、金龍靈先生、晏海波先生、夏新先生、唐桐蓀先生、造船學者厲汝尙博士、鞠鴻文先生、張達禮先生、卡保琦博士、航業家董浩雲先生、以及臺大金祖年院長、謝承裕教授、加州大學 J. R. Paulling 教授、荷蘭船模研究所 W.P.A. Van Lammeren 教授、Delft 工業大學 J. Gerritsma 教授、漢堡大學 H. Thieme 教授、杜伊斯堡船模試驗室 H. Schneekluth 教授、漢堡船模研究所 Schwanecke 博士、K. Remmers 博士，丹麥流體及空氣動力學試驗所 C.W. Prohoska 教授。作者在準備此文之時，得臺大船模試驗室許進男、張春男、陳生平三位先生之協助良多，在此一併致謝。

二、船模試驗之功用

船舶爲一龐大鋼料或木料結構且具有動力之物體，其航域經常受天候，潮汐之影響而變化不一，且任何兩艘船隻甚少完全相同。所以，船舶之設計多在某些假定設想並參考以往建造之船舶而爲之，因此建造完成

之船隻，其性能未必能完全符合設計階段中所預期者。如果在建造之先不能充分瞭解影響船隻性能之各種因素，完成後之船隻，即使發現缺陷之所在，亦不易彌補至理想程度；縱然此種缺陷在技術上可以改進，但在時間及經濟上均有浪費。因之而有舡模試驗室之興建，利用舡模探測其阻力，推動效率，耐海及廻轉等性能，藉以輔助造船之設計。此即舡模試驗對造船工程之功用。

在另一方面，造船學者存有一個崇高理想，即欲以理論解析方法求出船隻在航程中受力時之運動及船體應力情形，期能達到以最小推動馬力，最少材料及人工而建造船速最大，裝載最多，安全性最高之船隻。但此一理想面臨之難題甚多，而無法達成。目前僅能假定當研究某一特性時，其他對此特性影響較少之因素可以省略，藉以使問題簡化，例如在流體動力學方面，船隻之廻轉假設不受船體起伏及傾仰之影響（見文獻 Chen〔1969〕）。再如船舶之興波阻力（Wave Making Resistance）假定為佛氏常數（Froude Number）之函數，而摩擦阻力（Frictional Resistance）為雷氏常數（Reynolds Number）之函數，而事實上，摩擦阻力亦是佛氏常數之函數（見文獻 Tzou and Landweber〔1968〕）；即便將佛氏常數列入考慮，船舶摩擦阻力亦並非二維（Two-dimension）問題，而是與船體之幾何形狀有關之三維（Three-dimension）議題（見文獻 Uberoi〔1969〕）。至於船體結構方面，亦有類似做法，例如研究船體彎曲強度（Longitudinal Strength）時，一般多不考慮扭曲（Torsional）應力；但是，自從貨櫃船（Container Ship）出現後，由於其船甲板艙口較諸一般貨船（General Cargo Ship）者加大甚多，扭曲應力及縱向應力同為決定船體強度之主要因素（此類參考文獻可於陳、張、及戴〔1969〕介紹新近論著中得見）。雖然將問題如此簡化，理論之建立及求解亦非易事，而理論之準確程度，必須以船舶實際發生之情形加以印證。然而，船隻在自然境界中同時所遭遇之諸多因素影響，幾乎不可能使某一欲加深入研究之因素自其他影響隔離，此一目的，唯有於試驗室中以人為方法方能達到，此為舡模試驗對學術研究之功用。

三、船模試驗之沿革

早在十七世紀以前，甚多數學家及科學家即對如何改變物體或船體形狀使之具有最小阻力一問題發生濃厚興趣，如牛頓（Newton）以及以後之尤烈（Euler），柏努力（Bernoulli）諸氏均是。但是以船模試驗探求船舶阻力之建議尚為 Swedenborg 於 1721 年首先提出（見文獻 Todd〔1961〕），而於三十五年後第一座船槽始行出現。此一船槽為 Bird 氏於 1756 年所建，其長僅三十呎，自 1756 年至 1869 年之間，世界各地利用船槽，河流或船渠試驗模者，逐漸增加，其中頗值提及者有以下諸人氏：

1. Benjamin Franklin 氏在 1764 年利用舡模試驗研究淺水（Shallow Water）對船阻之影響；

2. D'Alembert, Condorcet 與 Bossut 三氏於 1775 年建立長 32.5 公尺、寬 17.2 公尺、深 2.1 公尺之船槽一座，研究船舶在淺水及運河中之阻力；

3. Beaufoy 氏於 1793～1798 年之間於倫敦之 Greenland 舡渠中試驗舡模，但其試驗結果於四十年後始公佈於世；

4. William Hall 在 1830 年左右於蘇格蘭利用長 10 呎，寬16英寸 12 英寸之玻璃水槽試驗船模；

5. William Froude 於1862（可能為1863）年在排水塘，後於 River Dart 做船模試驗。

在 1756 至 1869 年之間，所有試驗均用一定之重量牽引船模在水中作等速移動，其裝置之概要，與 D'Alembert, Condorcet 與 Bossut 三氏所用者（見第一圖）相似。吾人由此可知早期船模試驗裝置異常簡陋，但是此諸學者利用如此簡單之設備亦得到許多相當重要之結論，其中之一即為 William Froude 氏於1869年所定之「比較律」（Law of Comparison）。吾人所熟知之佛氏常數亦係以 William Froude 之姓冠之。

自 1869 年之後，船模裝備突有嶄新轉變，即用機械或電力推動之曳引車（Towing Carriage）或曳引裝置代替定量重置（見第二圖大型船槽所用之曳引車；第三圖小型船槽之曳引裝置）。最早成立之四座是類船槽為：

1.第一座配有曳引車之船槽為 William Froude 氏於1870年間向英國海軍部建議而成立者。此試驗室於1871年於英國 Torquay 地方建立完成，船槽計長 278 呎，寬36呎深10呎，所用之船模

圖一：早期船槽簡圖

長度爲 11 或12呎；
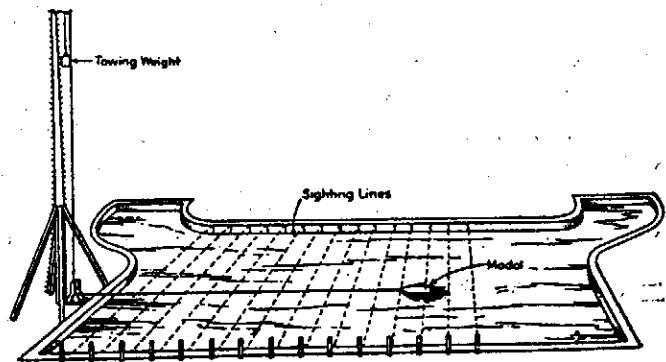
2.第二座是頗船槽爲B.J. Tideman氏於1873年爲荷蘭海軍在阿姆斯特丹 (Amsterdam) 所建立；

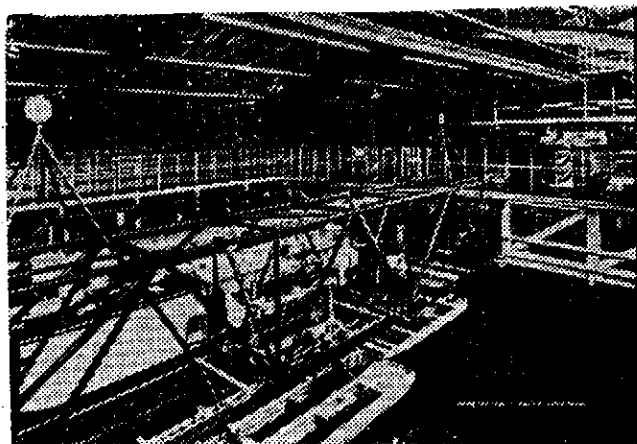3.第三座爲於1884年在蘇格蘭 Dumbarton 所建者，此試驗室亦爲第一座私人船模試驗機構；

4.第四座爲於1886年在英國 Hasler 由R.E·Froude (William Froude 之子) 所主持之長400呎，寬20呎、深9呎之船槽。

美國第一座船槽係於1900年建立於華盛頓海軍造船廠，此試驗機構之名稱爲 "U. S. Experimental Model Basin"，其船槽長度達470呎，水面寬度爲42呎，船槽中心線之水深爲14呎，曳引車重達40頓，由四具50匹馬力之馬達推動，曳引車最低速度爲½節，最高達15節(每節約等於每秒1.689呎之速度)。後於 1941 年美國海軍在馬利蘭州之 Carderock 建立新試驗所，即 David Taylor Model Basin (現改名爲海軍船舶研究發展中心，縮寫爲 NSRDC) (見文獻 Comstock 〔1966〕)，具有船槽兩座 (其一長 2,775 呎、寬 51 呎、深22呎，備有最高速度達24節之曳引車；另一長 2,968 呎，寬21呎，深 10 及 16 呎，備有最高速度達每秒100 呎之曳引車)，耐海性試驗池一座，廻轉性能試驗池 (見第四圖) 一座，推進器試驗用之 Cavitation Tunnel 等，而成爲目前世界上最大且裝備最精良之流體動力學研究場所。

歐洲各國中，除前述英國所建立之船模試驗機構及 National Physics Laboratory 外，在規模上可與美國之 NSRDC 媲美且研究成效卓著之試驗機構，厥推在荷蘭 Wageningen 之荷蘭船模試驗所 (Netherlands Ship Model Basin) (見文獻anon.(a) 〔1960〕)，該試驗所成立於 1929 年，而於1932年正式啓用。其次羅馬之國立造船試驗所 (Istituto Nazionale per Studi ed Esperienze di Architettura Navale)，德國漢堡之Hamburg Ship Model Basin (1913年開始成立，1915 年完成，見文獻 anon. (b) 〔1957〕)，丹麥哥本哈根之流體動力及空氣動力學試驗所 (成立於1959年，見文獻 Alf Jensen〔1959〕)，瑞典之國家造船試驗所 (The Swedish State Shipbuilding Experimental Tank，成立於 1940年) (見文獻anon. (c) 〔1958〕)，均有相當規模而爲世界最大造船研究機構之一。
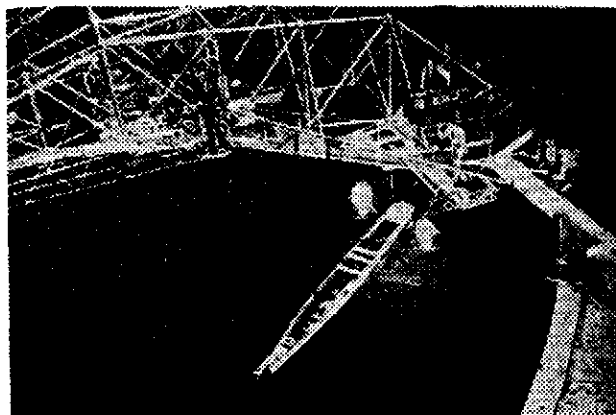
亞洲各國中，以日本建立船模試驗機構爲最早，其第一座船槽係於1927年建立於日本造船研究中心 (Shipbuilding Research Center of Japan)，至目前日本全國共有十九處船模試驗機構分置各大學，研究及工業機構 (見文獻北川弘光〔1969〕)，其中以船舶技術研究所 (Ship Research Inst-

圖二：大型船槽之曳引車
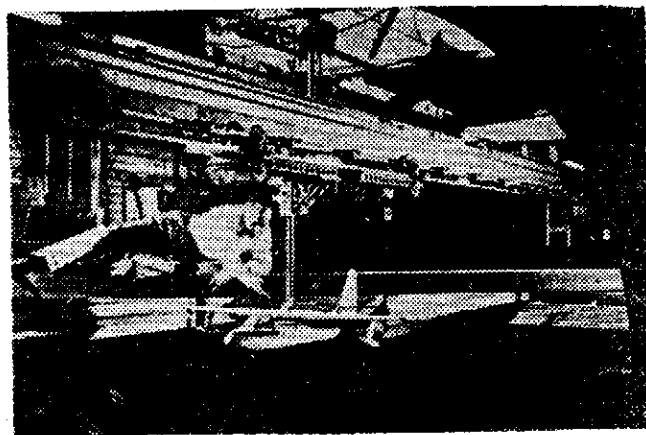
圖三：小型船模之曳引車

圖四：廻轉性能試驗池

itute）設備最完善，其船漕亦最大（計長400公尺，寬18公尺，深8公尺）。

　　自1900年之後，以迄於目前，世界各國現有船漕之數量已超過一百座，其中百分之四十為大型者（使用船模之長度自12呎至30呎不等），百分之六十為小型者（使用船標之長度小於 10 呎）。（見文獻陳、戴〔1970〕）。

四、船模試驗之理論依據

　　因次解析（Dimensional Analysis）為模型試驗之理論基礎。假設 $q_1, q_2 \cdots q_n$ 為關係實物（Prototype）之變數。$q'_1, q'_2 \cdots \cdots q'_n$ 為模型相對應之變數。模型試驗則在於尋求一個關於變數 q' 間之關係式，藉而測推變數 q 間之關係。如果將模型試驗尋獲的關係寫成無因次形式

$$G(\pi_1, \pi_2, \cdots \cdots \pi_{n-k}) = 0 \qquad (1)$$

此即所謂 π 定理（π Theorem）（見文獻 Wehausen〔1963〕），式中 k 表示導出無因次變數 π 所選用基本變數之數目，則式(1)在原則上可同樣地適用於實物。事實上，吾人無法使公式(1)同時適用於模型及實物，即不可能使模型各無因次變數完全與實物者相等，因此，研究之主題在於探測尋找何者無因次變數必須保持定值，何者可予省略而不產生顯著影響，以及尋求對於是等忽略變數之校正方法。
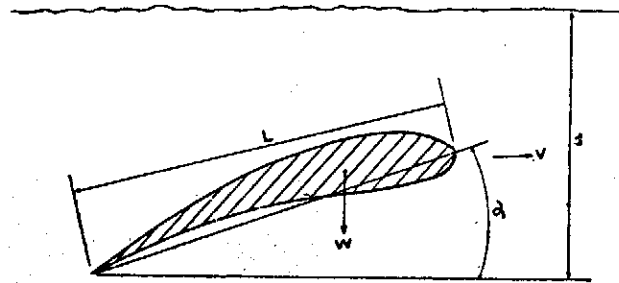
　　為說明 π 定理之應用及其所遭遇之難題，特舉以下各列：

(1)水翼試驗：假設水翼以等速在水面下運動（見圖五），其所受之力如以 F 示之，則

$$\vec{F} = F(L, d, \alpha, W, V, g, \rho, \nu, p_a, p_v)$$

HYDROFOIL

圖五：水翼試驗

$$\vec{F} = F(L, d, \alpha, W, V, g, \rho, \nu, p_v, p_a)$$

$$\frac{\vec{F}}{\frac{1}{2}\rho V^2 L^2} = \phi\left(\alpha, \frac{d}{L}, \frac{W}{\rho g L^3}, \frac{V}{\sqrt{gL}}, \frac{VL}{\nu}, \frac{p_a - p_v}{\frac{1}{2}\rho V^2}\right)$$

其中 L 為水翼之長度，d 為水翼沉入水中之深度，α 為切水角（Angle of Attack），W 為水翼之重量，V 為水翼速度，g 為重力加速度，ρ 為水之密度，ν 為水的黏性係數，p_v 為蒸氣壓力，p_a 為大氣壓力。如果應用 π 定理，則得

$$\frac{\vec{F}}{\frac{1}{2}\rho V^2 L^2} = \phi\left(\alpha, \frac{d}{L}, \frac{W}{\rho g L^3}, \frac{V}{\sqrt{gL}}, \frac{VL}{\nu}, \frac{p_a - p_v}{\frac{1}{2}\rho V^2}\right),$$

式中 $\dfrac{\vec{F}}{\frac{1}{2}\rho V^2 L^2} =$ 受力係數，$\dfrac{d}{L} =$ 深長比，$\dfrac{W}{\rho g L^3} =$ 重量係數，
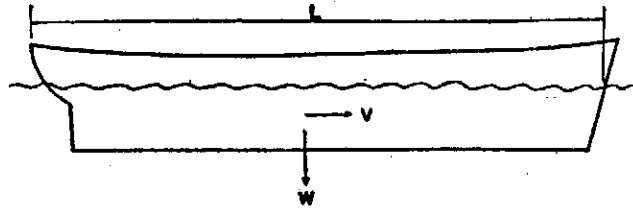
$\dfrac{V}{\sqrt{gL}} =$ 佛氏常數，$\dfrac{VL}{\nu} =$ 雷氏常數，$\dfrac{p_a - p_v}{\frac{1}{2}\rho V^2} =$ 空蝕常數。

　　顯而易見，事實上無法使模型之係數或常數與實物者完全相同。今若使佛氏常數相等，則模型之空蝕常數定比實物空蝕常數為大，除非將試驗室之大氣壓力降低，或使模型在密度比水為大之液體中試驗，方能達到模型與實物之佛氏常數及空蝕常數完全相同，即使如此，模型與實物之雷氏常數之差異仍然甚大。

(2)船模拖曳試驗 (Towed-ship Test) (見圖六)：

TOWED SHIP MODEL

圖六：船模拖曳試驗

$$R = F(L, V, W, \rho, \nu, g)$$

$$\frac{R}{\frac{1}{2}\rho V^2 L^2} = \psi\left(\frac{V}{\sqrt{Lg}}, \frac{VL}{\nu}, \frac{W}{\frac{1}{2}\rho V^2 L^2}\right)$$

$$\frac{R}{W} = \psi_1\left(\frac{V}{\sqrt{Lg}}, \frac{\nu}{L^{3/2}g^{1/2}}, \frac{\rho g L^3}{W}\right)$$

$$= \psi_2\left(\frac{V}{\sqrt{Lg}}, \frac{Lg^{1/3}}{\nu^{2/3}}, \frac{W}{\rho g L^3}\right)$$

$$= \psi_2(F, \Lambda, \forall)$$

NOTICE THAT REYNOLD NO. = FROUDE NO. $\times \Lambda^{2/3}$

假設船長為 L，重為 W 之船模，在密度為 ρ，動黏性係數為 ν 的液體中以等速 V 拖動，如果不考慮空蝕現象之發生，則其阻力 R 的函數關係可寫為

$$R = F(L, V, W, \rho, \nu, g)$$

應用 π 定理得

$$\frac{R}{\frac{1}{2}\rho V^2 L^2} = \phi\left(\frac{V}{\sqrt{Lg}}, \frac{VL}{\nu}, \frac{W}{\frac{1}{2}\rho V^2 L^2}\right), \qquad \frac{R}{\frac{1}{2}\rho V^2 L^2} \text{為船模阻力係數。}$$

上式並非阻力係數的唯一表示方式，其他形式尚有

$$\frac{R}{W} = \phi_1\left(\frac{V}{\sqrt{Lg}}, \frac{\nu}{L^{2/3}g^{1/2}}, \frac{\rho g L^3}{W}\right),$$

或

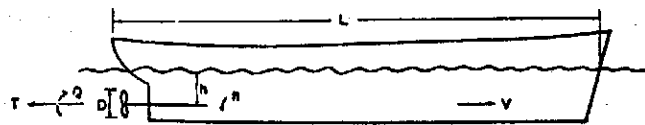$$\frac{R}{W} = \phi_2\left(\frac{V}{\sqrt{Lg}}, \frac{Lg^{1/3}}{\nu^{2/3}}, \frac{W}{\rho g L^3}\right) = \phi_2(F, \Lambda, \forall),$$

式中 $F = \dfrac{V}{\sqrt{Lg}}$ 佛氏常數，$\Lambda = \dfrac{Lg^{1/3}}{\nu^{2/3}}$，$\forall = \dfrac{W}{\rho g L^3}$

又雷氏常數 $R_n = \dfrac{VL}{\nu} = \dfrac{V}{\sqrt{Lg}}\left(\dfrac{Lg^{1/3}}{\nu^{2/3}}\right)^{2/3} = F\Lambda^{2/3}$ 。

吾人之所以使用 F，Λ，$\forall$ 表示阻力係數之函數關係，係因知無法使模型及實物之佛氏常數及雷氏常數同時相等，然為使模型試驗結果能用以預測實船情形，乃依 Froude 之假定將船舶全阻力 (Total Resistance)分為兩部，其一為與佛氏常數無關之表面阻力，另一為僅與佛氏常數有關之剩餘阻力 (Residual Resistance)。於第二節中，吾人亦曾提及此種假定並非完全合理，唯在實際應用上言之，不失為解決難題之方法。

(3)推進試驗 (見圖七)：

PROPULSION TESTS

圖七：推進試驗

$$T = \phi_1(g, n, D, \rho, p_a, p_v, \nu)$$

$$Q = \phi_2(g, n, D, \rho, p_a, p_v, \nu)$$

$$V = \phi_3(g, n, D, \rho, p_a, p_v, \nu)$$

$$K_T = \frac{T}{\rho n^2 D^4} = f_1(F, R, \sigma), \quad F = n\sqrt{\frac{D}{g}}$$

$$K_Q = \frac{Q}{\rho n^2 D^5} = f_2(F, R, \sigma) \quad R = \frac{nD^2}{\nu}$$

$$J = \frac{V}{nD} = f_3(F, R, \sigma) \quad \sigma = \frac{\rho g h + p_a - p_v}{\frac{1}{2}\rho V^2}$$

今以 L 代表單螺槳船 (Single Screw Ship) 之長度，其螺槳直徑爲 D，推進軸中心線在水下之深度爲 h，假定當轉矩爲 Q 時之伸葉每秒轉速爲 n，推進器產生推力爲 T，船速爲 V，在模型及船體之 h/D 及 L/D 二數相等之情形下，推力係數與 V, p_a, p_s, ρ, ν 及 g 之關係可由以下無因次式表示之：

$$K_T = f_1 (F, R_n, \sigma),$$

轉矩係數則是

$$K_Q = f_2 (F, R_n, \sigma),$$

前進率爲

$$J = f_3 (J, R_n, \sigma),$$

以上式中 $K_T = \dfrac{T}{\rho n^2 D^4}$, $K_Q = \dfrac{Q}{\rho n^2 D^5}$, $J = \dfrac{V}{nD}$ 分別爲推力係數，轉矩係數及前進率，$F = n\sqrt{D/g}$ 佛氏常數，$R_n = \dfrac{nD^2}{\nu}$ 雷氏常數，$\sigma = \dfrac{\rho gh + p_a - p_s}{\frac{1}{2}\rho V^2}$ 空蝕常數。

由以上三式可知，推進試驗中所遭遇之難題與第(2)種試驗者相同。爲解決此問題，通常將推進試驗分成數個，而於每種試驗中僅保留以上三函數中之某一變數，以使問題簡化。此諸個別試驗有：螺槳單獨試驗 (Opno Water Test)，自推試驗 (Self-propulsion Test)，超載試驗 (Overload Test) 及水渠試驗 (Water Tunnel Test)，其原理及有關文獻可見於上文所述之參考文獻。

以上所述之試驗並非船模試驗僅有之項目，僅藉以說明試驗之基本原理以及其難題所在。此外諸如自由廻轉試驗 (Maneuverability Test)，操縱性能試驗 (Steering Quality Test)，橫搖 (Rolling)，縱搖 (Pitching) 及起伏 (Heaving) 試驗，船舵試驗，與下水 (Lauching) 試驗等均屬船用流體動力學研究之課題 (見文獻 Comstock [1969])。

五、籌建中之船模試驗室之考慮因素及預期之研究工作項目

前節 π 定律之應用於船模試驗，並未有實物與模型間大小比例之限制與要求，但是，如以試驗剩餘阻力而言，模型之佛氏常數須與實船者相等，而雷氏常數無法成爲等值，於是，由試驗所得結果求出之船模剩餘阻力係數 (Coefficient of residual resistance) 與實船者有所差異，此即爲剩餘阻力係數比例差異 (Scale effect)，除非模型與實物同樣大小，此種比例差異亦存在於其他試驗結果中，如推進器試驗比例差異等 (見文獻 Meyne [1958])；此外，如使用模型過小，所謂非線性 (Non-linear) 影響無法由試驗測知，此種現象無論在阻力或船舶廻轉性能試驗等均會發現 (見文獻 Strom-Tejsen and Chislett [1966], Paulling and Wood [1962], Gertler [1936])。所以在試驗室中所允許使用之模型愈大則其試驗效果愈佳；然而，以現有之最大船槽使用其最大允許之船模測量近年來方始出現之三十萬噸油輪阻力，由於比例差異之存在，模型測量誤差最大可至百分之二十，於是，造船學者頗有船槽之理想尺寸究應多大之疑問產生。反言之，小型船槽使用小船模對學術研究之重要性及其貢獻，已爲世人所注意與重視 (見文獻 Abkowitz and Paulling [1953], Thornburg [1957], Davidson [1941], Murray, Korvin-Kroukowsky, and Lewis [1961])，所以小型船槽之存在價值勿庸懷疑。

由於上述小型船模試驗裝置對研究之價值，且基於目前無論在造船人才羅致之不易、經濟環境之限制、以及目前與最近之將來造船工業需要之程度，計劃興建之船模試驗室僅能及於小型船槽與其必要之附屬裝置與測量設備及儀器，以期使所需技術研究人員及所費減至最少數額，即使如此，建造設備費與經常研究維持費，預計已遠超出最初所能預料者。

臺灣大學船模試驗室之各主要裝備、建築與其選擇決定之考慮要點，概述如下：

1. 試驗室：試驗室之形式以其目的及環境之各異，甚少有相同者，茲將目前各國大型船槽及其試驗室斷面 (摘自文獻 Thornburg [1957]) 示於第八圖，船模試驗室第一階段建築外觀及其佈置 (見陳學信與戴堯天 [1970])，以便參照。

計劃之第一階段船模試驗室爲長約 90 公尺，寬 8 公尺之兩層建築：下層主要包括船槽一座及小型工場；上層包括研究室、一般試驗室、圖書資料室、儀器室、辦公室、繪圖室、儲藏室及盥洗室等 (見陳學信與戴堯天 [1970])。

2. 船槽：有關船用流體動力學研究設備，一般包括船模試驗槽 (船槽)，耐海性試驗池 (Seakeeping tank)，廻轉性能試驗池 (Manuevering tank)，以及推進器試驗用之旋廻水渠 (Water circulating tunnel)。臺大試驗室計劃中僅含船槽，作爲日後發展之基礎；在第一研究階段中，槽長計75.5公尺，寬 4 公尺，水深 2 公尺，槽深2.4公尺；第二階段中計劃將船槽長度伸延至150公尺。般槽尺寸之決定，其考慮各項因素如下：

Geteborg-Sweden

Toulouse-France

Sao Paulo-Brasil

El Pardo-Spain

Carderock-U.S.

Ottawa-Canada

Washington-U.S.

Teddington-England

Wageningen-Holland

Haslar-England

Hamburg-Germany

Rome-Italy
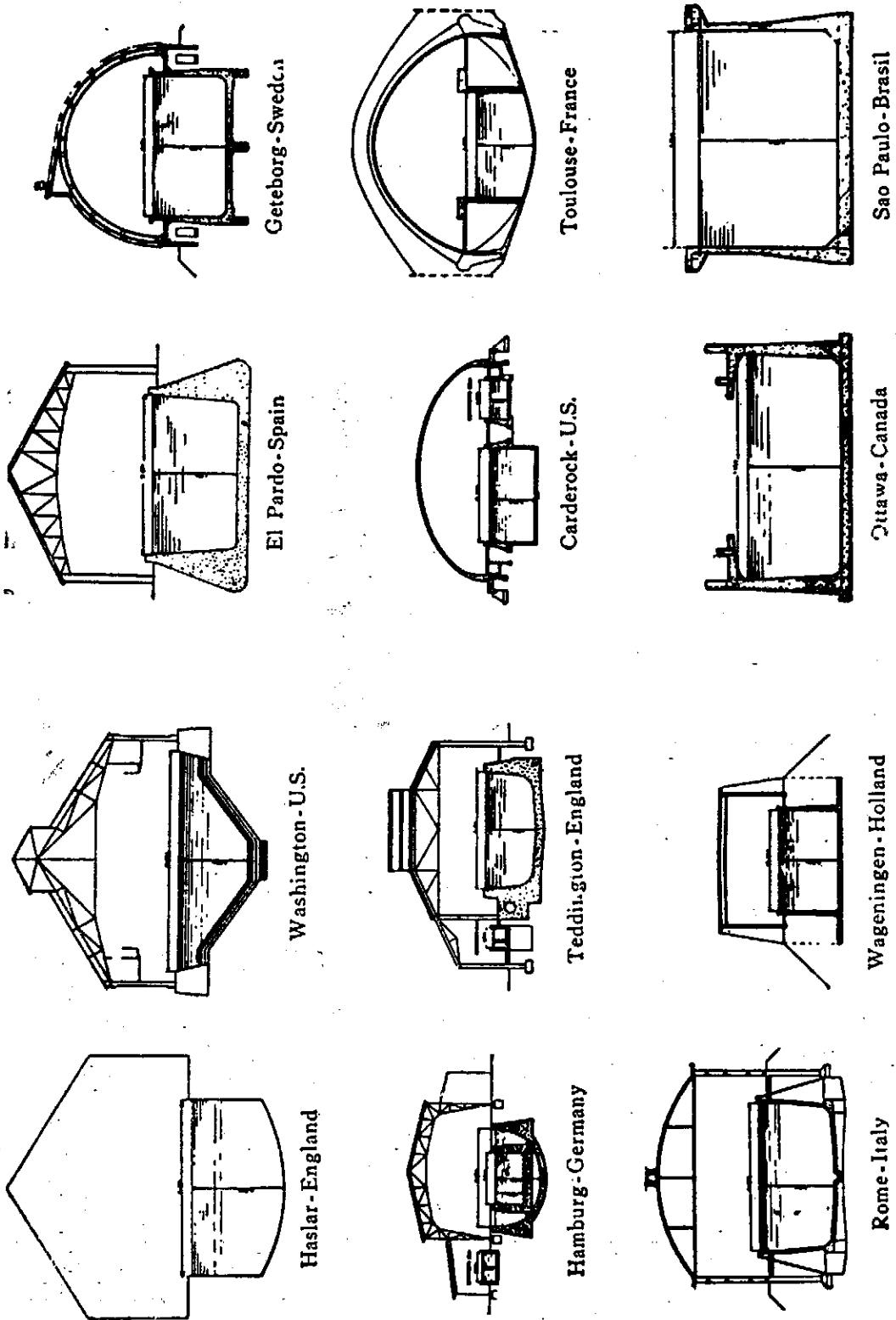
TOWING-TANK FACILITIES IN CROSS SECTIONS

圖八：各國船槽斷面圖

船槽長度視船模與實船長度之比例、船模最大速度、曳引車加速度及其減速度、以及所需測量時間之長短而定。如果實船與船模長度比例為α，欲保持佛氏常數為定值，則二者速度比為√α，以美國 Mariner 速級快貨輪為例，其排水量約18.000噸，長餘520呎，寬76呎，吃水27呎，航速每小時21節，推進器直徑22呎；如以2公尺長之船模試驗其阻力，二者長度比例約為80，船模速度每秒4呎，則船模行駛於第一階段74.5公尺之船槽中，可有充裕之測量時間。但若以長100呎，最高航速為40節之快艇而言，2米長之船模則應有最高速度約為每秒16.8呎（即約為每秒5公尺），以測量所需之時間為25秒計算，再加曳引車加速及減速所需之距離與船槽兩端為安裝其他設備所佔用之長度，船槽長度須達公150公尺方數使用。所以計劃中第二階段工作係將槽長延至如此之數。

船槽寬度與深度取決於所用之最大船模長度。如研究深海航行之船舶動態，則由船模運動所產生之波浪而由槽壁及槽底反射者應不影響船模動態為原則。一般言之，為達到此一要求，船槽寬度應不少於模型長度（見文獻 Comstock〔1966〕, Comstock and Hancock〔1942〕）。今若採用2公尺長之船模為標準，船槽寬度則應不少於4公尺，水深不少於2公尺；此外，為考慮船模在水浪中試驗時可能遭遇之波浪高度，槽深應為2.4公尺，而長2公尺之船模亦為此一船槽所允許使用之最大標準模型。如果研究淺水或運河行駛之船隻，此一限制自不存在，模型長度與水深及船寬間尺寸之比例視實際情形而定。

3. 曳引車：曳引車為帶動船模行駛船槽之裝置（見文獻陳、戴〔1970〕）。曳引車最大及最小速度取決於船模之可能試驗速度。為配合前項所述之快速船艇試驗，採用之曳引車最高速度為每秒5公尺，最低為每秒千分之22公尺，且在此兩速度範圍之內，車速可連續調整，以應各級船舶在不同航速時之試驗。

曳引車自靜止狀態至試驗速度之加速度以及自試驗速度至停止狀態之減速度，在可能及適當範圍內，應愈大愈佳，且應為等加及等減速度。

曳引車速度之穩定對試驗結果之準確性及試驗工作人員之舒適極為重要（見文獻Abkowitz and Paulling〔1953〕）。以測量船舶阻力為例，船模全阻（Total resistance）通常以全阻係數（Coeffcient of total resistance，見前節拖曳試驗）

$$C_t = \frac{F}{\frac{1}{2}\rho SV^2}, \qquad S=\text{船模表面浸水面積},$$

表示之。如將全阻分為剩餘及摩擦兩種阻力，而以 C_F 代表摩擦阻力係數，C_R 為剩餘阻力係數，則

$$C_t = C_F'\left(\frac{\rho VL}{\mu}\right) + C_R\left(\frac{V}{\sqrt{gL}}\right),$$

式中 ρ, V, L, μ, g 之定義與前節相同。今以5呎長之船模來作一般商用船舶之船模試驗，其阻力在船模速度為0.9節時約為0.05磅，在2.5節時約為0.6磅。如果曳引車速在試驗時經常變化不定而有±0.01節誤差，則 C_t 在低速、設計速度（Design speed）、最高速度時之誤差約分別為百分之2、百分之1.1、百分之0.8。一般商用船舶之剩餘阻力約佔其全阻之百分之二十，如此 C_R 在以上三種速度時之誤差，約分別為百分之10、百分之5.5、及百分之4。

臺大船模試驗室計劃使用之曳引車具有車輪四隻，藉電動設施推動行駛於船槽兩側壁之車軌上。基於上述曳引車速穩定性之重要，車軌必須十分光滑，兩側壁頂端水平亦須十分準確，曳引車須配備所謂 Ward-Leonard 裝置，四曳引車輪須予特別設計，方免車軌發生扭曲現象以及車身震動過鉅之憂。

4. 動力儀（Dynamometer）及測量記錄儀器：測量儀器及動力儀之精密及靈敏度直接影響試驗結果。以前述之船模試驗為例，假設身速絕對平穩，車速之測量記錄亦絕對準確，而阻力之測量有 ±0.001 磅之誤差，則在低速、設計速度及最大速度時，C_t 之誤差約分別為百分之2、百分之0.6、及百分之0.2；而剩餘阻力係數 C_R 在以上三種速度將分別有百分之10、百分之5.5、及百分之4之誤差，如果曳引車速之測量有±0.01節之誤差，同時阻力測量有±0.001磅之差別，則在以上三種速度全阻係數 C_t 將分別有百分之4、百分之2、及百分之1之誤差；C_R 將分別有百分20、百分之10、及百分之5之誤差；換言之，如果車速有±0.01節之不穩定，動力儀及儀器之靈敏準確度小於±0.001磅，即不適於研究所需，亦不適於一般阻力測量。曳引車速之穩定，動力儀及儀器之靈敏準確度對其他試驗（推進器單獨試驗等）具有同樣重要性，此即為小型船槽之特點，亦為小型船槽對研究設備之精密度較大型船槽所使用者要求尤高之說明，亦是臺大船模試驗室對此類設備考慮之原則。

5. 水波產生器（Wave generator）之裝置係為藉模型試驗研究實船在海浪中航行時之情形。計劃採用者為液壓推動之門型（flap type）水波產生器，所產生之水波為調周波（Simple harmonic waves）及複和

波 (Complex waves)，波浪產生之控制裝備有二：其一為機械裝置，另一則利用磁帶 (tape) 使產生器製做與海浪相似之水波或調和波。如僅研究實船在海浪中運動及受力情形等之造船學術問題，產生器所製之調和波長度應蓋括自四分之一至四趟船模長度之範圍，波浪高度應蓋括自零至最長波長之二十分之一高度之範圍。此為對水波產生器選擇考慮之要點。本船槽水波產生器之位置係置於船槽之一端，於其相對之一端備有斜度為45度之消浪斜坡，以使水波不致自相對之一端反射而改變波浪性質及影響船模動態。

6. 工作機及工具：試驗室以配置有關試驗所需之特殊且具高度精確性之工作機具為原則，如船模製作機、推進器模型鑄造及加工設備等，此諸機具之精密度直接影響模型之真實程度及試驗結果準確性，所以採用之是類機具以其精密程度為考慮之原則。至於其他小型金工加工機，如鑽床，木料刨光及鋸床等以及小手工具亦配合購置，以利工作之進行；而其餘可利用其他機構之機具則不在備置之列，以減少預算及所需工作人員之人數。

以所計劃之船槽與上述之配備，實可研究船用流體動力學多方面之課題，如船模拖曳試驗，推進器單獨試驗，操縱性能試驗，橫搖、縱搖及起伏試驗，船舵試驗等。唯利用小型船模試驗結果應用至實船，其間關係 (Correlationship) 則是研究主題之一。

六、結　　論

為研究一般水面船 (Conventional Surface Ship) 之用，小型船槽較諸大型船槽具有毫無疑間之優點：其一為初期建築設備費甚少，研究維持費用較少；其二，所用小型船模較大型輕便；其三，研究試驗所需操縱人員較少，尤適於學校及研究機構之情況。唯小型船模之雷氏常數遠較實船者為低，而存有較大之比例差異 (Scale Effect) 是其主要缺點，致使利用試驗結果預測實船問題之準確程度無法斷言，而有待試驗室建立完成後事試驗之後，方可確定，但是，如果船槽設備配置得當且使用高度精密之測量及儀 1.8 器至 2 公尺船模之試驗結果，當可做為部份實船設計及研究之用，而船模長度小於以上所列長度，其試驗結果則多偏於比較研究之用 (見文獻 Falkems〔1953〕及 Kempf〔150〕)。

參　考　文　獻

Abkowitz, M. A., and Paulling, J. R., "The ship model towing tank at MIT," *Transactions*, vol. 61, The Society of Naval Architects and Marine Engineers, New York, (1953).

Alf Jensen, *Vedtagter for Hydro- og Aerodynamisk Laboratorium, Lyngby*, Denmark, (1959).

anon. (a), *Bulletin of Netherlands Ship Model Basin*, Wageningen, December (1960).

anon. (b), *Bulletin of Hamburgische Schiffbau-Versuchsanstalt GmbH.*, Hamburg, (1967).

anon. (c), *Bulletin of the Swedish State Shipbuiding Experimental Tank*, Gothenburg, Sweden, (1958).

Chen, Hsao-Hsin, "Some aspects of ship maneuverability," *Journal of Ship Research*, vol. 13, No. 2, The Society of Naval Architects and Marine Engineers, New York, (June 1969).

Comstock, J. P., and Hancock, C. H., "The effect of size of towing tank on model resistance," *Transactions*, vol. 50, The Society of Naval Architects and Marine Engineers, New York, (1942).

Comstock, J. P., *Principles of Naval Architecture*, The Society of Naval Architects and Marine Engineers, New York, (1966).

Davidson, K. S. M., "The growing importance of small models for studies in naval architecture," *Transactions*, vol. 49, The Society of Naval Architects and Marine Engineers, New York, (1941).

Falkemo, C, "On the possibilities of estimating the towing resistance of ships by tests with small models." *Transact, of the Royal Institute of Technology Stockholm.* Göteburg 1953, Nr. 64

Gertler, M., "The ITTC standard captive-model-test program —a review and preliminary

analysis of data received prior to May 1966," Repprt of maneuverability Committee, Appendix 2, 11*th Conference of International Towing Tank Conference*, Tokyo, (1966).

Kempf, G. "Kleine Modellschleppkanäle fürpkleine Schiffsmodelle." *Hansa*. (1950)

Meyne, K., "Experimental and theoretical considerations on scale effect in propeller model investigations," *Forschungsh. Schiffsteck.*, 15, (1968).

Murray, A. B., Korvin-Kroukovsky, B. V., and Lewis, E. V., "Self-propulsion tests with small models," *Transactions*, 59, The Society of Naval Architects and Marine Engineers, New York, (1961).

Paulling, J.R., and Wood, Lloyd W., "The dynamic problem of ships operating on parallel courses in close proximity," *Inst. Engrg. Res., Univ. of California, Berkeley, Report Series No.* 189, Issue No. 1, (1962).

Strom-Tejsen, J., and Chislett, M. S., "A model testing technique and method of analysis for the prediction of steering and maneuvering qualities of surface vessels," *6th Symposium on Naval Hydrodynamics*, Washington, (1966).

Thornburg, F. L., "The convair towing tank—first year problem," *Transactions*, vol. 65, The Society of Naval Architects and Marine Engineers, New York, (1957).

Todd, F. D., "The fundamentals of ship model testing" *Transaction*, vol. 59, The Society of Naval Architects and Marine Engineers, New York, (1961).

Tzou, K. T. S., and Landweber, L. J., "Determination of the viscous drag of a ship models." *Journal of Ship Research*, 12, (1968).

Uberoi, S. B. S., "Viscous resistance of ships and ship models," *Report No. Hy*-13, *Hydro and Aerodynamics Laboratory*, Lyngby, Denmark, September (1969).

Wehausen, J. V., *Dynamics of ships*, Naval Architecture Department, University of California, (1963).

北川弘光，「國內船舶試驗水槽一覽」，日本造船學會誌，七月號，日本東京，(1969)。

王先登，「臺船公司十萬噸超級油輪建造進行報告」，中國造船工程學會第十七屆年會專輯，民國五十八年十一月，(1969)。

陳學信、張達禮、鞏鴻文，「新近論題及論著介紹」，中國造船工程學會第十七屆年會專輯，民國五十八年十一月，(1969)。

陳學信與戴堯天：「船模試驗理論簡介與本校船模試驗室計劃一覽」國立臺灣大學工學院機械研究所船模試驗室研究報告第C—1號，民國五十九年五月 (1970)

籌議中之颱風研究計劃

汪　羣　從(Chun-Tsung Wang)

Institute of Physics, Academia Sinica

摘　　要

鑒於颱風於臺灣島之密切關係，物理所流力組同仁擬對颱風做一列串有系統之研究。本文簡略介紹研究內容之方針暨籌議中初期研究計劃之背景，期能喚起各界對此問題之興趣，並於研究進行中能予協助，合作暨指敎。

一、簡　　介

颱風自生至滅，不過十日左右，然其挾帶之狂風、暴雨及洶浪却常造成難以計數之災害。臺灣位於西太平洋颱風侵襲內區，自不能不對颱風稍加注意。

近年來許多大氣科學家研究颱風之生成、結構、能量及運動，然而由於基本觀測及理論研究進度遲緩，颱風預報祗能仰賴經驗公式。同樣的，在未能了解及仿製大氣因素前，室內模型試驗也難言有成。測站不足，資料缺乏與難解之基本數學公式使吾人對颱風仍然不甚了解。

一般相信颱風乃由熱帶擾動而成，其生成之可能原因有三[10]。1.極槽侵入 (Polar trough intrusion)：當西風中之低壓槽滲入熱帶，而其入侵槽之南端變成半滯留狀態或拼入東風中時，可能演變而成颱風。2.東風波 (Easterly wave)：低空之渦旋因受過量之對流或高空渦旋影響時，會形成颱風。3.間熱帶輻合區 (ITCZ)：在溫暖天氣，當間熱帶輻合區在赤道北面受地球旋轉力，而產生低壓系統時，亦會形成颱風。一九六八年 Yanai[12] 分析 Doris 颱風時，分熱帶氣旋之形成爲三期：第一期時，一個低空之擾動與其東邊的一個高空的反氣旋發生關連，而產生大規模規律化的垂直運動，此時上升的氣流冷於其周遭的氣流。第二時期，上升氣流由於凝結時所發出之潛熱，而逐漸由對流層之上方向下開始變暖。原有之冷心 (Cold-core) 擾動開始變爲熱心擾動。第三期時，熱心充滿了對流層，此時高空之反氣旋座落在低空氣旋之上方，上空氣流加強外流，海面氣壓驟然下降，熱帶氣旋生成。

除了早期發現颱風成螺旋雲分佈及其能量主要來自凝結熱外，颱風之細部結構及其各種變化尙不爲人知。一般來說[7]，颱風總是生成在海面溫暖的地方（溫度在 27°C 以上），是一個挾風帶雨，具有颱風眼特徵的低壓，海面溫暖的濕氣捲入颱風中心，上升凝結放出熱能而持續颱風之成長。雖然颱風之熱功率極低（3%左右），但是一個颱風一天內所放出之凝結熱仍相當於四百個二千萬頓氫彈所能產生的熱能。

在颱風成長及運動方面，隨着高速電子計算機之進展，利用數值分析去解基本方程式 (Primitive equations) 或近似地轉方程式 (Quasi-geostropic equations)，而研探颱風之技術也日益進步。假設颱風係對稱而研究颱風成長者近年有 Ooyama[6]、Yamasaki[11]及 Rosenthal[8]。在颱風運動方面，前幾年 Nitta[5]修訂 Gambo 的渦旋方程式而更進一步的預測颱風之變化，最近 Manabe 及 Smagorinsky 等人[3]藉一般大氣環流模型直接研探大氣暨颱風之變化及運動等原則。

當颱風轉入海面溫度較低之處或登陸陸地上後，熱來源劇然喪失（陸地上摩擦阻力亦加大），龐大的颱風不一會就失去了威風而漸漸消失。然而它所挾帶的雨量却仍可能持續爲害一段時間[9]。

鑒於颱風强大的破壞力，近期有 Project Stormfury 試圖改進颱風[10]。此計劃以碘化銀注入颱風眼周遭，使超冷的水凝結成冰，放出的熱量使颱風中心低壓附近之壓力減低。如此颱風眼周遭壓差減小，而使颱風威力減小。唯其成效迄今尙難斷言。

二、研　究　內　容

颱風研究大致上可分爲三類：

第一類是對颱風本身的研究，可分爲四項：

1.) 颱風觀測 (Observational Research)：蒐集、整理、歸納及分析颱風資料，研究與颱風因有關素之變化、颱風運動之原則等。

a. 颱風之動力及熱結構等。

b. 颱風之運動、加强或减弱與下列因素之關係：
baroclinity, topograph, static stability distribution, pressure and wind distribution, time change of atmospheric states in the vicinity of typhoons etc.

c. 颱風能量之計算。

d. 颱風未發前之觀測分析及(1b)中因素對颱風形成之影響。

e. 颱風雲雨之觀測分析。

2.) 颱風理論（Theoretical Research）：研究颱風之成因、結構、能量、動態及風雨等之變化。

a. 颱風及熱帶擾動之動力及熱力理論。

b. (1b)中因素對颱風之生成、加强、運動及減弱之影響。

c. 歸納暨分析颱風實驗之成果。

d. 分析數值颱風模型。

3.) 颱風實驗（Experimental Research）：

a. 室內研究：以模型仿製觀測結果及試驗理論之可靠性。

b. 室外研究：颱風取樣及改造等。

4.) 颱風操作（Operational Research）：

a. 分析及改進現有颱風預報方法。

b. 根據觀測理論及實驗結果，改進操作技術。

第二類是對颱風可能釀成災害之研究，可大致分爲三項：

1.) 暴風：研究及分析風力與結構物之關係，以爲結構物設計之規範等。

2.) 暴雨：研究颱風可能降雨量與地形及洪水之關係，以爲颱風可能降雨量先期預報之根據及防洪之依據。

3.) 浪潮：研究颱風湧浪對河川、港口及港內船隻之影響。

第三類爲有關之大氣科學問題，如雲物理、動力氣象學等。

三、初期研究計劃

本所初期研究計劃側重於颱風運動方面之研究：在設置一個 Physico-mathematical typhoon model: The basic hydrodynamic and thermodynamic equations used in atmospheric circulation system only represent systems large enough to be strongly influenced by the Earth's rotation and to obey the hydrostatic equation. Thus, in the numerical simulation of tropical cyclone motions, many small-scale phenomena have to be parameterized, in terms of the large-scale dependent variables.

Ooyama[6] used the gradient wind assumption in forming a numerical model for the life cycle of tropical cyclones. He carried horizontal velocity at three levels in the vertical and represented temperature only at an upper level and in the Ekman layer. No allowance for the vertical variation of static stability is provided and water vapor content is predicted only in the boundary layer. Yamasaki[11] and Rosenthal[8] employed primitive rather than balanced equations in forming numerical model for tropical cyclone development and had substantially greater vertical resolution. They differ in that the former uses (P) and the latter uses (Z) coordinates. And Rosenthal's system is open at the lateral boundary, whereas Yamasaki's is closed. The accuracy of the finite-difference methods used in solving the model equations has been discussed by Molenkamp[4]. Incorporating the effect of the non-adiabatic heating in the lower troposphere into the baroclinic model used by Gambo, Nitta[5] employed a quasi-geostropic four level numerical model in weather prediction. The predicted displacements of typhoons show a great extent of retardation possibly due to the crude difference cells he was using. Recently, a moist-convective global atmospheric circulation model with realistic orography was constructed by Manabe et al.[3] to analyze the structure and energetics of the tropical circulation. The proposed research intends to form a physical-mathematical typhoon model in predicting the dynamics and structures of typhoon concerning Taiwan island.

參 考 文 獻

(1) Baker, D.J. and Robinson, A.R., A Laboratory Model for the General Ocean Circulation, *Phil. Trans. Roy. Soc. London*, 265, 533,(1969).

(2) Chang, C.C. and Chen, C.M., Laboratory Modelling Relevant to Hurricanes, *Bull. Am. Meteor. Soc.*, 50, 760,(1969).

(3) Manabe, S., Smagorinsky, J., Holloway, J.L. and Stone, H.M., Simulated Climatology of a General Circulation Model with a Hydrologic Cycle, *Monthly Wea. Rev.*, 98, 175,(1970).

(4) Molenkamp, C.R., Accuracy of Finite-Difference Methods Applied to the Advection Equation, *J. Appl. Meteoro.*, 7, 160,(1968).

(5) Nitta, T., Some Examples of Numerical Weather Prediction, with the Special Emphasis on the Development and Maintenance of Relatively Smalll Scale Cyclones, *J. Meteoro. Soc. Japan*, 43, 148,(1965).

(6) Ooyama, K., Numerical Simulation of the Life Cycle of Tropical Cyclones, *J. Atmos. Sci.*, 26, 3,(1969).

(7) Palmén E. and Newton, C.W., *Atmospheric Circulation Systems*, Academic Press, N.Y. (1969).

(8) Rosenthal, S.L., A Circularly Symmetric Primitive Equation Model of Tropical Cyclone Development Containing an Explicit Water Vapor Cycle, *Monthly Wea. Rev.*, 98, 643,(1970).

(9) Schwarz, F.K., The Unprecedented Rains in Virginia Associated wrth the Remnants of Hurricane Camille, *Monthly Wea. Rev.*, 98, 851,(1970).

(10) U.S. Departmet of Commerce, *Hurricane*, ESSA,(1969).

(11) Yamasaki, M., A Tropical Cyclone Model with Parameterized Vertical Partition of Released Latent Heat, *J. Meteor. Soc. Japan*, 46, 202,(1968).

(12) Yanai, M., Evolution of a Tropical Disturbance in the Carribben Sea Region, *J. Meteor. Soc. Japan*, 46, 86,(1968).